III-V epitaxy by RP-CVD : from thin film growth to solar cell devices

Lise Watrin

INSTITUT POLYTECHNIQUE DE PARIS

ÉCOLE POLYTECHNIQUE

IP PARIS

NNT : 2024IPPAX075

Thèse de doctorat

III-V epitaxy by RP-CVD: from thin film growth to solar cell devices

Thèse de doctorat de l'Institut Polytechnique de Paris
préparée à l'Ecole polytechnique

École doctorale n°626 Institut Polytechnique de Paris (ED IP Paris)
Spécialité de doctorat : Sciences et technologies industrielles

Thèse présentée et soutenue à Palaiseau, le 4 novembre 2024, par

Lise Watrin

Composition du Jury :

Ignacio Rey-Stolle Professor, Polytechnic University of Madrid (Solar Energy Institute)	Président
Maria Losurdo Director, National Council Research Institute of Padova (ICMATE)	Rapporteuse
Françoise Massines Director, Université Perpignan Via Domitia (PROMES-CNRS)	Rapporteuse
Charles Renard Researcher, Université Paris-Saclay (C2N-CNRS)	Examinateur
Nils-Peter Harder Lead Scientist Solar Energy, TotalEnergies	Examinateur
Pere Roca i Cabarrocas Professor, IPVF and Ecole polytechnique (LPICM)	Directeur de thèse
Karim Ouaras Researcher, Ecole polytechnique (LPICM)	Co-Directeur de thèse
Jean Decobert Research Department Head, Nokia Bell Labs	Invité
Erik V. Johnson Research Director, Ecole polytechnique (LPICM)	Invité

Little blue, be my anchor
Be my light, my compass star
Be my darkness, be my danger
Be the strings of my guitar
Little blue, how I love you
Something strong and something true
In your arms, so dear and gentle
There’s a light that leads me back to you

Little blue (Mahogany sessions), Jacob Collier.

Remerciements

J’aimerais tout d’abord remercier tous les membres du jury d’avoir accepté d’évaluer mon travail : Françoise Massines et Maria Losurdo en tant que rapporteuses, Ignacio Rey-Stolle, Charles Renard et Nils-Peter Harder en tant qu’examinateurs, Jean Decobert et Erik Johnson en tant qu’invités.

Je tiens ensuite à exprimer ma profonde gratitude à ma direction de thèse, en commençant par mon directeur de thèse, Pere Roca i Cabarrocas. Pere, tu m'as offert l'opportunité de travailler sur ce projet passionnant qui, je le sais, te tenait particulièrement à cœur. Je te remercie pour la confiance que tu m'as accordée dès le début et tout au long de cette aventure, en me confiant ce réacteur qui, il faut le dire, nous a bien mis à l'épreuve. Ton soutien constant m'a permis d'aborder ces obstacles avec optimisme et détermination. Ta passion inébranlable pour la recherche, toujours émerveillé par un nouveau résultat et toujours prêt à lancer de nouvelles expériences, a été une source d'inspiration énorme pour moi. Je tiens également à souligner ta disponibilité exceptionnelle, malgré ta double casquette de professeur à l’Ecole polytechnique et de directeur scientifique à l’IPVF, sans oublier tous les autres rôles que tu endosses. Je mesure pleinement la chance que j'ai eue de bénéficier de ton expertise, de ton encadrement bienveillant et de ton engagement sans faille. Merci pour tout.

Mes prochains mots iront à Karim Ouaras, mon co-directeur de thèse. Je souhaite également te dire un grand merci Karim, pour ta présence et ton soutien tout au long de ces trois dernières années. Tu as investi pleinement ton rôle de co-directeur de thèse, et j'ai énormément appris au fil de nos nombreuses discussions. Ton approche toujours réfléchie et tes conseils avisés m'ont été d'une grande aide. Au-delà d'être un chercheur remarquable, tu es une personne profondément bienveillante. Je te suis très reconnaissante pour ta disponibilité constante tout au long de cette belle aventure.

Enfin, je remercie Erik Johnson, qui a également contribué à l'encadrement de ce travail en tant que co-directeur de thèse. Ton expertise précieuse a été un atout important pour mener à bien ce projet, et je te suis reconnaissante pour les conseils et les retours que tu as partagés. Merci pour ton soutien et ta contribution Erik.

C’est ensuite à toute l'équipe *plasma III-V* du LPICM que je souhaiterais m’adresser. Tout d’abord à Cyril Jadaud et Jean-Charles Vanel, le duo de choc. Cyril, ton aide précieuse sur tous les aspects mécaniques du réacteur et les questions de sécurité a été inestimable, merci car je sais que cela n'a pas toujours été de tout repos ! Jean-Charles, ton travail acharné sur l'automatisation du réacteur avec LabVIEW a également été un sacré défi, mais ta persévérance et ton expertise ont fait toute la différence. À vous deux, je suis reconnaissante non seulement pour votre expertise, mais aussi pour votre grande bienveillance. Un grand merci ensuite à Pavel Bulkin, dont l'ingéniosité et les larges connaissances ont été précieuses. J'ai énormément appris de toi, que ce soit sur l'ellipsométrie, la maintenance du réacteur ou sur de nombreux autres aspects du projet. Merci Pavel pour avoir souvent été une référence indispensable tout au long

de cette aventure. Enfin, un grand merci à François Silva, le concepteur du réacteur sans qui la thèse n'aurait pas vu le jour. J'admire ton optimisme et tes compétences impressionnantes en simulation qui m'ont permis d'avoir de belles images pour illustrer cette thèse. Ta vision et ton expertise ont évidemment grandement contribué à la réussite de ce projet.

Je souhaite exprimer ma gratitude aux nombreuses personnes dont l'expertise a été précieuse pour ce projet. Tout d'abord, je tiens à remercier Jean Decobert et Nicolas Vaissière du III-V Lab pour leurs conseils d'experts sur les matériaux III-V, qui nous ont aidés à surmonter bien des verrous dans la compréhension du réacteur. Un merci tout spécial à toi, Nicolas, pour les innombrables allers-retours d'échantillons et les mesures d'ECV ! Ensuite un merci, et non des moindres, à toutes les personnes qui ont travaillé sur les caractérisations de mes échantillons : Kassiogé Dembélé et Jean-Luc Maurice pour le TEM au LPICM, Ludovic Largeau et Nathaniel Findling pour la DRX au C2N, Mirella Al Katrib et Muriel Bouttemy pour la XPS et François Jomard pour le SIMS à l'ILV, Dominique Muller pour la NRA et la RBS à iCube, Alexandre Jaffré pour le Raman et la PL au Geeps, Stefano Pirotta pour la CL au C2N et Aitana Cano Pérez pour les mesures sous simulateurs solaires à l'IES Madrid. Et enfin les supers experts de l'IPVF : Baptiste Bérenguier, Alexandra Levtchenko, et Daniel Ory pour les caracs de photolum et Alexandre Blaizot pour l'AFM. Un grand merci à Florian Hilt et Stéphane Collin pour votre expertise et votre management sur le programme COSY. Merci à Elie de Panafieu pour ses précieux conseils.

Je suis profondément reconnaissante pour toutes les superbes rencontres faites à l'IPVF au cours de ces quatre années de stage puis de thèse. Il est difficile de tous vous nommer, mais je tiens à mentionner quelques-uns d'entre vous : Marion et Aurélien qui m'ont permis d'intégrer ce bel institut, Jean, Nao (merci pour les fous rires), Vincent, Célia, Lauriane, Van-Son, Amadéo, Maxime, Jérémie, Karim, Ange, Jeronimo, Sophie, Nicolas, Julie, Régis, Armelle, Sonia, Arthur, Aubin, Loukiana, Javid, Estelle, Liam, Pierre, Amelle, Daniel, Camille, Emmanuelle, Pilar, Anatole, Iwan, Géraud, Isabelle, Bérengère, Bénédicte… Vous me manquerez ! De même pour mes collègues du LPICM : un merci tout spécial à Lakshman mon coloc de labo et aussi à Yvan, Chandralina, Monalisa, Holger, Haifa, Denis, Junkang, Martina, Deyan, Aymeric, Alexandre, Francesco, Mateusz, Guili, Pingping, Inass, Shenming, Michel, Hindia, Aram, Christian, Mbaye, Jean-Eric, Ileana, Martin, Laurence, Khaoula, Gabriela, Fabien, Jean-Luc, Marc, Jonathan, Antonio, Tatiana, Eric…
Yves et Alba, je vous souhaite tout le meilleur pour vos thèses.

Joseph, quelques mots tout spécialement pour toi. Merci d'avoir été mon partner in crime durant ces trois années intenses. La thèse sans toi aurait été une expérience bien différente. Je suis heureuse d'avoir trouvé un véritable ami. Maintenant, c'est bientôt ton tour, alors je te souhaite plein de courage dans cette dernière ligne droite !

Un grand merci aussi à tous les autres copains du Plateau. Rémi, je suis convaincue que tu vas briller dans ta thèse ! Merci également à tous les amis du cours de danse et Mélaine, pour avoir animé ces séances qui m'ont offert une évasion hebdomadaire. Charlotte, Naomie, Cléo, Guillaume, Katia, Laurie, Nam, bon courage pour vos thèses. Une pensée pour Inés que j'ai eu la chance de rencontrer à l'IES Madrid, je te souhaite tout le meilleur pour la suite, peut-être avec un passage à l'IPVF ?

Et bien sûr, il y a les amis. Ceux de Paris : ma Nouche, Guigui, ma Milie, Ougo, Cait, Saulet, Marie, Hugo, toute l'Apocaliste, ceux de Nancy : Elise, Nathan, Andrea, Belin, Thibaut et tous les autres. Vous êtes des compagnons de route fantastiques, votre soutien a été précieux tout au long de ce parcours. Votre présence et vos encouragements à tous ont été une source inestimable de réconfort. J'ai hâte de continuer à partager de nombreux moments et aventures avec vous à l'avenir.

Enfin, je souhaite adresser mes plus profonds remerciements à ma famille et à ma belle-famille pour leur soutien et leur accompagnement tout au long de ce parcours. Vous apportez une douceur précieuse dans ma vie, je vous aime.

À mes parents, merci pour votre amour et votre soutien sans faille. À Nanette, merci pour ta douceur et ton amour, je t'admire profondément. À mes deux sœurs, Claire et Cécile, vous comptez plus que les mots ne peuvent le dire, je vous chéris du plus profond de mon cœur.

Hokis, merci pour tout, ես սիրում եմ քեզ.

Content

Chapter 1. Introduction 14

A. III-V semiconductors 14
I. Overview 14
II. Exploring specific cases: GaN and GaAs 15

B. III-V in the context of photovoltaic energy 18
I. Fundamentals of solar cells 18
II. Photovoltaics at the heart of the energy transition 20
III. Tandem solar cells: integrating III-V with silicon 22

C. Challenges in epitaxial growth of III-V on Si 24
I. A technical challenge: material incompatibilities 24
II. A cost challenge: current solutions 26

D. Overcoming challenges using plasma 30

E. Objective of the thesis project 32

Chapter 2. A custom-build reactor for III-V growth – Remote Plasma CVD 36

A. Plasma basics 36
I. Key properties of plasmas 36
II. Interest of remote plasma assistance in CVD 39

B. Architecture of the RP-CVD reactor 42
I. Plasma generation system 42
II. Gas injection system 45
III. Substrate holder and heating system 46

C. Plasma characteristics 48
I. E-H transition 48
II. Plasma power process window 50

Chapter 2. Summary 51

Chapter 3. Growth of GaN thin films by RP-CVD as a proof of concept 54

A. GaN growth on sapphire 55
I. Growth process 55
II. Main structural and morphological features 55
III. Plasma as a lever for the in-situ growth of buffer layers 57

B. Direct growth of highly oriented GaN thin films on silicon 59
I. Growth process 59
II. Structural and morphological features 61
III. GaN polarity determination 64
IV. Chemical composition analysis 65

C. Ultrathin SiN barrier enables improved GaN growth on Si 67
I. Growth process 68
II. Effects of *'meltback etching'* 69
III. Proposed ultrathin SiN barrier solution 70
IV. Enhancement of GaN film properties 73
V. Proposed growth model 74

Chapter 3. Summary 77

Chapter 4. Study and optimization of GaAs thin film growth by RP-CVD 80

A. GaAs homoepitaxial growth 80
I. Main structural and morphological features 80
II. Chemical composition analysis 83
III. Electronic properties investigation 84

B. GaAs direct growth on c-Si 86
I. On the particular role of growth temperature 86
II. Main structural and morphological features 87

C. GaAs growth on virtual substrate 89
I. What is a virtual substrate: fabrication process 89
II. Structural and morphological features 91
III. Electronic properties investigation 96

Chapter 4. Summary 99

Chapter 5. Doping optimization for effective integration into solar cells 102

A. The role of plasma in doping control 102
I. The purpose and methods to achieve doped layers 102
II. Doping level targets in our solar cell architecture 103
III. The role of plasma in GaAs doping during RP-CVD growth 103

B. Fine tuning of the doping level with TMGa 107
I. Arsine introduction: in the plasma versus out-of-plasma 108
II. Effect of deposition temperature 109
III. Effect of plasma power 110
IV. Effect of chamber pressure 111

C. A drastic approach for doping reduction: TEGa 112
I. TMGa versus TEGa precursor decomposition 112
II. Evaluation of the doping reduction 113
III. Still a wafer-grade film quality 114

D. First RP-CVD grown GaAs absorber integration into a solar cell 115
I. TMGa-based solar cells 115
II. TEGa-based solar cells 122

Chapter 5. Summary 126

General conclusion 127

Perspectives 128

Appendix A. 130

Characterization techniques 130

Appendix B. 134

Supplementary TEM images 134

Appendix C. 135

MBE-grown solar cell 135

Appendix D. 139

Optimization of homoepitaxial GaAs electronic properties 139

Appendix E. 140

Résumé long en français 140

General bibliography 143

List of figures 157

List of tables 161

Scientific contributions 162

List of Acronyms

AFM atomic force microscopy

ALD atomic layer deposition

AM1.5 air mass coefficient at 1.5 times the thickness of the atmosphere

BF bright field

BSF back surface field

CL cathodoluminescence

c-Si crystalline silicon

CVD chemical vapor deposition

EDX energy dispersive X-ray

EHT electron high tension

EQE external quantum efficiency

ETL electron transport layer

FF fill factor

FWHM full width at half maximum

GaAs gallium arsenide

GaN gallium nitride

Ge germanium

HAADF high-angle annular dark-field

HRXRD high resolution X-ray diffraction

HRTEM high-resolution transmission electron microscopy

MBE molecular beam epitaxy

MOCVD metalorganic chemical vapor deposition

PCE power conversion efficiency

PECVD plasma enhanced chemical vapor deposition

PL photoluminescence

PV photovoltaic

QE quantum efficiency

RP-CVD remote plasma chemical vapor deposition

SE spectroscopic ellipsometry

SEM scanning electron microscopy

STEM scanning transmission electron microscope

TDD threading dislocation density

TEGa triethylgallium

TMGa trimethylgallium

TRPL time-resolved photoluminescence

Chapter 1. Introduction. 14

A. III-V semiconductors 14
I. Overview 14
II. Exploring specific cases: GaN and GaAs 15

B. III-V in the context of photovoltaic energy 18
I. Fundamentals of solar cells 18
II. Photovoltaic at the heart of the energy transition 20
III. Tandem solar cells: integrating III-V with silicon 22

C. Challenges in epitaxial growth of III-V on Si 24
I. A technical challenge: material incompatibilities 24
II. A cost challenge: current solutions 26

D. Overcoming challenges using plasma 30

E. Objective of the thesis project 32

Chapter 1. Introduction

A. III-V semiconductors

I. Overview

The advent of integrated circuits marked a significant milestone in the semiconductor industry, with silicon emerging as the predominant material owing to its advantageous characteristics such as its high thermal conductivity, abundancy and low-cost fabrication thanks to very high-throughput production[1]. Nevertheless, the inherent limitations of silicon, characterized by its indirect energy band structure, compromise its efficiency as a light-emitting material[2]. Additionally, silicon exhibits relatively low electron mobility, making it less than ideal for applications requiring high-speed device components.

In response to emerging technological demands, research shifted towards exploring new materials to compensate for silicon's limitations. III-V materials emerged as a solution in this pursuit. This class of crystalline materials is composed of groups III and V elements from the periodic table (**Figure 1.1**). They take their name from the combination of their constituent elements, such as aluminium (Al), gallium (Ga), boron (B) and indium (In) for Group III, and nitrogen (N), phosphorus (P), arsenic (As) and antimony (Sb) for Group V. These compounds may be in binary form (GaAs, InP, BN, etc.) or contain more constituent elements (GaInP, AlGaAs, AlGaInP, etc.).

These compound materials have remarkable optoelectronic properties, resulting from the specific combination of their constituent atoms. Especially, III-V semiconductors are generally known for their high electron mobilities and direct band gaps, which means that they efficiently facilitate the generation and recombination of electron-hole pairs, making them particularly attractive for optoelectronic device applications such as laser diodes, high-frequency transistors, photodetectors and solar cells[3].

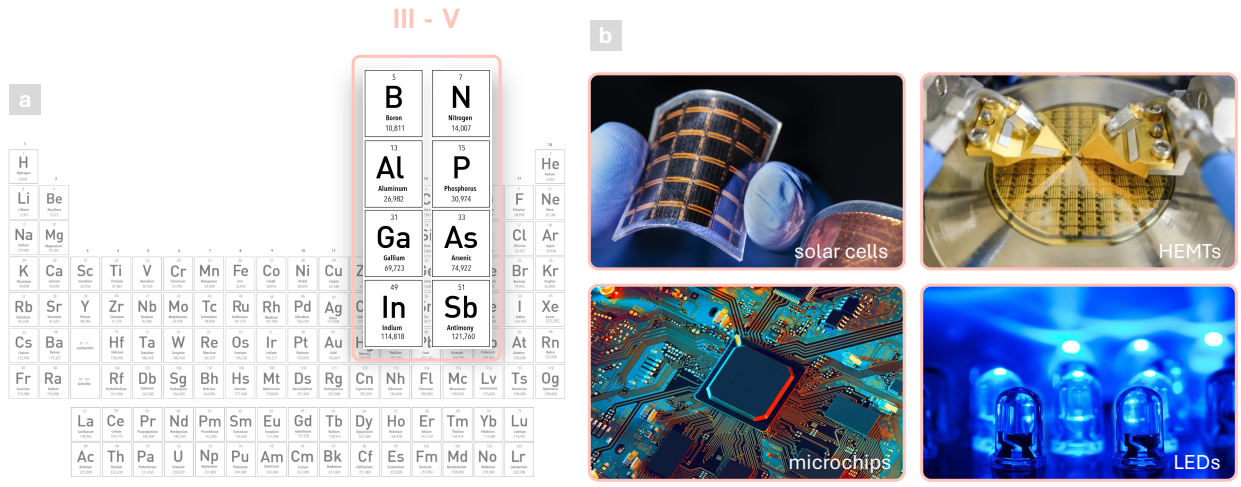

Figure 1.1. *a) III and V elements highlighted in the periodic table and b) some examples of III-V applications.*

Indeed, III-V compounds offer a crucial advantage in creating novel functional devices through bandgap engineering to form heterostructures. This process involves stacking semiconductor thin films with varying energy bandgaps (**Figure 1.2**), resulting in devices with designed electrical and optical properties[4,5]. As a result, ongoing research efforts continue to explore innovative applications of III-V semiconductors across diverse fields, aiming to harness their capabilities for further technological breakthroughs and advancements[6].

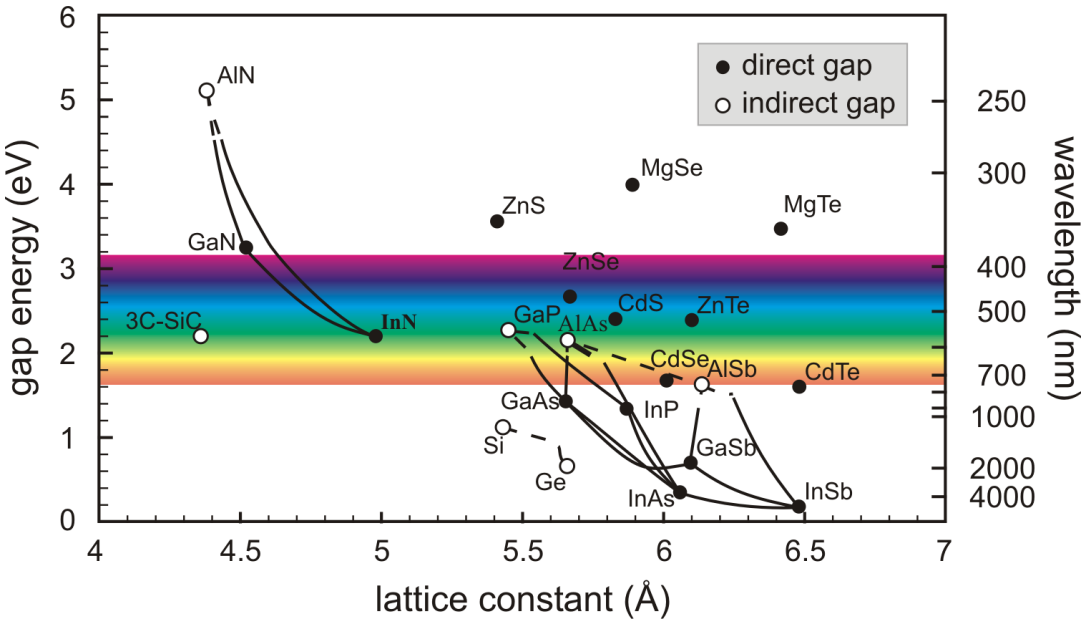

Figure 1.2. *III-V semiconductors bandgap versus lattice parameter at 300 K*[7].

In particular, the future of III-Vs is also taking shape in its integration with silicon, in the form of "III-V on silicon devices". This integration combines the advantageous properties of III-V materials, such as high electron mobility and direct bandgaps, with the established process and cost-effectiveness of silicon technology. These devices hold promise for a wide range of applications, including high-speed electronics, optoelectronics, and photovoltaics[8–10]. We will see in the course of this manuscript that this integration poses, nevertheless, a number of technological challenges to overcome.

II. Exploring specific cases: GaN and GaAs

1. Gallium nitride (GaN)

Since the emergence of white light-emitting diodes was made possible by the development of blue LEDs based on GaN, for which the 2014 Nobel Prize in Physics was awarded, this material from the III-Nitride family has completely revolutionised the semiconductor industry[11].

Under standard ambient conditions, GaN typically adopts the thermodynamically stable wurtzite (WZ) structure (**Figure 1.3**)[12] but other structures such as zinc blende and rock salt also exist (cubic phase) even though achieving them is more challenging. Hereafter, our discussion will concentrate on the wurtzite properties as this is the preferred structure for most applications.

This structure is characterized by a hexagonal unit cell with two lattice constants, denoted as c (5.186 Å) and a (3.189 Å), containing six atoms of each type. The space group assigned to the wurtzite structure is P63mc in the Hermann–Mauguin notation system[13]. This structure consists of two closely packed hexagonal sublattices. One sublattice is occupied by atoms from column III of the periodic table, here gallium, while the other sublattice is occupied by atoms from column V, here nitrogen. These two sublattices are offset from each other along the crystallographic c-axis by a distance denoted as "u" where u = 3c/8 [14].

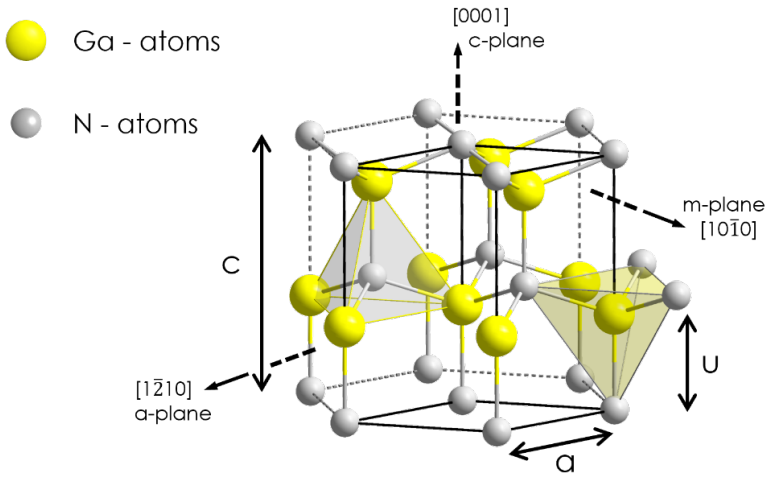

Figure 1.3. *GaN hexagonal wurtzite structure.*

A special feature of III-nitrides compared with other III-V compounds is that films can exhibit a Ga- or N- polarity (**Figure 1.4**). This unique property arises from the crystal structure's lack of inversion symmetry along the c-axis, attributed to the presence of two hexagonal lattices within the material. In Ga-polarity, also known as metal polarity, the growth direction aligns with the +c direction when three bonds on a Ga atom with tetrahedral coordination face towards the substrate. Conversely, in N-polarity, the growth direction aligns with the -c direction when three bonds face in the growth direction. This distinction in polarization directions significantly influences the material's properties and behaviour. For example, the polarity can affect the surface energy, surface morphology, and chemical reactivity of the crystal[15]. It also influences the electronic properties of GaN-based devices[16]. Understanding and controlling the polarity of III-nitrides are crucial for optimizing their performance in various applications, including electronics, optoelectronics, and photonics.

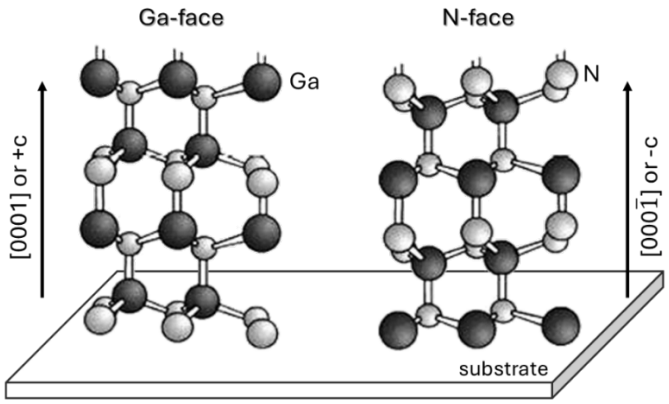

Figure 1.4. *Schematic illustration of polarity along c-axis in wurtzite crystal. Adapted from [17].*

Table 1.1 shows the various optoelectronic characteristics of GaN at T = 300 K. This material possesses a wide direct bandgap of around 3.4 eV at room temperature. This direct bandgap facilitates effective generation and recombination of electron-hole pairs and makes GaN the material of choice for blue and ultraviolet applications[18,19]. Its other attributes, such as a low dielectric constant, a high thermal conductivity, and a high electron mobility make it very promising for devices such as for LEDs, lasers, transistors and photodetectors[20]. Moreover, thanks to its high resistance to radiation and corrosive environments due to its good chemical resistance, it is also well suited for high-power, high voltage and high temperature applications, competing with SiC[21].

Parameter	Symbol	GaN
Energy gap (eV)	E_g	3.39
Electron affinity (eV)	E_a	4.1
Electron mobility ($cm^2/V.s$)	μ_n	1000
Hole mobility ($cm^2/V.s$)	μ_p	200
Dielectric constant	ε	8.9
Thermal conductivity ($W.cm^{-1}.K^{-1}$)	k	1.3
Thermal expansion coefficient ($10^{-6}K^{-1}$)	α	4.3
Density (g/cm^3)	ρ	6.15

Table 1.1. *Some GaN material properties at room temperature[22–24].*

While GaN bandgap may not be ideal for serving as the active layer in solar cells because of the low presence of blue light in the solar spectrum, it nevertheless exhibits promise for applications within the photovoltaic domain. In particular, researchers have explored the potential of GaN to be used as contact layers in InGaN based solar cells, where the bandgap can be tuned from 0.7 to 3.4 eV[25,26].

2. Gallium arsenide (GaAs)

Carver Mead's pioneering work in 1965, which involved fabricating and testing the first GaAs Schottky barrier gate field effect transistor (MESFET)[27], catalyzed widespread interest and rapidly thrust GaAs into the spotlight of III-V materials. It is notably well-recognized for its high electron mobility and its direct bandgap giving it important advantages that silicon lacks. GaAs, along with InP, are now the most widely used III-V materials for integrated photonic components mainly because of their widespread use in fiber optic communications[28]. We will see later that its significance is no less important in the field of photovoltaics.

GaAs films crystallize in the zinc-blende (ZB) lattice structure which is a diamond-like network where we have two interpenetrating face-centered-cubic (fcc) lattices, one made of Ga atoms and the second made of As atoms. The space group assigned to the ZB structure is F-43m in the Hermann–Mauguin notation system. As can be seen in **Figure 1.5**, each Ga atom is tetrahedrally bonded to four As atoms. The lattice constant a is 5.65 Å [29].

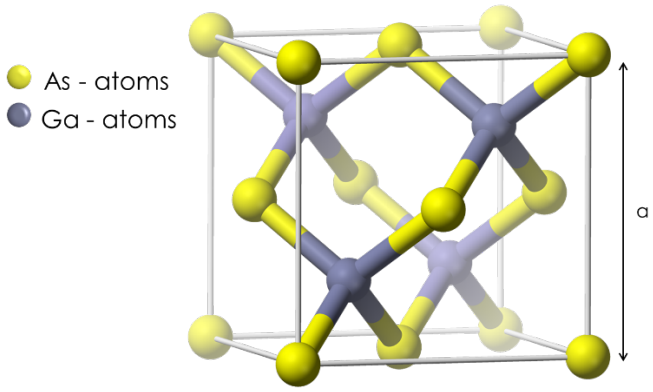

Figure 1.5. *GaAs zinc-blende structure.*

Table 1.2 shows the various optoelectronic characteristics of GaAs at T = 300 K. As we mentioned earlier, its high electron mobility is one of the most important features of this compound. In fact, it enables the fabrication of high-speed transistors and integrated circuits, making GaAs particularly suitable for applications requiring rapid signal processing, such as microwave and radio frequency devices. Also, the direct bandgap at 1.42 eV allows for efficient emission and absorption of light which is of major importance for optoelectronic devices such as light-emitting diodes and solar cells.

Parameter	Symbol	GaAs
Energy gap (eV)	E_g	1.42
Electron affinity (eV)	E_a	4.07
Electron mobility ($cm^2/V.s$)	μ_n	8500
Hole mobility ($cm^2/V.s$)	μ_p	400
Dielectric constant	ε	12.9
Thermal conductivity ($W.cm^{-1}.K^{-1}$)	k	0.5
Thermal expansion coefficient ($10^{-6}K^{-1}$)	α	5.8
Density (g/cm^3)	ρ	5.32

Table 1.2. *Some GaAs material properties at room temperature*[24,30].

B. III-V in the context of photovoltaic energy

I. Fundamentals of solar cells

1. Historical introduction

The photovoltaic effect was first observed by Alexandre Edmond Becquerel in 1839[31]. He made the marvellous discovery using a small wooden vat containing slightly acidic water and in which two metal electrodes coated with silver iodide or chloride were immersed, as illustrated on **Figure 1.6**. After exposure to light and using a galvanometer, he was able to detect very weak

generated currents and observe the wavelength influence on the photocurrent generated, i.e. the predecessor of spectral response[32]. This experiment allowed him to describe for the first time the generation of electric current in a material upon exposure to light. Nearly fifty years later, Charles Fritts produced the first functional solar cell (1% efficiency) by depositing copper and gold contacts on one side and the other of a selenium film[33]. It was another 50 years before Russell Ohl produced the first silicon solar cell, which gave a major boost to the deployment of photovoltaic energy[34].

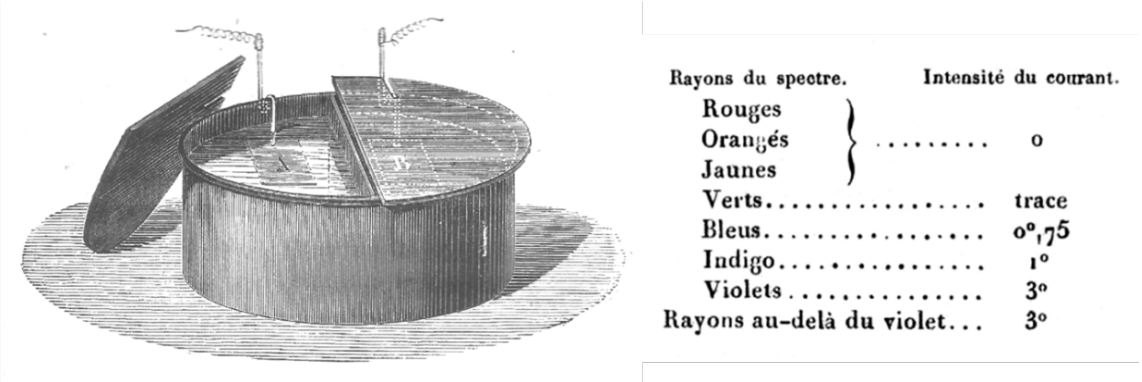

Rayons du spectre.	Intensité du courant.
Rouges, Orangés, Jaunes	0
Verts	trace
Bleus	0°,75
Indigo	1°
Violets	3°
Rayons au-delà du violet	3°

Figure 1.6. *Drawing of the electrochemical cell designed by Edmond Becquerel and his table of results on the influence of wavelength on photocurrent[31].*

2. Solar cell working principle

Let's take a closer look at how a solar cell works using **Figure 1.7**. When photons strike the surface of a semiconductor with an energy greater than its bandgap, they transfer this energy to electrons in the material, exciting them from the valence band to the conduction band and thus creating electron-hole pairs **(1)**. The p-n junction then plays an important role in preventing the electron and hole from recombining across the band gap by creating an electric field that separates the electron-hole pairs. The electrons thus join the n-type layer (electron-rich), while the holes join the p-type layer (hole-rich) **(2)**. The electrical contacts on the front and rear sides collect the photogenerated charge carriers in an external circuit **(3)**, thus generating a photocurrent **(4)**.

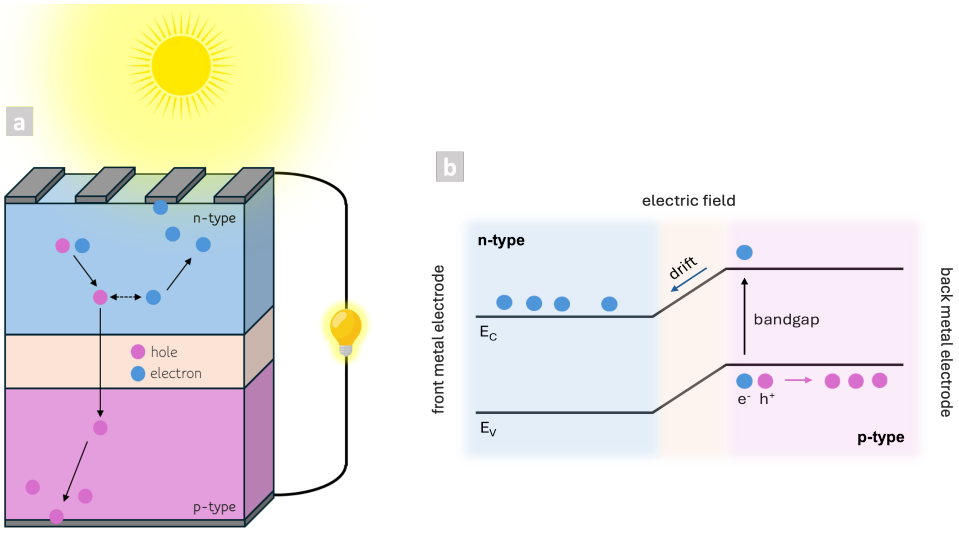

Figure 1.7. *a) Working principle of a solar cell and b) band diagram representation of the p-n junction.*

II. Photovoltaics at the heart of the energy transition

1. A concrete need to accelerate PV energy deployment

"Solar PV is lighting a path forward for clean energy transitions"
World Energy Outlook 2023, IEA[35]

To effectively steer the world towards the goal of limiting global warming to 1.5 degrees Celsius, the pace of transition must accelerate substantially. In 2015, global production capacity of solar PV stood at around 50 gigawatts (GW) and then jumped to 220 GW in 2022. Forecasts projected it to hit 500 GW by 2030 under the Stated Policies Scenario (STEPS), as illustrated in **Figure 1.8**. However, a recent update indicates that global solar PV manufacturing capacity is now anticipated to double to nearly 1,000 GW by 2024[36]! The rapid growth of solar manufacturing is even exceeding the escalation in solar PV deployment which represents opportunities to accelerate the urgently needed energy transition[35]. Various strategies to reduce CO_2 emissions have been developed, with the most ambitious one being the Net Zero Energy (NZE) which aims for carbon neutrality by 2050. Under this scenario, the International Energy Agency (IEA) estimates that by 2050, around a third of the world's electricity production could be powered by photovoltaic solar energy[37].

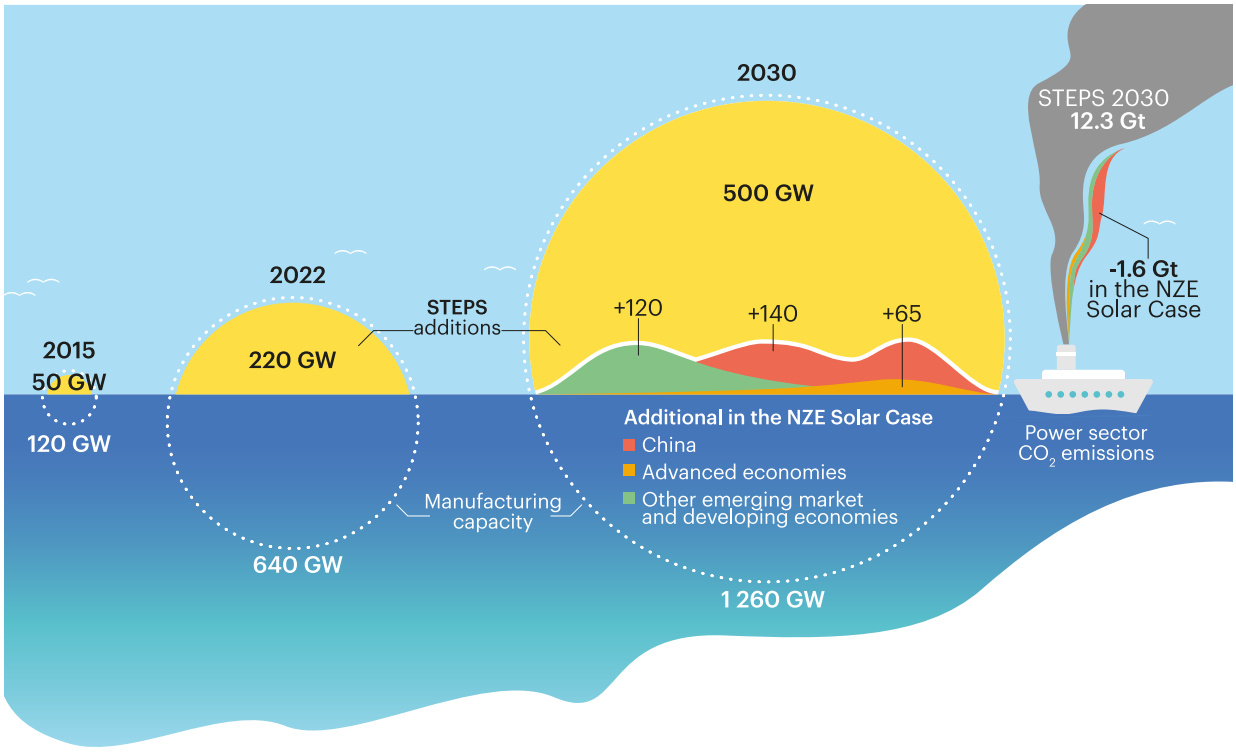

Figure 1.8. *Solar PV capacity additions in the Stated Policies Scenario and manufacturing capacities, 2015-2030[35].*

To continue to meet the huge demand generated by these ambitious targets, the photovoltaic industry needs access to high-performance technologies that remain economically viable.

2. Exploring high-performances solar cell technologies

Recent decades have seen a significant increase in interest and research efforts into a variety of solar cell technologies, **Figure 1.9** shows three key ones[38]. It has been fuelled by the relentless search for improved performance to provide sustainable energy solutions. This quest is of paramount importance in the light of growing concerns about global warming, indeed percentage-by-percentage efficiency optimisations make a huge difference in a TW market.

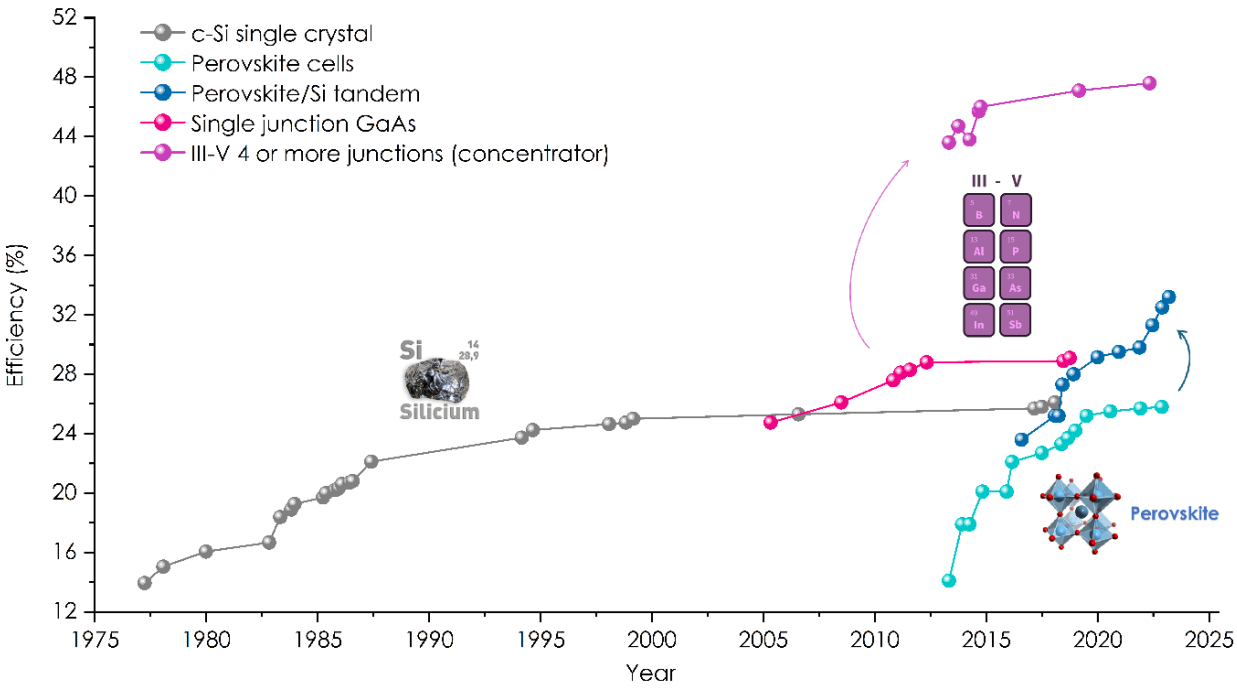

Figure 1.9. *Evolution of the efficiency of solar cells using different technologies over time, adapted from[38].*

Silicon solar cells

Crystalline silicon stands as the most established technology, currently constituting 95% of the global solar energy market. The reason for this is its low cost (levelized cost of energy (LCOE) of around 0.05 USD/kWh in 2022[39]) and its stability (around 25-30 years of lifetime[40]). Nonetheless, silicon is not the most optimal material for converting solar energy due to its relatively inefficient light absorption. To address this limitation, thick layers (typically in the range of 50 to 200 microns[41,42]) are required to obtain adequate absorption and with high crystallinity to ensure effective charge transport. Moreover, we are approaching the efficiency limit predicted by the Shockley-Queisser limit (~ 30%), which defines the maximum efficiency for a single-junction solar cell[43].

Perovskite solar cells

Looking for more absorbing materials for efficient solar cells, research has in recent years shifted its focus to thin film solar cells. This category of cells, as implied by its name, consists of thin layers of material, typically on the scale of a micron. The reduction in the quantity of materials used implies a potential to reduce costs and save resources. Also, the thinness of these cells could enable integration into flexible devices[44]. Perovskite solar cells are a good example of new thin-film solar cell technology as can be seen on **Figure 1.9**. This crystalline material, extensively

studied at IPVF, can absorb light across a wide range of wavelengths in the solar spectrum thanks to the adjustment of its bandgap. Thanks to their cost-effective production, perovskites have attracted considerable attention and seen remarkable advancements, resulting in a competitive efficiency of approximately 26%[45]. However, there are still hurdles to overcome, particularly concerning issues related to its stability stemming from its hygroscopic nature, its toxicity from the use of lead and the difficulties of scaling-up[46].

III-V solar cells

Last but not least, III-V solar cells represent a third technology primarily valued for their unrivalled efficiency. Indeed, this technology stands as the most efficient by far both in single and multijunction configurations (**Figure 1.9**) thanks to its widely tunable composition leading to a remarkable energy conversion potential. Moreover, these cells present a better temperature stability and a higher radiation resistance than silicon. However, despite their exceptional performance, III-V solar modules are associated with higher production costs due to the complexity of their fabrication process and the cost of materials, about a 400 times more expensive than a silicon module[47]. As a result, they are currently dedicated to space or niche market applications[48]. We will explore more in details their potential and the strategies to mitigate the cost of this high risk – high gain technology in the next sections.

III. Tandem solar cells: integrating III-V with silicon

The single-junction solar cells presented above have a limitation in terms of conversion efficiency linked to the nature of the material, in that they can only efficiently convert a limited range of the solar spectrum into electricity. This efficiency limit in solar cells is known as the Shockley-Queisser limit and is intricately tied to the bandgap of the material composing the single junction[49], as represented on **Figure 1.10**. Due to optical and electrical loss mechanisms, a large part of the solar spectrum remains unused, i.e. the higher or lower wavelengths that do not correspond to the bandgap energy of the material.

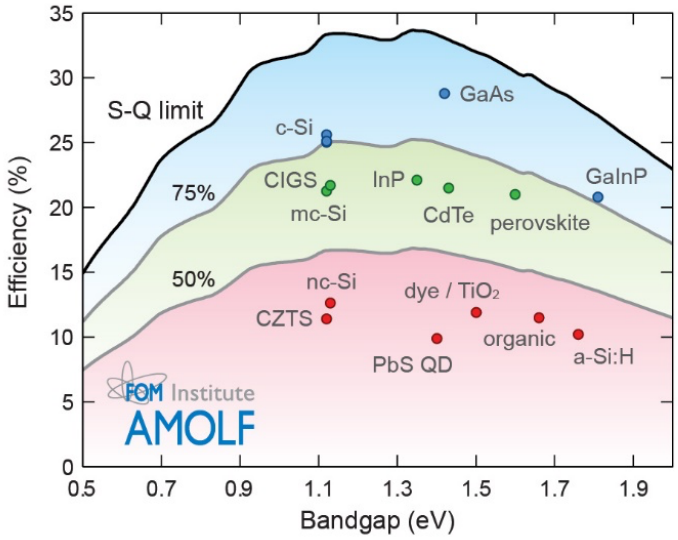

Figure 1.10. *Representation of Shockley-Queisser detailed-balance limit (black line) achieved by record cells, grey lines showing 75% and 50% of the limit (grey lines). Figure taken from the work of A. Polman [50].*

This is where tandem solar cells come in. Rather than using a single photoactive semiconductor material, tandem (or multijunction) solar cells combine two (or more) cells of semiconductors having different bandgaps. Each cell is optimised to efficiently absorb a specific part of the solar spectrum. Typically, the solar cell positioned on top of the stack possess a wide bandgap, enabling to efficiently convert UV and blue light while minimizing thermalization losses and transmitting the solar spectrum in the close-infrared region to the bottom of the stack which features narrower bandgaps. The next step is to combine the most complementary bandgaps in the solar spectrum in order to maximize conversion efficiency to the fullest extent possible, as shown in **Figure 1.11**.

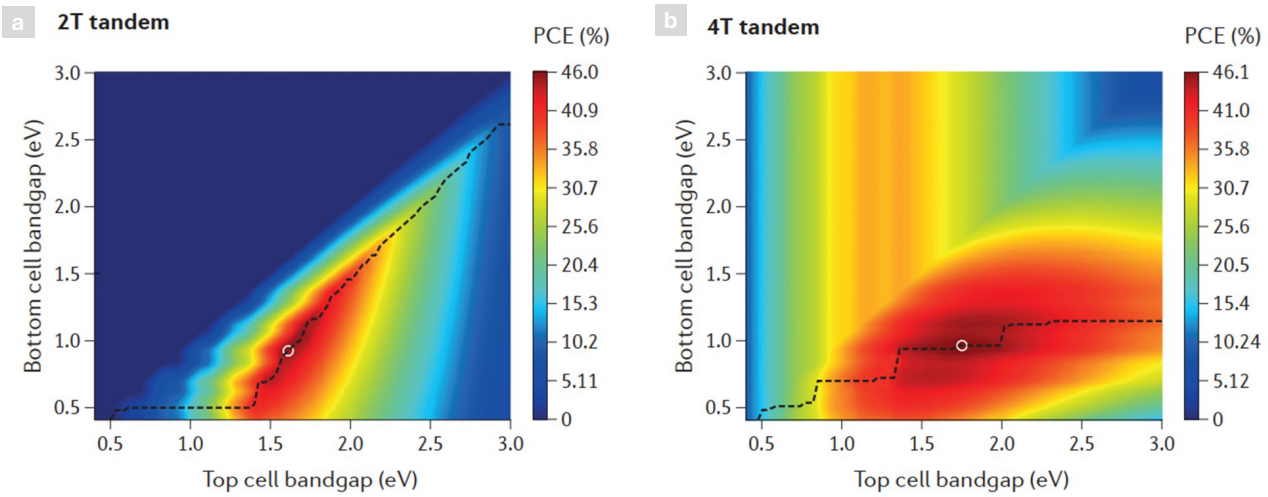

Figure 1.11. *Theoretical maximum power conversion efficiency (PCE) as a function of front (top) and rear sub-cell bandgap for 2T (left) and 4T (right) architectures, assuming no absorption losses. The dashed line traces the peak efficiency for the whole range of front-cell bandgaps, and the white circles indicate the maximum power conversion efficiencies. Figure taken from the work of G.E. Eperon*[51].

Tandem solar cells can therefore be made up of different combinations of semiconductor materials assembled in “sandwiches”: perovskite/silicon, III-V/silicon, III-V type 1/III-V type 2, and so on. To make these combinations, the two parts need to be stacked together in a stable manner and electrically connected. Bonding is carried out either directly, by growing the second cell on top of the first, or indirectly, by bonding the two cells previously grown separately. Two solutions are commonly used for the electrical connection: the 2-terminal configuration (2T) and the 4-terminal configuration (4T) represented in **Figure 1.12**. In the 2T configuration, the cells are connected monolithically in series and two electrodes are used to collect the current generated by the tandem. In this configuration, top and bottom cells must be current-matched, according to Kirchhoff ’s law[52]. 4T configuration offers independent control over each cell in the tandem using four separate electrodes. Thus, in this scenario, the constraints of current matching are circumvented, requiring less rigorous adjustments to the bandgap as can be seen on **Figure 1.11. b)** with a larger range of E_g values leading to high efficiency values compared to **Figure 1.11. a)**. Although the 4T configuration offers advantages in terms of efficiency and stability management, it requires more complex design and manufacture than the 2T configuration. Consequently, 2T is favored in industry.

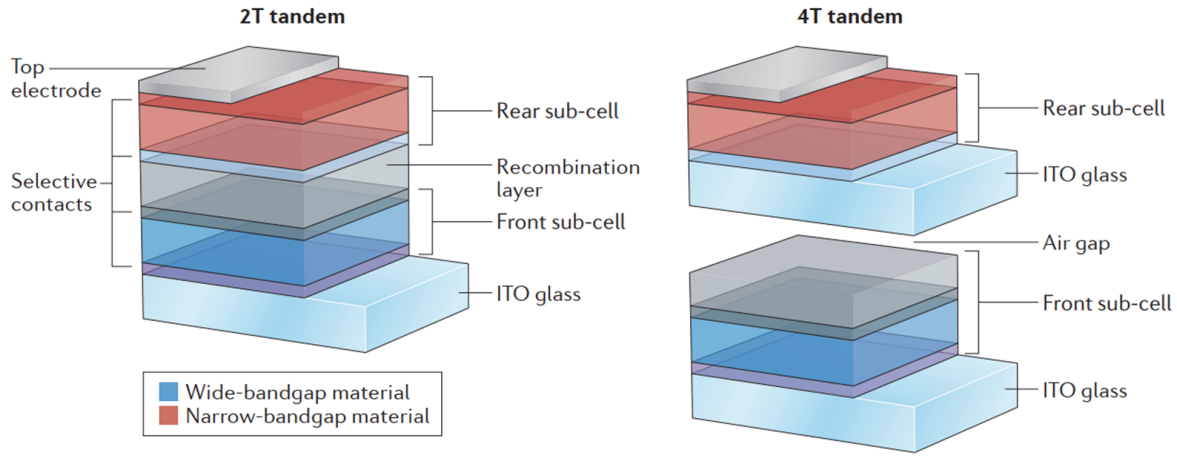

Figure 1.12. *Diagram of the architecture of two-terminal (2T) and four-terminal (4T) tandem solar cells. Figure taken from the work of G.E. Eperon*[51].

The actual record cell for III-V / Si multijunction is 36.1 % for a triple junction solar cell composed of a silicon TOPCon bottom cell and two top cells of GaInP and GaInAsP in a two-terminals configuration[53]. However, the production of III-V / Si tandem solar cells is not easy and presents various technological and cost-related obstacles that must be addressed in order to fully leverage its advantages. We will present these challenges in the next section.

C. Challenges in epitaxial growth of III-V on Si

I. A technical challenge: material incompatibilities

The production of high-quality crystalline materials for use in devices requires so-called epitaxial growth. The term "epitaxy" derives from the Greek roots "epi", meaning "above", and "taxis", meaning "in an orderly manner", and can be translated as "to arrange above". The epitaxial growth of semiconductor materials, involving a well-defined crystalline orientation, represents a non-trivial challenge. Here we will present some of the fundamental problems of III-V-on-Si heteroepitaxy: lattice mismatch, thermal mismatch, antiphase boundaries and meltback etching.

1. Lattice mismatch

The epitaxial growth process involves the use of an initial substrate, with its own properties and in particular a specific atomic arrangement. When this arrangement does not exactly match that of the material to be grown, mismatches in the lattice parameters occur, leading to significant mechanical stresses during the growth process that jeopardise the epitaxy. This is why III-V materials are usually grown homoepitaxially, which means that we grow them on a substrate made of the same material. However, for all the reasons outlined above, we will concentrate here

on growing III-V materials on silicon, thus using heteroepitaxy. III-V materials have lattice parameters that differ to a greater or lesser extent from those of silicon (see **Figure 1.2**). For example, GaP has a lattice parameter fairly close to that of silicon, with a difference of only 0.37%. However, in the context of making a tandem cell, this material does not attract considerable interest because of its high energy gap of 2.26 eV, which does not promise to be highly efficient when combined with silicon. On the other hand, the materials studied as part of this thesis project, GaN and GaAs, both show a significant difference with the silicon lattice parameter, i.e. 16% and 4% respectively. This difference leads to the formation of crystal defects such as dislocations. Indeed, when the thickness of the epilayer surpasses a specific threshold known as the critical thickness, the strain energy accumulated is relieved through the creation of misfit dislocations (MDs) along the interface with silicon and threading dislocations (TDs) toward the surface[54]. As TD introduce electronic states in the bandgap which will cause non radiative recombination centers in the epitaxial layer and thus reduce carrier mobility, the TD density (TDD) can be used as a quality indicator. The generally accepted threshold above which dislocations have a significant impact on device performance is 10^6 cm^{-2} [55,56]. TDD can be determined by several techniques including etch pit density determination through etching, cathodoluminescence (CL) mapping, X-ray diffraction (XRD), transmission electron microscopy (TEM) or electron channelling contrast imaging (ECCI) analyses[57–61].

2. Thermal mismatch

The substrate also possesses a specific coefficient of thermal expansion (CTE) which expresses how the material expands upon heating. A significant disparity in the coefficient of thermal expansion (CTE) between the substrate and the grown layer leads to the introduction of thermal strain throughout temperature variations, such as heating before processing and subsequent cooling[62]. The accumulated thermal stress is likely to be released by the formation of thermal cracks. It is important to highlight that these cracks originate from pre-existing defects, indicating that the presence of any imperfections within the epitaxial layer promptly correlates with crack formation[63]. This phenomenon is particularly important in the context of GaAs growth on silicon, where GaAs possesses a larger CTE (5.8×10^{-6} K^{-1}) compared to silicon's (2.6×10^{-6} K^{-1}). It is estimated that thermal cracks initiate propagation when the thickness of the GaAs layer surpasses approximately 3 µm. Moreover, as the thickness of the GaAs layer increases, the number of cracks tends to increase, potentially resulting in the formation of electrical leakage paths and light scattering centers[64]. The effects of thermal mismatch are not better in the case of GaN, which has a thermal coefficient difference of 54% with silicon[65].

3. Antiphase boundaries

Antiphase boundaries (APBs) in III-V on Si heteroepitaxy arise as a consequence of the intricate interplay between the polar nature of III-V semiconductors and the nonpolar silicon substrate. When III-V layers are grown on top of Si substrates, the heteroepitaxial process introduces various atomic stacking configurations, leading to the formation of APB defects[66]. Specifically, in the ideal zincblende structure of GaAs, Ga and As atoms should exhibit alternate coordination. However,

deviations from this ideal structure, such as changes in atomic coordination, result in the creation of two-dimensional structural defects at the interface, known as APBs. These deviations can occur due to the presence of steps with odd atomic thickness on the silicon surface and the uneven distribution of group III or V sources during the pretreatment of the silicon surface. In GaAs, two distinct substructures can emerge, one maintaining the zincblende structure while the other involves a 90° rotation of the unit cell around the [001] direction, leading to the formation of antiphase domains (APDs). At the interface between two APDs, monoatomic bonds consisting of Ga-Ga or As-As pairs, termed antiphase boundaries, are formed. This structural asymmetry, propagated during epitaxial growth, detrimentally impacts the electrical and optical properties of the material. At these interfaces, the GaAs loses its electron neutrality, resulting in localized doping imbalances due to the presence of Ga double bonds with a deficit of two electrons and As double bonds with an excess of two electrons. Consequently, the material becomes locally heavily doped, either p or n type, leading to electrical defects in the antiphase walls and nonradiative recombination of surrounding charge carriers[54]. Thus, the presence of APBs significantly affects the overall performance and reliability of III-V semiconductor devices integrated on Si substrates.

4. Meltback etching

The interface between gallium-based material and silicon substrates also experiences issues due to high reactivity between gallium and silicon, hindering device performance. This phenomenon is commonly called *meltback etching* in literature and defines the deteriorating chemical reaction between Ga and Si under typical deposition process of Ga-based materials at high temperatures such as during the growth of GaN (~1000°C). This reaction leads to the formation of a Ga-Si alloy which compromises the interface integrity[67]. This phenomenon has been identified in many Ga-V semiconductors[68,69]. Examining the Si-Ga phase diagram reveals a eutectic transformation occurring at approximately 30°C, near the melting point of gallium. Furthermore, gallium exists in the liquid phase between 29.77°C and 2237°C, and the formation of gallium droplets in the liquid phase and their interaction with silicon during the initial growth stages constitute the primary mechanism underlying meltback etching. We will study such effect in **Chapter 3**.

II. A cost challenge: current solutions

1. Process-related costs: conventional manufacturing processes of III-V

The most widely used techniques for the deposition of III-V thin films are MetalOrganic Chemical Vapor Deposition (MOCVD) and Molecular Beam Epitaxy (MBE)[70]. These are robust techniques that enable to obtain high quality thin films, but they suffer from the drawback of being both costly and complex as they involve either high pressure (~500 mbar) or ultrahigh vacuum, respectively.

Metal Organic Chemical Vapor Deposition (MOCVD)

This technique, as its name suggests, is based on the growth by chemical reactions of gases on heated substrates. An illustration of MOCVD operation is given in **Figure 1.13**. Precursors are delivered in gaseous form, either directly or via a carrier gas that passes through a bubbler into a liquid precursor canister. For example, ammonia (NH_3) can be used for GaN growth, and arsine (ASH_3) for GaAs growth. Gallium can be supplied via trimethylgallium (TMGa), an organometallic that is stored in liquid form in a canister. Dissociation of these precursors takes place thermally at the substrate level, at relatively high temperatures such as those mentioned in the table of **Figure 1.13** for GaN and GaAs. Since group V precursors are often challenging to dissociate, even at elevated temperatures, employing high V/III ratios and high pressure becomes essential. However, this implies high consumption of costly and often toxic gases resulting in low precursor utilization which makes the technique quite expensive in operational expenditures (OPEX). Even so, this technique is largely used in industry as it provides a high growth rate (few microns per hour) and allows high throughput fabrication.

Temperature	Pressure	Growth rate
∽ 600-700°C for GaAs ∽ 1000°C for GaN	∽ **500 mbar**	∽ 1-10 µm/h

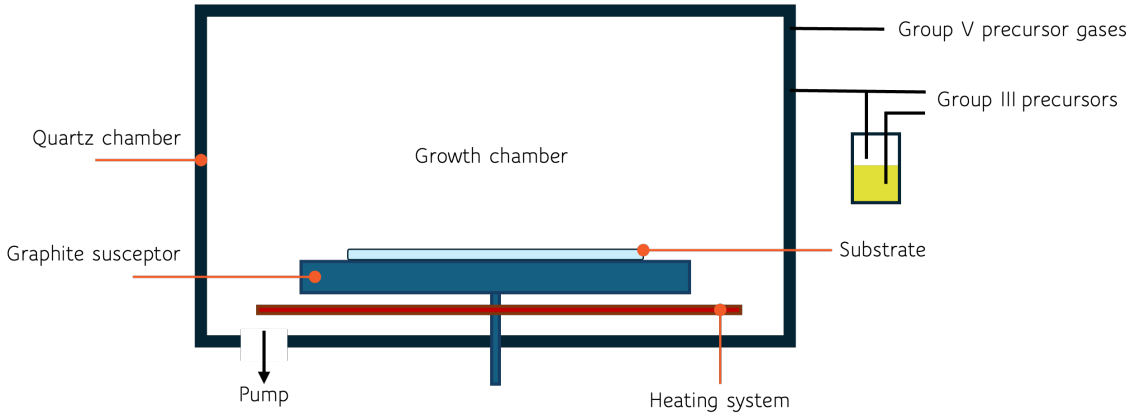

Figure 1.13. *Schematic diagram of a MOCVD reactor and table of MOCVD typical process conditions*[71].

Molecular Beam Epitaxy (MBE)

This technique uses ultrapure solid sources enclosed in effusion cells as illustrated in **Figure 1.14**. These cells consist of crucibles surrounded with heating resistances, promoting sublimation of the material they contain. Thus, under ultra-high vacuum (UHV) conditions ($< 10^{-12}$ bar), ballistic transport of atoms towards the substrate is made possible with a very low level of contamination. This allows an ultra-precise control of layer interfaces and thicknesses. A shutter effectively controls the opening and closing of each source, ensuring precise monitoring of the atomic flow. UHV also enables the application of advanced in-situ characterization techniques, in particular reflection high-energy electron diffraction (RHEED), which has been in place since the early days of MBE[72] and enables the evolution of epitaxial growth to be monitored in real time. This extremely low-pressure atmosphere is made possible by the use of sophisticated pumps such as cryopumps, ion pumps, turbomolecular pumps and sublimation pumps, as well as robust cooling and sealing systems, particularly in the growth chamber. This equipment requires significant CAPEX (acquisition and regular maintenance) and OPEX (liquid N_2

consumption) investments. Moreover, the growth rates obtained by MBE are generally relatively low, on the order of 0.5-1 µm/h, a speed often considered insufficient for industrial applications.

Temperature	Pressure	Growth rate
GaAs: ∽ 600-650°C GaN: ∽ 700-800°C (PA-MBE) or 1000°C	**UHV**	∽ 0.5-1 µm/h

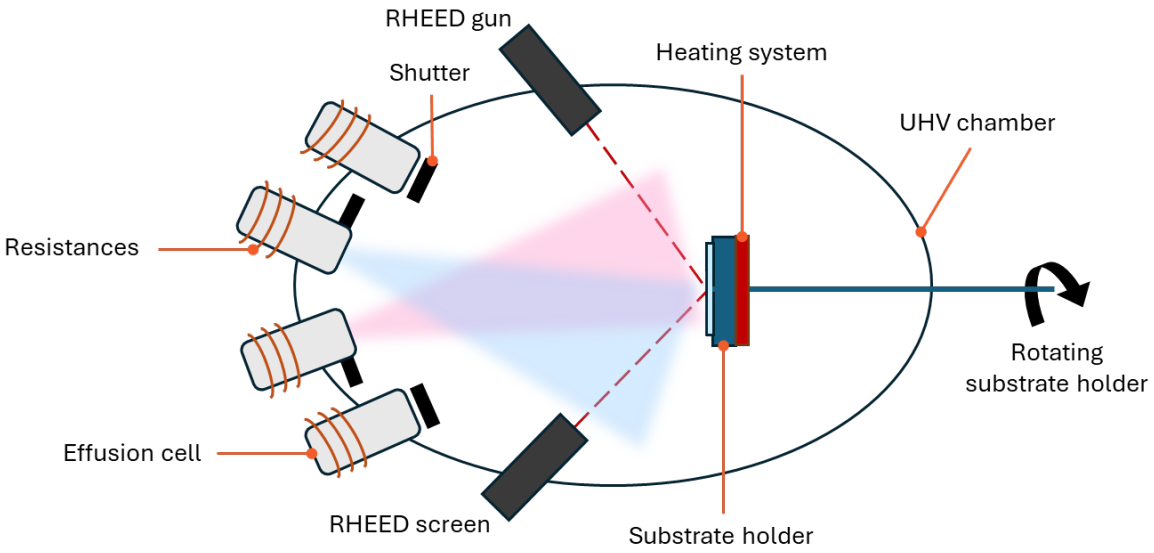

Figure 1.14. *Schematic diagram of a MBE reactor and table of MBE typical process conditions*[73].

Other III-V semiconductor deposition techniques also exist (ammonothermal growth, physical vapor transport, hydride vapor phase epitaxy[74]…) but are for various reasons less commonly used than MOCVD and MBE, despite their potential in specific applications.

2. Substrate-related costs: conventional approaches to integrate III-V and silicon

III-V materials are usually grown on expensive substrates made of materials with similar lattice parameters. For the growth of GaAs, these are mainly substrates of GaAs itself or germanium (Ge), while for GaN growth sapphire (Al_2O_3) and silicon carbide (SiC) are widely used. The high cost of these substrates, due to the scarcity of materials or the complexity of manufacturing techniques, represents a major issue. The use of silicon is being considered as a potential solution to reduce costs and increase efficiencies as explained earlier, but it is essential to overcome the material related challenges mentioned just above. Although technological progress has been made in developing various approaches to overcome these obstacles, these methods also present challenges, particularly in terms of cost.

Direct growth

The direct growth of III-V layers on silicon substrates is one of the most widely studied approaches for integrating these two materials. The use of offcut Si substrates with various angles of around

5° is for example effective to reduce APBs formation[75]. This method offers the advantage of a simplified process but with all the other constraints that were presented in part **C.I**. Also, it requires expensive equipment presented in **C.II.1**.

Buffer layers

To reduce strain and improve the crystalline quality of III-V layers, the use of intermediate semiconductor buffer layers is common practice. For example, AlN for GaN growth[76–78], InGaP, or GeSi for GaAs growth[64,79] as shown in **Figure 1.15**. The intermediate layer helps to attenuate the mismatch by approaching the lattice parameter of the layer to be grown. However, the manufacture of these buffer layers requires expensive processes, similar to those used for the growth of the film itself. Also, buffer layers are often too thick to allow tunnelling and therefore the use of both III-V and silicon in devices.

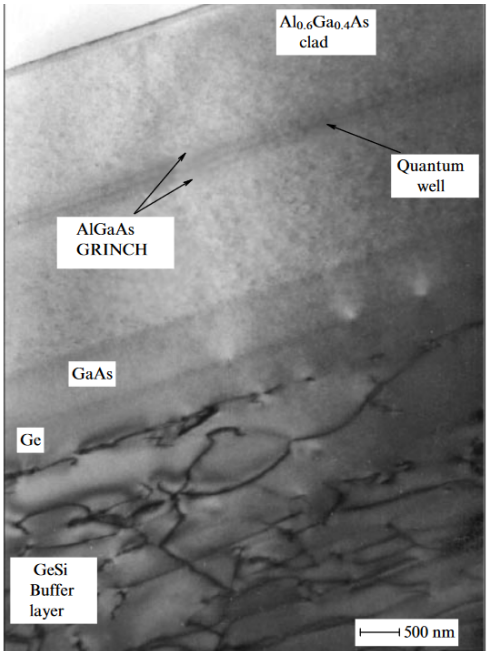

Figure 1.15. *Example of buffer layer stack taken from Bolkhovityanov et al.[80]*

Lateral or directed epitaxy

Localized epitaxy techniques aim to transfer crystalline order from the substrate to the target layer through narrow openings to prevent defect transmission. Epitaxial Lateral Overgrowth (ELO) involves depositing a III-V seed layer on silicon, applying a mask with open windows, and performing epitaxial growth at these openings (**Figure 1.16**). This results in growth lattice-matched to the seed layer, followed by lateral expansion to reduce defect density[81].

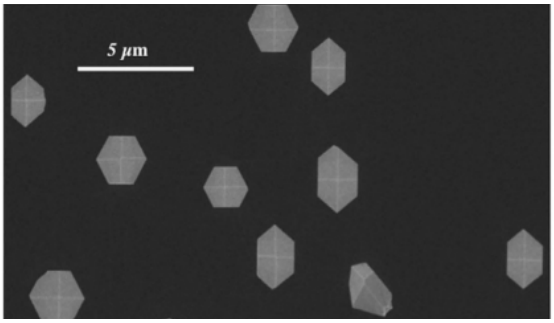

Figure 1.16. *Example of ELO of GaAs taken from Renard et al.[82]*

In Selective Area Growth (SAG), a SiO_2 masking layer is first grown on the silicon surface, and then small apertures are etched into the SiO_2 to define nucleation areas for the III-V layer growth. These techniques are costly because they require great precision to form the openings, nucleate only on them[83] and to obtain a continuous film on a large surface.

Remote epitaxy

Remote epitaxy, which enables the epitaxial growth of III-V layers on expensive but reusable substrates, is promising because it allows the advantage of growth on a suitable substrate to be used while avoiding high cost at the end[84]. To do this, a two-dimensional (2D) material-based layer transfer is added between the substrate and the III-V layer to grow. During the growth process, the intermediate layer is thought to mimic the orientation of the substrate lattice from a distance while resting on the graphene[85]. The prevailing theory has been challenged by a more plausible one suggesting that growth occurs from pinholes within graphene[86,87]. Presently, the viability of this technique is hindered by the expensive fabrication of high-quality materials with precise management of chemical interactions between substrate and epitaxial layers. To then combine it with silicon, it will be necessary to use bonding techniques such as those presented below.

Bonding

Bonding involves using assembly techniques that enable the two desired materials to be bonded together, either directly (direct bonding or molecular bonding) or via an intermediate layer (metallic or adhesive bonding)[88]. Since this technique does not involve epitaxy between Si and III-V, it avoids the problems of heteroepitaxy presented in **C.I**. The issue with this technique is that it can be costly due to the complex preparation steps and manufacturing processes involved. However, a cost effective bonding solution is about to be patented by the IPVF.

In conclusion, although current approaches to integrating III-V materials with silicon offer promising prospects for the development of advanced electronic and optoelectronic devices, the high cost associated with these techniques remains a major obstacle to their widespread adoption in industry. Continued research and development efforts are needed to make these technologies more accessible and economically viable.

D. Overcoming challenges using plasma

1. To address process-related challenges

Plasma assisted growth, such as in the case of plasma-enhanced chemical vapor deposition (PECVD), offers a cost-effective method in which a plasma discharge is used to dissociate precursors at intermediate pressure (0.1-1 mbar)[89]. Indeed, since this technique allows working at reasonably low pressure, the consumption of precursors which is, along with the substrate, the main source of costs in CVD[47], can be considerably reduced. In addition, PECVD is well-established in the semiconductor industry, e.g. for the production of silicon-based materials[90–93].

Some studies showing the feasibility of plasma-assisted processes for III-V semiconductors deposition were published in the 1980s[94–98] and the subject is again attracting interest[99–102] due to the strong growth of the III-V semiconductor market. Indeed, plasma processes can be operated at lower temperature than conventional CVD while demonstrating an efficient dissociation of challenging-to crack gas precursors such as N_2 for instance, generating highly reactive species. Consequently, one can conduct deposition at significantly lower temperatures which is, for instance, particularly beneficial to avoid undesirable reactions occurring at high temperatures. It opens the opportunity to grow on temperature-sensitive substrates, which provides access to flexible applications in particular[103]. Furthermore, the addition of plasma holds great promise for creating a manufacturing technique for high-quality III-V semiconductor growth on silicon. Indeed, on one hand crack defects and meltback etching observed in high-temperature processes can be reduced and, moreover, plasma can promote the emergence of a high precursor dissociation, encouraging crystal growth[104] while maintaining a low-cost process.
Finally, using a process that includes the possibility of plasma application would pave the way for in-situ surface treatments just before growth. We will present some of these substrate opportunities in the next section.

2. To address substrate-related challenges

The use of plasma in the whole semiconductor growth process offers several significant advantages for surface preparation. First, plasma can be used to effectively clean the substrate surface by removing contaminants, organic residues and unwanted particles[105,106], which is essential to ensure a clean and homogeneous interface between the substrate and the growing layer. This is of particular interest when growing on silicon which has an oxide that forms very quickly. To give a few examples, the work of Thomas *et al.* has shown that carbon and oxygen contamination on the surface of silicon can be eliminated using a simple hydrogen plasma and annealing[107]. According to them, this elimination is achieved by evacuating hydrocarbons through hydrogenation. Similarly, Kondo *et al.* demonstrated the same principle for the decontamination of a GaAs substrate using electron cyclotron resonance (ECR) plasma at low temperature in an MBE reactor[108]. They were able to use in-situ RHEED analyses to confirm their findings and secondary ion mass spectrometry (SIMS) to check the interface. This type of substrate preparation is quick and easy to carry out, unlike certain chemical techniques which require the use of highly toxic solutions like hydrofluoric (HF) acid[109].
In addition, one can imagine that plasma can be used to chemically modify the surface of the substrate to alter its properties, for example in terms of adhesion or wettability, in order to aid the anchoring of semiconductor atoms during subsequent deposition. This plasma capability could also be used to grow interface layers having the role of barrier or buffer layer to prevent various problems with silicon such as the aforementioned meltback etching or lattice mismatch, thus being of paramount importance in obtaining high quality III-V semiconductor layers with optimum optoelectronic properties. This aspect of the use of plasma was initially explored by Monalisa Ghosh during previous work at LPICM[110]. Her research led to the creation of a so-called "virtual" substrate, incorporating a thin layer of germanium on a Si wafer for a low-cost wafer solution. This approach is taken up and developed further in **Chapter 4** of this thesis.

In summary, the use of a plasma in the semiconductor growth process for substrate preparation has the potential to result in clean, chemically modified, and reactive surfaces, promoting high-quality, well-controlled growth of subsequent semiconductor layers.

E. Objective of the thesis project

In this introductory chapter, the overall context of the opportunities and challenges associated with the low-cost growth of III-V semiconductors has been presented, with particular emphasis on the prospect of reducing the production costs of high-efficiency III-V / Si tandem cells. This issue is a key concern for the work package 2 (WP2) of the IPVF's COSY program. We have identified that the costs associated with the III-V technology arise mainly from two aspects: i) the substrate and ii) the fabrication process. The former is primarily tackled within our team through the advancement of remote epitaxy solutions and III-V integration processes on Si, employing spalling and bonding techniques. In this context, the main objective of this PhD thesis has been to address the cost-issue of the fabrication process, while offering some preliminary insights into the substrate issue. To this end, we have developed at LPICM, a new approach for the epitaxial growth of III-V materials by using a custom-built Remote-Plasma Chemical Vapor Deposition (RPCVD) reactor. This kind of plasma CVD system has the distinctive feature of having a plasma located away from the substrate, thus preventing ion bombardment effects which can damage the substrate and induce carbon contaminations from organometallics[95]. Moreover, with this technique, we are exploring an intermediate pressure range (see **Figure 1.17**), enabling us to present a process that requires lower precursor consumption than MOCVD, while being less CAPEX intensive to implement than MBE. This reactor also enables simple, rapid, and in-situ plasma surface treatments to be carried out. Designed entirely within the LPICM laboratory at Ecole Polytechnique, this reactor was optimised for the first time as part of this thesis for the growth of GaN and GaAs.

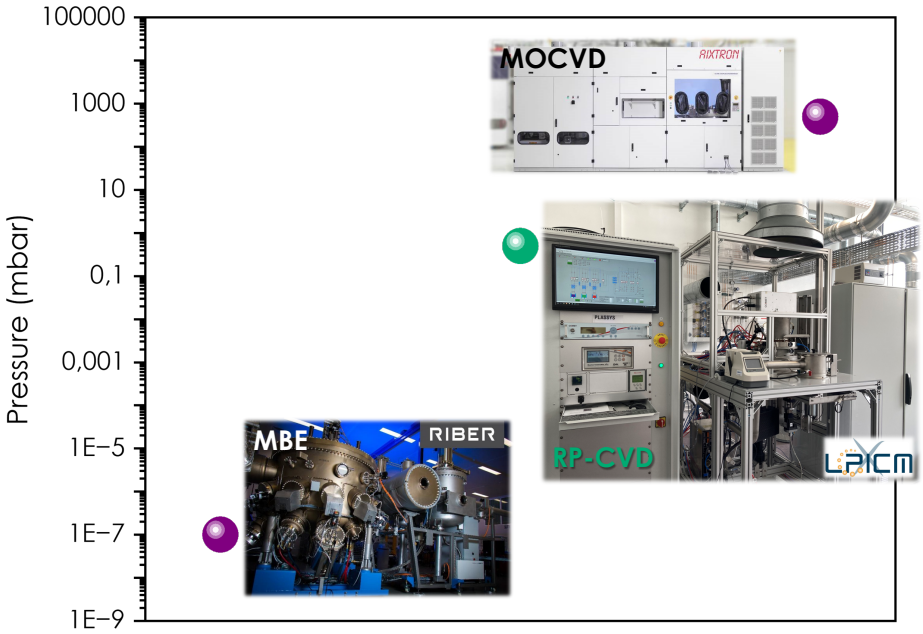

Figure 1.17. *Representation of existing III-V fabrication processes compared to RP-CVD in terms of pressure.*

Chapter 2 unveils the RP-CVD reactor, introduced by an exploration of the fundamentals of plasma physics. The architecture of the custom-designed reactor is then explained in detail, followed by a step-by-step description of the deposition process. Finally, initial results on plasma characterisation are presented.

Chapter 3 is devoted to the optimisation of GaN growth, providing a first example of the operational functioning of the RP-CVD reactor. We begin with an initial study of GaN growth on sapphire, a well-suited substrate for GaN growth. A second optimization study of direct growth on silicon shows that we can produce highly oriented polycrystalline GaN at a low temperature of 500°C. The challenges inherent in accurately quantifying the chemical composition of GaN are then outlined, enabling a conclusion to be drawn from a comparative study of the techniques currently employed by the community. Finally, the incorporation of an interface barrier generated simply and in-situ by plasma has made it possible to overcome the meltback etching phenomenon associated with direct growth, providing a perspective on the growth mechanisms involved in the fabrication of GaN by RP-CVD on Si.

Chapter 4 focuses on the growth of GaAs by RP-CVD. We begin by presenting the results of homoepitaxial growth obtained by process optimization. Various characterisation tools are used to justify the quality of the layers. A comparison is also made between growth with plasma and without plasma under the same conditions, highlighting the interest of working in a H rich environment. Next, we undertake the direct growth of GaAs on Si, which lead us to develop a strategy for achieving epitaxial growth of GaAs on Si at lower cost by taking advantage of plasma to create a “virtual substrate”.

Chapter 5 examines the optimisation of the doping level in GaAs layers produced by RP-CVD to reach optimal values for integration into PV devices. Several approaches have been studied, firstly, by examining the impact of process parameters on the incorporation of dopants, and secondly, by exploring the use of a new organometallic gallium precursor. This chapter concludes with the presentation of the first results of the integration of GaAs obtained by RP-CVD into solar cells devices.

The conclusion succinctly encapsulates the PhD research project, highlighting its key contributions to the field and suggesting promising directions for future investigation.

Chapter 2. A custom-build reactor for III-V growth – Remote Plasma CVD. 36

A. Plasma basics 36
I. Key properties of plasmas 36
1. Plasma temperature 36
2. Plasma discharges 37
3. Plasma density 38
4. Pressure effect 38
II. Interest of remote plasma assistance in CVD 39
1. Low pressure 39
2. Low temperature 39
3. Surface treatments 39

B. Architecture of the RP-CVD reactor 42
I. Plasma generation system 42
II. Gas injection system 45
III. Substrate holder and heating system 46

C. Plasma characteristics 48
I. E-H transition 48
II. Plasma power process window 50

Chapter 2. Summary 51

Chapter 2. A custom-build reactor for III-V growth – Remote Plasma CVD

Over the past twenty years, researchers at LPICM (Ecole Polytechnique) have extensively explored the field of low-temperature plasma epitaxy delving into both the fundamental aspects of plasma-material interactions[111], including ab initio molecular dynamics modelling[112,113], and the growth of thin films for applications in photovoltaics and microelectronics[90,114]. Regarding the latter, research has primarily focused on the epitaxial growth of silicon and germanium[115–118]. Building on this expertise, recent efforts have aimed to develop plasma processes for other semiconductors with superior or complementary optoelectronic properties: III-V materials, to integrate them with silicon. The project is structured into two complementary axes: epitaxial growth of III-V using plasma assisted Chemical Vapor Deposition (CVD), studied in this thesis, and epitaxial growth of III-V using plasma Physical Vapor Deposition (PVD)[102]. This initiative launches the beginning of a new field of fundamental and applied research at LPICM.

A. Plasma basics

I. Key properties of plasmas

Plasma is characterised as a state of matter in which the gas is ionised, comprising electrons and ions that move freely and randomly. This definition encompasses a wide variety of plasmas, which may differ in origin (whether natural or artificial), temperature of electrons and ions, density of charged species, pressure and so on... Plasmas, after referred to as the fourth state of matter, are ubiquitous in the universe, appearing in phenomena as close to us as neon lights and in objects as distant as stars[119]. Over the years, humans have also developed the ability to produce artificial plasmas. Hereafter, we present some of the most important parameters when studying plasma systems, namely plasma temperature, density and pressure. These parameters will be most of the time described through the example of an RF-ICP discharge which is the type of plasma we used.

1. Plasma temperature

Figure 2.1 shows different kinds of plasmas according to their electron densities, energies and temperatures. We propose to show here a classification according to their thermal equilibrium, i.e. whether or not the temperature or average energy of the particles that compose the plasma is equal for each type of particle[120]. For example, for plasmas in thermal equilibrium, such as those at the sun's core or in controlled fusion plasmas (e.g. ITER project in Cadarache, France), all the particles, including electrons or heavy species, have the same temperature. These plasmas,

known as thermal or hot plasmas, reach temperatures of the order of millions of degrees. Conversely, in non-equilibrium plasmas, also known as cold plasmas, the electrons temperature is much higher than that of neutral and ion species. This thesis will focus on this specific type of plasma, which is generated by an electrical discharge.

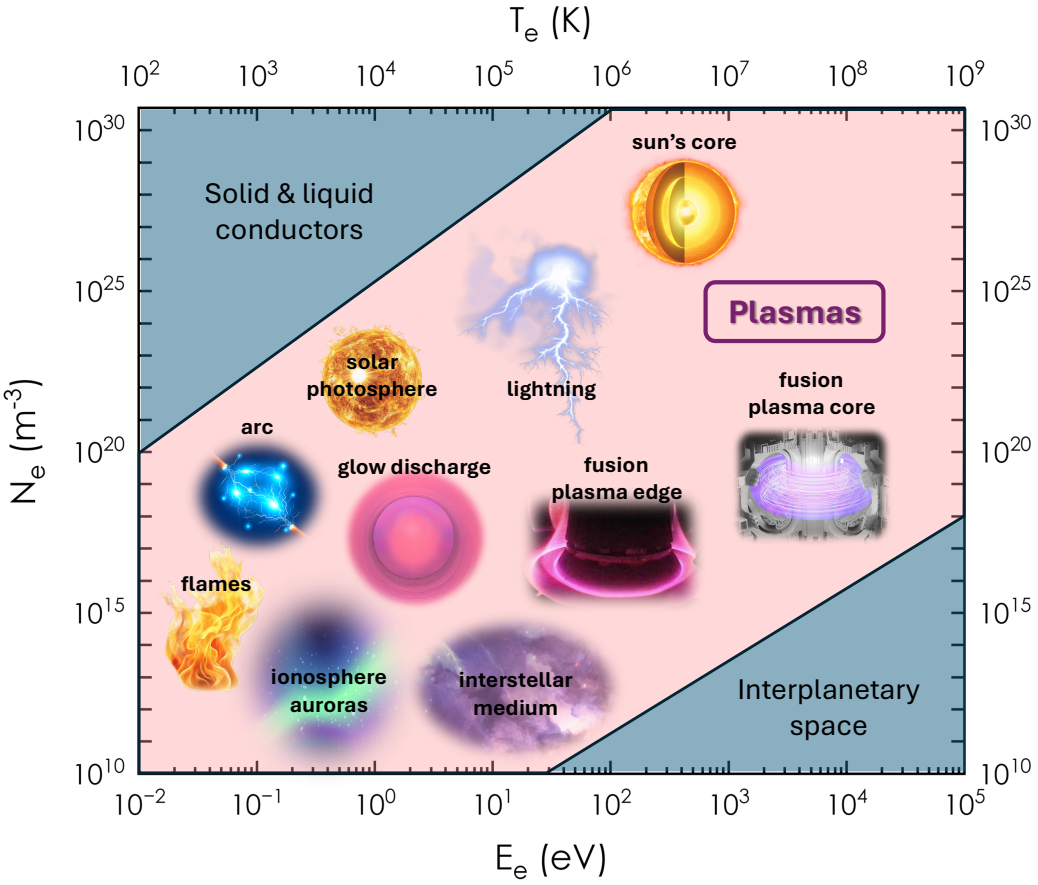

Figure 2.1. *Classification of plasmas based on electron densities, energies and temperatures. Adapted from the review of Francisco L. Tabares and Ita Junkar*[120].

2. Plasma discharges

Electrical discharges can be generated by various means, from a direct current (DC), a radiofrequency (RF) or a microwave (MW) source for instance (**Table 2.1**), which causes ionisation of the gas and maintains the discharge. In this thesis, the study focuses on weakly ionised RF plasmas, which mainly contain neutral species such as molecules, atoms, and free radicals. RF discharges, mostly operating at a frequency of 13.56 MHz, are widely used in industrial applications such as etching and PECVD deposition, due to their efficiency in promoting ionization and their ability to generate stable plasmas[121], as well as to process insulating substrates.

DC and low-frequency	f < 1 MHz
RF	1 < f < 500 MHz, usually 13.56 MHz
MW	0.5 < f < 10 GHz, usually 2.45 GHz

Table 2.1. *Different frequency ranges for plasma sources*[121].

3. Plasma density

Plasma density refers to the number of charged particles (ions and electrons) per unit volume in a plasma, typically expressed in particles per cubic meter[122]. In the case of RF plasmas, the plasma density strongly depends on the design chosen to generate the excitation. On the one hand in capacitively coupled plasma (CCP) discharges (**Figure 2.2. a)**), the electron density is of the order of 10^{15} - 10^{16} m^{-3} On the other hand, inductively coupled (ICP) discharges (**Figure 2.2. b)**) offer higher plasma density in the range of 10^{16} - 10^{18} m^{-3}, so they are often used in applications where high plasma density is preferred, offering a greater degree of gas dissociation[123]. It is for that reason that we selected this second configuration for the design of our RP-CVD reactor.

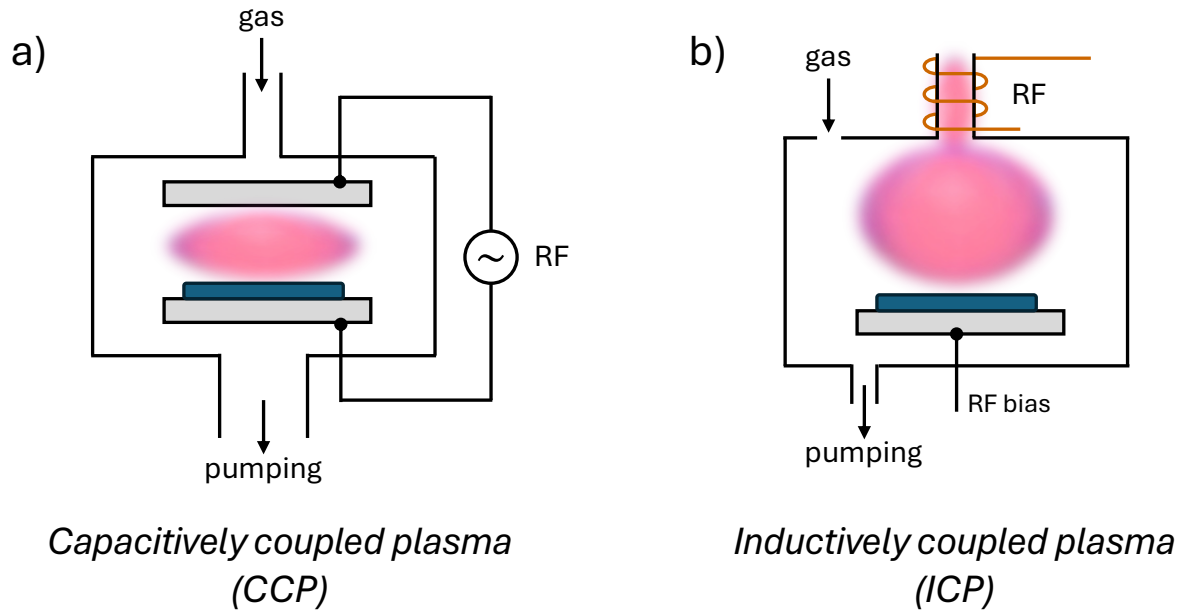

Figure 2.2. *Schematic of reactors with a) capacitively coupled plasma and b) inductively coupled plasma.*

4. Pressure effect

As mentioned earlier, a wide variety of plasmas exist, operating at pressure values spanning from a few Pascals to atmospheric pressure. Cold plasmas are generally sustained at low pressure. In essence, this low-pressure environment reduces the frequency of particle collisions, thereby facilitating effective ionization by reducing energy losses and allowing more efficient diffusion of species without raising the temperature. Operating at low pressure offers the significant advantage of fostering a more stable plasma[124]. Inductively coupled plasma (ICP) systems are particularly suitable for low pressures in the range of 0.1 – 10 mbar, as they can maintain a high plasma density. It is under these conditions that we chose to design the plasma source for the RP-CVD reactor studied in this PhD thesis. Its operation is described in detail in section **B.I** of this chapter.

II. Interest of remote plasma assistance in CVD

Plasma-assisted CVD offers a range of advantages that transcend the limitations of conventional CVD. In this section, we develop the main advantages identified in the introduction chapter regarding the addition of plasma in CVD.

1. Low pressure

In conventional chemical vapor deposition (CVD) processes, the reactions take place at relatively high pressures of about hundreds of millibars[125]. Sustaining such high pressure requires large flows of reactive gases that are most of the time expansive and toxic. This considerably influences the operational costs (OPEX) of the process. Conversely, plasma-assisted processes, such as well-established plasma-assisted chemical vapour deposition (PECVD), commonly used for the industrial production of silicon-based materials, are more cost-effective as they operate at low-pressure, between 0.1-1 mbar[89], so contributing to a drastic reduction of gas precursor quantities. In addition, this reduction in pressure allows more precise control of the thin film growth, which can lead to more uniform growth due to a lower mass transport rate.

2. Low temperature

Another advantage of plasma over classical CVD process lies in the presence of an electric field that provides the energy for the electrons to efficiently dissociate the precursor gases, generating a highly reactive medium made up of ions, excited species, and radicals, while maintaining an overall gas temperature close to ambient temperature[126]. While conventional CVD relies solely on temperature to decompose the precursor gases, plasma-assisted CVD exploits the energy provided by the charged and excited species to facilitate the decomposition of these gases. As a result, it becomes possible to reduce potential defects linked to thermal stress and other undesirable reactions.

3. Surface treatments

As previously mentioned plasmas can be used to carry out in situ surface treatments, such as oxide or organic residues removal[127–130]. We will demonstrate some of the advantages of this type of treatment in the **Chapter 3** of this manuscript.

Due to the interest in reducing III-V costs, various research teams have developed innovative plasma-assisted processes for III-V growth. Some plasma-assisted CVD works can be found in the early 1980s and late 1990s as highlighted by pink cells in **Table 2.2** of bibliographical references, with renewed interest in recent years. In contrast, Remote Plasma Chemical Vapor Deposition (RP-CVD) has been less studied. Interestingly, RP-CVD offers the advantage of using a plasma located away from the growth chamber, thereby avoiding the harmful effects of ion bombardment on the substrate. Most research conducted primarily by three teams (blue cells in

Table 2.2): the one of Gerald Lucovsky from North Carolina State University in the USA[131,132], the one of Maria Losurdo at the Plasma Chemistry Research Center in Bari, Italy[133], and the one of Ian Mann from Macquarie University in Sydney, Australia whose work led to the creation of the company Bluglass[134,135]. We have not identified any work on GaAs by RP-CVD; the closest studies are those by Huelsman from the late 1980s (green cells in **Table 2.2**). We will now delve into a comprehensive presentation of our reactor, showcasing the innovative system that sets it apart in the realm of plasma-assisted III-V growth technologies.

Reference	Process	Substrate	Pressure (Torr)	Temperature (°C)	Type of films	Growth rate
Knights *et al.* (1978)[136]	'Plasma CVD' RF plasma	NaCl	0.15	300-350	Polycrystalline GaN and amorphous GaP	0.18 (GaN) 0.39 (GaP)
Segui *et al.* (1982)[94]	'Plasma based MOCVD' -	Aluminium-metallized glass	10	Room T	Amorphous GaAs	0.6 – 3
Pande *et al.* (1984)[95]	'Plasma MOCVD' DC plasma	(100) GaAs	0.8-1.5	425-500	Crystalline GaAs	~ 4.8
Pande *et al.* (1986)[137]	'Plasma MOCVD' DC plasma	(100) GaAs	1-1.5	400-430	Crystalline GaAs	~ 6
Heinecke *et al.* (1986)[96]	'Plasma stimulated MOCVD' DC plasma	(100) GaAs	3.75	550-900	Crystalline GaAs	~ few
Huelsman *et al.* (1987)[97]	'Plasma controlled MOCVD' RF plasma	(100) GaAs	2-3	610	Crystalline GaAs	12
Huelsman *et al.* (1988)[138]	'Plasma controlled MOCVD' RF plasma	(100) GaAs	1	550-600	Crystalline alternating layers of GaAs and GaAsP	1.1 – 1.8
Leiber *et al.* (1989)[98]	'Plasma stimulated MOCVD' DC plasma	(100) Si	2.25-3.75	650	Crystalline GaAs and InP	-
Lukovski *et al.* (1990)[131]	'Remote plasma CVD' RF plasma	Si (111)	1	500	Crystalline GaN	0.2
Pihlstrom *et al.* (1992)[139]	'Downstream hydrogen afterglow plasma CVD' MW plasma	(100) GaAs	-	460	Crystalline GaAs	0.1-2

Reference	Process	Substrate	Pressure (Torr)	Temperature (°C)	Type of films	Growth rate (µm/h)
Sato *et al.* (1995)[140]	'Plasma assisted MOCVD' MW plasma	GaN / (100) GaAs	0.22	500	Crystalline GaAs	-
Losurdo *et al.* (1999)[133]	'Remote plasma CVD' RF plasma	AlN/Sapphire	0.1-10	600	Crystalline GaN	0.36
Mann *et al.* (2008)[134,135]	'Remote plasma CVD' MW plasma	-	-	700	Crystalline GaN	-
Lu *et al.* (2014)[141]	'Radical-enhanced MOCVD in the downflow of a very high frequency plasma'	Sapphire	0.75	800	Crystalline GaN	0.42
Liang *et al.* (2020)[99]	'Plasma enhanced CVD' RF plasma	Sapphire	-	850-950	Crystalline GaN	0.25-0.9
Zhang, Yu *et al.* (2021, 2022)[142,143]	'ICP MOCVD' RF plasma	AlN/sapphire	~ 0.02	580-600	Crystalline GaN	0.3-0.48

Table 2.2. *Bibliographical survey on plasma CVD growth of III-V materials.*

B. Architecture of the RP-CVD reactor

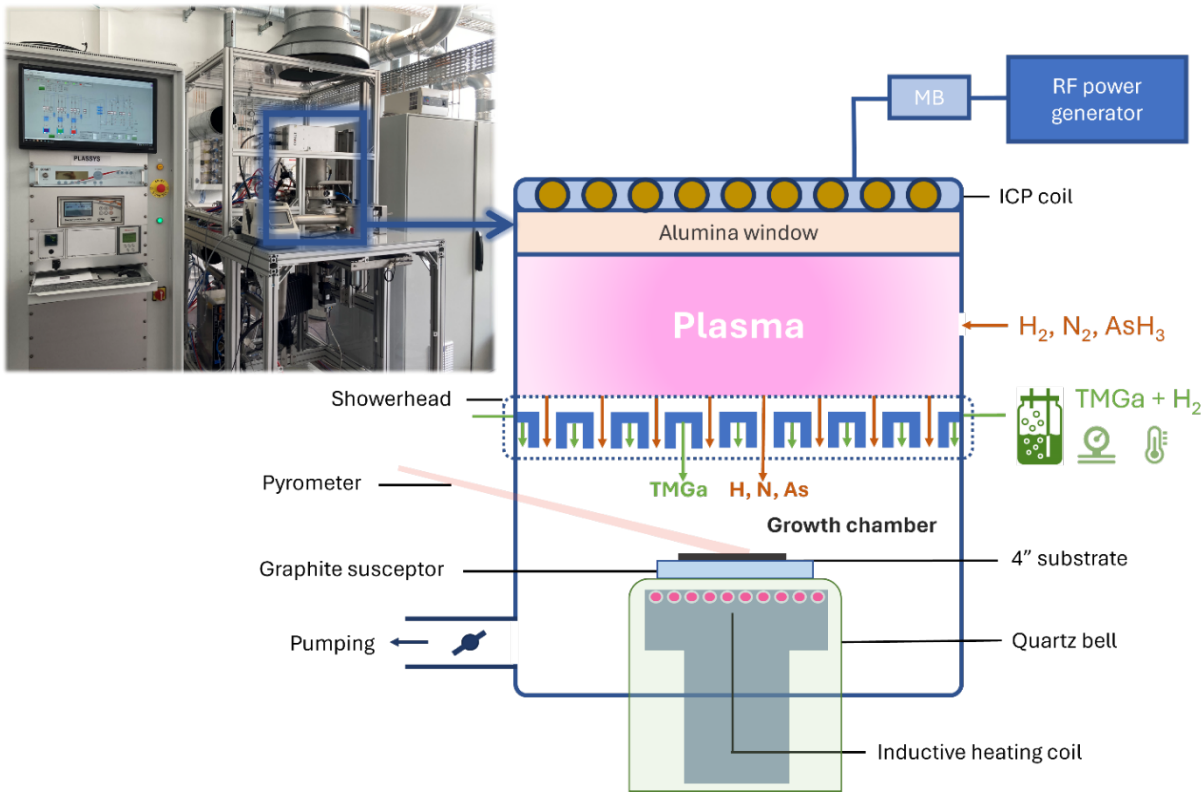

Figure 2.3. *Photo and schematic representation of the RP-CVD reactor.*

Figure 2.3 shows a schematic of the in-house custom designed Remote Plasma CVD reactor based at LPICM (Ecole Polytechnique) and optimized in this thesis project. In the following sections, we will delve into the various components of the reactor to gain a deeper understanding of its operation.

I. Plasma generation system

To design the plasma source, after selecting the ICP system as presented in the previous section, the antenna system had to be chosen. The two options studied were helicoidal and flat architectures using SolidWorks® modelling software as illustrated in **Figure 2.4**. Rather than a helicoidal coil, we opted for a flat one to achieve a more compact design for the plasma source, which integrates well with the showerhead. A helicoidal coil would have increased the volume of the source and complicated the design of the reactor. In addition, at the working pressure (around 1 mbar), there was a risk of the plasma adhering to the wall of the tube, which would have disturbed the uniformity of the hydrogen atoms flow. With a flat coil, we favor a denser plasma with strong diffusion, allowing a uniform flow of hydrogen at the surface.

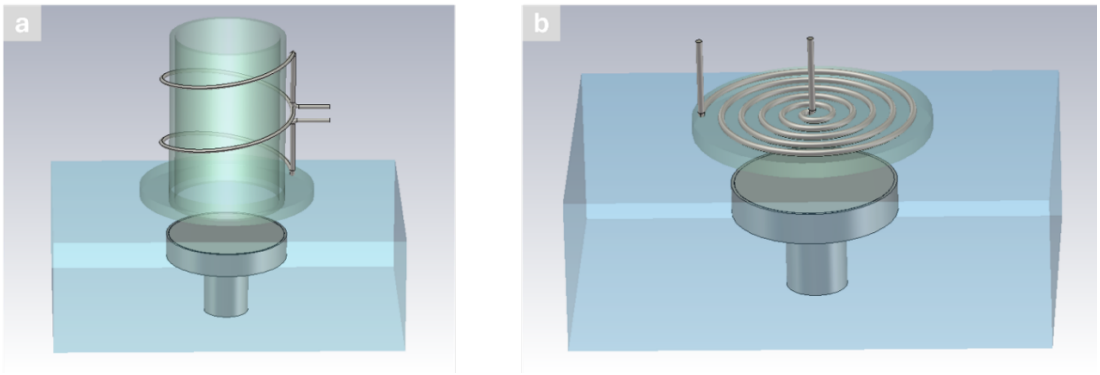

Figure 2.4. *a) Helicoidal and b) flat coils for ICP antennas.*

The ICP is thus generated in the reactor by a flat coil antenna powered by a 13.56 MHz radiofrequency (RF) generator connected to a matching box (MB), as represented on **Figure 2.5**. An alumina window allows to transmit the electromagnetic RF field to the discharge zone. As mentioned at the end of section **A**, the plasma is generated at a distance from the growth zone. It facilitates the efficient dissociation of molecules into neutrals and radicals, which can diffuse to the wafer surface. Simultaneously, the specific remote arrangement of the plasma prevents premature cross reactions between III- and V-precursors and allows spontaneous and collision-induced quenching of high-energy ions to occur well above the substrate, safeguarding the growth surface from ion bombardment[134,135]. Indeed, it is worth noting that plasma can also be used in etching processes, intentionally interacting with the substrate to selectively alter its topography or composition.

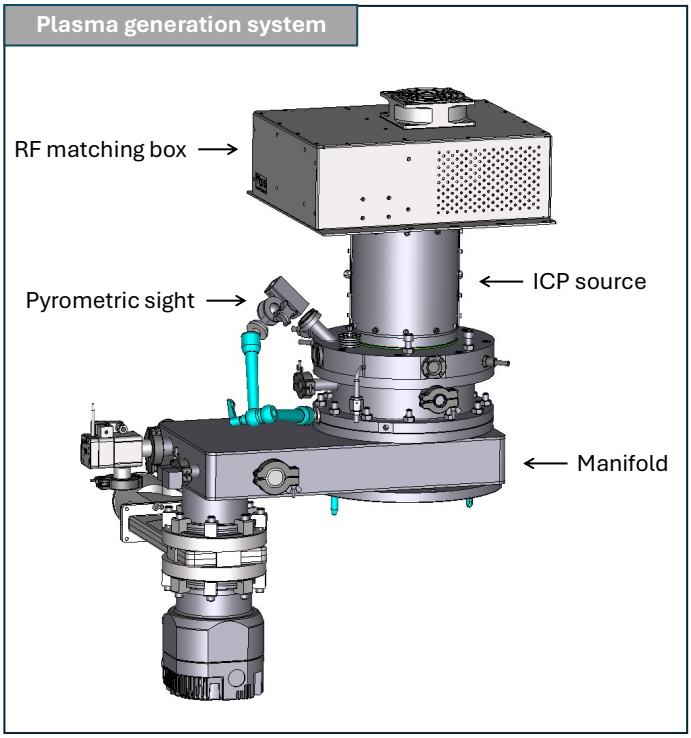

Figure 2.5. *Scheme of the ICP source integration in the plasma reactor.*

The homogeneity of gas flow within the plasma over the substrate is a crucial factor to ensure a uniform deposition on the substrate. During this research, we observed differences in the

thickness of the deposits between the center and the edge of the 4 inches samples. This trend was reversed for the growth of GaN and GaAs. In fact, in the case of GaN, we observed thicker growth at the center than at the edge of the wafer (**Figure 2.6** illustrates this thickness difference through ellipsometry mapping), whereas for GaAs, the opposite was true. We hypothesize that this is due to GaN growth being limited by the flux of nitrogen, which is difficult to dissociate, whereas GaAs growth is controlled by the dissociation of the gallium precursor (TMGa).

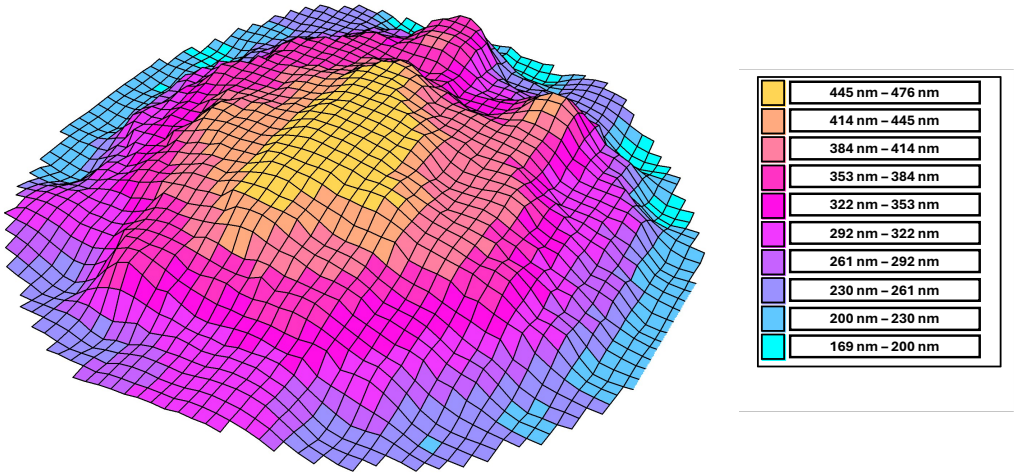

Figure 2.6. *Ellipsometry mapping showing GaN thickness variations.*

We will attempt to determine the source of this thickness inhomogeneity. In this section**,** we first investigate whether this inhomogeneity could be due to uneven distribution of the plasma gases reaching the wafer. To this end, we employed the hydrogen plasma reduction method for indium tin oxide (ITO). This method is based on the fact that H_2 plasma reduces ITO thin films, producing In-rich surfaces[144]. Therefore, we introduced an ITO film deposited on a 4-inch Si wafer into the reactor and exposed it to an H_2 plasma. The surface state of the wafer was then examined using top-view SEM, as shown in the **Figure 2.7**. In each of the studied areas (center, mid-side, and edge), white spots corresponding to indium droplets were observed. Calculating the surface density of these droplets is challenging due to their coalescence. However, it is clear that they are present in each zone with comparable densities. Therefore, the reduction of the ITO sample by hydrogen plasma appears to be quite homogeneous, indicating that H production and flux to the substrate are homogeneous. If we assume that the same is true for N_2 plasma, then the radial distribution of the thickness inhomogeneity cannot be attributed to this factor.

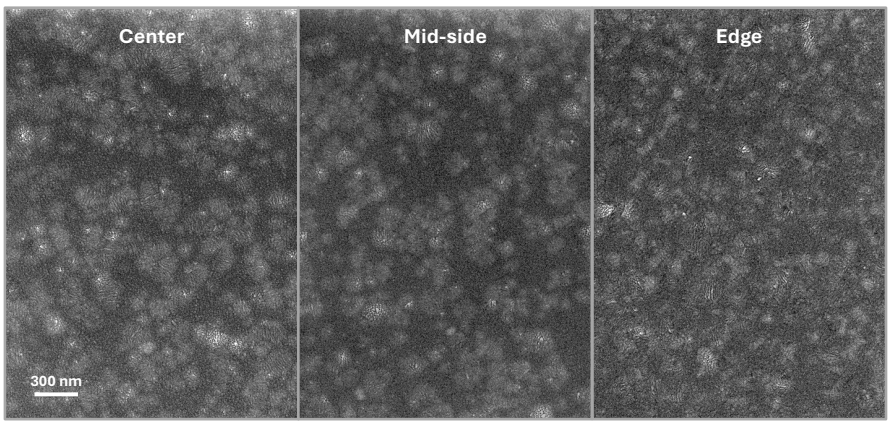

Figure 2.7. *SEM top view images of different areas of the ITO sample after H_2 plasma exposure.*

II. Gas injection system

The gas decomposition process can be divided into two distinct paths: plasma dissociates one portion of the gas (within the plasma zone), while the other part undergoes thermal dissociation (in the growth zone). To accommodate this decomposition logic, a specific gas injection system was required. For this purpose, a custom-built showerhead was designed, enabling gases to be introduced at various levels within the reactor, relative to both the plasma and growth zones. Group-V precursors (N_2 and AsH_3 with addition possibility of H_2 and argon (Ar)) are introduced in the plasma zone for dissociation into N- or As-atom radicals, for GaN or GaAs growth respectively. Radicals then pass through the showerhead toward the growth zone. The group III precursor, typically trimethylgallium (TMGa) in liquid form in a bubbler and its carrier gas hydrogen (H_2), are directly injected into the showerhead through the "Organometallic" (OM) inlet toward the growth chamber. Injecting gallium organometallic away from the plasma prevents cross reactions with V-precursors. It is also possible to inject additional gases other than organometallics through a "Hydride" inlet, which works like the OM inlet, i.e. brings gases directly into the growth chamber. The gas panel depicted in **Figure 2.8** illustrates the different gas inlets and the reactor's integration capabilities. It is via this gas panel that we control the gas supply to the different inlets of the showerhead. The reactor can accommodate 3 organometallic lines, for the moment only one has been installed for gallium but it allows for potential future investigations involving other group III sources. Other lines of group V precursors could also be connected in the future to allow other combinations of III-V or intentional doping. For the moment, only those shown in **Figure 2.8** are available (H_2, AsH_3, N_2 and Ar).

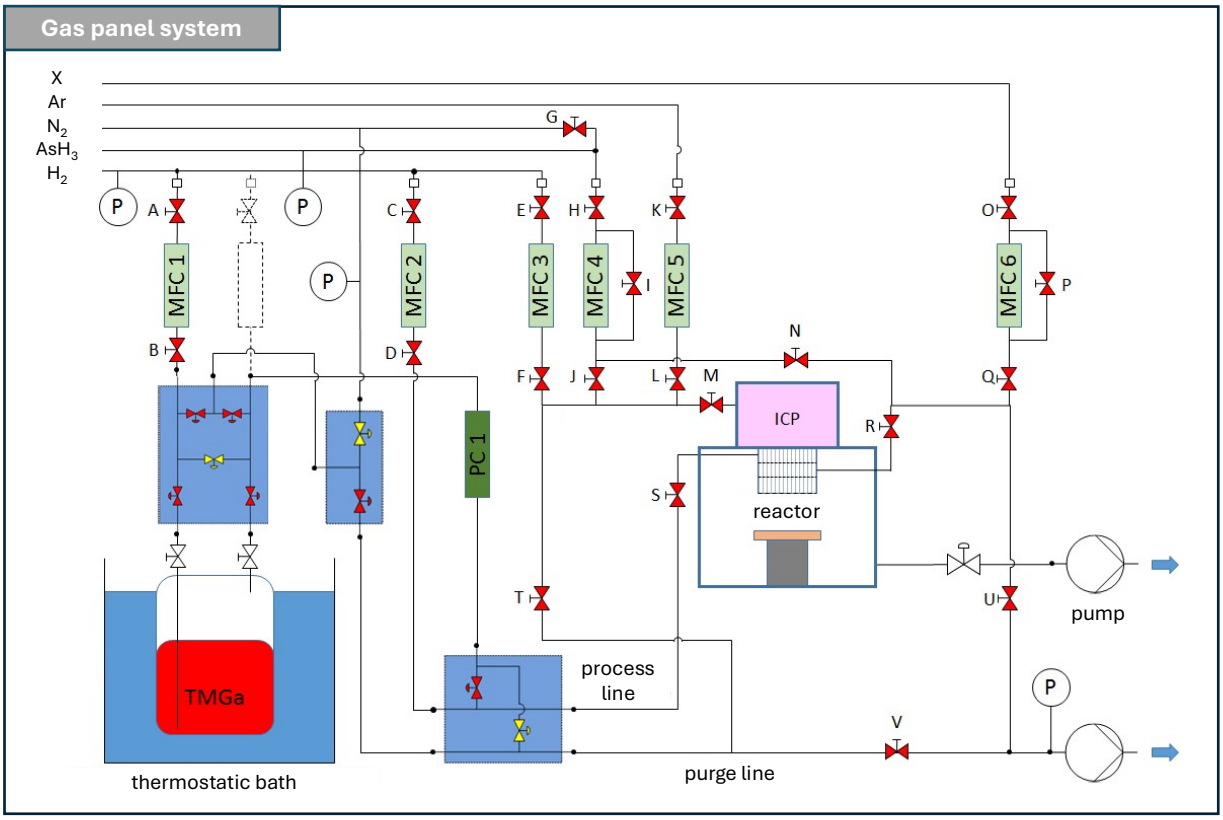

Figure 2.8. *Simplified gas panel schematic.*

III. Substrate holder and heating system

The reactions between the group III and V species take place in the growth zone, at the level of the heated substrate. The substrate holder system is composed of a stainless-steel base surmounted by a quartz bell protecting the inductive heating system, fitted with a quartz spacer (not represented on the diagram) on top of which a graphite susceptor can receive substrates as large as 4 inches in diameter. The substrate holder with the susceptor is represented in **Figure 2.9**. The quartz spacer is a simple shim designed to optimise inductive heating, it positions the susceptor at the right distance from the coil. This part also avoids direct contact between the susceptor and the bell. Inductive coupling is employed to ensure a local heating of the substrate, which is crucial to avoid decomposition of TMGa and subsequent gallium contamination on the reactor wall surfaces.

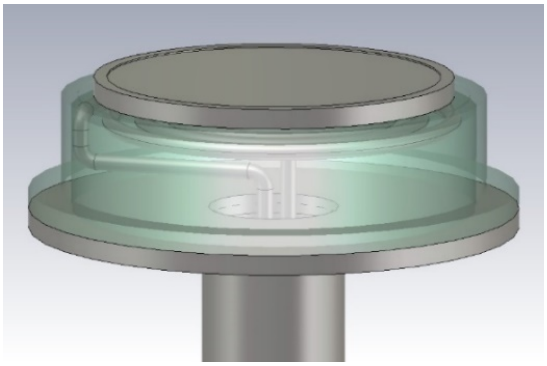

Figure 2.9. *Substrate holder system diagram with the susceptor in transparency.*

The substrate temperature is controlled via a regulation unit (Master Controller v3+®, CEIA) as shown on **Figure 2.10** and monitored with a pyrometer (SH15/SLE®, CEIA). After deposition, a motorized translation allows the substrate holder to be moved out to a position through which the samples can be loaded or unloaded.

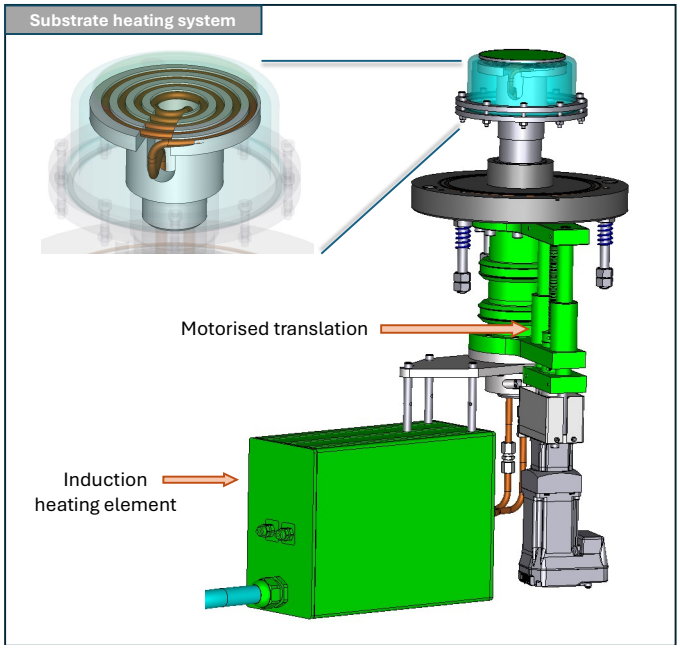

Figure 2.10. *Substrate heating system diagram.*

Let's return to the problem of thickness homogeneity introduced in part **B.I**. Just as the homogeneity of gas flow is crucial, the uniformity of the temperature at the susceptor level is also an important parameter for ensuring a uniform deposition on the substrate. Simulations conducted with ANSYS® software allowed us to visualize the distribution of magnetic flux density across the entire surface of the susceptor providing inductive heating **Figure 2.11. a)**. We observed that this parameter is quite uniform across most of the surface that hosts the substrate, except at the center where the coupling is much less effective (**Figure 2.11. b)**) and at the outermost edges due to side effects. This simulation hypothesis is confirmed by **Figure 2.11. c)**, in which we heated the susceptor until it glowed red (N.B.: at atmospheric pressure, i.e., not under our typical growth conditions). The laser pointer of the pyrometer is visible at the center. Here, we notice that the center of the susceptor is slightly less intensely red than the rest of the disc. This indicates a lower temperature at the wafer's center as suggested by the simulation. The thickness trend of the GaAs film, which is thinner at the center and thicker at the edges, aligns well with this result, unlike the inverse trend observed for GaN in **Figure 2.6**.

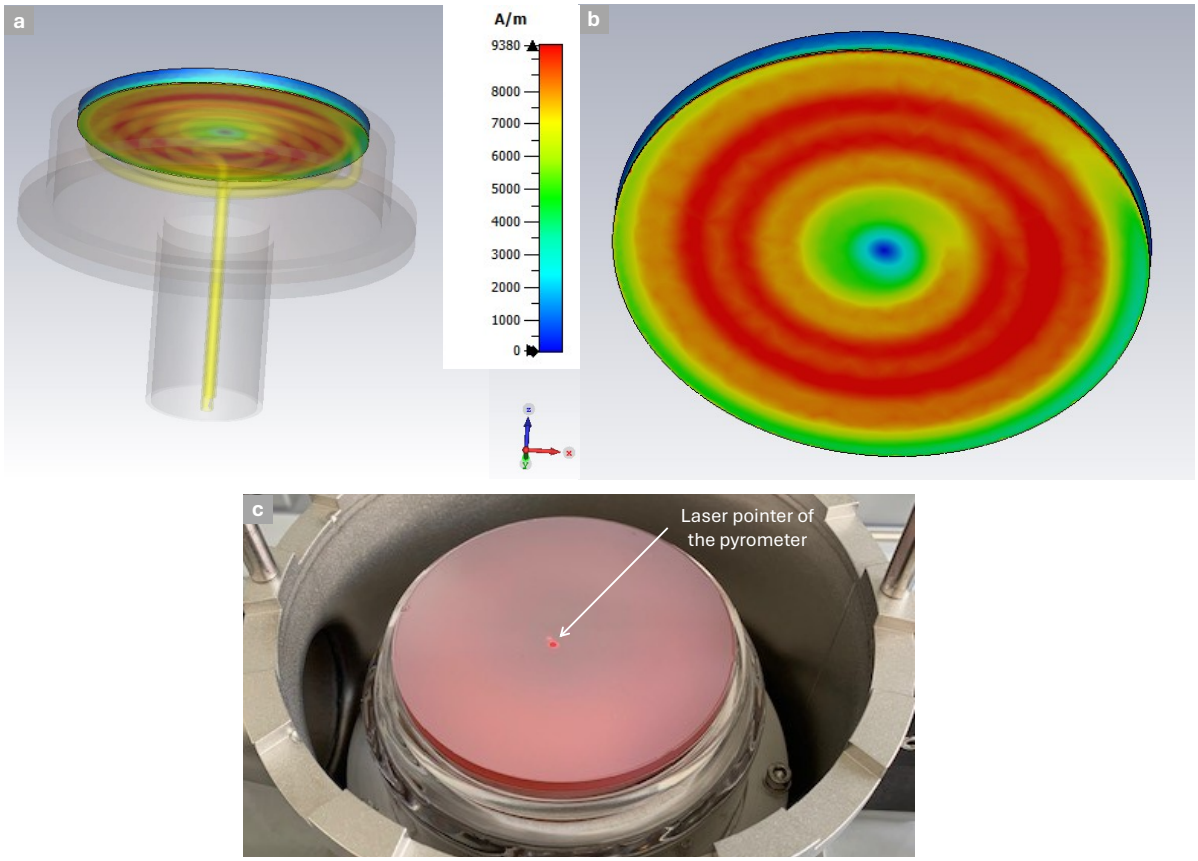

Figure 2.11. *a), b) Simulations of the substrate heating system using Ansys® and c) a photo of the heated susceptor.*

To confirm the temperature uniformity on the rest of the wafer (excluding the center), temperature homogeneity tests under usual growth pressure conditions (0.5 mbar) were conducted using thermal stickers on c-Si wafers, as shown in **Figure 2.12**. The test in **Figure 2.12. a)** was conducted under process pumping at 0.5 mbar, using a setpoint temperature of 190°C. The maximum temperature reached, as read by the pyrometer during heating, was 206°C. The temperature was stabilized at 190°C for 5 minutes before the test ended. The results indicate that it gets slightly hotter towards the mid-border of the wafer (upper sticker in **Figure 2.12. a)**), where

the maximum temperature reached is between 216°C and 224°C. The maximum temperature reached at the border (lower sticker in **Figure 2.12. a)**) is between 210°C and 216°C. These results do not show significant deviations from the setpoint temperature, differing slightly due to the pyrometer's emissivity, which is not precisely calibrated for the specific properties of the silicon wafer used. A higher temperature test was conducted, shown in **Figure 2.12. b)**, where the setpoint temperature was 240°C, with a maximum temperature read by the pyrometer of 252°C. The results were consistent for both stickers placed at different positions on the wafer (one closer to the center and one closer to the edge), indicating good uniformity. The actual maximum temperature on the substrate is therefore between 254°C and 260°C for both positions, with no significant deviations from the setpoint temperature. It appears that uniformity improves with higher temperatures, which is comforting given that most deposition are made between 300°C and 600°C.

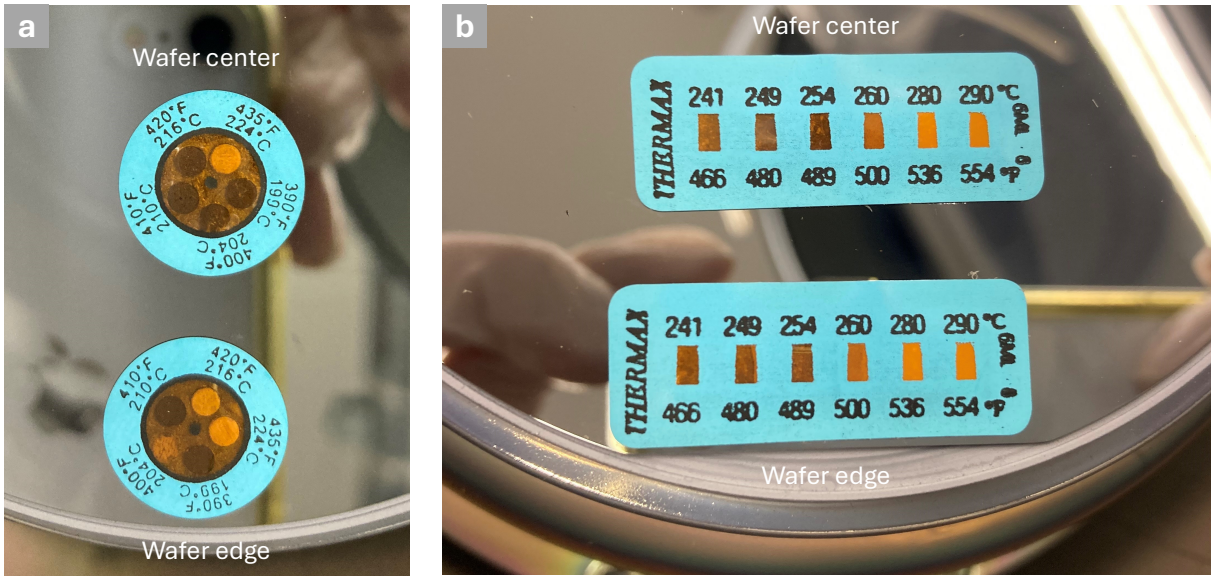

Figure 2.12. *Photos of results of thermal sticker tests on the substrate at 0.5 mbar and for a setpoint temperature of a) 190°C and b) 240°C.*

It is concluded that the difference in thickness homogeneity may correspond mainly to the fact that the substrate temperature is slightly lower when going to the center of the wafer (**Figure 2.11**), given that the gas flow from the plasma is quite uniform (**Figure 2.7**). Additionally, the dynamics of the precursors used for the growth of GaN and GaAs, combined with the specific deposition conditions for each material, may play on atoms diffusion on the substrate and allow for the reversal of the thickness distribution trend.

C. Plasma characteristics

I. E-H transition

In ICP discharge, there are two modes of operation: (i) the electrostatic regime (E) for capacitive coupling and (ii) the electromagnetic regime (H) for inductive coupling. Typically, the

plasma starts in E mode (plasma density of 10^{14} - 10^{16} m^{-3}), then undergoes an E-H transition when the plasma density reaches a critical level (10^{16} - 10^{18} m^{-3}) as the plasma power is increased[145]. The transition between E-mode and H-mode is marked by an abrupt increase in electron density when the discharge power exceeds the critical threshold as represented on **Figure 2.13**.

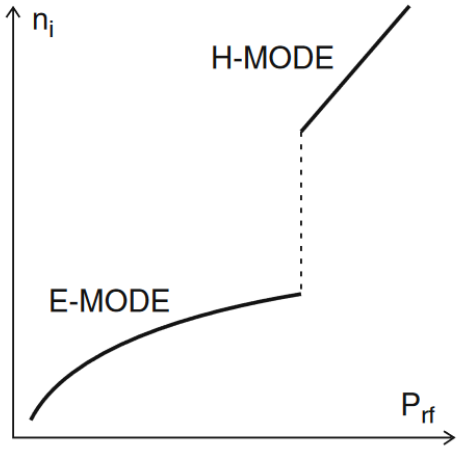

Figure 2.13. *Diagram of the E-H transition taken from Piel book[119].*

In our reactor, an ICP plasma was first generated in a mixture of nitrogen and hydrogen so that N-atoms and NH_x radicals can be produced for GaN growth[141]. The high-power mode where inductive coupling dominates (H-mode) with high plasma density is of particular interest for improving N_2 dissociation[146]. For this purpose, we searched for the plasma power condition required to reach this transition using Optical Emission Spectroscopy (OES) with an AVANTES Avaspec-ULS4096 CL-EVO system.

Figure 2.14. a) represents the optical emission spectrum of H_2/N_2 plasmas at 3 W, 10 W and 50 W. Above 10 W, we observe a jump in emission intensities as illustrated in **Figure 2.14. b)**, such an increase of the light emission was even visible to the naked eye. Therefore, we set a power value greater than 50 W to ensure an inductive mode that would promote higher N-atoms production.

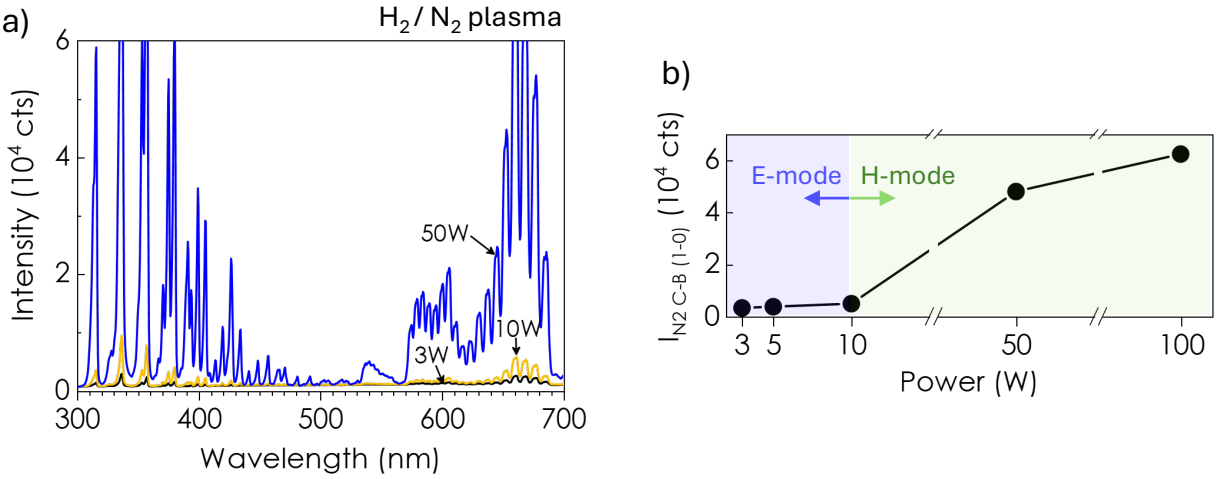

Figure 2.14. *Optical emission spectra of (a) H_2/N_2 (1:40) plasma at 3 W, 10 W and 50 W under a total pressure of 0.3 mbar, (b) N_2 C-B (1-0) line tracking as a function of plasma power to identify the E-H transition.*

II. Plasma power process window

The determination of the adequate plasma power for the deposition process requires further analysis at extended power range especially if a higher growth rate is targeted. For this purpose, OES spectra are captured at RF power values spanning from 30 to 300 W as shown in **Figure 2.15. a)** with a focus on the H_α atomic hydrogen line intensity **Figure 2.15. b)**. These results clearly show that H line monotonically increases from 30 to 200 W after which point a drastic increase is observed. It happens that this trend aligns with the enhanced growth rate for power greater than 200 W along with a reduction in carbon contamination, as it will be described later in **Chapter 3**. In addition, we found that such high RF power values enable the growth of better quality GaN films in terms of crystallinity. Thus, RF power was identified as the main parameter that drives the growth process in two manners: (i) promoting atomic nitrogen generation that contributes to high growth rate of GaN films, while (ii) generating atomic hydrogen which helps in removing carbon contamination from the growth surface.

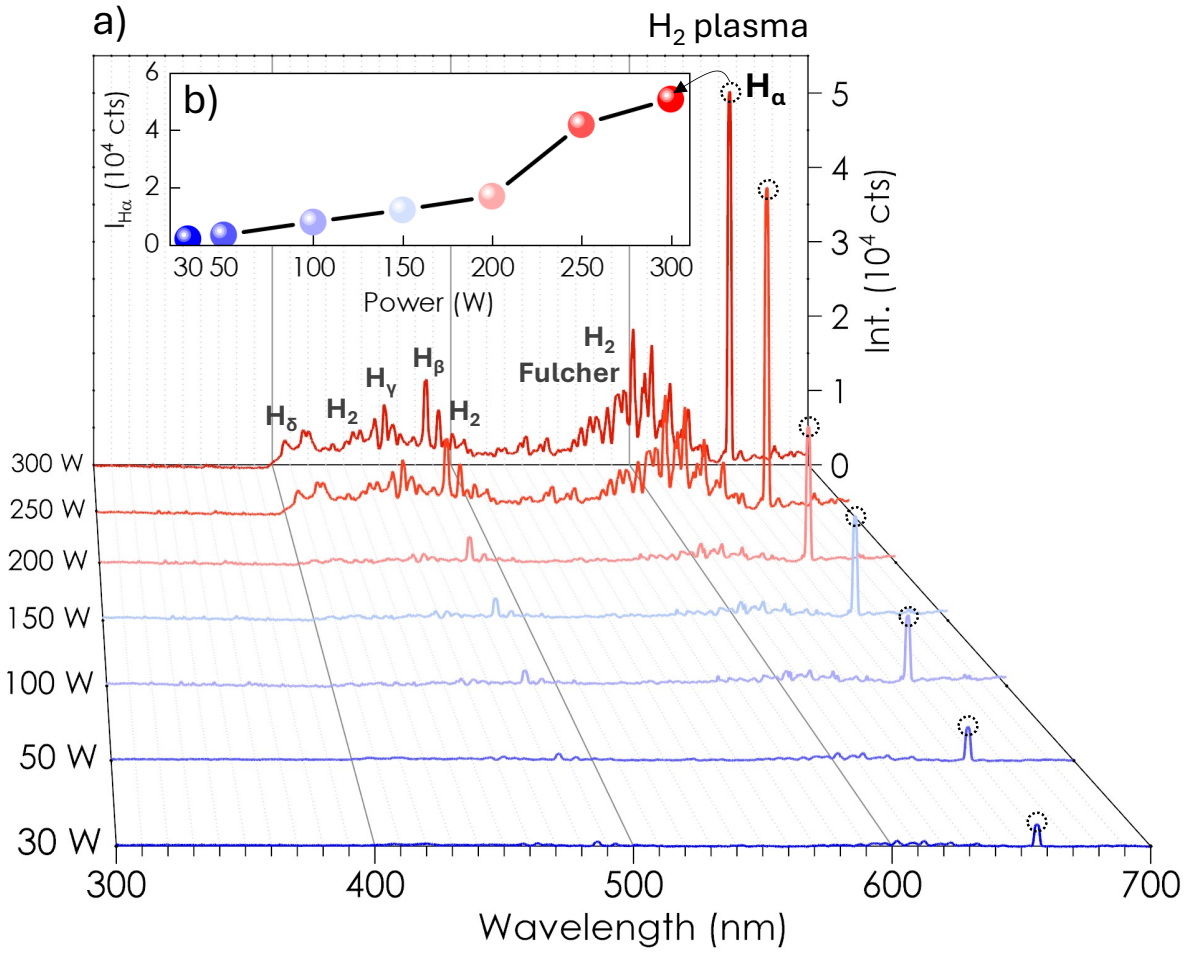

Figure 2.15. *(a) A pure H_2 plasma at different plasma powers and (b) H_α line tracking as a function of plasma power.*

Chapter 2. Summary

This chapter has introduced the architecture and operational principles of our custom-built Remote Plasma Chemical Vapor Deposition (RP-CVD) reactor for III-V growth.

We first introduced the fundamental aspects of plasma, including its definitions, temperature, discharge, density, and pressure, which are crucial for understanding plasma generation and its role in CVD processes. Key advantages of plasma-assisted processes, such as low pressure, low temperature, and the capability for in-situ substrate cleaning plasma treatment, were highlighted.

The design of the RP-CVD reactor, including the plasma generation, gas injection, substrate holder and heating systems were presented. This highlighted the innovative features that distinguish this reactor in the realm of plasma-assisted growth technologies.

We examined the characteristics of the plasma source using OES, focusing on RF power influence on the process. This analysis demonstrated where to position the ICP power to optimize the plasma contribution to the growth process.

Overall, this chapter underscores the innovative features of the RP-CVD reactor and its promising advantages to be an efficient and cost-effective way to produce high-quality III-V semiconductors.

Chapter 3. Growth of GaN thin films by RP-CVD as a proof of concept. 54

A. GaN growth on sapphire 55
I. Growth process 55
II. Main structural and morphological features 55
III. Plasma as a lever for the in-situ growth of buffer layers 57

B. Direct growth of highly oriented GaN thin films on silicon 59
I. Growth process 59
II. Structural and morphological features 61
III. GaN polarity determination 64
IV. Chemical composition analysis 65

C. Ultrathin SiN barrier enables improved GaN growth on Si 67
I. Growth process 68
II. Effects of *'meltback etching'* 69
III. Proposed ultrathin SiN barrier solution 70
IV. Enhancement of GaN film properties 73
V. Proposed growth model 74

Chapter 3. Summary. 77

Chapter 3. Growth of GaN thin films by RP-CVD as a proof of concept

The results section of the manuscript starts with this chapter dedicated to the study of gallium nitride (GaN) thin films. Although GaN is not of significant interest for photovoltaic applications, we chose to investigate it because, at the time, we were unable to work with GaAs due to safety concerns related to the use of arsine. Additionally, GaN remains a highly relevant and trendy material in the fields of microelectronics and photonics. Therefore, we decided to use the existing nitrogen line in the reactor to study the growth of GaN on various substrates as an initial proof of concept, demonstrating the reactor's proper functioning and its ability to produce crystalline III-V semiconductor layers. This period also provided an opportunity to adjust certain reactor components and enhance the control software under LabView, which led to extended periods of reactor downtime.

A critical challenge in GaN growth is selecting an appropriate substrate that matches its structural, lattice, and thermal properties. This choice significantly affects the crystal quality of the grown GaN film. Given the lack of bulk GaN wafers, substrates such as sapphire (Al_2O_3), aluminium nitride (AlN), and silicon carbide (SiC) are commonly used. Sapphire is the most used solution for GaN growth despite the notable difference in lattice parameter of 16%[147]. Indeed, this discrepancy is mitigated by the similarity between the hexagonal geometry of the atomic configuration of the sapphire basal plane and that of the c-plane of a thermodynamically stable GaN single crystal, which has a wurtzite structure[148]. Moreover, sapphire is distinguished by its excellent chemical and thermal stability[149]. Usually, a buffer layer is added to better match the crystalline structure between GaN and the substrate[150]. The issue with this additional layer is that it adds to the complexity and cost of production, as it is fabricated using complicated techniques. Some of these layers, along with their fabrication techniques and process temperatures, are presented in **Table 3.1**.

Buffer layer	**AlN**	**AlGaN**	**SiC**	**SiN**
Growth method	MBE / MOCVD	MBE / MOCVD	CVD	RP-CVD
Growth temperature (°C)	~ 1100°C[21]	~ 1035°C[22]	~ 1300°C[23]	500°C this work
GaN layer quality	Epitaxial	Epitaxial	Polycrystalline[24]	Polycrystalline, highly c-axis oriented

Table 3.1. *Comparison of buffer layer growth techniques, temperatures and GaN crystalline quality obtained.*

Given our ultimate goal of providing a low-cost global solution for III-V thin film growth, we need to investigate the growth of those materials on economically viable substrates. Unfortunately, the substrates most commonly used for GaN growth including sapphire, aluminium nitride and silicon carbide, are not economically competitive, and have the disadvantage of being insulating in nature and hardly available in large diameter which make them poor candidates for high-volume production of high-power devices[151]. Silicon (Si) became an interesting candidate as a substrate for GaN growth when the first GaN LED grown on Si was demonstrated via MBE[152,153], which proved that functional devices could be fabricated on it. Silicon can meet the requirements

of a low-cost, large-area, and conductive substrate and would thus allow the integration of high-power GaN optoelectronic or electronic devices with Si-based electronics. However, this remains very challenging given the lattice mismatch between Si and GaN of nearly 17% (leading to a significant dislocation density in the GaN layers), and the thermal expansion coefficient mismatch, which amounts to 54% and can induce mechanical stress in the epitaxial layers, leading to cracking and delamination.
Therefore, before addressing the growth of GaN on silicon which presents numerous challenges, we decided to carry some growths on sapphire. Then, we will move to the direct growth of GaN on c-Si substrates and finally we will also explore the potential of a SiN buffer layer grown in the RP-CVD reactor just before the GaN.

A. GaN growth on sapphire

I. Growth process

Depositions were performed on c-plane (0001) sapphire substrates, previously cleaned with deionized water and solvents (acetone and isopropanol). The substrates were then immediately loaded into the reactor. The chamber was pumped to a base pressure of around 3.10^{-7} mbar. Under vacuum, the substrate temperature was gradually increased (~ 100°C/minute) up to the process temperature. Prior to deposition, a H_2 plasma treatment was applied to the sapphire substrate to remove any residual contaminations from its surface. The group III precursor used for GaN growth is trimethylgallium (TMGa), which is stored in liquid form within a bubbler, with hydrogen (H_2) serving as the carrier gas. The group V precursor is nitrogen (N_2) diluted in hydrogen (H_2). Nitrogen was chosen over ammonia (NH_3) for simplicity of use as NH_3 is toxic and corrosive. Nevertheless, it is well known that N_2 is very difficult to crack as the dissociation energy of this molecule stands at 946 kJ/mol[146]. This becomes possible thanks to the ICP source, which in its bright mode (H-mode, see **Chapter 2**), is highly efficient at dissociating nitrogen (N_2)[154].

II. Main structural and morphological features

Figure 3.1. a) shows the x-ray diffraction pattern in the Bragg-Brentano geometry of the GaN film grown on sapphire. In this graph, the characteristic peak of the (0002) plane of GaN in its hexagonal wurtzite structure is identified at 34.3°. The peak observed at 41.7° corresponds to the c-plane of the sapphire substrate. The absence of additional peaks associated with GaN indicates that the growth is occurring in a well-defined crystalline direction on the sapphire substrate. The graph in **Figure 3.1. b)** zooms in on the sharp peak (0002), from which we have determined full width at half maximum (FWHM) of 0.3°. Therefore, we successfully achieved crystalline GaN growth via RP-CVD which is a very promising result given that the growth has not been optimized yet.

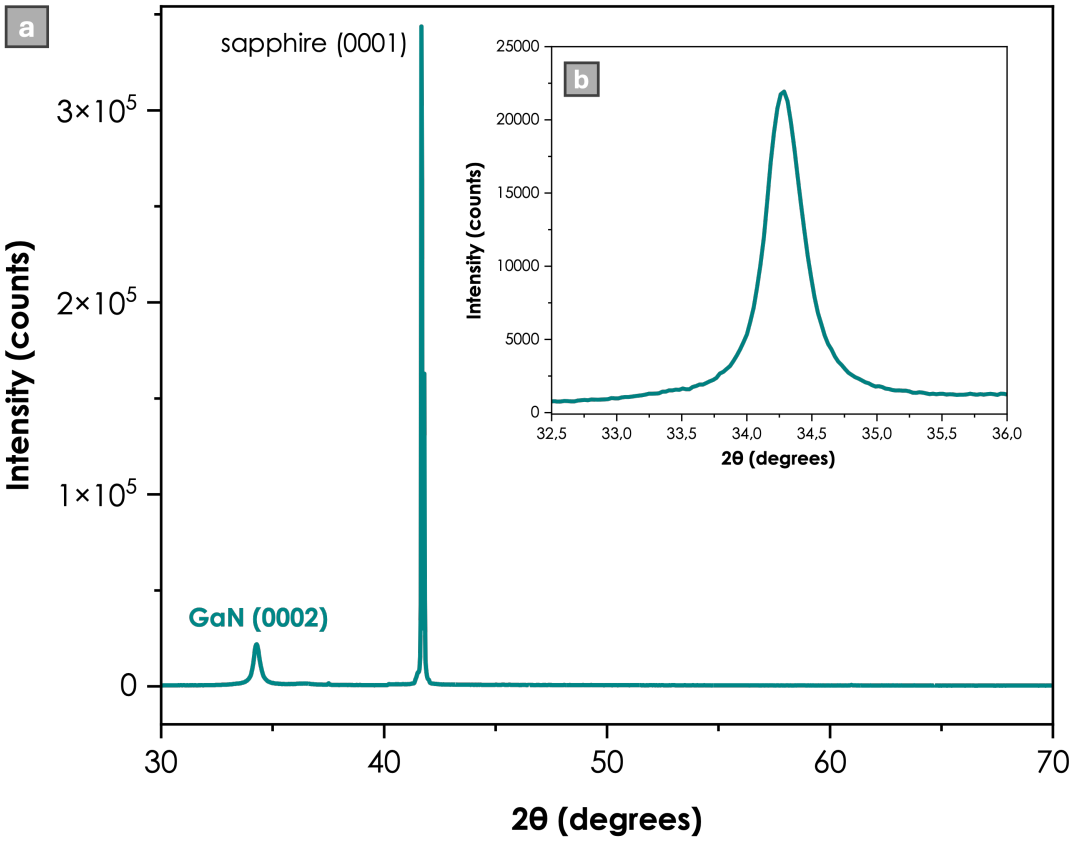

Figure 3.1. *a) θ-2θ scans of GaN-on-sapphire by RP-CVD at 500°C, 150 W and 0.5 mbar. The inset in b) shows a zoom on the (0002) GaN peak.*

In terms of morphology, SEM images in **Figure 3.2** reveal a film of around 330 nm, i.e. a growth rate of 0.33 µm/h, with a very smooth top-surface **(a)** and a cross-section **(b)** showing no columnar growth (typical of polycrystalline phase) contrary to the growth on c-Si substrate[155], as will be presented in the next section.

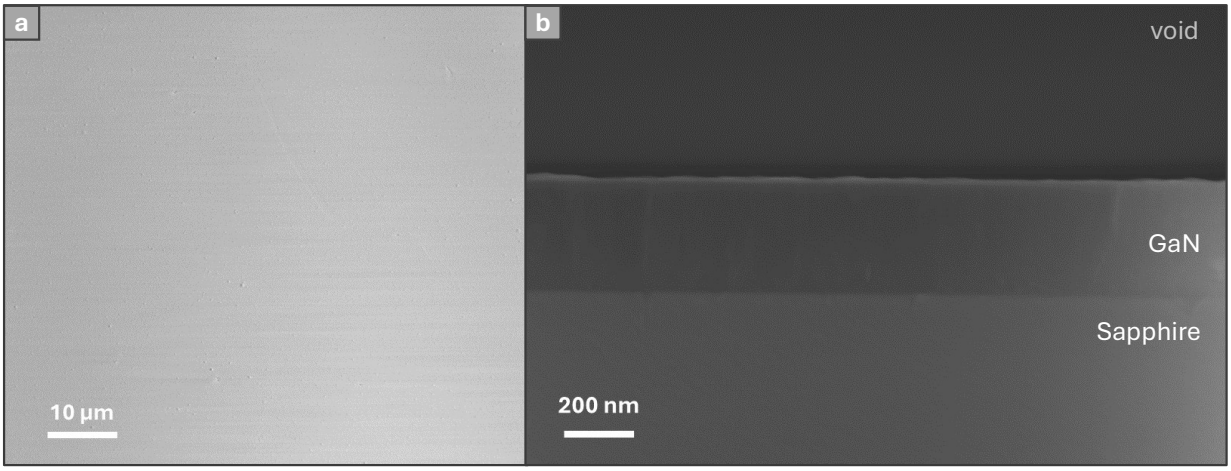

Figure 3.2. *a) SEM surface image and b) SEM cross-section image of GaN-on-sapphire sample.*

It should be noted that imaging with precision using SEM is challenging due to the insulating nature of the sapphire substrate, which causes significant charging effect. Therefore, we aimed at examining the film structure more closely using TEM. In **Figure 3.3. a)**, it is noticeable that in

the upper half of the GaN film, small grains start to appear within the structure of the layer. In **Figure 3.3. b)**, high-resolution imaging reveals well-aligned GaN crystal planes in the first 5 nanometers, suggesting a beginning of epitaxial growth. However, the film becomes polycrystalline and defective beyond this point. A similar observation was made by Motamedi *et al*. in their study on direct GaN growth on sapphire using PEALD[156]. They attributed this breakdown of epitaxy to edge dislocations and impurities as the primary causes. Daudin *et al*. hypothesized that edge misfit dislocations in GaN layers act as nucleation centers, leading to the formation of GaN dots on top of the initial epitaxial layers and ultimately causing the breakdown of epitaxy[157]. Since the issue most likely originates from the interface, it will be necessary to improve it in order to maintain epitaxy throughout the entire thickness of the film.

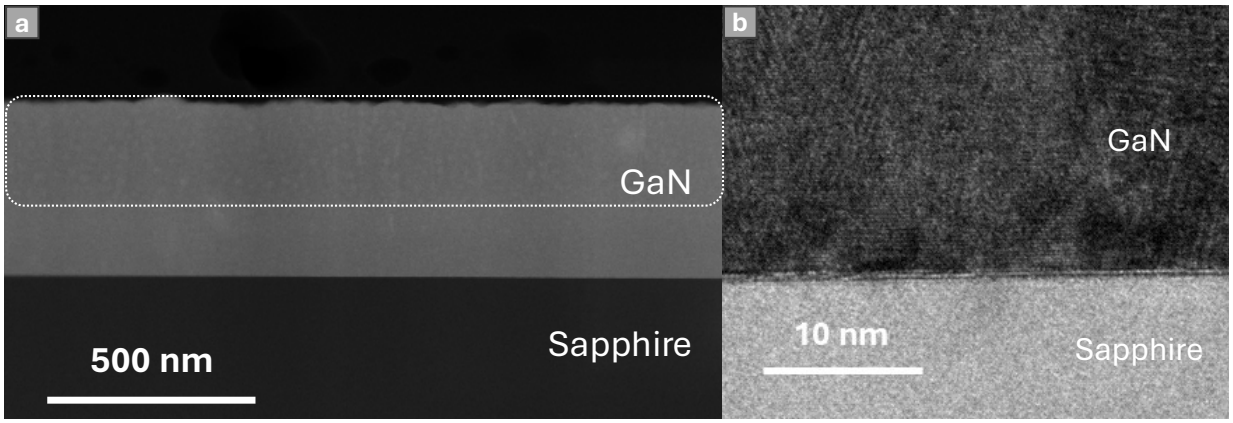

Figure 3.3. *a) Cross-sectional STEM-HAADF with the upper part of the film (dotted line area) containing small grains and b) HRTEM image of GaN-on-sapphire sample.*

III. Plasma as a lever for the in-situ growth of buffer layers

As introduced earlier in this chapter, a buffer layer is typically employed to improve thin film quality by creating a gradient between the foreign substrate and the GaN layer that enhances lattice match. Specifically, an AlN buffer layer is often used for the growth of GaN as there is a low lattice mismatch of 2.4 % between the two materials[158–161]. This type of interlayer could potentially prevent the breakdown of epitaxy in the GaN layer observed in **Figure 3.3**. The recent article by Zhang[142] provides insights into what occurs when GaN is directly grown on sapphire or on an AlN interlayer using ICP-MOCVD, a process similar to ours, as shown in **Figure 3.4**. Due to the significant lattice mismatch between sapphire and GaN, direct growth on sapphire leads to great stress and thus inconsistent in-plane orientations of nucleating GaN crystals. This inconsistency prevents complete merging of the crystal islands during subsequent growth, resulting in the formation of amorphous regions with rough surfaces at the edges of the islands (**Figure 3.4. a)**). In contrast, the lattice mismatch between AlN and GaN being much smaller, GaN crystal nuclei can achieve more consistent in-plane orientations when grown on an AlN buffer layer, which facilitates the merging of the crystal islands during the subsequent growth (**Figure 3.4**. **b)**).

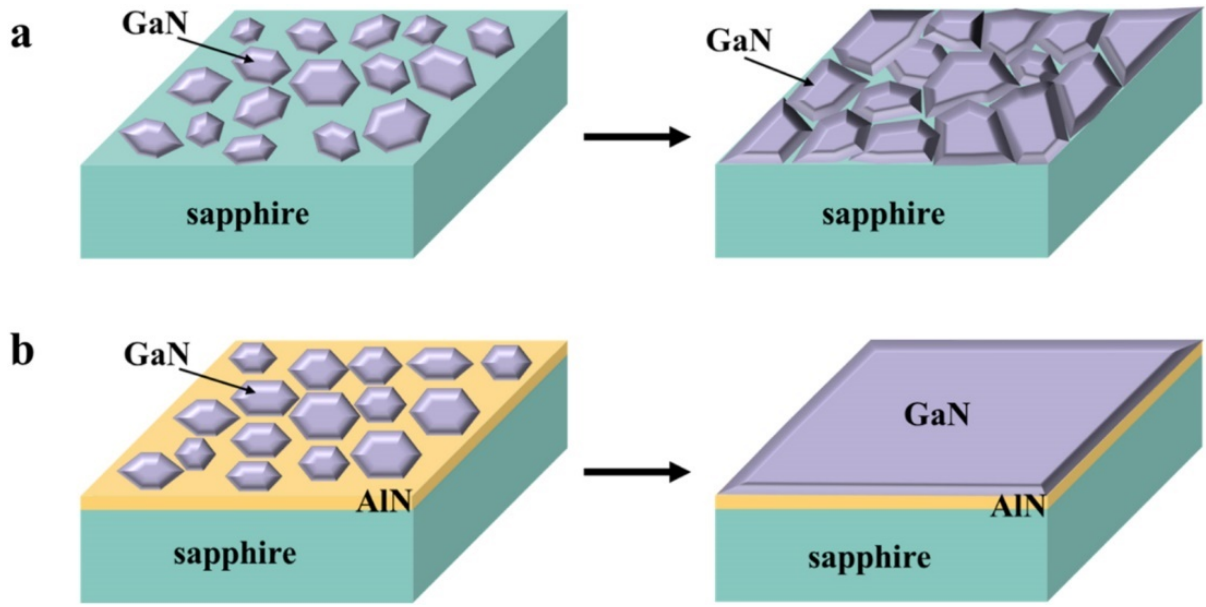

Figure 3.4. *Schematic diagram of the GaN growth process from the nucleation stage to the merging stage of the crystal islands on (a) sapphire substrate and (b) AlN/sapphire template*[142].

However, as previously mentioned, this approach is not economically ideal due to the expensive growth techniques required or the need to modify the process, which can extend production steps, as seen in Zhang's study where they used sputtered AlN[142]. In our case, we wondered whether it would be possible to reproduce such a layer by leveraging our plasma process. Losurdo *et al.* have already evidenced its feasibility in a paper where they investigated the kinetics of surface reactions on sapphire substrates when exposed to H-atoms and N-atoms from RF remote plasma by means of ellipsometry and x-ray photoelectron spectroscopy (XPS) analysis[162]. Similarly, we have demonstrated the possibility of creating a thin AlN layer by applying a nitrogen plasma treatment to the sapphire substrate prior to growth in our RP-CVD reactor. This layer was effectively detected using ellipsometry in **Figure 3.5**. The fitting is highly accurate (χ^2 = 0.29), indicating an AlN layer thickness of approximately 26 nm, with the GaN layer grown on top being about 300 nm thick. Thus, a thin AlN layer can be created at low temperature of 500°C using a simple N_2 plasma for 15 minutes, just before GaN growth. Furthermore, hydrogen was added to the plasma and, according to the work of Y-C Chen[163], could reduce oxygen incorporation and thereby improve the quality of GaN. Unfortunately, this discovery was made at the very end of our project, so we do not yet have TEM images or X-ray data to confirm that the GaN film quality is improved with this intermediate layer. However, this remains an avenue for future investigation of GaN growth on sapphire in our reactor. Nonetheless, in part **C** of this chapter, we will demonstrate in greater detail how a similar approach of nitridation can be used for GaN growth on silicon, yielding more detailed results.

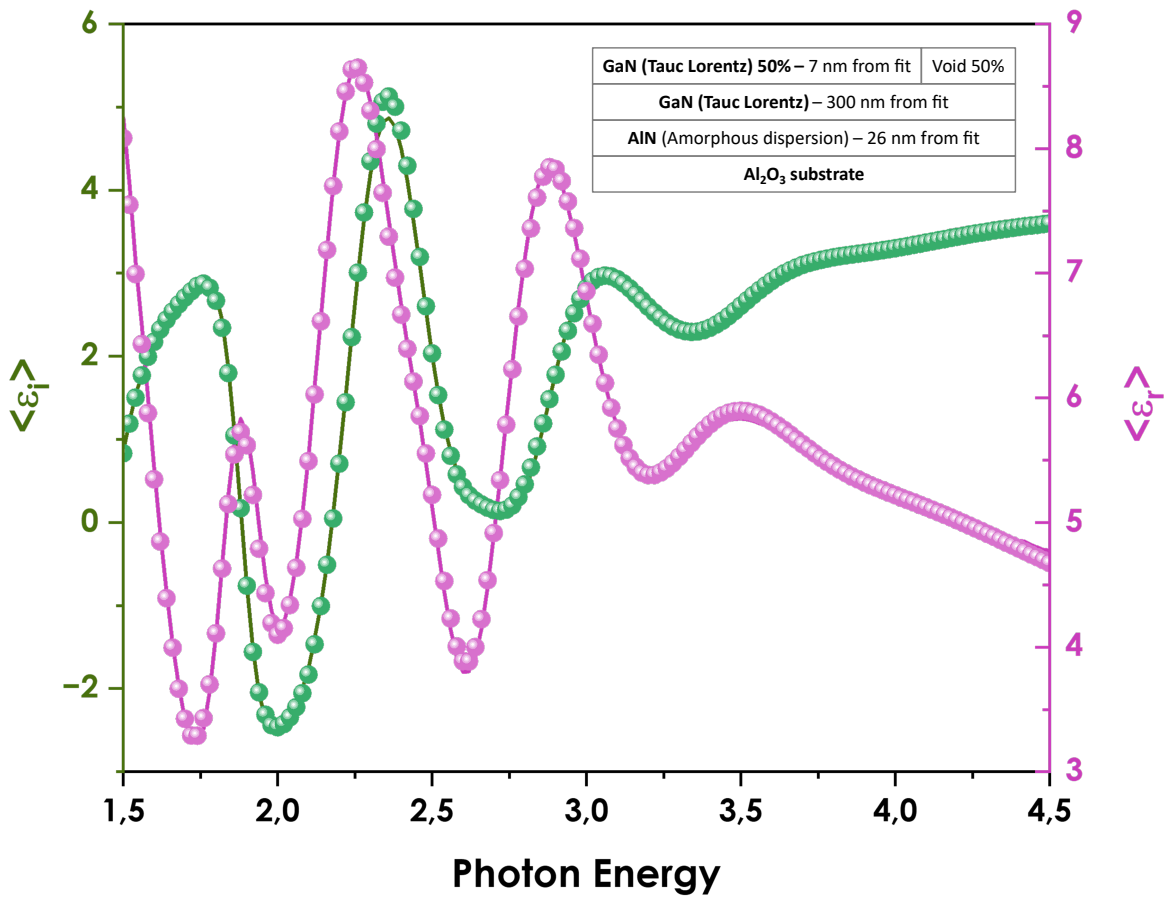

Figure 3.5. *Ellipsometry measurement of GaN-on-sapphire by RP-CVD with N_2 plasma pretreatment with the corresponding optical model (layer stack) used to fit the data (the symbols represent the measured data points, while the lines correspond to the fit).*

B. Direct growth of highly oriented GaN thin films on silicon

In this section we demonstrate that highly textured GaN thin films can directly be grown on low-cost silicon substrates using a remote inductive coupled plasma operating at RF power of 250 W. The growth was performed at a pressure of 0.3 mbar and a temperature of 500°C. We will present the results related to the obtained GaN films, in terms of crystalline structure, morphology and composition.

I. Growth process

Depositions were performed on 4-inches (100) p-type silicon substrates, doped with boron ($\rho \approx 0.001$ Ohm.cm). The native oxide layer on the bare wafers was removed by performing a 45 seconds dipping into a bath with hydrofluoric acid (HF) diluted to 5% with deionized water.

The substrate was then immediately loaded into the reactor. The chamber was pumped to a base pressure of around 3.10^{-7} mbar. Under vacuum, the substrate temperature was gradually increased (~100°C/minute) up to the growth temperature. Prior to deposition, a plasma treatment was applied to the silicon substrate to remove organic contaminations from its surface. It consisted of a H_2 plasma (100 sccm) at 150 W of RF power under a pressure of 0.3 mbar, lasting 10 minutes[164]. In order to determine the optimal conditions that ensure both a high growth rate and a film of high crystalline quality, we performed a parametric study by varying the growth temperature, the substrate's surface state (i.e. with or without nitridation) and the plasma power (**Table 3.2**).

Sample name	Substrate temperature	Chamber pressure	RF plasma power	Group-III precursor TMGa flow / H_2 flow	Group-V precursor H_2 flow/ N_2 flow
S1	300°C	0.5 mbar	150 W	2 sccm / 60 sccm	10 sccm / 400 sccm
S2	400°C	0.5 mbar	150 W	2 sccm / 60 sccm	10 sccm / 400 sccm
S3	500°C	0.5 mbar	150 W	2 sccm / 60 sccm	10 sccm / 400 sccm
S4	500°C	0.5 mbar	150 W	2 sccm / 60 sccm	10 sccm / 400 sccm
S5	500°C	0.3 mbar	150 W	1 sccm / 30 sccm	5 sccm / 200 sccm
S6	500°C	0.3 mbar	200 W	1 sccm / 30 sccm	5 sccm / 200 sccm
S7	550°C	0.3 mbar	200 W	1 sccm / 30 sccm	5 sccm / 200 sccm
S8	600°C	0.3 mbar	200 W	1 sccm / 30 sccm	5 sccm / 200 sccm
S9	**500°C**	**0.3 mbar**	**250 W**	**1 sccm / 30 sccm**	**5 sccm / 200 sccm**
S10	550°C	0.3 mbar	250 W	1 sccm / 30 sccm	5 sccm / 200 sccm
S11	500°C	0.3 mbar	300 W	1 sccm / 30 sccm	5 sccm / 200 sccm

Table 3.2. *Growth conditions for 11 samples of GaN thin films produced by RP-CVD. S9 conditions have been chosen for the detailed characterization of the film in this section.*

Figure 3.6 shows the results of the optimization of the process parameters in terms of growth rate. Samples from S1 to S3 illustrate the effect of increasing the substrate temperature from 300 to 500°C at fixed pressure of 0.5 mbar and RF power of 150W. The increase in the growth rate can be explained by an enhanced dissociation of TMGa at the substrate level. When fixing the temperature at 500 °C, adding a SiN interface layer (S4) or even reducing the pressure to 0.3 mbar (S5) did not affect the growth rate, while a significant improvement was observed by increasing the RF power from 150 to 200 W (S6), nearly doubling the deposition rate. At 200 W, further increment in substrate temperature to 550°C (S7) and 600°C (S8) leads to the increase of the growth rate, likely due to improved thermally activated TMGa dissociation. In the same way, further increasing the RF power to 250 W (S9) and 300 W (S11) resulted in even higher deposition rate close to 0.7 µm/h. Finally, we choose the process conditions of S9, represented with a green circle in **Figure 3.6**. This particular set of conditions enabled us to achieve a reasonable growth rate of 0.55 µm/h (comparable with conventional methods) while having a film that exhibits the best characteristics in terms of crystalline quality. The properties of the GaN film resulting from this process conditions are further discussed in the subsequent subsections.

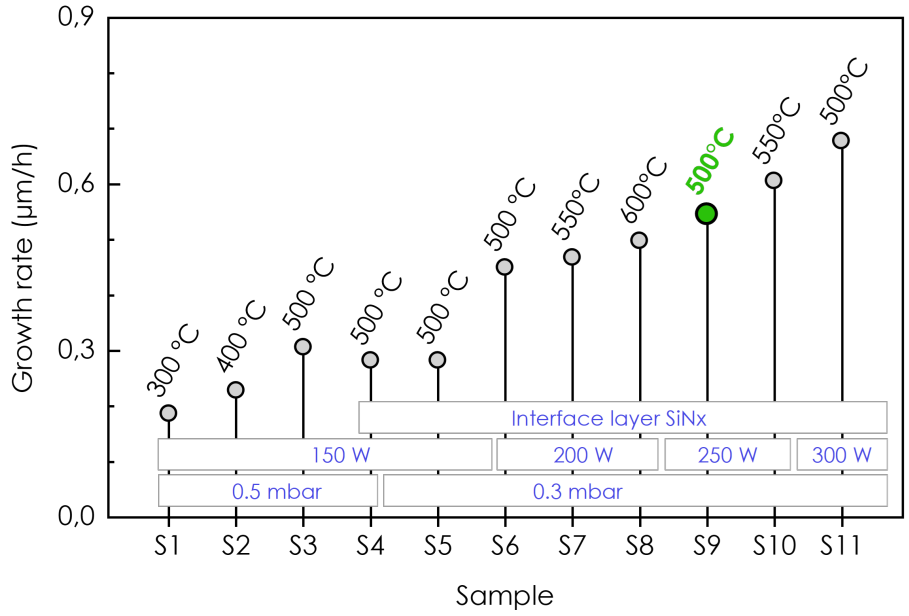

Figure 3.6. *Optimization of growth conditions with parameter-by-parameter effect on growth rate.*

II. Structural and morphological features

Figure 3.7 shows the X-ray diffraction pattern in the Bragg-Brentano geometry of a GaN thin film grown under the working conditions of S9 given in **Table 3.2**. It presents a main peak at 34.2°, corresponding to the (0002) characteristic peak of GaN in the wurtzite structure. The FWHM of this peak is 0.3°, similar to what was achieved for growth on sapphire substrates (**Figure 3.1**). The additional peaks between 45° and 60° originate from forbidden reflections of the silicon substrate[165] and/or source contamination. This shows that the films have a well-defined texture with grains oriented in the c direction. Despite the challenges posed by the fourfold symmetry of the Si (100) surface[166], which typically results in two distinct domain alignments, we successfully achieved well-oriented GaN growth through RP-CVD.

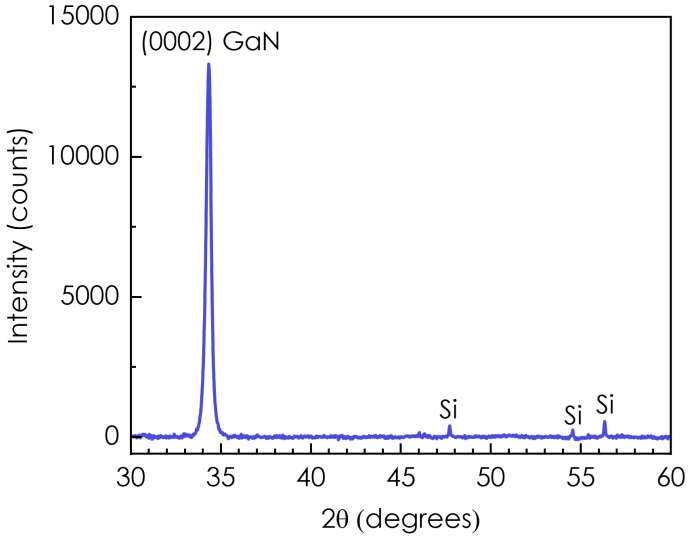

Figure 3.7. *XRD spectrum of a GaN thin film grown by remote-plasma CVD. Operating conditions of sample S9 (see **Table 3.2**).*

The average crystallite size has been calculated using the Scherrer formula given in **Equation (1)** where D is the average crystallite size in nm, *IB* the integral breadth, *K* is a numerical factor frequently described as the crystallite form factor or Scherrer constant (here K=1.07 corresponding to a spherical crystallite for a calculation with IB), λ is the incident wavelength ($\lambda = 1.54$ Å, Cu-K_α radiation), θ_{hkl} the Bragg diffraction angle of the corresponding (hkl) plane. The integral breadth (IB) is a measurement of the peak width. To calculate IB_{film} in **Table 3.3**, corresponding to the GaN (0002) peak, one has to consider the artefacts induced by the equipment (slit size, instrumental width...). For this purpose, another value, the instrumental integral breadth (IB_{instru}) was introduced and obtained by measuring a reference peak on the Si substrate. Fortunately, unlike the case of diffraction from powder sample, IB_{instru} is independent of the angle. The instrumental width is subtracted from the total width and a corrected IB value of the GaN film is obtained (see **Table 3.3**). Finally, an average crystallite size of 97 nm has been calculated, which we will discuss in more detail later.

$$D = \frac{K\lambda}{IB\ cos\ \theta_{hkl}} \qquad (1)$$

Parameters						
K	λ (Å)	Peak position 2θ (°)	IB totale (°)	IB instru (°)	IB film (°)	D (nm)
1.07	1.54	34.24	0.20	0.10	0.10	97.95

Table 3.3. *Crystallite size calculation from Scherrer formula. Operating conditions of sample S9 (see **Table 3.2**).*

Ellipsometry measurement in **Figure 3.8** shows the real and imaginary parts of the pseudo-dielectric function of the sample S9. The experimental data were fitted using a Tauc-Lorentz dispersion function (**Equation (2)**) and the layer stack presented in the inset, where a thin SiN interfacial layer of 17 Å was added between the c-Si substrate and the grown layer. This layer results from the nitridation treatment introduced earlier, the effects of which will be discussed in detail in section **C**. Its thickness value was determined using ellipsometry performed on the c-Si wafer exposed to a H_2-N_2 plasma prior to GaN deposition. On top of the ultrathin SiN, a layer of GaN corresponding to the bulk material and a second layer described as a mixture of GaN and voids to simulate the roughness of the film via Effective Medium Approximation (EMA) were used. The experimental data could be reproduced by the optical model with the following fitting parameters: an optical bandgap E_g of 2.06 eV, an amplitude A of 54, a resonant energy E_0 of 5.13 and a disorder parameter C of 3.29. From this simulation, a GaN thickness of 550 nm, having a surface roughness of 10 nm, was deduced. Subsequent SEM and AFM measurements presented in **Figure 3.9** confirm the reliability of this fit.

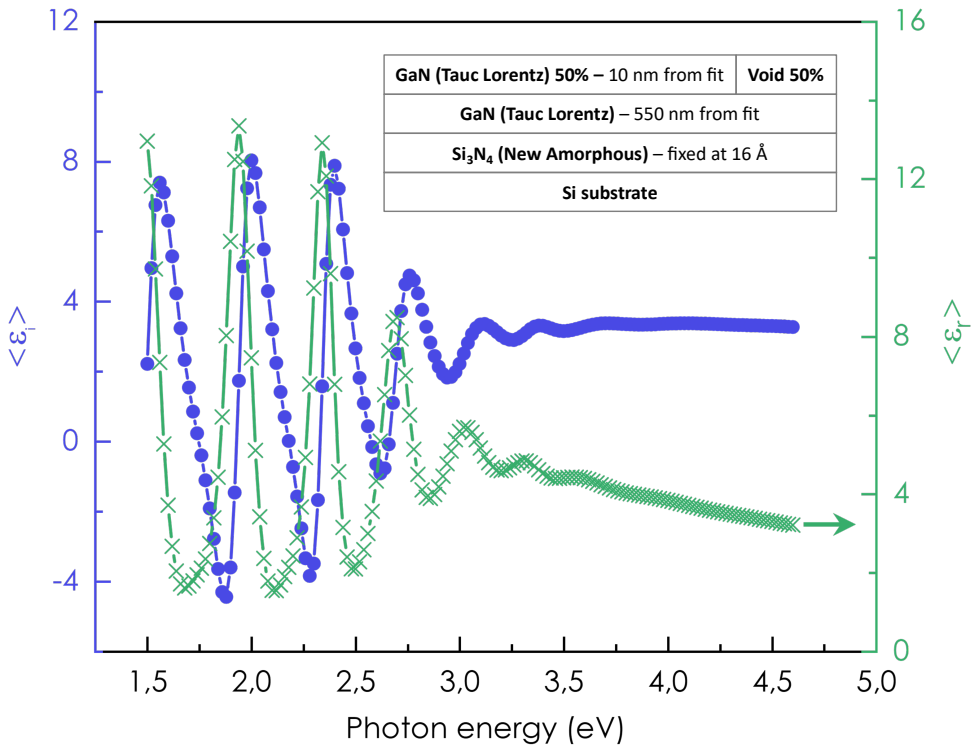

Figure 3.8. *Ellipsometry measurement of GaN-on-Si by RP-CVD with the corresponding optical model (layer stack) used to fit the data. Operating conditions of sample S9 (see **Table 3.2**).*

$$\varepsilon_2(E) = \frac{AE_0C(E-E_g)^2}{(E^2-E_0^2)^2+C^2E^2}\frac{1}{E} \quad (E > E_g) \qquad \varepsilon_2(E) = 0 \quad (E \leq E_g) \qquad (2)$$

In terms of morphology, **Figure 3.9. a)** shows the cross-sectional SEM micrograph of the GaN film (S9) on Si. Contrary to the growth on sapphire (**Figure 3.2. b)**), the GaN film deposited on c-Si exhibits a columnar structure with well-defined boundaries. As GaN has a significant lattice mismatch with silicon, it inevitably leads to the formation of a structure of slightly misoriented sub-grains. We should mention that the thickness extracted from SEM, i.e. ~550 nm) is consistent with that obtained from the modelling of the ellipsometry data (**Figure 3.8**). The top-surface morphology is shown in **Figure 3.9. b)** It reveals grains that are fairly uniform in size. For confirmation, a statistical analysis of the grain size was conducted using ImageJ software[167]. The corresponding Gaussian distribution is shown in **Figure 3.9. b')**. The average grain size is around 94 nm, which is in good agreement with the 97 nm crystallite size calculated from X-ray diffraction (**Table 3.3**). This means that overall, within each grain, a coherent crystalline orientation is achieved. As for topographical aspects, AFM measurements on the GaN film reveal a relatively smooth surface with a root mean square (RMS) roughness of 6.5 nm in the scanning area of $6.25\mu m^2$ as shown in **Figure 3.9. c)**, a value very close again to the one obtained with ellipsometry. The results show that the RP-CVD reactor is capable of producing GaN layers with strong crystalline orientation at a low temperature of 500°C, using N_2 as the nitrogen source. We will now delve deeper into the analysis of this layer to examine it thoroughly.

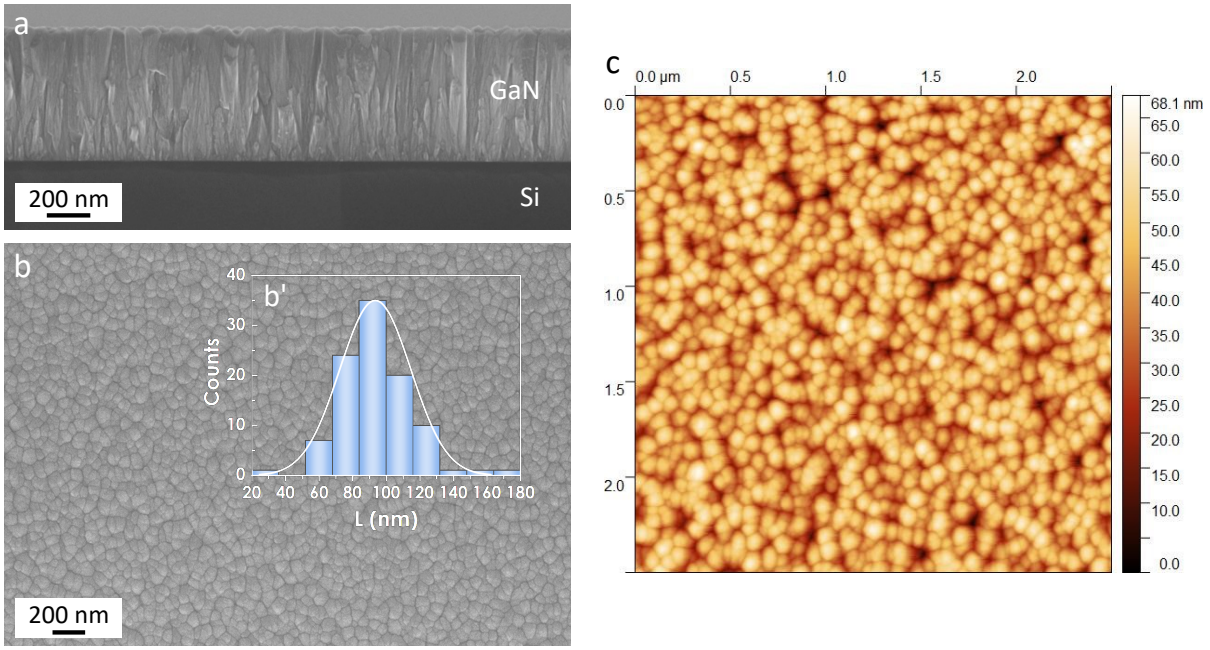

Figure 3.9. *Cross-section a) and top-view b) SEM images of a 550 nm thick GaN film on c-Si, b') statistical distribution of the grain size and c) AFM image of the GaN thin film. Operating conditions of sample S9 (see* ***Table 3.2****).*

III. GaN polarity determination

As our GaN films have a wurtzite structure and exhibit a growth strongly oriented along the polar axis c, we can determine the polarity (+c or -c) of the film by revealing it through chemical etching. The anisotropic KOH (potassium hydroxide) etchant is commonly used to reveal the polarity of GaN. For this purpose, we diluted KOH pellets in purified water as the high dielectric constant of water allows KOH to polarise into K^+ and OH^- which oxidise the atoms in the GaN film[168]. A 1 M solution of KOH was heated to 70°C with a gentle magnetic stirring. Once the temperature of the solution was stabilized, the GaN sample was dipped into the solution for 5 minutes. It was then thoroughly rinsed in three baths of deionized water to ensure that all residual KOH was removed, and dried in nitrogen atmosphere. The surface appearance before and after etching was investigated using SEM as shown in **Figure 3.10. a)** and **b)**, respectively. Overall, the KOH treatment did not induce major changes on the morphology when comparing **Figure 3.10. a)** and **b)**, except for minor modifications coming from classical etching, i.e. reduction of the grain size. Therefore, one may conclude that the film is Ga-polar (i.e., +c plane oriented or metal polar). Indeed, hydroxide ions etch the Ga atoms but are repelled by the electronegativity of the N dangling bond. In consequence, the morphology of Ga-polar surfaces is preserved while films with N-polar surfaces would have been modified with the appearance of pyramids over the entire surface corresponding to planes etched[169]. This Ga-oriented polarity is the one usually obtained when producing smooth epitaxial thin films by conventional CVD. Moreover, it confers to the film some interesting properties for the bulk to be developed for various applications (e.g.: FETs, quantum wells) and especially a high chemical stability[170].

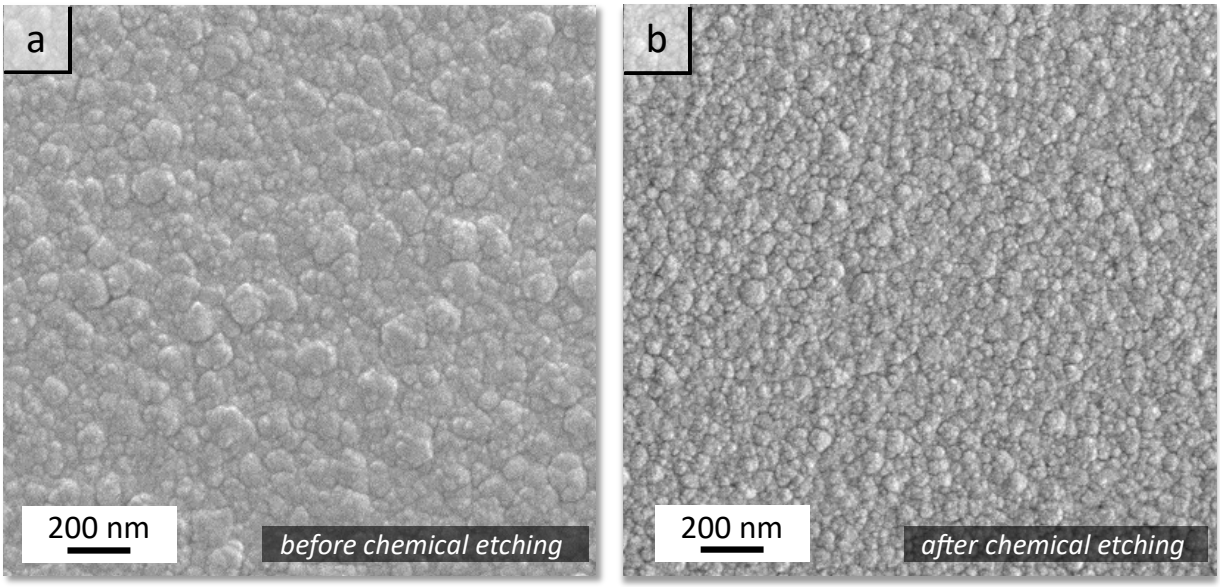

Figure 3.10. *SEM surface image (a) before and (b) after KOH etching on GaN thin film by RP-CVD.*

IV. Chemical composition analysis

Several methods exist in literature to analyze the chemical composition of materials, yet most are not well-suited for accurately quantifying GaN due to various limitations, such as the lack of calibration sample and nitrogen being a low-Z element. Consequently, we opted for Ion Beam Analysis (IBA) techniques, enabling direct quantification of the material without relying on fittings or calibration samples. To determine the in-depth composition of the GaN films, we employed a combination of two IBA techniques: RBS was used to examine gallium, a high-Z element, while NRA was employed to check the distribution of low-Z elements, specifically nitrogen, oxygen, and carbon impurities. The analyses first showed that oxygen content was extremely low, falling below the detection limit of NRA, which is typically on the order of 1%. This achievement can be attributed to the walls and substrate cleaning achieved via a plasma treatment performed in the reactor before the growth process. We combined the results obtained from NRA and RBS to generate the depth profile of Ga, N, and C within a GaN layer as shown in **Figure 3.11**. It reveals that the content of each element remains rather constant within the layer's depth, despite some minor variations observed in the nitrogen composition coming from the higher error associated with its measurement, i.e. ± 10%. Also, the spread of the N profile towards negative values is attributable to the depth resolution, which is closely linked to the energy resolution of the detector. A significant observation derived from this graph is the stoichiometric nature of the GaN film, presenting a Ga/N ratio close to 1 consistently across the entire depth of the film.

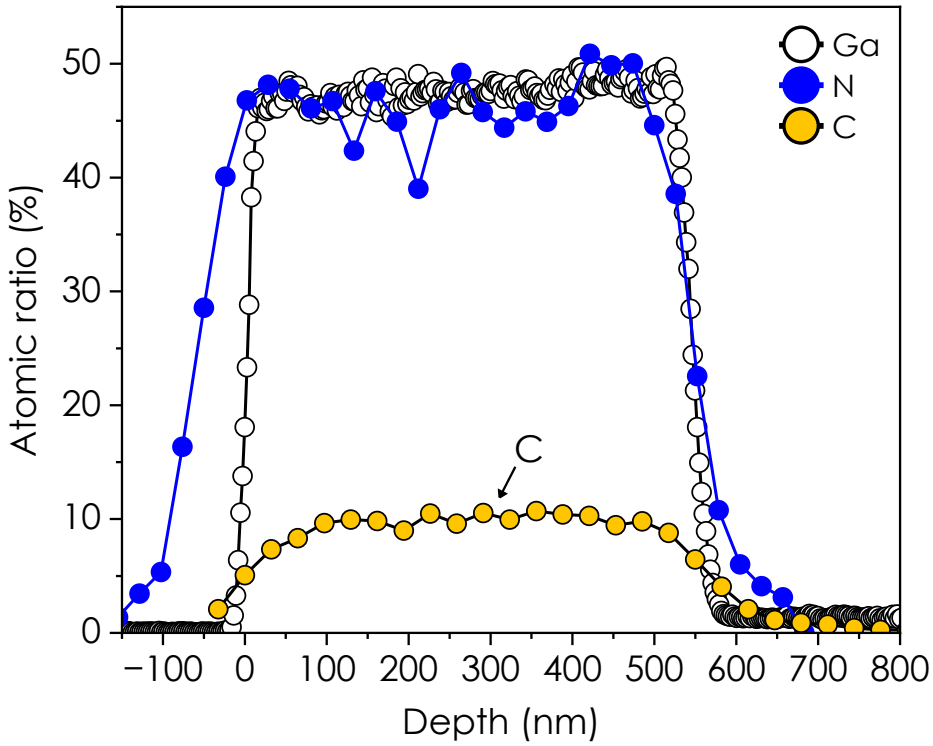

Figure 3.11. *Plot of combined RBS-NRA in-depth profile of GaN on Si by RP-CVD. Operating conditions of sample S9 (see **Table 3.2**).*

However, the film presents a carbon content as high as 10% (originating from TMGa decomposition). To reduce the carbon impurities, a route investigated here, was to increase the H_2 dissociation in the ICP source by increasing the RF power so that a higher flux of H-atoms would promote the removal of C from the growing surface. Indeed, as previously shown in **Figure 2.15**, the increase of the RF power induces a large increase in the intensity of atomic H emission lines, especially above 150 W. **Figure 3.12** illustrates the influence of the RF plasma power on the film composition where Ga/N ratio as well as C atomic percentage are shown. It should be noted that concentrations depicted here reflect the average concentration across the layer, encompassing both surface and interface influences. This figure highlights that higher plasma power leads to reduced carbon contamination, with C content dropping from 11.5% to ~7.5%, by varying the power from 150 to 300 W. As mentioned before, this would likely result from the higher density of atomic hydrogen generated in the ICP source and, most importantly, surface reactions leading to removal of carbon atoms and binding them into stable carbon-containing species, thus leading to a decrease in carbon incorporation during the growth[171,172]. Interestingly, the increase in H-atoms density does not influence the Ga and N concentration in the films, which is a valuable aspect of this process as one may tune the density of C in the layer without affecting the Ga/N ratio. Carbon incorporation in GaN has proven to be an effective method for achieving semi-insulating GaN, which is particularly challenging due to the significant n-type background doping typically present in GaN layers grown by conventional techniques[173]. This is especially valuable for HEMTs, where a highly resistive GaN base layer is essential for both device isolation and optimal RF performance[174].

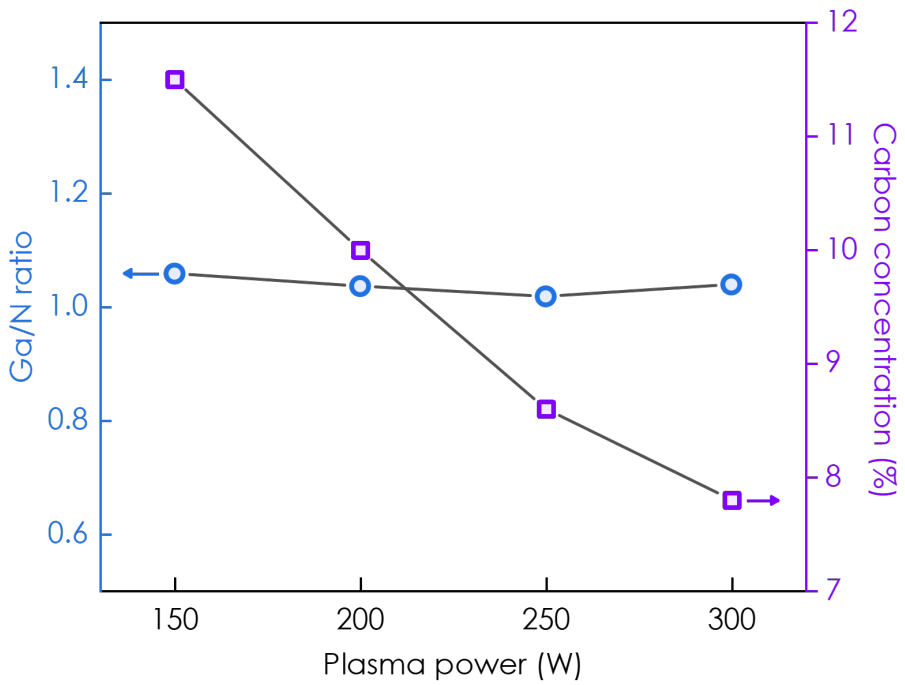

Figure 3.12. *Carbon concentration and III/V ratio over the thickness of the GaN layer as a function of RF plasma power from combined NRA and RBS analyses. Operating conditions of sample 9 except for the RF power (see* ***Table 3.2****).*

C. Ultrathin SiN barrier enables improved GaN growth on Si

"The interface is the device."
Herbert Kroemer, Nobel Lecture, December 8, 2000

In this section, we address another issue related to the direct growth of GaN on silicon that has not been extensively discussed in the previous section. Specifically, we focus on a challenge that arises at the interface between the GaN layer and the silicon substrate where a so-called "*meltback etching*" phenomenon may occur[175]. This issue is closely related to the eutectic transformation observed in the Si-Ga phase diagram, occurring at a temperature close to the melting point of gallium, approximately 30°C. During the initial deposition stages, these two elements can readily react to form a Si-Ga mixture that penetrates into the c-Si substrate[69]. The formation of liquid-phase gallium during the early growth stages intensifies this interaction with silicon and contributes significantly to the occurrence of this "*meltback etching*" phenomenon which can be highly detrimental to the film properties. In most papers, the term *meltback etching* is used to describe the process of interface mixing. However, we employ this term cautiously, as our initial insights—validated by the results presented in this section—indicate that the use of the term "etching" is not accurate in this context.

To address the challenges posed by the direct contact between Ga and Si, the use of buffer layers is once again seen as a route to mitigate lattice mismatch-induced strain and reduce defects of GaN growth on silicon substrates[76–78,176]. **Table 3.1** gathers the main ones: aluminium nitride (AlN) for close crystal structure with GaN leading to a lattice mismatch of 2.4%[77,177], aluminium gallium nitride (AlGaN) is a ternary compound whose lattice parameter can be tailored by varying aluminium content, to even better match that of GaN[178] and, while not as common as AlN or AlGaN, silicon carbide (SiC) can also be used as a buffer layer as it has a relatively close lattice matching (3.5%)[179]. However, these buffers are grown with expensive processes and necessitate high temperatures (**Table 3.1**) which can be the source of structural issues at the interface due to the thermal expansion coefficient mismatch.

In this section, we use RP-CVD to synthetize both a buffer layer and a GaN film on a silicon substrate at low temperature, reducing the number and complexity of processing steps. Indeed, we introduce a simple and rapid process to allow the direct growth of GaN on Si with a sharp interface using a low-temperature (500°C) nitrogen (N_2/H_2) plasma. This treatment results in the formation of a SiN layer acting as a barrier between the silicon substrate and the GaN grown immediately after in the same reactor. We show hereafter the effect of this plasma step on the nucleation and the quality of the interface using transmission electron microscopy (TEM) and composition profiles (STEM-EDX). Moreover, we also compare some GaN film properties obtained with and without the use of the SiN interface layer using atomic force microscopy (AFM) and X-ray diffraction (XRD). Finally, we propose growth mechanisms in the cases of growth with and without the SiN barrier layer.

I. Growth process

Figure 3.13. a) shows the successive processing steps employed to deposit GaN thin films with an intermediate SiN layer using the RP-CVD reactor[155]:
(1) & (2): Silicon substrates (100) are prepared by removing their native oxide by dipping them into a 5% HF bath followed by an in-situ hydrogen plasma treatment in the RP-CVD reactor to eliminate remaining organic contaminants from their surface.
(3) Then, a SiN layer is formed by submitting the c-Si substrate to a N_2/H_2 plasma (200 sccm of N_2 and 5 sccm of H_2) at 200 W and 500°C for 10 minutes.
(4) Finally, we grow the GaN layer using TMGa as the Ga-precursor and a plasma of H_2/N_2 for N-precursor, at 500°C and 0.3 mbar.

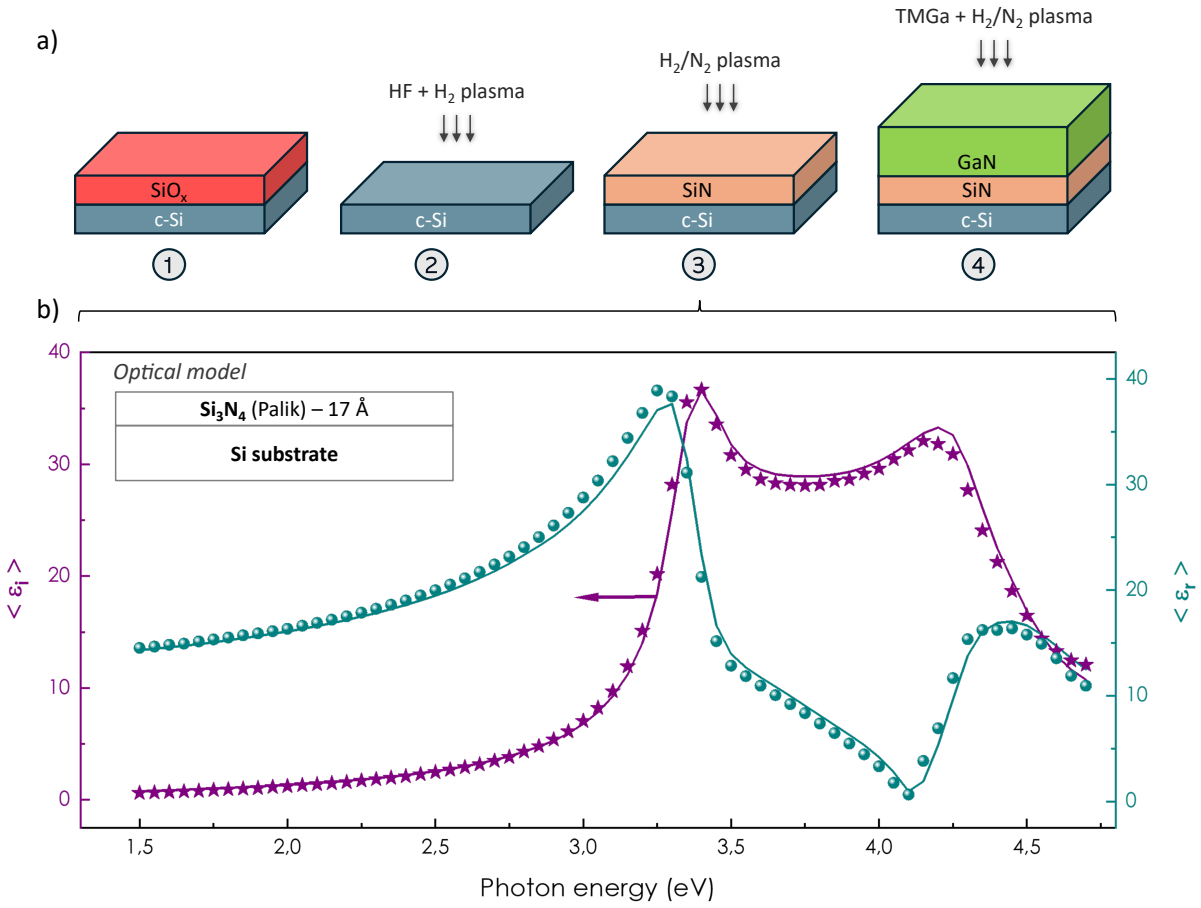

Figure 3.13. *a) The growth process of GaN via RP-CVD including the in-situ surface cleaning step (2) and the silicon surface nitridation step (3). b) Ellipsometry measurement of the SiN layer formed on silicon substrate with the corresponding optical model used to fit the data.*

The SiN thickness was determined from the modelling of spectroscopic ellipsometry measurements. **Figure 3.13. b)** shows the real and imaginary parts of the pseudo-dielectric function of the nitridation layer. A thickness of 17 Å of SiN has been obtained by fitting the experimental data using the layer stack[180] presented in the inset of **Figure 3.13. b)**.

II. Effects of *'meltback etching'*

As presented above, growing GaN films directly on silicon is a significant challenge. The first evidence of this issue appears right after the start of the growth process, namely during the initial interaction between the trimethylgallium (TMGa) introduced and thermally dissociated on the heated c-Si substrate which leads to the formation of liquid gallium in direct contact with the crystalline silicon substrate. This leads to macroscopic defects of varying sizes, as illustrated in **Figure 3.14**, which gathers examples from the literature along with an example from our own samples.

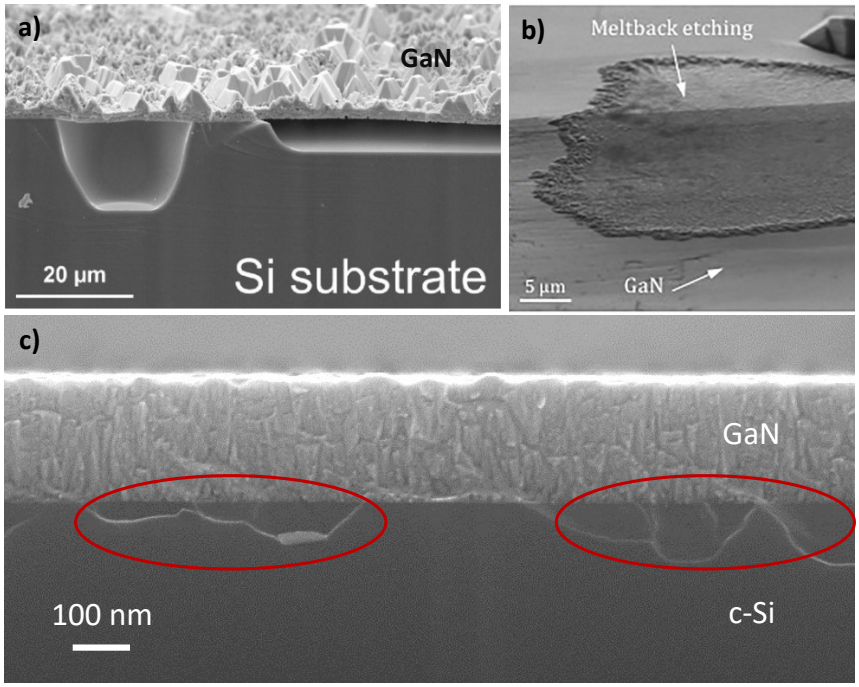

Figure 3.14. *a)[181], b)[175] Examples of SEM images highlighting macroscopic effects of 'meltback etching' at the GaN/Si interface from the literature and c) SEM image of our sample.*

III. Proposed ultrathin SiN barrier solution

To understand and observe what happens at the very beginning of the process when a SiN layer is added or not, we carried out a short (3 minutes) GaN growth process in the RP-CVD reactor and observed the surface appearance using SEM and AFM. In **Figure 3.15. a_1)** and **b_1)**, we present the top-view SEM images when growing GaN directly on a silicon substrate (without nitridation) and for the growth on a Si substrate onto which an ultrathin SiN layer of 1.7 nm was grown. The difference is visually evident; without nitridation, gallium 'puddles' of a few tens of micrometres appear on the surface (**Figure 3.15. a_1)**), the AFM image shown in the inset reveals that these features are rather flat, having about 1 µm of height for a 30 µm diameter. On the contrary, when a SiN layer is formed on silicon, the surface is exempt of gallium agglomerates (**Figure 3.15. b_1)**). This can be explained by the fact that the surface energy is increased when adding the nitridation layer, leading to lower liquid gallium contact angle[182]. This allows to enhance the migration of gallium across the surface. Moreover, by preventing direct contact between gallium and silicon, we mitigate the effects of the high reactivity of silicon with gallium. **Figure 3.15. a_2)** and **b_2)** show cross-section SEM micrographs of the c-Si/GaN interface after the complete growth of a GaN layers without and with SiN intermediate layer, respectively. These SEM images were acquired in backscattered electron mode in order to have information about the spatial distribution of atoms in the GaN layers. Indeed, backscattered electrons are high-energy electrons which enable to capture the contrast between areas with different chemical compositions. This is especially efficient in detecting gradients in compound materials that have large differences in atomic number such as GaN. In the absence of nitridation (**Figure 3.15. a_2)**), a gradient of contrast is observed with a bright region in the GaN layer at the interface with the

silicon substrate. As gallium is heavier than both silicon and nitrogen, we assume that this bright region corresponds to a Ga-rich layer. This can be the result of a growth initiated on the gallium puddles shown in **Figure 3.15. a_1)**. In contrast, the GaN film grown on top of the SiN layer appears columnar and much more homogeneous in composition, with no evidence of gallium-rich interface as shown in **Figure 3.15. b_2)**, which is consistent with the absence of gallium puddles at the early stages of the growth (**Figure 3.15. b_1)**).

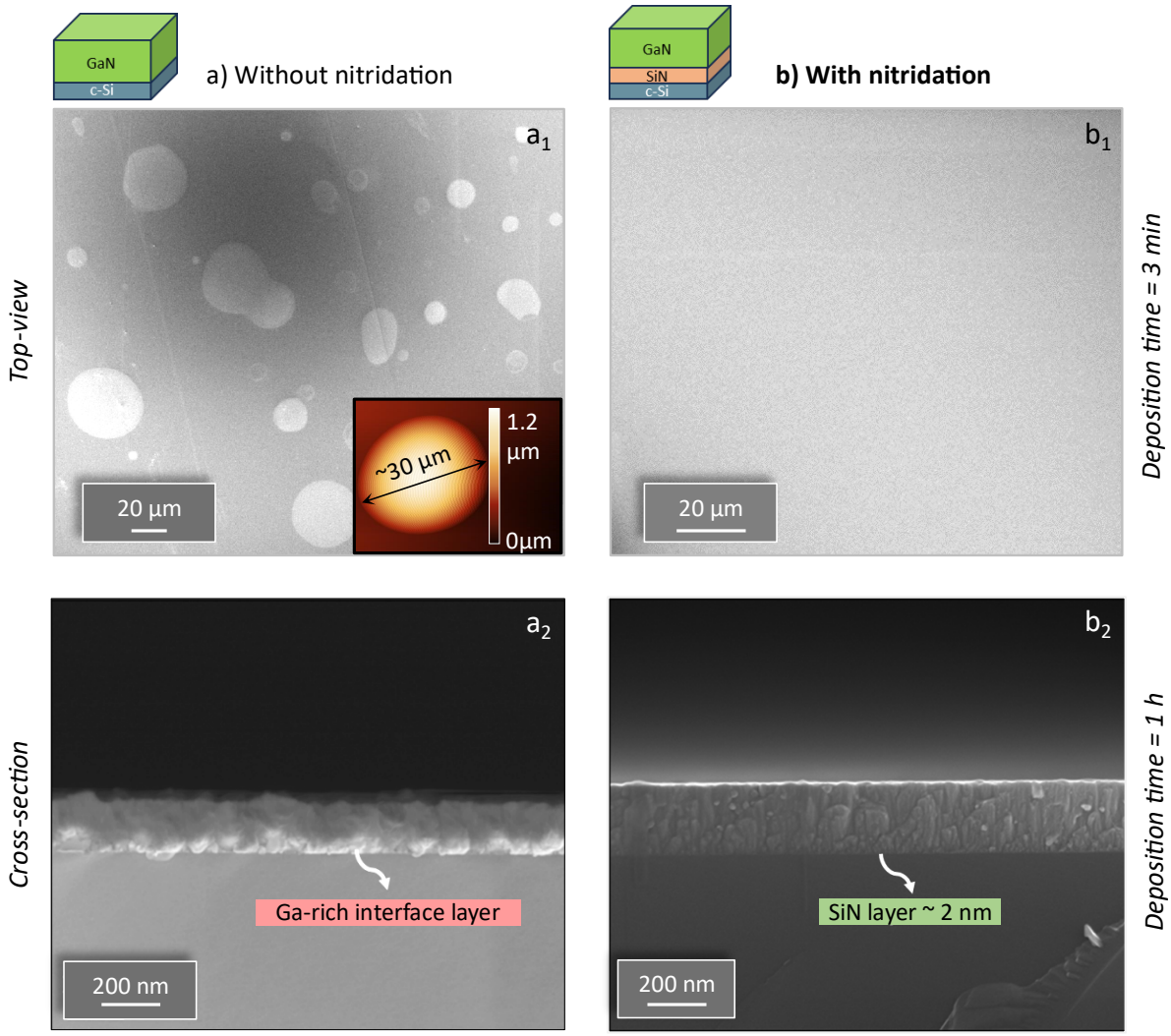

Figure 3.15. *a_1) SEM top-view at early stages of GaN direct growth with AFM inset showing the height of the Ga puddles, b_1) similar image obtained on the sample having a SiN barrier layer. a_2), b_2) SEM cross-section of thick GaN films grown on c-Si without and with SiN barrier layer respectively.*

To get further evidence on the phenomena that happens at the interfaces, we finely analysed the effect of adding (or not) the SiN layer using TEM as shown in **Figure 3.16. a)** and **b)**, respectively. Without nitridation, the bright-field (BF) TEM image in **Figure 3.16. a_1)** clearly reveals the presence of a modified zone of a few tens of nm in the c-Si substrate. In a closer view of the interface using HRTEM imaging (**Figure 3.16. a_2)**), we selected two regions in which we analysed the structure by applying fast Fourier transforms (FFT). The analyses have shown the polycrystalline nature of the GaN films (**Figure 3.16. a_3)**) and the amorphous nature of the modified c-Si zone (**Figure 3.16. a_4)**). When it comes to the silicon substrate that received a SiN treatment before GaN deposition, the

BF-TEM and HR-TEM analyses in **Figure 3.16. b_1)** and **b_2)** confirm the cleanliness and sharpness of the interface, without any modified zone appearing in the silicon substrate. **Figure 3.16. b_2)** clearly shows a distinguishable SiN layer, with a thickness ranging from 1.4 to 2 nm, which well corresponds to the value deduced from the modelling of the ellipsometry data (1.7 nm) in **Figure 3.13. b)**. As far as the GaN layer structure is concerned, the FFT analysis reveals its polycrystalline nature (**Figure 3.16. b_3)**).

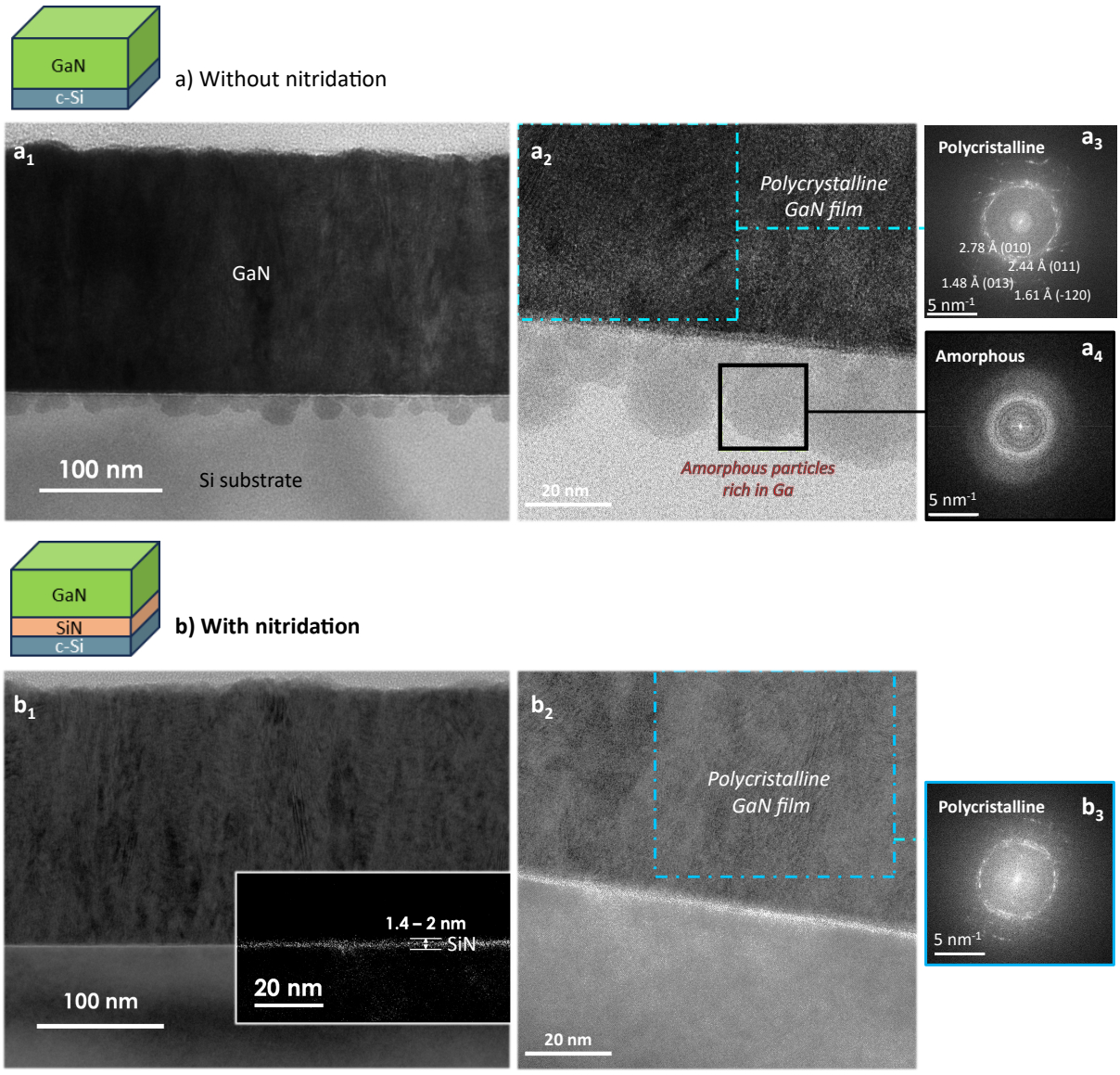

Figure 3.16. *TEM analysis of GaN-on-Si a) without nitridation and b) with nitridation. a_1), b_1) BF-STEM images, a_2), b_2) HR-TEM images and a_3), a_4) and b_3) local fast Fourier transforms images.*

To ascertain the nature of the modified c-Si zone and to get further local information about the interface, a composition profile was performed on both samples using STEM-EDX (**Figure 3.17**). The STEM-EDX profile and associated composition imaging show that the above-mentioned modified zone is made of both gallium and silicon, which results in a broad GaN/Si interface over a range of about 100 nm **(Figure 3.17. a_1)** and **a_2))**. However, for the sample having the SiN layer, the chemical composition profile displays an abrupt interface between the substrate and the

grown layer, with no further intermixing of gallium and silicon elements (**Figure 3.17. b_1)** and **b_2)**). Thus, we can conclude that the SiN produced via a simple nitridation step serves as a highly effective barrier against Ga-Si mixture formation.

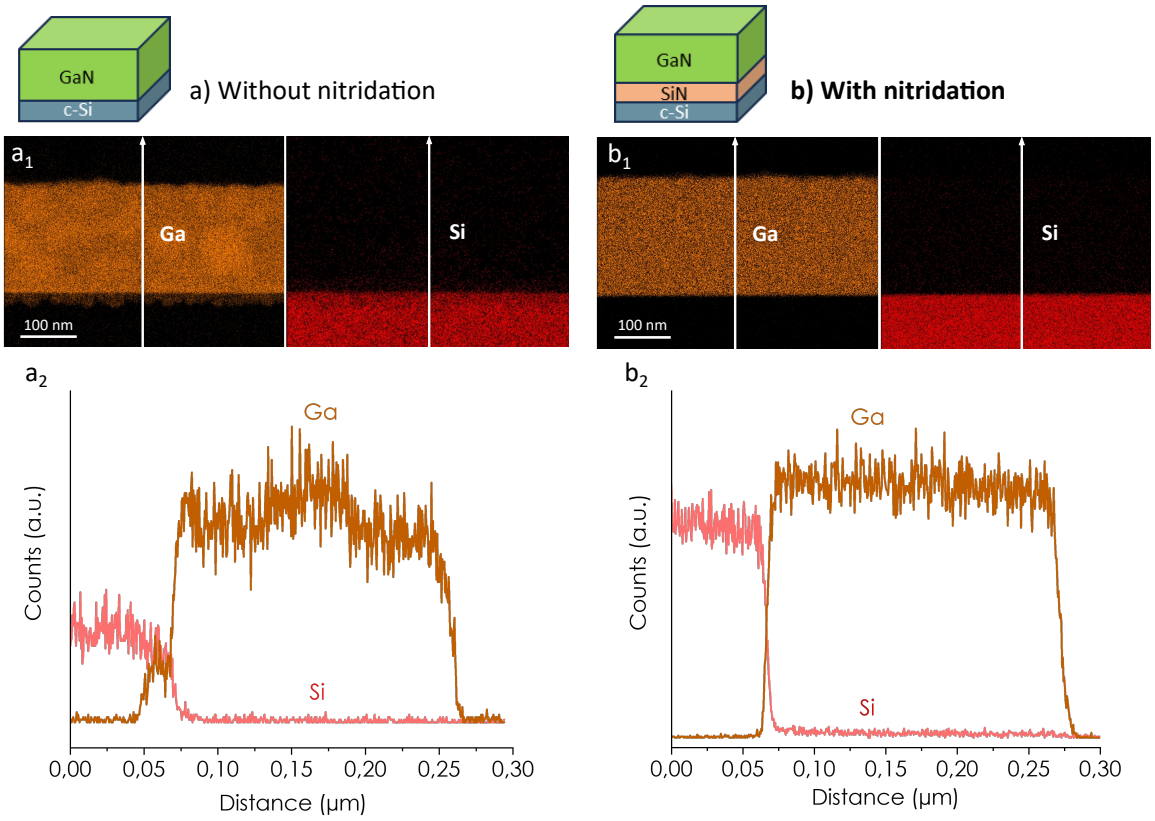

Figure 3.17. *STEM-EDX a_1), b_1) mapping and a_2), b_2) line-scan of gallium and silicon elements for GaN-on-Si growth (a) without and (b) with SiN.*

IV. Enhancement of GaN film properties

Now that we have examined the effectiveness of nitridation as an ultrathin barrier layer, it is time to assess its impact on the properties of the GaN film grown on top of it. To that end, we first used Atomic Force Microscopy (AFM) in **Figure 3.18. a_1)** and **a_2)**, which revealed that the surface roughness of the GaN film grown with the SiN layer is much lower than for the film grown without SiN, with root mean square roughness values of 1.7 nm and 7 nm, respectively. The grains in the GaN layer grown without nitridation also appear to be more inhomogeneous in size and themselves composed of smaller grains. This is also in line with what we observed using HAADF-STEM imaging in **Figure B.1** (**Appendix B**), where we observe small grains in the depth of the GaN film when no SiN barrier is used, while we have columnar growth when using SiN. FFT HRTEM analysis at the start of the growth showed that there is a growth texture along the c axis in both cases, but much more pronounced when the SiN layer is used (**Figure 3.18. a_2)** and **b_2)**). Furthermore, when examining the X-ray diffraction spectra, **Figure 3.18. c)** confirms a more pronounced 002 texture on the resulting GaN film grown on the SiN barrier layer with comparable film thicknesses.

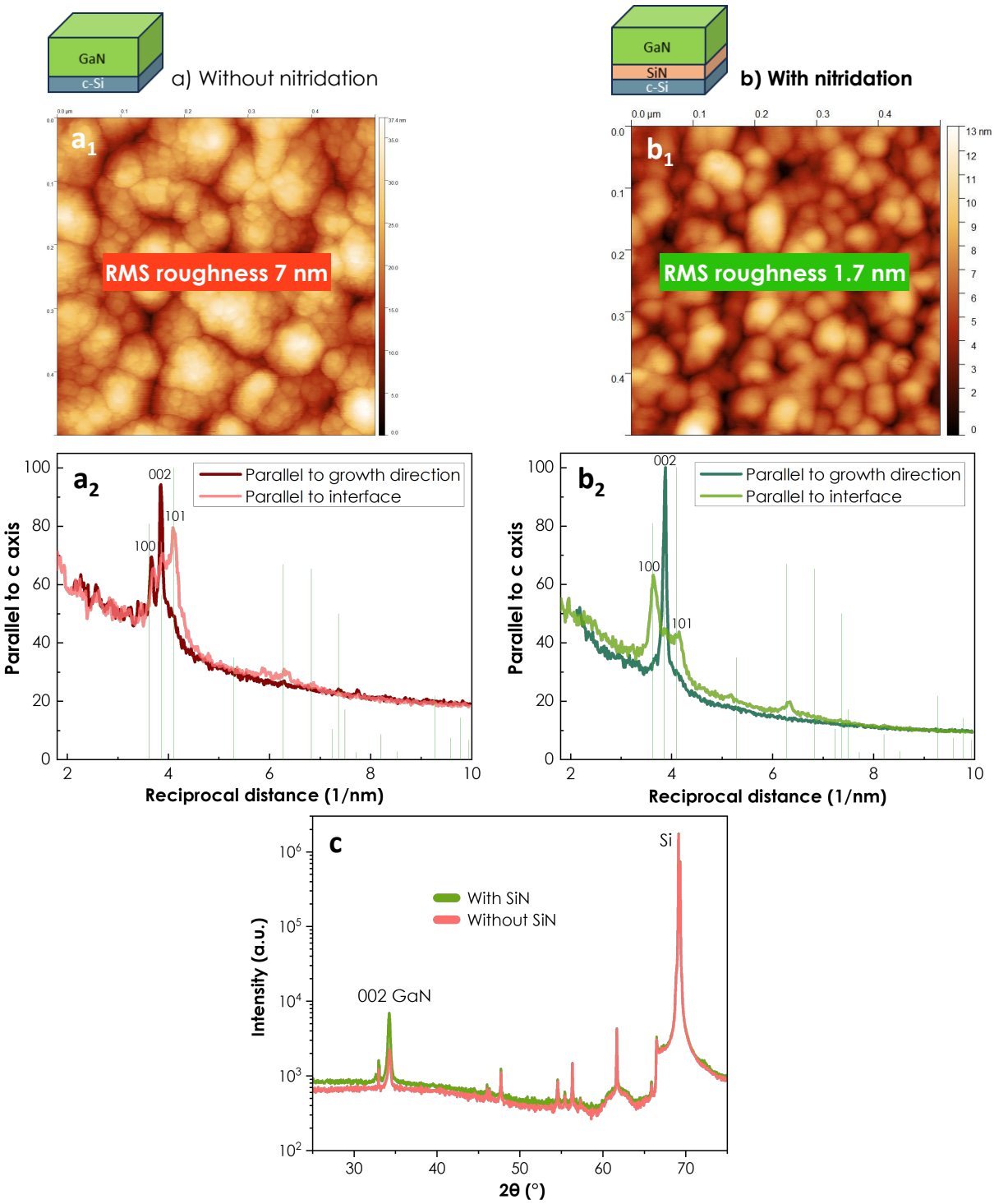

Figure 3.18. *GaN-on-Si a) without and b) with SiN. a_1), a_2) AFM images of GaN surface. a_2), b_2) intensity scans of HRTEM FFT pattern parallel and perpendicular to the interface and c) superposed XRD spectra.*

V. Proposed growth model

Figure 3.19 illustrates our hypothesis regarding the mechanisms of GaN growth by RP-CVD for the two scenarios: **A)** direct growth on c-Si substrate, and **B)** growth with the SiN barrier layer on top of the c-Si substrate.

In scenario **A**, gallium precursor molecules (TMGa diluted in H_2) are delivered to the substrate, where they undergo thermal dissociation and react with products of the dissociation of N_2/H_2, which have been dissociated in the plasma. Gallium reacts strongly with silicon atoms of the c-Si substrate due to the eutectic transformation evident in the Si-Ga phase diagram at around 30°C as explained in the introduction. The strong reactivity between silicon and gallium prevents effective diffusion of gallium atoms on the surface, leading to the formation of metallic liquid puddles by the coalescence of gallium atoms **(1)**, as observed experimentally in **Figure 3.15. a$_1$)**. These puddles begin to coagulate on the surface of the silicon until they form a gallium-rich 'continuous' layer on the substrate surface **(2)**, as observed in **Figure 3.15. a$_2$)**. At the same time, the strong reactivity between liquid Ga and Si leads to the formation of a modified region in the c-Si substrate, as supported by the TEM results shown in **Figure 3.16. a)** and **Figure 3.17. a)**. Therefore, the result is not so much an 'etching', as suggested by the term 'meltback etching,' but rather a dissolution of the interface into a Ga-Si mixture. Simultaneously, the growth of the GaN film is progressively established through the continuous supply of nitrogen and gallium atoms above the gallium-rich layer **(3)**, resulting in an inhomogeneous GaN film in terms of composition **(4)** and not well-defined columnar growth as shown in SEM, AFM and HAADF-STEM images in **Figure 3.15. a$_2$)**, **Figure 3.18. a$_1$)** and **Figure B.1** respectively.

In scenario **B**, the presence of the SiN layer prevents the intermixing of gallium and silicon atoms **(1)**, acting as an effective barrier against Ga-Si mixing as evidenced from TEM results in **Figure 3.16. b)**. Consequently, the diffusivity of gallium on the surface is improved **(2)**, leading to more uniform nucleation. This results in a more homogeneous GaN film growth with a clean and sharp interface in terms of composition **(3)**, as shown in **Figure 3.17. b)**.

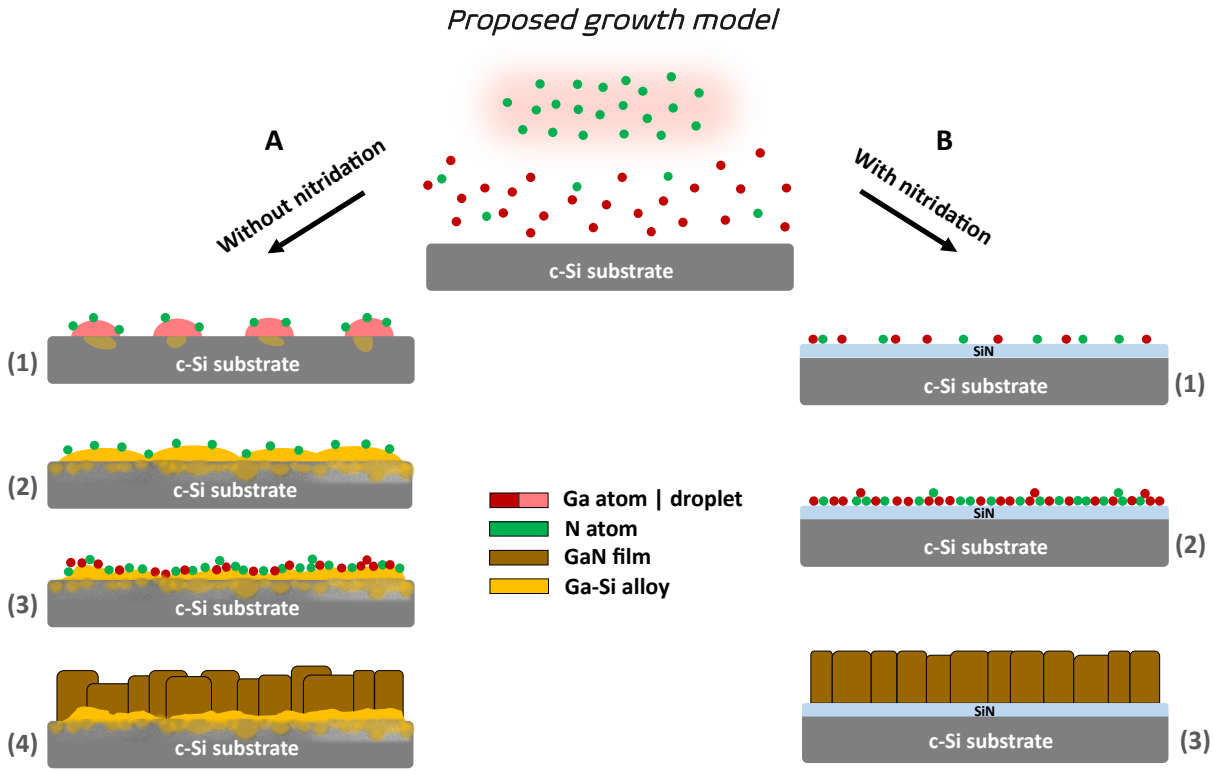

Figure 3.19. *Proposed growth scenarios for GaN-on-Si by RP-CVD for A) without nitridation and B) with nitridation.*

The growth on the SiN barrier layer is akin to a Frank-van der Merwe growth mode[183] (or layer-by-layer growth), resulting in smoother and more crystalline films compared to scenario **A**, as confirmed by AFM, TEM and XRD measurements (**Figure 3.18**). Indeed, Frank-van der Merwe growth occurs when the surface energy is high, leading to enhanced wetting. This results in a more homogeneous growth with complete wetting of the surface, leading to smooth films. In scenario **A**, direct growth on silicon results first in a Volmer-Weber growth mode (island growth), because Ga atoms react with Si atoms before they have time to form a GaN layer, so that they immediately form the interfacial Ga-Si eutectic, which is liquid at the growth temperature. After that, the growth mode transition to a Frank-van der Merwe type at the top of the gallium-rich region.

Chapter 3. Summary

This chapter presents the growth of GaN layers on various substrates at a low temperature of 500°C using RP-CVD. Starting with growth on sapphire and then on silicon, we also explored strategies to accommodate GaN growth by leveraging plasma techniques.

Regarding the direct growth of GaN on sapphire, we demonstrate that our RP-CVD reactor is capable of producing highly crystalline GaN films, with a FWHM of the 0002 peak measuring 0.3°. Although the growth appears smooth under SEM, TEM analysis shows that only the first 5 nm are epitaxial, after which the growth transitions to a polycrystalline structure. We explain the underlying reasons for this transition and introduce the potential of an in-situ AlN layer grown using a simple N_2 plasma to improve the quality of GaN grown on sapphire.

GaN layers grown on c-Si have been shown to be quasi-stoichiometric across the film's depth, emphasizing their uniformity while being almost free of O (less than 1% at., i.e. the detection limit of NRA). The investigations have established that GaN layers have a well-defined texture with most of the grains oriented in the +c direction, with a highly dense columnar structure. These films displayed nanometer-scale roughness, with uniform grain sizes in the hundred-nanometer range, consistent with the crystallite size of 98 nm determined from XRD analysis. We show that the efficient dissociation of H_2 allows to reduce the carbon contamination in the layer from 11.5% down to 8% when the RF power was increased from 150 to 300 W without affecting the Ga/N ratio.

The last section demonstrates the remarkable effect of an ultrathin (1.7 nm) SiN barrier in improving the interface between GaN and c-Si substrates by preventing the mixing of gallium and silicon, resulting in a very clean and sharp interface. The presence of the SiN barrier also enhances the surface diffusivity of gallium, promoting a more uniform nucleation and GaN growth resulting in higher film quality. Indeed, AFM measurements confirmed that the GaN films grown with the SiN intermediate layer exhibit significantly lower surface roughness (1.7 nm) compared to those grown without the layer (7 nm). Additionally, XRD analysis showed a reduction in the FWHM of the 0002 peak, from 0.19° to 0.10°. Based on the gathered results, we propose a comprehensive growth model providing hypotheses on growth mechanisms in RP-CVD of GaN.

These results clearly highlight the advantages and challenges of each substrate, as well as the potential of the custom-built RP-CVD reactor in growing III-V films. In the next chapter, we will explore the growth of gallium arsenide (GaAs) films by RP-CVD.

Chapter 4. Study and optimization of GaAs thin film growth by RP-CVD. 80

A. GaAs homoepitaxial growth 80
I. Main structural and morphological features 80
II. Chemical composition analysis 83
III. Electronic properties investigation 84

B. GaAs direct growth on c-Si 86
I. On the particular role of growth temperature 86
II. Main structural and morphological features 87

C. GaAs growth on virtual substrate 89
I. What is a virtual substrate: fabrication process 89
II. Structural and morphological features 91
III. Electronic properties investigation 96

Chapter 4. Summary. 99

Chapter 4. Study and optimization of GaAs thin film growth by RP-CVD

In the previous chapter, we focused on optimizing GaN growth using the remote plasma CVD reactor. That study began as an initial proof of concept demonstrating the effective operation of our new deposition process while we awaited the secured connection of arsine line to the reactor. Having gained significant insights into the reactor operation, we now turn our attention to the material of interest for III-V photovoltaics: gallium arsenide (GaAs). In this chapter, we will present the achievements in optimizing GaAs growth by RP-CVD on various substrates, ranging from conventional but costly substrates to a promising low-cost solution.

A. GaAs homoepitaxial growth

The ability to produce high quality GaAs thin films is essential to ensure the efficiency of solar cells, as the performance of electronic devices is highly dependent on the crystalline quality and uniformity of the layers[184]. Therefore, we first decided to optimize the growth of GaAs on the most suitable substrate, i.e. GaAs, to avoid any limitation due to the substrate and thus determine the ultimate level of quality we can achieve with our new process. A detailed parametric study will be presented in the next chapter (**Chapter 5**) to discuss the influence of growth conditions on electronic properties. Here, we focus on a detailed characterization study of the optimized homoepitaxial GaAs films.

Depositions are performed on 4-inch (100) GaAs substrates, n-type doped with Si (ρ ≈ 0.02 Ohm.cm). A hydrogen plasma treatment is applied to the GaAs substrate to remove oxygen and organic contaminants from its surface. Subsequently, an arsine (AsH_3) plasma is performed for a few minutes to saturate the surface with arsenic (As). The deposition process is then initiated by introducing trimethylgallium diluted in hydrogen (H_2). The GaAs layer is grown at 500°C, 150 W and 0.5 mbar.

I. <u>Main structural and morphological features</u>

The deposited GaAs film structure was first investigated by XRD measurements. To begin, we analyse the symmetrical 2Theta-Omega curve in **Figure 4.1** where only the 002 and 004 diffraction peaks are visible revealing that the layer has the same crystalline structure and orientation as the substrate. The inset of **Figure 4.1** shows the HRXRD rocking curve of the 004 diffraction peak that exhibits a full width at half maximum (FWHM) of 0.004°, which indicates a very high film quality. In fact, with the instrumental configuration used, a monocrystalline (100)

GaAs wafer has a FWHM of around 0.00446°. Therefore, the structural quality of the GaAs film grown by RP-CVD is comparable to that of a commercial GaAs substrate.

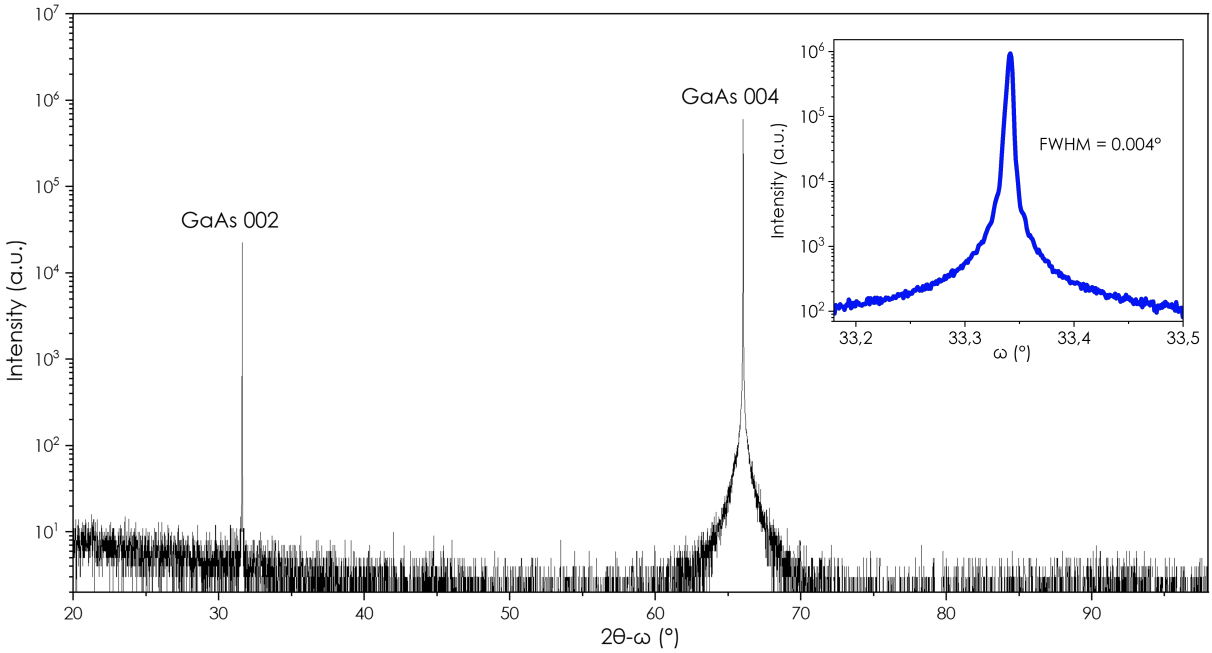

Figure 4.1. *XRD 2theta-omega scan with HRXRD rocking curve of 004 peak at ϕ = 0° in inset of homoepitaxial GaAs grown by RP-CVD.*

A pole figure of the same sample presented in **Figure 4.2** displays a distinct spot pattern with very sharp orientations. The 4 spots correspond to the {111} planes inclined at 54.7° to the 001 surface. The clarity and exclusivity of these spots on the pole figure indicate that the GaAs layer grown by RP-CVD exhibits no twinning or an extremely low degree of twinning, which would not be detectable here. This is consistent with a wafer-grade quality of the film.

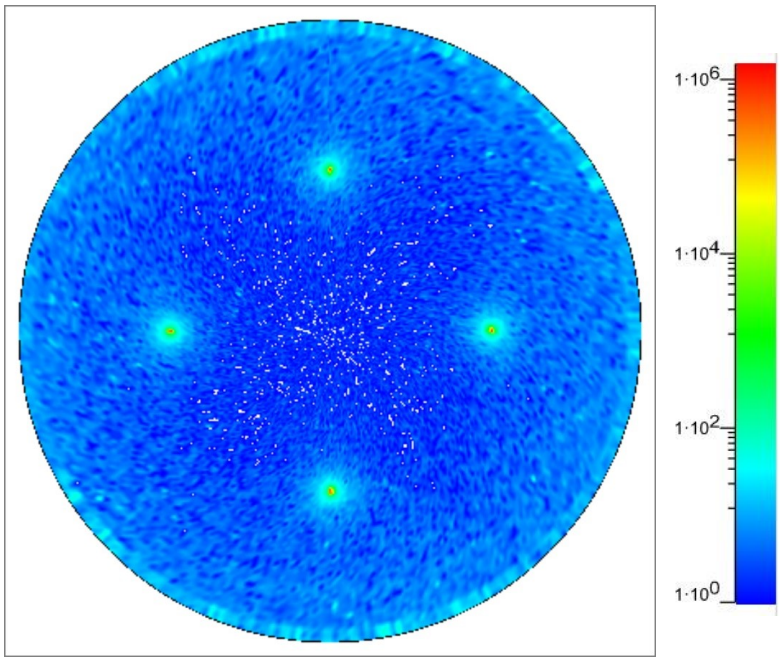

Figure 4.2. *111 in-plane pole figure of homoepitaxial GaAs grown by RP-CVD.*

We also conducted TEM analyses to corroborate the XRD results. A lamella of the sample is prepared using a focused ion beam (FIB) to obtain a thin (< 100nm) foil to analyse via TEM measurements. A thin protective layer of carbon is deposited by electron beam deposition to protect the surface area of interest during the ion beam imaging and ion beam assisted etching process used for the lamella preparation. **Figure 4.3. a)** presents a bright field (BF) STEM image of the lamella, showing no apparent dislocations. The interface between the substrate and the layer is not clearly discernible, confirming a wafer-grade quality and suggesting that the plasma cleaning treatment of the substrate is beneficial for the growth. Additional analyses of the structure were achieved by selected-area electron diffraction (SAED) using a small aperture of 10 µm and a camera length of 37 cm. The diffraction pattern of the epitaxial layer shown in **Figure 4.3. b)** exhibits distinct spots, confirming the epitaxial growth and excellent crystalline quality of the grown GaAs layer. It indicates spots which correspond to the reflections from the set of planes 111 (0.326 nm) and 200 (0.286 nm), observed along the [011] zone-axis.

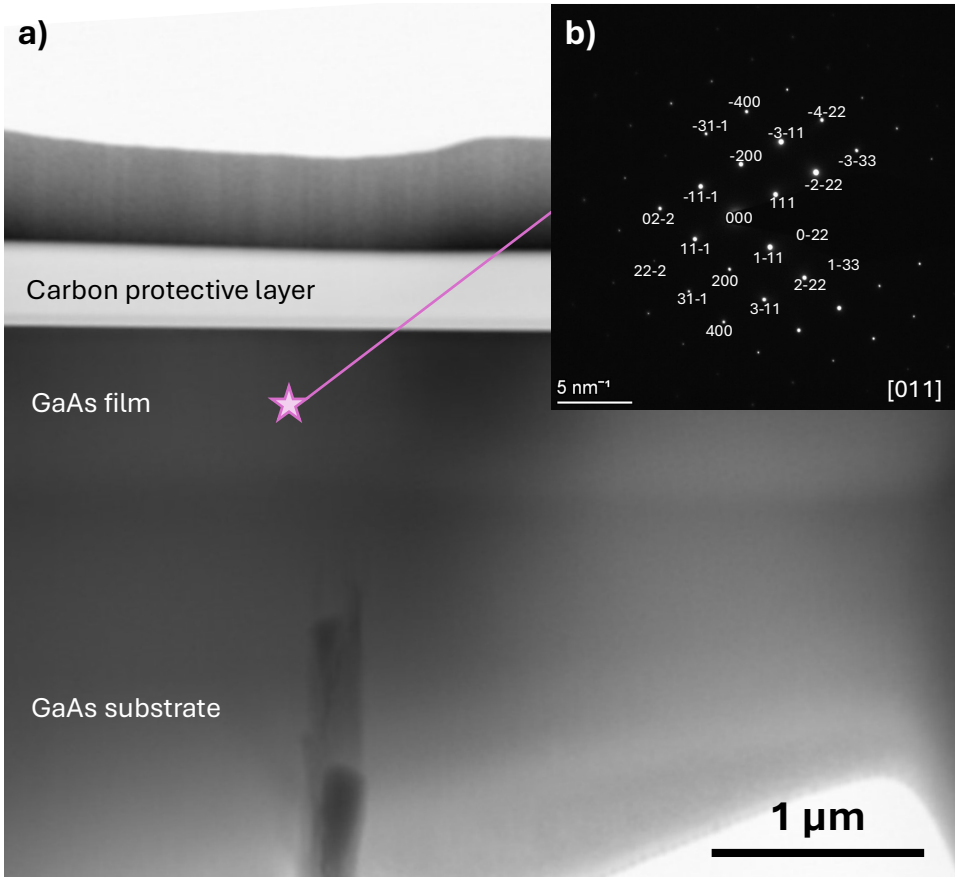

Figure 4.3. *a) BF-STEM image of homoepitaxial GaAs grown by RP-CVD and b) the SAED pattern corresponding to the star symbol zone in inset.*

In terms of morphology, **Figure 4.4. a)** shows the cross-sectional SEM image of the GaAs film grown on GaAs substrate. The layer appears to be continuous without columnar features, only traces of mechanical cleavage from sample preparation are visible and the interface with the substrate is sharp, demonstrating the effectiveness of plasma treatment to clean the GaAs wafer. Here, the grown GaAs can be distinguished from the substrate unlike in the TEM image, thanks to the difference between its doping level and that of the substrate (see **Figure 4.6. b)**), to which

secondary electrons are sensitive[185,186]. Additionally, **Figure 4.4. a)** indicates that the film grown in 1 hour has a thickness of 2.9 µm, corresponding to a growth rate of approximately 3 µm/h, which is comparable to the one achieved by MOCVD for GaAs[187]. As can be seen in **Figure 4.4. a)**, the layer seems to be very flat. To confirm and quantify this, we analyzed the top surface roughness using AFM in **Figure 4.4. b)**. We measured a root mean square (RMS) roughness of 0.2 nm, a value comparable to that of a commercial GaAs wafer.

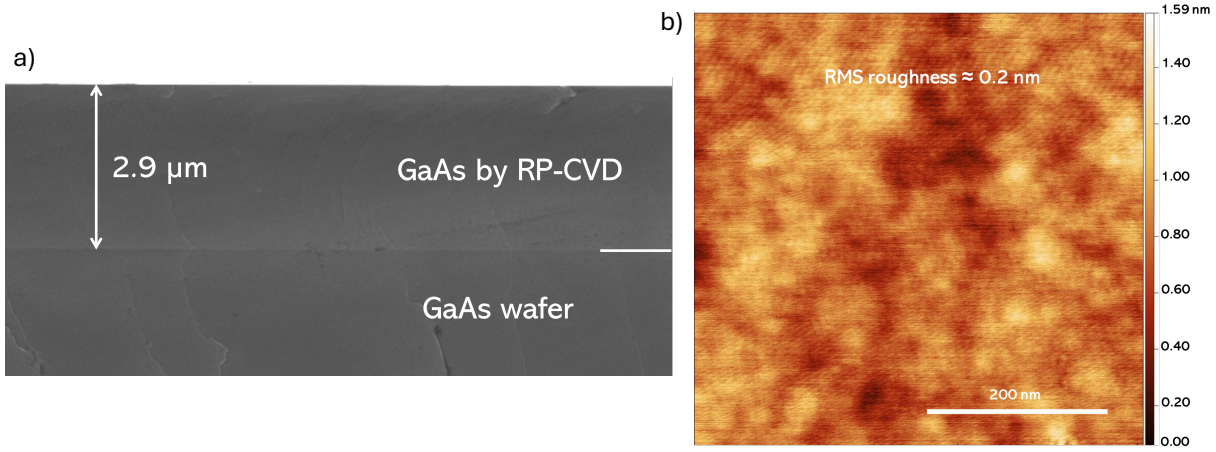

Figure 4.4. *a) SEM cross section image and b) AFM surface image of homoepitaxial GaAs grown by RP-CVD on a n-type GaAs substrate (doping level of 1.10^{18} cm^{-3}).*

II. Chemical composition analysis

We now come to the in-depth composition profile of the layer using XPS in **Figure 4.5. a)** for a total sputtering duration of 1000 s (substrate not reached). We observe surface contamination by carbon and oxygen, which is expected since the sample was exposed to air during transport from the growth reactor to the XPS instrument. Adventitious contamination and surface native oxide are removed after the first sputtering step, as demonstrated by the carbon- and oxygen-related peaks disappearance (C 1s, O 1s, Ga-O, As-O,) in the spectra presented in **Figure 4.5. b-e)** for etching times greater than 100 s. The III/V ratio is excellent, in fact As/Ga = 1.005 ± 0.005 over the entire probed depth, indicating an homogeneous stoichiometry is reached, which was expected given the high crystalline quality of the layers highlighted just before. The highly sensitive O-KLL Auger transition was also recorded, attesting that no O is incorporated inside the layer or below the detection limit of the technique (0.01 at.%). We will not discuss chemical composition in the subsequent sections when examining growth on other substrates, as the growth process will be similar. Therefore, we do not anticipate changes in stoichiometry or the presence of contaminants.

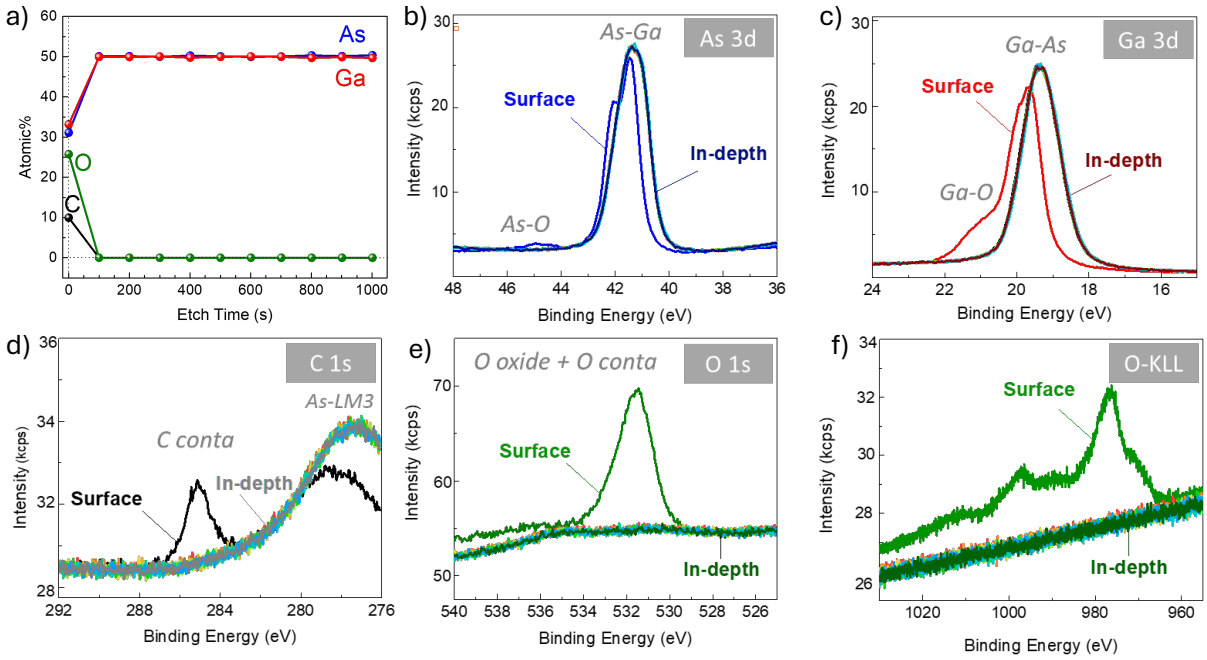

Figure 4.5. *a) In-depth profile of As, Ga, C and O from the surface to the bulk of the GaAs layer grown by RP-CVD and b-f) corresponding high energy resolution spectra of As 3d, Ga 3d, C 1s, O 1s photopics and O-KLL transition. Note that after the first etching, the peaks shapes and intensity remain the same, what is an indication that de composition and chemistry are remarkably constant inside the layer. The stoichiometry was calculated by averaging the 10 analysis points within 100-1000 s etch time.*

III. Electronic properties investigation

We will now focus on the electronic properties of the RP-CVD grown GaAs layers to evaluate its potential for device applications (refer to **Chapter 5** for this purpose). **Figure 4.6. a)** shows the photoluminescence spectra with normalized intensities of the GaAs film produced by RP-CVD and of a n-type GaAs wafer doped with Si (~ 1.10^{18} cm^{-3}). Bare RP-CVD grown GaAs, i.e. without any passivation, shows a sharp PL peak (FWHM ~ 55 meV vs. 89 meV for the wafer) indicating good crystalline quality and low defect density, in line with the previous structural results. The sample and the reference wafer exhibit a strong PL peak around the same photon energy (~1.4 eV), corresponding to the theoretical bandgap energy of GaAs. However, there is a little shift towards low energies for GaAs layer grown by RP-CVD (peak position at 1.42 eV) compared to the GaAs n-type wafer (peak position at 1.44 eV), which suggests a p-type doping[188]. Therefore, we analysed the layers using ECV and Hall effect measurements to confirm our doping hypothesis and determine its level. **Figure 4.6. b)** illustrates the results of the ECV analysis, showing the doping level and type as a function of etch depth within the layer. Two distinct regions are evident: a green region corresponding to the GaAs layer produced by RP-CVD, and a purple region corresponding to the substrate. The RP-CVD GaAs layer is identified as p-type, consistent with photoluminescence analysis, and exhibits uniform doping throughout its thickness at a value of approximately 1.04×10^{18} cm^{-3}. This doping arises from carbon present in the decomposition products of the organometallic gallium precursor, trimethylgallium (see **Chapter 3**). Hall effect

measurements provided a comparable doping level value (~1.10^{18} cm^{-3}) and also give the supplementary information that the mobility within the layer is very good at 172 $cm^2.V^{-1}.s^{-1}$, in the range of measured values for this level of doping according to H.F. Wolf handbook[189]. The wafer is confirmed to be n-type with a doping level consistent with supplier specifications (~ 1.10^{18} cm^{-3}).

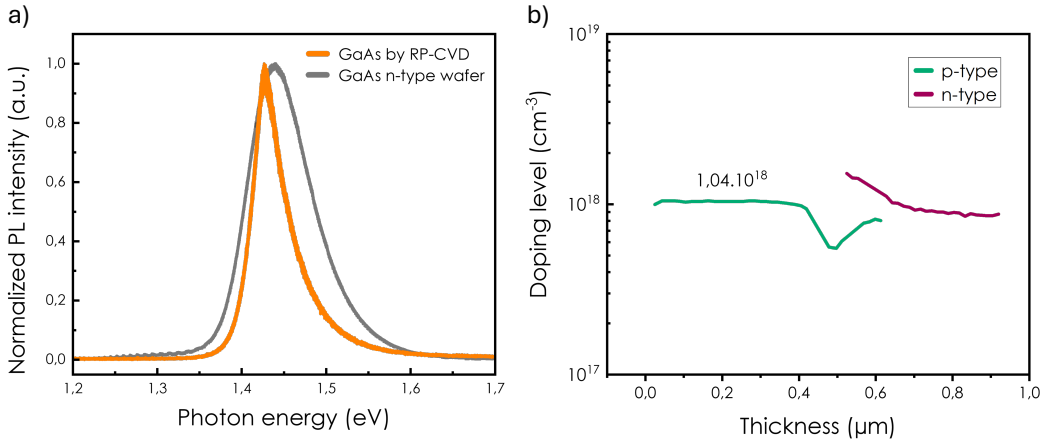

Figure 4.6. *a) Photoluminescence spectra and b) ECV profile of homoepitaxial GaAs grown by RP-CVD and GaAs n-type wafer.*

Additional cathodoluminescence analyses demonstrated the homogeneity of the electronic properties of the layer on the surface as shown in **Figure 4.7**. Notably, these analyses revealed the excellent uniformity in **a)** the position of the luminescence peak and **b)** the associated intensity (in contrast with the little dust defect on top of the surface). A Planck law fit was applied to the CL spectrum (for details, see **Appendix A**). This generalized Planck law fit involves modeling the CL emission data to account for the optical and transport properties of the material. From this fit, the doping level is estimated to be approximately 9.25 ± 2.75 × 10^{17} cm^{-3}, which is consistent with results obtained via ECV profiling or Hall effect measurements.

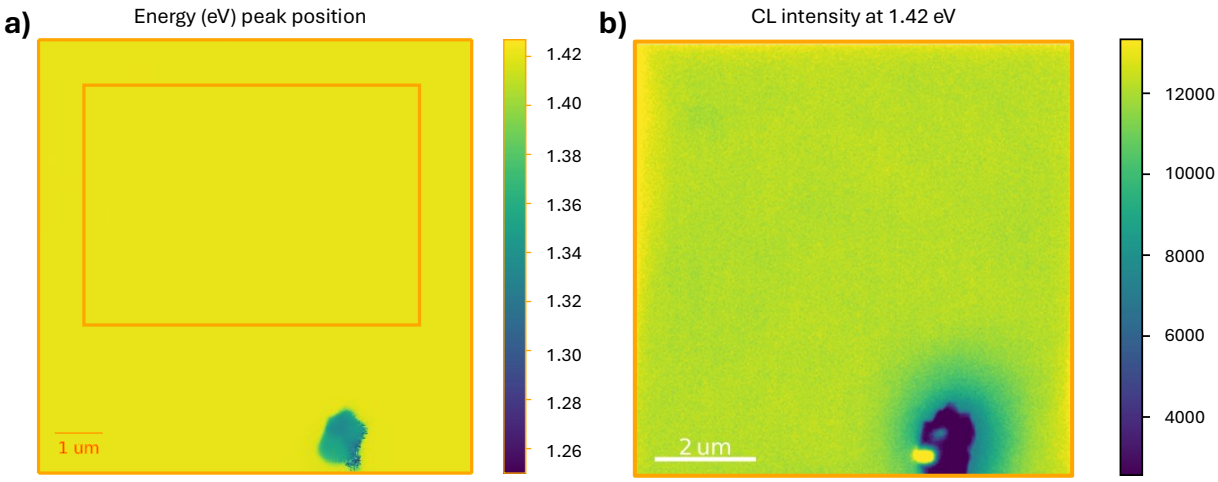

Figure 4.7. *Cathodoluminescence mapping of a) the energy peak position and b) the intensity around the CL peak at 1.42 eV (with width of 0.1 eV) of homoepitaxial GaAs grown by RP-CVD.*

B. GaAs direct growth on c-Si

Now that we have demonstrated that RP-CVD can produce high-quality homoepitaxial GaAs layers, we must continue to address the critical aspect of this research: cost reduction. With the successful implementation of RP-CVD process, our new objective is to minimize expenses elsewhere. As the high cost of III-V solar cells is largely attributable to the substrate[47], we have attempted to grow GaAs on low-cost silicon substrates. Integrating GaAs on Si is not only economically advantageous but also broadens the scope of GaAs applications on Si, particularly in photovoltaics with tandem configurations. However, the monolithic integration of GaAs (and III-V compounds more generally) on Si has been a significant challenge for several decades[190]. This challenge stems from issues related to both thermal coefficient difference and lattice mismatch, and polar on nonpolar material systems, which lead to defects in the grown layer, as discussed in **Chapter 1**. These defects can severely impact the performance and reliability of the devices. Despite numerous advances and various techniques developed to address these issues, achieving high-quality GaAs on Si remains a complex task[191]. We will see that we are no exception to the rule.

I. <u>On the particular role of growth temperature</u>

We conducted a series of growth experiments at three deposition temperatures: 550°C, 500°C, and 450°C, on 4-inch c-Si (100) substrates doped with phosphorus (ρ ~ 1-5 Ohm.cm). The macroscopic results of the growth are presented in **Figure 4.8**, showing photographs of the samples for the three temperatures of interest. Two distinct regions are visible on each sample: a very rough area at the edge of the wafer, which increases in diameter with temperature, and a "mirror-like" region that becomes wider as the temperature decreases.

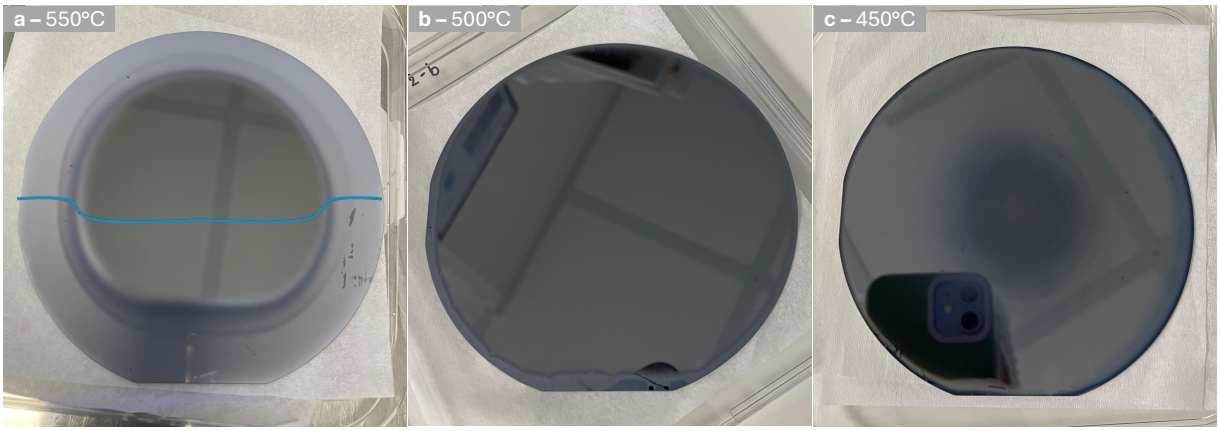

Figure 4.8. *Photos of GaAs samples on c-Si produced at different substrate temperatures, after 30 minutes of growth with in blue a representation of the thickness profile according to the region, either diffuse or non-diffuse.*

II. Main structural and morphological features

We decided to investigate the crystalline structure of the different regions of these samples using X-ray diffraction analysis. The figure below shows the spectra obtained for the three samples on two distinct regions: the mirror-like zone at the center of the wafer and the rough zone at the edge of the wafer. The results are shown in **Figure 4.9. a)** and **b)**, respectively. First, looking at the results from the center of the wafer, we observe a typical spectrum of our Si 100 substrate for all three temperatures. There is no indication of GaAs layer formation in this region. However, examining the rough edge of the wafer at a deposition temperature of 550°C, we observe a clear GaAs signature, with highly textured growth indicated by strong 002 and 004 Bragg diffraction peaks. As the temperature decreases, the intensity of the GaAs-related peaks diminishes. At 450°C, there is no longer significant GaAs signal. These results indicate that GaAs deposition has been achieved at the highest temperature of 550°C and only around the edges of the wafer.

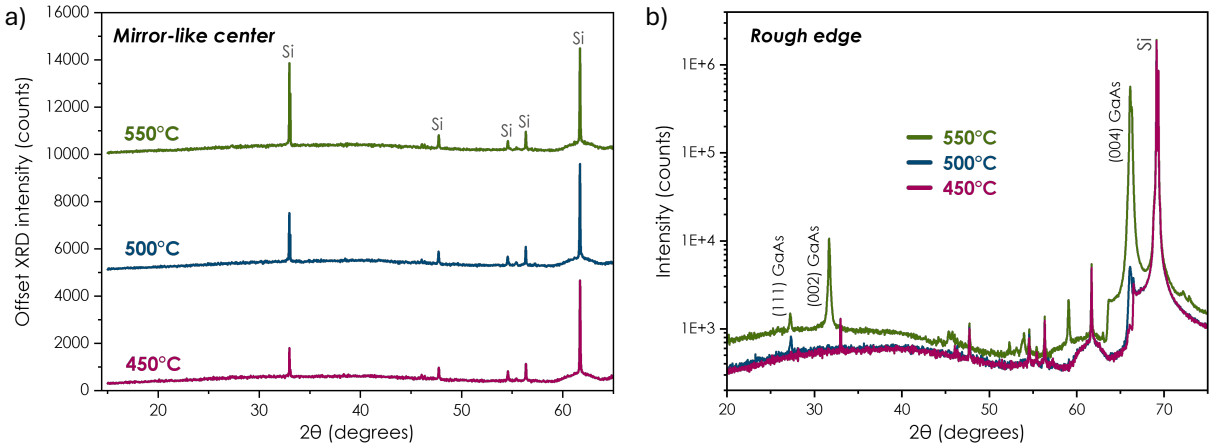

Figure 4.9. *XRD spectra of GaAs on c-Si at different temperatures for acquisitions taken from a) the bright center and b) the rough edge of the samples.*

To better understand what happens in terms of growth, we examined the different areas (mirror-like and rough) more closely using SEM. The surface images for the sample grown at 550°C are shown in **Figure 4.10**. In the mirror-like region, there is no continuous film, but rather isolated and spaced nucleation sites corresponding to micrometric size GaAs particles and crystals, as is clearly observable in **Figure 4.10. a-b)**, which shows the intermediate region between zones a and b. This explains why there is no GaAs XRD signal in this area (**Figure 4.9. a)**). As we move closer to the rough region, these nucleation sites become denser and closer, eventually forming a continuous and rough film on the rough edges of the wafers. This GaAs formed layer exhibits the pronounced crystalline texture along the (002) axis (**Figure 4.9. b)**). This trend is consistent with the temperature behavior of the substrate heating system discussed in **Chapter 2**, i.e. the center of the wafer is cooler than the edges. Consequently, there is greater dissociation of the TMGa precursor towards the edge of the wafer, resulting in increased thickness. We observed the same trend for the growth carried out at 500°C and 450°C, with narrower areas of roughness and lower GaAs microcrystals density (images not shown here).

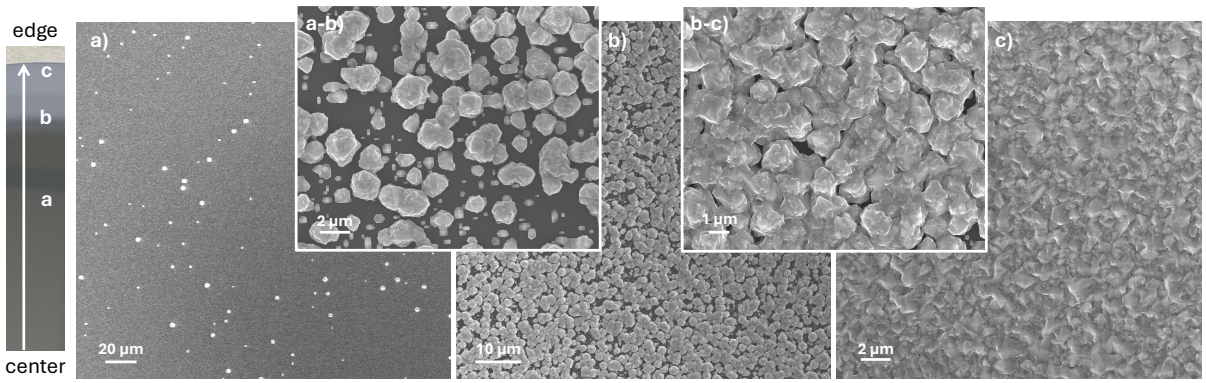

Figure 4.10. *SEM surface images of GaAs-on-Si grown at 550°C for different positions on the wafer as shown on the left.*

The thickness decreases as the growth temperature is reduced, as confirmed by the cross-section images in **Figure 4.11**. This explains why the XRD signal of GaAs at the rough edges is weaker for film grown at 500°C and ever more at 450°C (**Figure 4.9. b)**). The significant change between 450°C and 500°C is aligned with the dissociation kinetics as the complete decomposition of TMGa is observed at temperatures above 475°C, as indicated by the concentration of CH_4 produced during the process reported in the paper of S.P. DenBaars[192]. Thus, between growth at 550°C and 500°C (**Figure 4.11. a)** and **b)**, respectively), there is no significant change in film thickness, but there is a noticeable difference in film quality. However, at 450°C, the film thickness is substantially lower (**Figure 4.11. c)**).

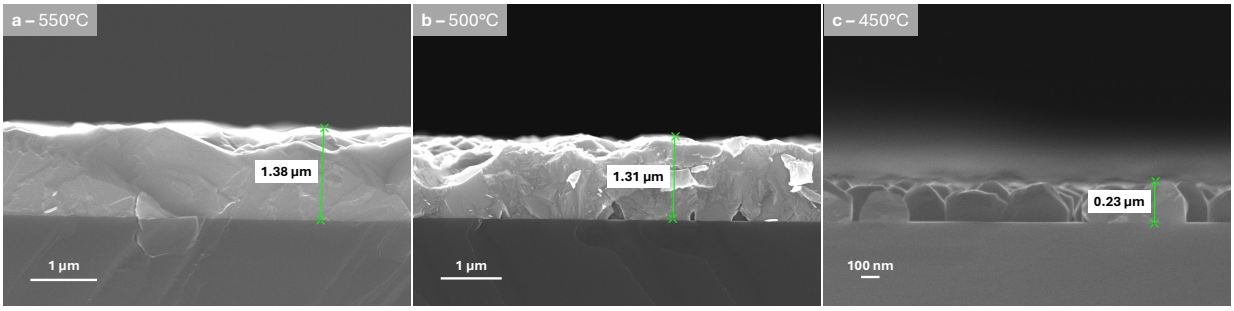

Figure 4.11. *SEM cross section images GaAs samples on c-Si produced at different substrate heating temperatures, after 30 minutes of growth.*

Additional images of the interface of the sample grown at 550°C were acquired using TEM, and the results of this analysis are presented in **Figure 4.12**. The images of **Figure 4.12 a)** and **b)** reveal that the layer is heavily microtwinned due to the constraining effects of the silicon substrate. Crystal twinning corresponds to the symmetrical intergrowths of crystals. Nevertheless, the HRTEM image in **Figure 4.12. c)** shows that, despite a not sharply defined interface, the film is still epitaxially grown. Therefore, the GaAs films grown on c-Si are pluridomain monocrystals with a very high level of twinning.

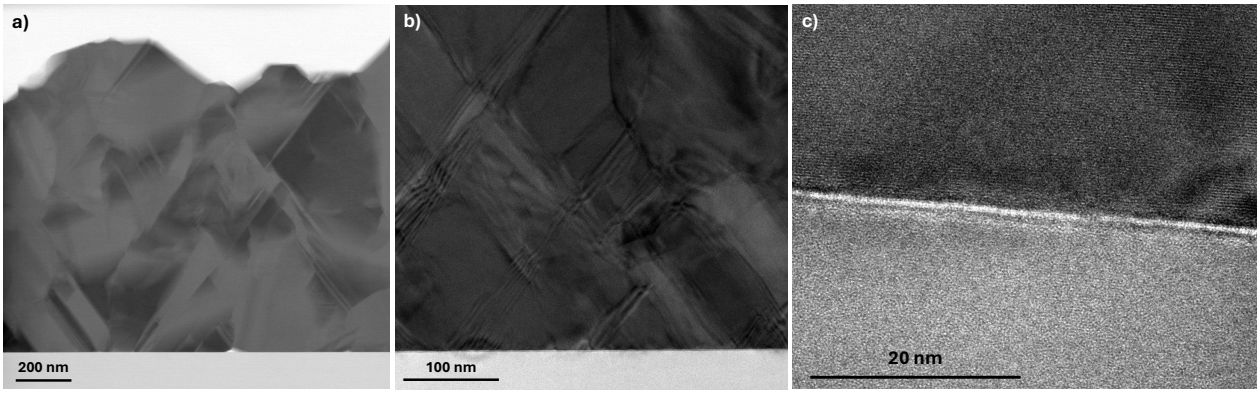

Figure 4.12. *a) BF-STEM image, b) higher magnification TEM image and c) HRTEM image of GaAs-on-Si grown at 550°C.*

We did not persist further in optimizing GaAs through direct growth on c-Si, regarding the huge challenge it represents, and quickly transitioned to a strategy accommodating GaAs lattice mismatch by leveraging plasma assistance once again. To achieve this, we employed pre-engineered virtual substrates developed via PECVD at LPICM[110], the use of which for RP-CVD grown GaAs will be detailed in the following section.

C. GaAs growth on virtual substrate

The strategy of using virtual substrates involves depositing a thin germanium (Ge) film on a crystalline silicon wafer, providing a cost-effective solution for growing GaAs. Indeed, this approach leverages the near-perfect lattice match between Ge and GaAs (only 0.07% of mismatch)[193–195], facilitating high-quality epitaxial growth. By using low-cost c-Si wafers instead of traditional germanium wafers, this method significantly reduces substrate costs[47].

I. <u>What is a virtual substrate: fabrication process</u>

The fabrication of these virtual substrates is based on a low-temperature plasma-enhanced chemical vapor deposition (PECVD) process. Specifically, Ge films are deposited on Si wafers at 175°C using a capacitively coupled radio frequency plasma[196]. The Ge deposition process is represented in **Figure 4.13**. The native oxide layer on the silicon wafers is removed by dipping them for 30 seconds in a dilute hydrofluoric acid solution (5% HF in deionized water). Before the deposition process, the wafers undergo a SiF_4-H_2 plasma treatment to eliminate any residual contamination, particularly water absorption and surface oxidation. Germane (GeH_4, 1% in hydrogen) and hydrogen (H_2) are used for the epi-PECVD process. Then, the Ge-virtual substrate is introduced in the RP-CVD reactor for GaAs deposition under the conditions described earlier.

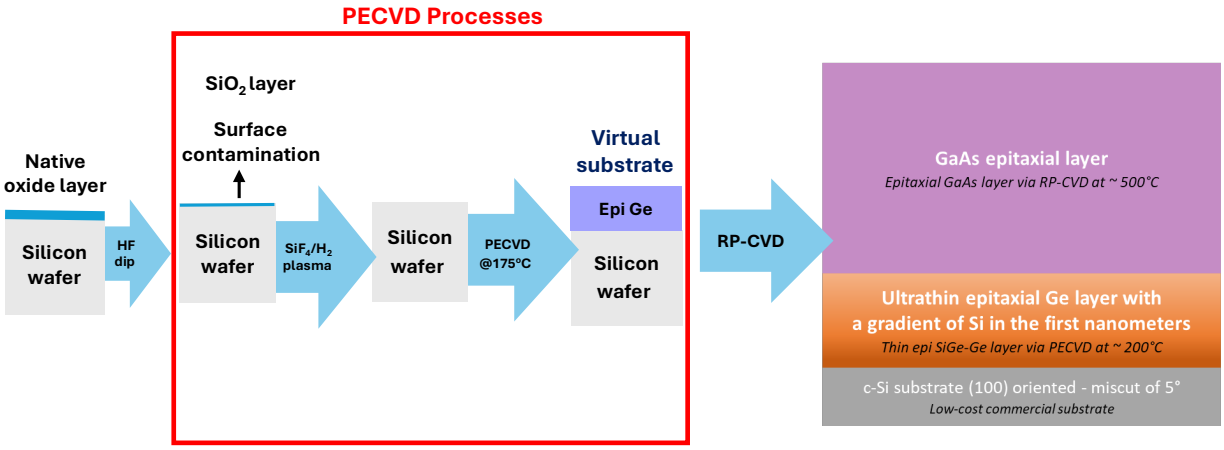

Figure 4.13. Schematic illustration of the experimental process flow for the production of virtual (epi Ge/c-Si) substrates and their application for the growth of GaAs layers by RP-CVD[110].

Figure 4.14 illustrates the real and imaginary components of the pseudodielectric function of a GaAs layer grown on the virtual substrate described above. The measurement was taken at the centre of the 4-inch wafer. The inset details the layer stack: a thin Ge layer grown on a c-Si substrate, followed by a 1.3 µm thick GaAs layer. The GaAs layer exhibits here a surface roughness of approximately 12 nm.

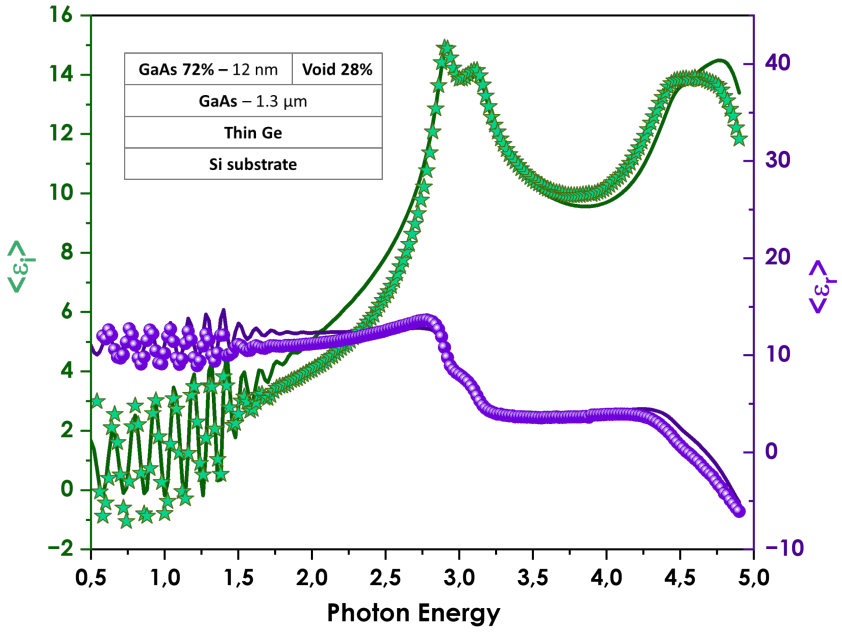

Figure 4.14. Ellipsometry measurement of GaAs grown on virtual substrate with the corresponding optical model (layer stack) used to fit the data.

We will not delve into the details of the parametric study conducted to enhance the growth of the Ge nor GaAs layers. Instead, we aim to present here a comprehensive analysis of the highest quality sample we have achieved in terms of structural and electronic properties.

II. Structural and morphological features

1. Crystal twinning

We conducted an X-ray study to understand the structure of GaAs on the Ge-virtual substrates. In **Figure 4.15. a)**, the pole figure for GaAs 111 is represented. Spots 0, 1, 2 and 3 (a = 35.3°) on the GaAs 111 pole figure correspond to {111} planes inclined at 54.7° to the (001) surface. They are well aligned with the {111} planes of the Si, identifiable on the Si 111 pole figure on **Figure 4.15. b)**, so the GaAs is well epitaxially grown on the Ge-virtual substrate. Spots 4, 5, 6 and 7 (a = 74.2°) correspond to planes inclined at 15.8° to the surface, spots 8 to 15 (a ~ 11°) correspond to planes inclined at ~ 79° to the surface. They result from twinning of the GaAs crystal, represented in **Figure 4.15. c)**. This analysis demonstrates that our GaAs layer grown on a virtual substrate is a pluridomain monocrystalline GaAs containing little twinning, i.e. from the first order only. Crystalline defects are present, but not in significant quantities, which preserves monocrystallinity and is thus very promising. This indicates room for improvement that will be addressed in future optimizations.

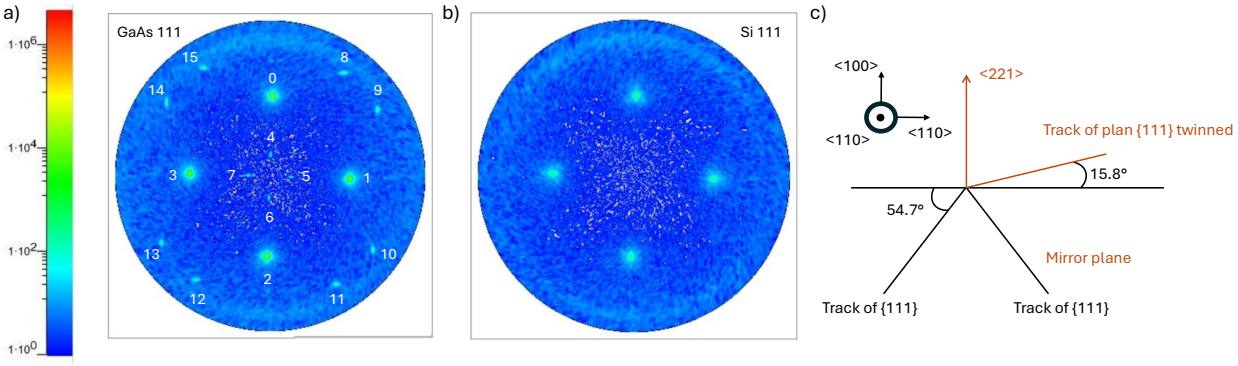

Figure 4.15. *a) 111 in-plane pole figure of GaAs and Si and b) the corresponding scheme showing the crystal twinning of the GaAs grown layer.*

A TEM study allowed us to visualize the presence of crystal twinning suggested by the pole figure. **Figure 4.16. a)** and **b)** present images at varying magnifications of this type of twin, while **Figure 4.16. c)** shows the FFT signature of this symmetrical intergrowth phenomenon. It is not surprising to find crystal twinning defects in our samples, as twinning in thin films often occurs to reduce the elastic (misfit) strain energy induced by heteroepitaxy[197]. Their effects on electronic properties are not well understood. K. Shimamura *et al.* work reveals that twins in GaAs nanowires significantly impact electronic properties[198]. Indeed, the radiative decay time of an exciton is found to increase due to twin scattering, it also affects electron mobility. These effects can profoundly impact device efficiency. However, when comparing these images to those obtained from GaAs direct growth on c-Si (**Figure 4.12**), the amount of crystal twinning is significantly lower here. This further demonstrates the advantage of using a Ge intermediate layer in improving the quality of GaAs growth.

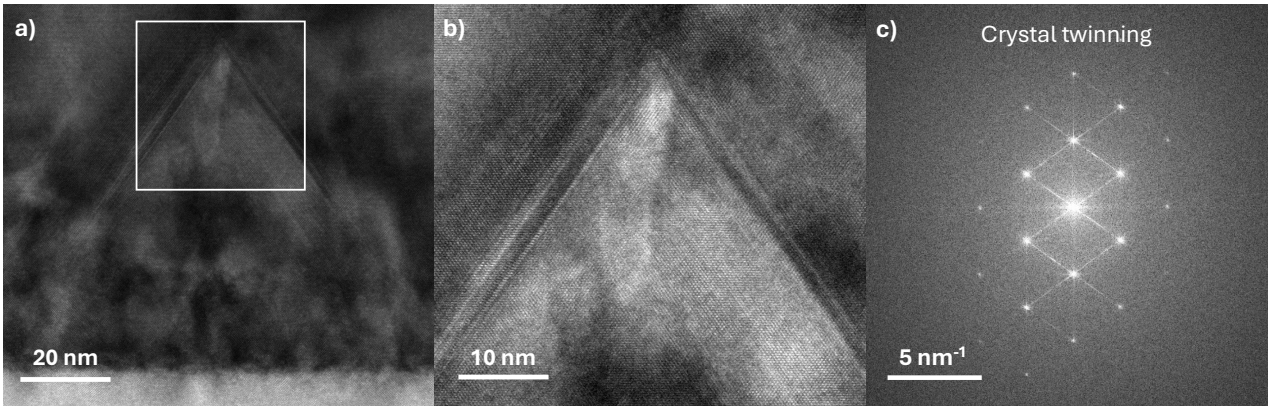

Figure 4.16. *a), b) HRTEM images of a crystal twinning in GaAs on virtual substrate and c) its local fast Fourier transforms image.*

2. Lattice deformation

We then aimed to study the lattice deformation of the GaAs by calculating the epi-layer lattice parameter. To achieve this, we first performed a high resolution XRD 2θ/Ω scan, presented in **Figure 4.17**, to study the diffraction from the {004} crystallographic planes parallel to the surface in order to determine $a_{\perp}$. By analysing the angle position of the diffracted peaks, we can accurately calculate the lattice parameters and identify any deviations from the ideal structure, indicating lattice deformation or strain within the epitaxial layer. From this scan, we obtained the experimental interatomic distance $d^{exp}_{GaAs\ 004}$ = 1.4127 Å, which is slightly lower than the nominal value (1.4133 Å), and from which we deduced $a^{exp}_{\perp}$ = 5.65112 Å.

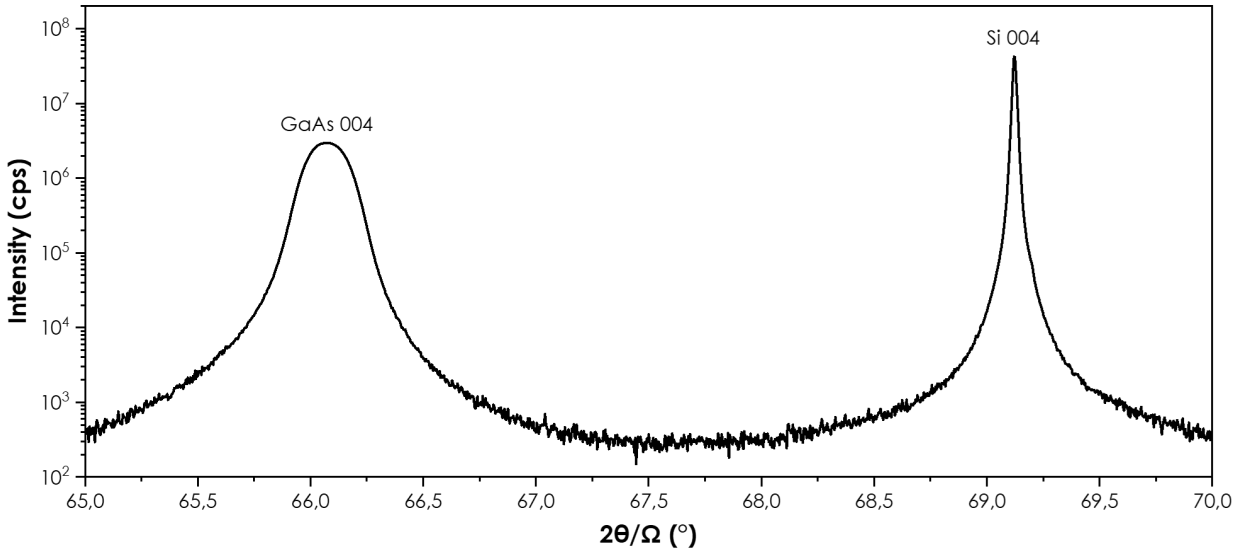

Figure 4.17. *HR-XRD measurement of reflection from the (004) planes of the GaAs thin film grown on a virtual substrate.*

We then acquired a 2θχ/ϕ scan as shown in **Figure 4.18**, to study the diffraction from the {220} crystallographic planes perpendicular to the surface and determine $a_{\parallel}$. From it, we deduce the $a^{exp}_{\parallel}$ = 5,66016 Å and an experimental mismatch of interatomic distances of

$(d_{exp} - d_{theo})/d_{theo}$ = 0.00122. This difference may be due to the thermal expansion coefficients which must also be considered, as the substrate imposes its temperature evolution on the layer. The theoretical values at room temperature are α_{Si} = 2.6 x 10^{-6} K^{-1} et α_{GaAs} = 5.73 x 10^{-6} K^{-1} [199], resulting in a mismatch of 0.00236. Although this does not exactly fit the measured value, it is quite close. Therefore, we consider that the crystalline deformation in the thin layer is partially due to the difference in thermal expansion coefficients between Si and GaAs. We calculate the final deformation of the GaAs lattice a_{bulk}^{exp}, knowing that:

$$\frac{(a_{\perp}-a_{bulk})}{a_{bulk}} = -\frac{2\nu}{1-\nu} \times \frac{(a_{\parallel}-a_{bulk})}{a_{bulk}} \quad \text{and} \quad \frac{(a_{\perp}-a_{bulk})}{a_{bulk}} = -\frac{2C_{12}}{C_{11}} \times \frac{(a_{\parallel}-a_{bulk})}{a_{bulk}}$$

And the elastic constants of GaAs being:

$$C_{12} = 5.372 \text{ and } C_{11} = 11.877$$ [200]

We obtain a_{bulk}^{exp} = 5.65541 Å.This experimental value is thus greater than the nominal value which is of 5.65325 Å [201], indicating a slight lattice relaxation. In addition to the thermal mismatch, this lattice modification could also be associated with the presence of hydrogen in the lattice[116]. However, this possibility was ruled out by a SIMS measurement presented in **Chapter 5**, showing no presence of hydrogen (or below the detection limit). Therefore, the remaining probable causes are arsenic antisite defects, vacancies, or carbon incorporation in the lattice[202].

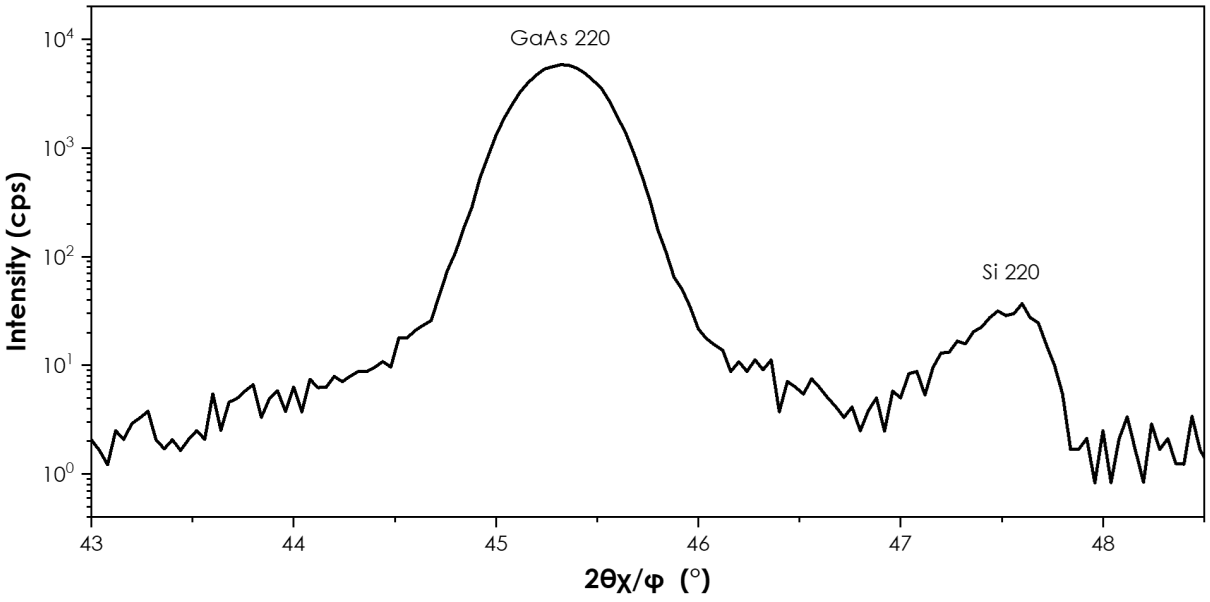

Figure 4.18. *In-plane grazing incidence XRD measurement of reflections from the {220} planes of the GaAs thin film grown on a virtual substrate.*

3. Evaluation of the monocrystalline quality

Figure 4.19 shows an HRXRD rocking curve of the 004 peak of the GaAs layer grown on a virtual substrate. It was acquired with a rotating anode diffractometer. The rocking curves have widths around 0.098 degrees, significantly broader than those of the homoepitaxial grown sample which are of 0.004° (see **Figure 4.1**). It should be noted that the monochromator of the rotating anode diffractometer is less precise than that of the tube diffractometer (e.g., rocking curves collected on the homoepitaxial sample show FWHM of approximately 0.0082 degrees, whereas on the tube diffractometer, the FWHM is around 0.004°). Nevertheless, in the virtual substrate sample, the FWHM of the rocking curve is significantly larger than this instrumental width, indicating that the calculated FWHM is reliable. This difference in quality is easily explained by the fact that the epitaxial growth of Ge ultrathin films on c-Si poses challenges, primarily due to the 4.18% lattice mismatch between germanium and silicon[203]. As a result, germanium films deposited on silicon wafers generally exhibit high threading dislocation densities (TDD), above 10^8 cm^{-2} [204], which can be propagated to the GaAs layer. Strategies have been developed to reduce threading dislocation densities in Ge layers. One such approach involves using solid-source molecular beam epitaxy with a thick graded SiGe layer (4 µm thick) and a surfactant mediation technique involving antimony (Sb). A single monolayer of Sb effectively relieves the stress caused by the significant lattice mismatch between Si and Ge[205]. However, this technique is complex, and the thickness of the buffer solution avoids achieving a tunnelling effect between the GaAs layer and the Si substrate, unlike our solution, which is essential for future tandem cell applications. We will further explore the question of threading dislocation density of our strategy in the next section.

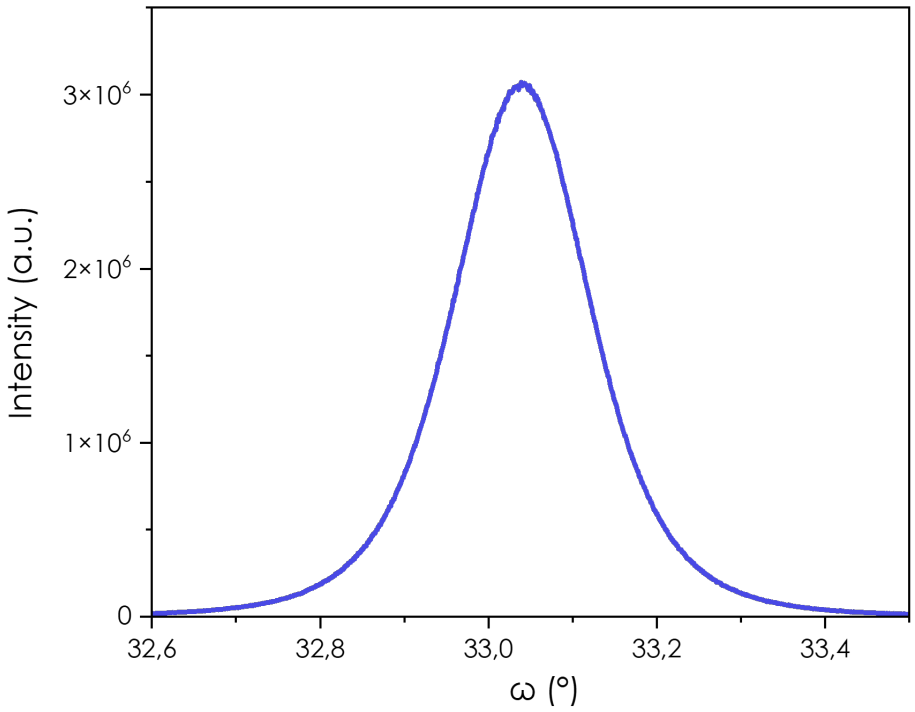

Figure 4.19. *HRXRD rocking curve of 004 peak at ϕ = 0° of homoepitaxial GaAs grown by RP-CVD on Ge-virtual substrate.*

4. Threading dislocation densities

In **Figure 4.20**, we present TEM images at varying magnifications of GaAs grown on a virtual substrate. **Figure 4.20. a)** shows that the dislocations originate from the thin Ge layer, which can be identified in **Figure 4.20. b)**. The dislocation density appears to decrease as we move away from the Ge/GaAs interface. Indeed, dislocations recombine and quickly form locks, preventing further propagation into the GaAs.

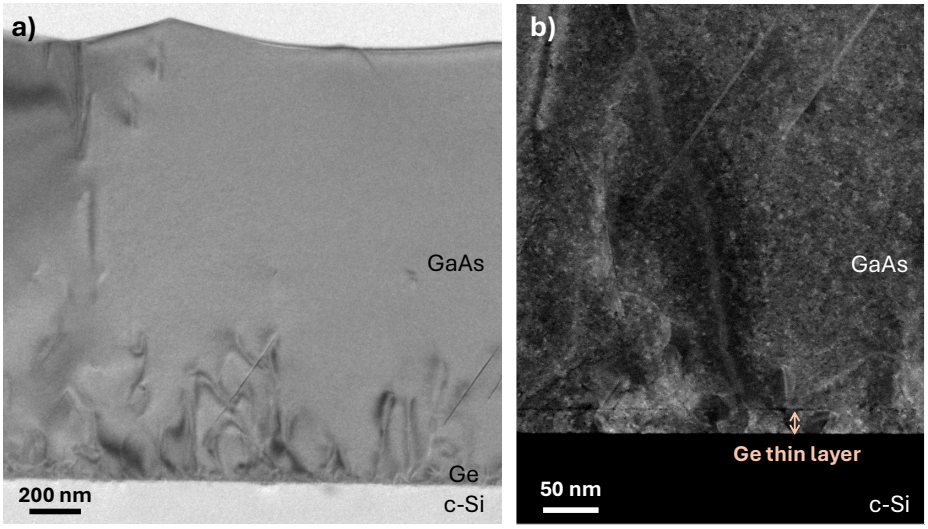

Figure 4.20. *a) Low magnification TEM image and b) higher magnification BF-TEM image with the arrow showing the ultrathin Ge layer between the GaAs RP-CVD grown layer and the virtual substrate.*

To quantify this, we determined the dislocation densities at various regions from the interface to the top of the GaAs layer by counting the number of dislocations in high-resolution TEM images. The results are shown in **Figure 4.21**. The threading dislocation density (TDD) decreases as we move into the GaAs layer, from 2–3.10^9 cm^{-2} at the Ge/GaAs interface level to 3.10^8 cm^{-2} in the GaAs top area. These values are very high, and we absolutely must reduce this density. To achieve this, optimizing the growth of Ge by PECVD is essential. This includes finding ways to better accommodate Si and Ge, such as by engineering a SiGe gradient interlayer. This task will continue to be developed in the laboratory in the frame of Yves Bois's thesis.

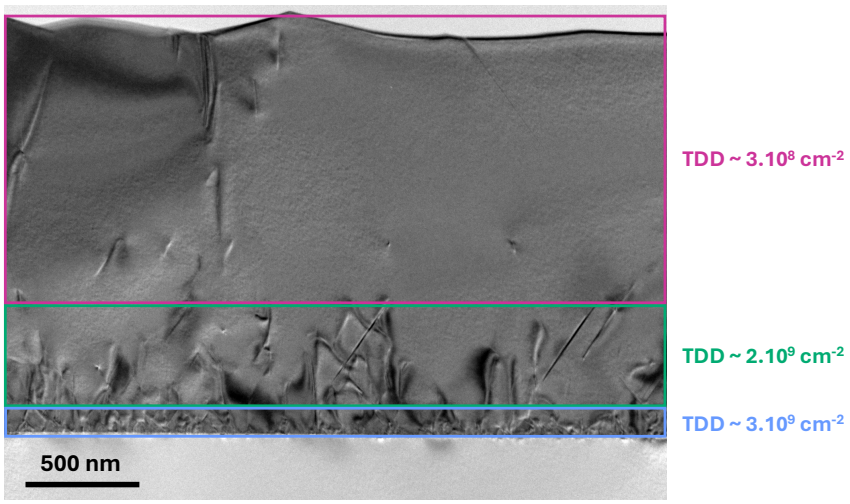

Figure 4.21. *TEM cross-section image with the TDD values on different areas.*

5. Chemical composition

Finally, the STEM-HAADF EDX chemical maps obtained for this sample are shown in **Figure 4.22**, which provides a comprehensive image of the distribution of the principal components, i.e. Si, Ge, Ga, and As. Elemental maps were extracted at energies of 1.74 keV (Si Kα), 9.8 keV (Ge Kα), 9.24 keV (Ga Kα), and 10.53 keV (As Kα). We observe a clear chemical composition repartition in the stack, with no unexpected mixing of chemical species. It would appear that Ge and Si are detected within the GaAs layer, but this is merely attributable to noise in the detector signal. In reality, there is no Ge or Si present in the GaAs layer.

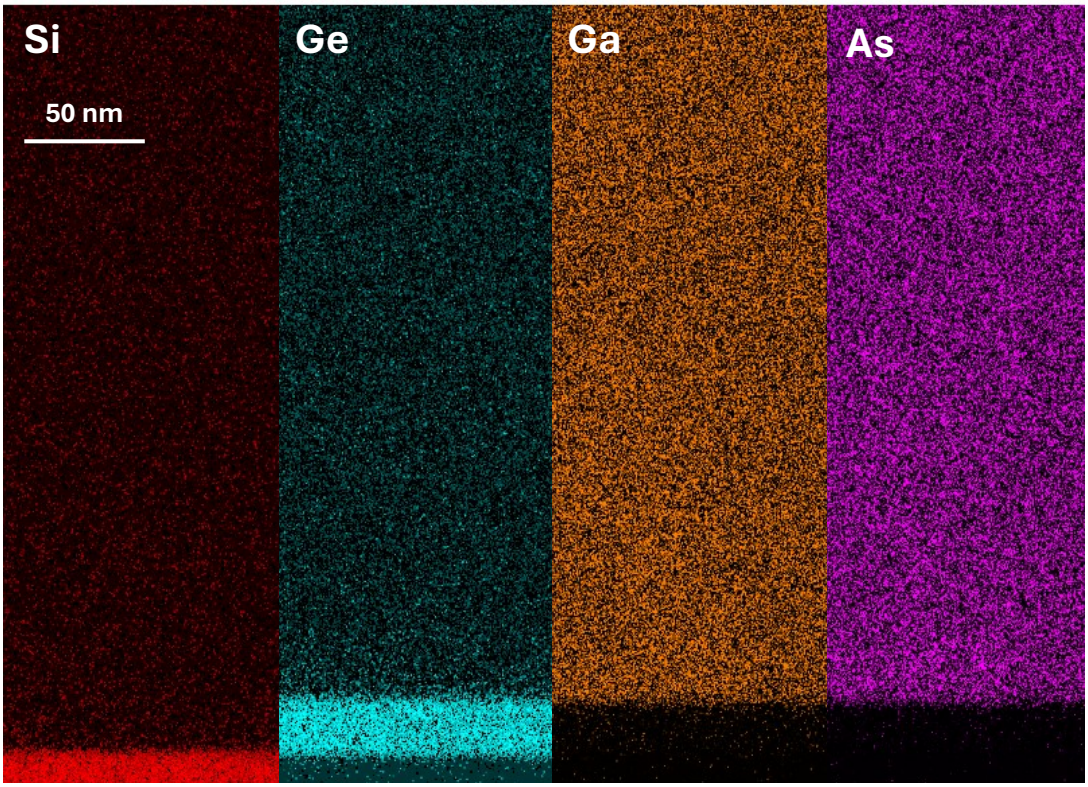

Figure 4.22. *STEM-EDX mapping of GaAs grown on a virtual substrate made of ultrathin Ge on c-Si substrate.*

III. Electronic properties investigation

Figure 4.23 presents the normalized photoluminescence spectrum of the GaAs layer grown on a virtual substrate compared to a GaAs wafer. The PL peak is sharp, with a relatively narrow peak compared to the reference wafer (~ 30 meV vs. 89 meV for the wafer), like for homoepitaxial growth (**Figure 4.6. a)**). Similar to homoepitaxial GaAs, the GaAs on the virtual substrate shows a peak shift towards lower energies (from 1.44 eV to ~ 1.42 eV for this sample), indicating p-type doping likely due to carbon from the organometallic gallium source. However, PL intensity of the GaAs on the virtual substrate is very low (not visible here as the data is normalised for better viewing), suggesting significant recombination at the Si/Ge interface, which is consistent with the high defect density found at this interface in above investigations.

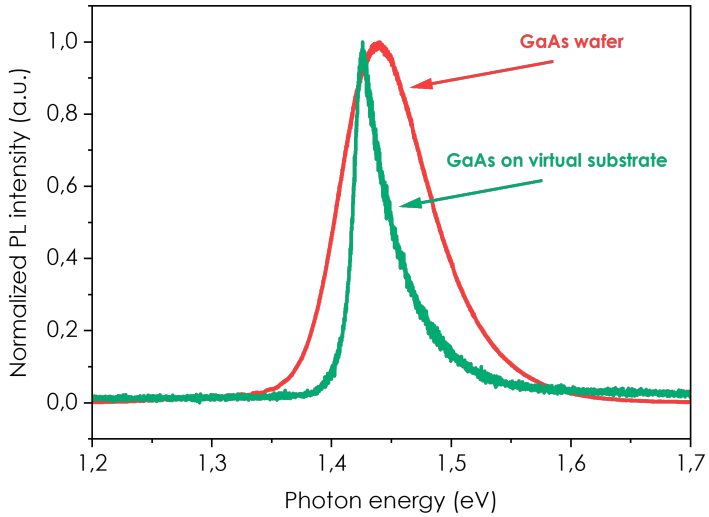

Figure 4.23. *Normalized photoluminescence spectra of GaAs on virtual substrate and GaAs wafer.*

To map the luminescence properties of the GaAs layer grown on a virtual substrate over a larger area and gain insight into its homogeneity, we performed a cathodoluminescence mapping. The results are presented in **Figure 4.24**. The figure **Figure 4.24. a)** shows a fairly good homogeneity of the position of the CL energy peak across the analysed area, with a bandgap varying from approximately around 1.410 eV to 1.428 eV. The most inhomogeneous regions (appearing in dark blue on the map) correspond primarily to areas with a shift of the bandgap to the lower energy, so potentially more carbon doped, and thus more defective. These areas of relief are predominantly associated with higher CL intensity, as illustrated in **Figure 4.24. b)**, where each pixel represents the integrated CL intensity over a spectral band centred at the CL peak position of 1.42 eV, with a width of 0.1 eV. This inhomogeneity was somewhat expected given the roughness of the film, which is visible in the TEM image of **Figure 4.20** and **Figure 4.21**. There is room for improvement if we compare to the homoepitaxially grown GaAs CL results in **Figure 4.7**. A Planck law fit was applied to the CL spectrum (for details, see **Appendix A**). From this fit, the doping level is estimated to be approximately $1.4 \pm 0.4 \times 10^{18}$ eV. This value is comparable to what is observed under similar growth conditions for homoepitaxial GaAs. Consequently, it is not surprising that the same carbon-induced p-type doping phenomenon occurs during the growth of GaAs on a virtual substrate.

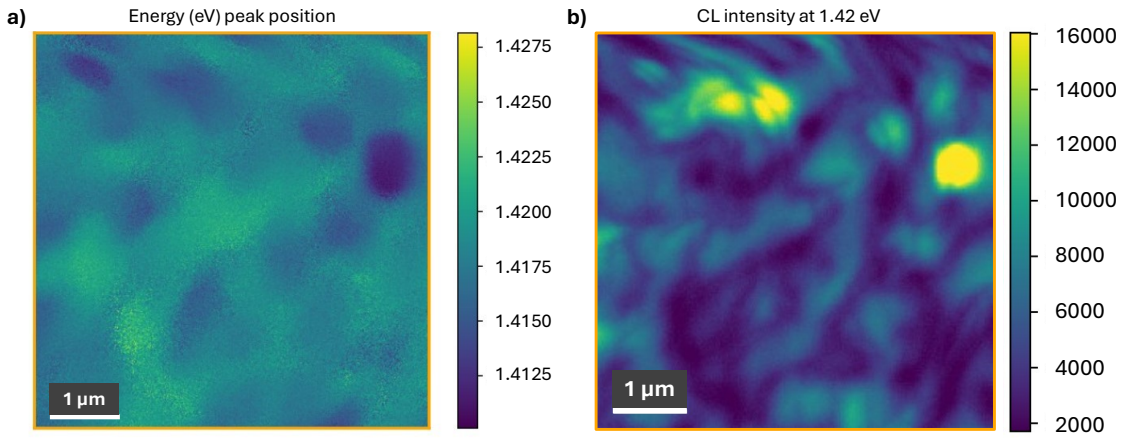

Figure 4.24. *Cathodoluminescence mapping of a) the energy peak position and b) the intensity around the CL peak at 1.42 eV (with width of 0.1 eV) of GaAs grown on a virtual substrate.*

These first results of GaAs growth on virtual substrates are very encouraging. Despite a limited study, as this optimisation work started at the very end of the thesis project, we have already achieved promising results. Further optimization of the Ge growth on the Si substrate will ultimately enable higher quality growth of GaAs layer and of the overall low-cost substrate solution. With this approach, we anticipate producing cost-effective substrates for various III-V industry applications (patent filed and startup creation in progress). In the long term, this solution could also be further developed to produce high-efficiency tandem solar cells, as the silicon part of the virtual substrate can be directly used as the bottom cell of a tandem solar cell.

Chapter 4. Summary

This chapter has provided a comprehensive study of the optimized growth of thin GaAs layers using TMGa and AsH_3 in the RP-CVD reactor, on different substrates: GaAs, Si and virtual substrates (thin Ge layer on Si). The results clearly illustrate the advantages and challenges associated with each substrate, as well as the potential of this innovative process for III-V growth.

For GaAs homoepitaxial growth, we have successfully demonstrated that the films exhibit remarkable characteristics comparable to commercial GaAs wafers, including excellent crystalline quality (FWHM of 004 peak rocking curve = 0.004°), along with a surface roughness of 0.2 nm for a growth rate of 3 µm/h. Chemical analysis via XPS confirm a homogeneous composition in depth with a constant stoichiometry of 1/1 for As and Ga, no traces of oxygen (no oxygen present during deposition) or carbon contamination is detectable. Furthermore, the samples display favorable electronic properties, featuring a sharp photoluminescence peak, a p-type doping concentration of around 10^{18} cm^{-3}, and a high mobility of 172 $cm^2.V^{-1}.s^{-1}$. These results confirm that our reactor is capable of producing high-quality GaAs layers.

During the direct growth of GaAs on c-Si, many studies have revealed significant challenges related to differences in thermal expansion coefficients and lattice parameters between GaAs and Si. Through the investigation of various deposition temperatures, we analysed how growth initiates on such a mismatched substrate. Results showed that highly oriented GaAs can technically be formed directly on Si. However, the defective structure discouraged further pursuit, leading us instead to seek a strategy to accommodate the GaAs lattice and facilitate growth.

Thus, the growth of GaAs on a low-cost virtual substrate began to be studied in the last months of the thesis and has already produced encouraging results. Despite a significant dislocation density that decreases away from the Ge interface (from $2–3.10^9$ cm^{-2} to 3.10^8 cm^{-2}), we still have a pluridomain monocrystalline film (FWHM of 004 peak rocking curve = 0.098 °) and sharp PL peak. A doping level similar to that found in homoepitaxy is measured by CL. Initial analyses suggest that this substrate could provide an economical solution for producing high-quality GaAs layers, with direct applications in high-efficiency tandem solar cells.

In the next chapter, we will explore how GaAs electronic properties have been optimized to meet the requirements for a successful integration in solar cell devices.

Chapter 5. Doping optimization for effective integration into solar cells 102

A. The role of plasma in doping control 102
I. The purpose and methods to achieve doped layers.....102
II. Doping level targets in our solar cell architecture 103
III. The role of plasma in GaAs doping during RP-CVD growth 103

B. Fine tuning of the doping level with TMGa 107
I. Arsine introduction: in the plasma versus out-of-plasma 108
II. Effect of deposition temperature 109
III. Effect of plasma power.....110
IV. Effect of chamber pressure 111

C. A drastic approach for doping reduction: TEGa 112
I. TMGa versus TEGa precursor decomposition 112
II. Evaluation of the doping reduction.....113
III. Still a wafer-grade film quality.....114

D. First RP-CVD grown GaAs absorber integration into a solar cell..... 115
I. TMGa-based solar cells.....115
II. TEGa-based solar cells.....122

Chapter 5. Summary..... 126

Chapter 5. Doping optimization for effective integration into solar cells

In the previous chapter, the growth of GaAs on various substrates was investigated. We have shown that homoepitaxial samples exhibit superior layer quality, essential for device integration. Therefore, in this chapter, we will exclusively focus on exploring in detail the doping of homoepitaxial GaAs layers for integration into III-V solar cells.

A. The role of plasma in doping control

I. The purpose and methods to achieve doped layers

Doped layers are essential in the fabrication of III-V solar cells as they significantly influence the electrical properties and overall performance of the device. In III-V semiconductor solar cells, doping is used to introduce specific types and concentrations of charge carriers, electrons or holes, into the semiconductor material. This process creates distinct regions within the solar cell, such as n-type and p-type layers, which are crucial for forming a p-n junction. The p-n junction is the fundamental component that separates and directs the flow of charge carriers generated by photon absorption. Proper doping ensures efficient charge carrier collection and reduces recombination losses, which are critical for maximizing the cell's efficiency. Therefore, achieving precise control over doping is important for optimizing the efficiency of III-V solar cells. For n-type GaAs, the majority carriers result from the addition of excess electrons, donor impurities such as silicon (Si), tellurium (Te), sulfur (S), or selenium (Se) are used. In contrast, p-type GaAs is achieved by introducing holes through acceptor impurities such as zinc (Zn), magnesium (Mg), beryllium (Be), or carbon (C). Carbon can be introduced either via extrinsic sources, notably via halomethane gases (like CBr_4 or CCl_4)[206], or directly using precursors involved in the growth of the GaAs compound, thus via intrinsic sources, namely trimethylarsine (TMAs) or trimethylgallium (TMGa)[207]. Indeed, as discussed in the previous chapter, the methyl radicals resulting from TMGa decomposition can lead to carbon incorporation, thereby naturally introducing p-type doping in our material. Carbon is an amphoteric impurity but is preferentially incorporated as an acceptor at arsenic sites, even at high doping levels[208]. However, carbon dopants can be more or less activated by hydrogen through the formation of C-H bonds[209]. In this section **A**, we will investigate this phenomenon further, verifying our hypothesis regarding the doping source. We will also set the target doping level for our first solar cell device, which will then guide the doping optimization study (sections **B** and **C**) and the subsequent device fabrication (section **D**).

II. Doping level targets in our solar cell architecture

Figure 5.1 illustrates the proposed architecture for the solar cell we aim to develop by incorporating our RP-CVD grown GaAs as the base layer, also known as the absorber layer, the rest of the cell being grown by a conventional method (MOCVD at IES – UPM in Madrid, Spain). Testing the quality of our RP-CVD-grown layer as absorber is particularly interesting for two reasons: (i) this will provide a comprehensive assessment of our RP-CVD system effectiveness and potential in producing functional solar cells and ii) it is the thickest part of the solar cell and the most significant one. Indeed, this base layer drives the solar cell performance due to its role in capturing and converting sunlight into electrical energy. For optimal efficiency, this layer must be lightly doped (10^{15} – 10^{17} cm^{-3}), despite the fact that higher doping levels can lead to increased open-circuit voltage (V_{oc}) and reduced resistance[210,211]. Light doping is important because it preserves the material's high absorption capability while minimizing the negative effects of doping-induced carrier recombination, which can impair solar cell efficiency. Typically, we aim for a doping level of approximately 1 x 10^{16} cm^{-3} for the GaAs base layer[212,213]. The rest of the solar cell stack, produced by MOVPE at IES – UPM in Madrid, will be detailed in section **D.I**.

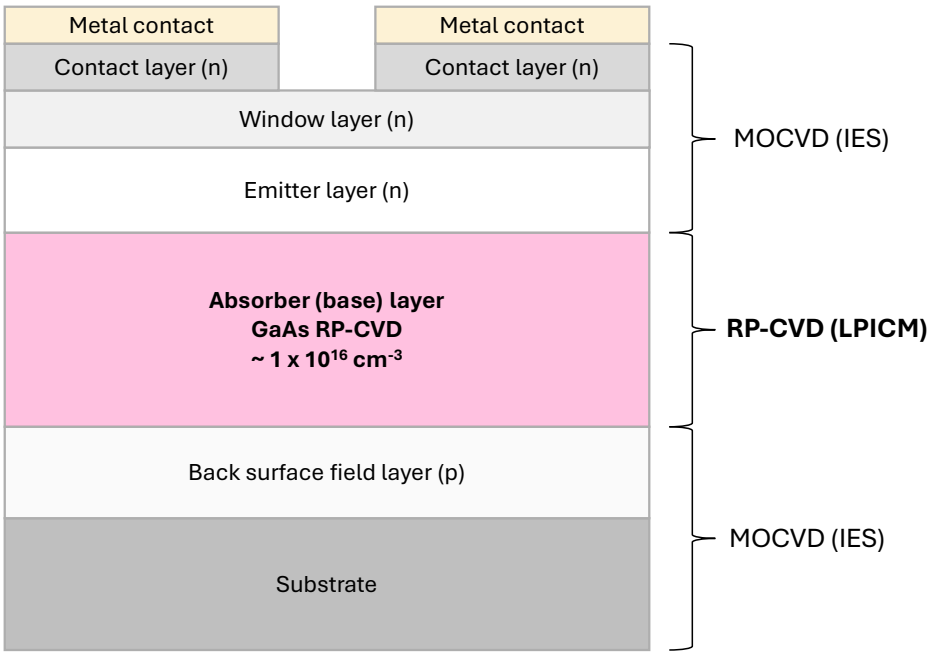

Figure 5.1. *Targeted solar cell stack.*

III. The role of plasma in GaAs doping during RP-CVD growth

1. Assessing the intrinsic doping induced by TMGa decomposition in RP-CVD

First and foremost, we aim at verifying the assumption made in the previous chapter, i.e. to confirm that the GaAs layers are indeed p-type doped and that this doping is due to the carbon

incorporation resulting from the dissociation of trimethylgallium. To this end, we have grown a specific stacked sample by RP-CVD (**Figure 5.2. a)**), with a top layer grown without plasma, thus in a 'MOCVD-like' mode, under the conditions described in **Figure 5.2. b)**. On the n-type GaAs substrate, we have grown a layer with plasma (RF plasma of arsine (AsH_3) diluted at 3% in H_2), hence in a 'RP-CVD' mode, and under the same other conditions than the top layer as shown in **Figure 5.2. b)**. With this stack, we will be able to investigate, through in-depth analyses, the effect of plasma on gas decomposition and the potential incorporation of impurities, particularly carbon, into the GaAs.

a)

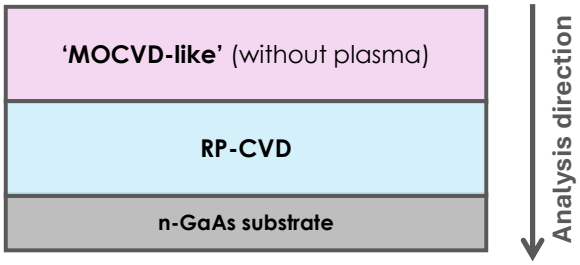

b)

Sample	Plasma power	Temperature	V/III	Pressure	Deposition time	Thickness
'MOCVD-like'	**0 W**	500°C	18	0.5 mbar	30 min	450 nm
RP-CVD	**150 W**	500°C	18	0.5 mbar	90 min	2250 nm

Figure 5.2. *a) Sample stack with analysis acquisition direction and b) table of RP-CVD growth conditions used.*

Figure 5.3 shows a cross-sectional SEM image of this stack. The top part of the image reveals the layer grown in 'MOCVD-like' (no plasma) mode, which is approximately 450 nm thick. Below this, we see the thick RP-CVD layer, with a thickness of 2250 µm, and then the substrate. Differences in contrast between the layers are observed, which correspond to doping contrast, as the secondary electrons used for image acquisition are sensitive to doping levels[185,186]. So we can already guess that the level of p-type doping is influenced by the presence of plasma.

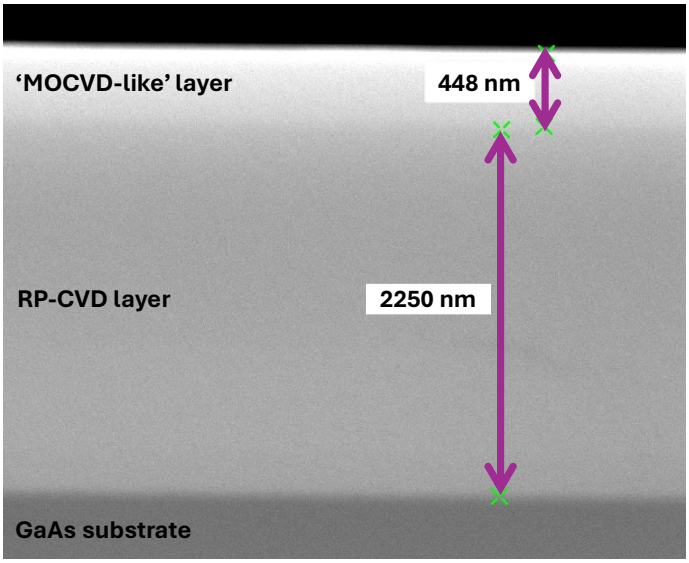

Figure 5.3. *SEM cross section image of the stack described in* ***Figure 5.2****.*

On this 'MOCVD-like'/RP-CVD stack, we performed electrochemical capacitance-voltage (ECV) profiling measurements to determine the carrier concentration in each layer and secondary-ion mass spectrometry (SIMS) measurements to determine the sample composition, in particular the concentration of carbon that we suspect to be responsible for the doping. We also aim to investigate the passivation of carbon doping through C-H bonds[209]. Therefore, we will closely examine the correlation between carbon concentration and carrier concentration. We will also take this opportunity to compare the growth of GaAs without plasma ('MOCVD-like') and with plasma ('RP-CVD').

The results of the comparative analysis by ECV and SIMS measurements are presented in **Figure 5.4**. In panel **a)**, we examine the 'MOCVD-like' and RP-CVD layers, focusing on impurity and carrier concentrations as a function of depth. For both layers, oxygen is below the detection limit. In the 'MOCVD-like' layer, a significant hydrogen concentration of 6–7 × 10^{18} cm^{-3} is observed. However, when the plasma is activated (i.e. RP-CVD layer) the hydrogen concentration drastically decreases, reaching 1-2 × 10^{18} cm^{-3}. However, this hydrogen concentration is the same as on the n-type GaAs substrate, indicating that such hydrogen level corresponds to the baseline level of the SIMS system (see panel **b)**) rather than to the actual hydrogen present in the RP-CVD GaAs layer (further details are available in the characterization section in **Appendix A**). Additionally, the hole concentration closely follows the carbon concentration in both the 'MOCVD-like' and RP-CVD layers, confirming that the doping is indeed due to carbon, with no evidence of hydrogen passivation. The doping level is notably higher in the 'MOCVD-like' layer compared to the RP-CVD layer, 4–5.10^{19} cm^{-3} versus 1.10^{18} cm^{-3}, respectively. This demonstrates that plasma has the ability to modulate the doping level in GaAs.
We previously observed a similar effect in the study of GaN in **Chapter 3**, where increasing the dissociation of H_2 in the ICP source by raising the RF power led to a higher flux of H-atoms, which in turn promoted the removal of carbon from the growing surface. It appears that a similar process is occurring here.

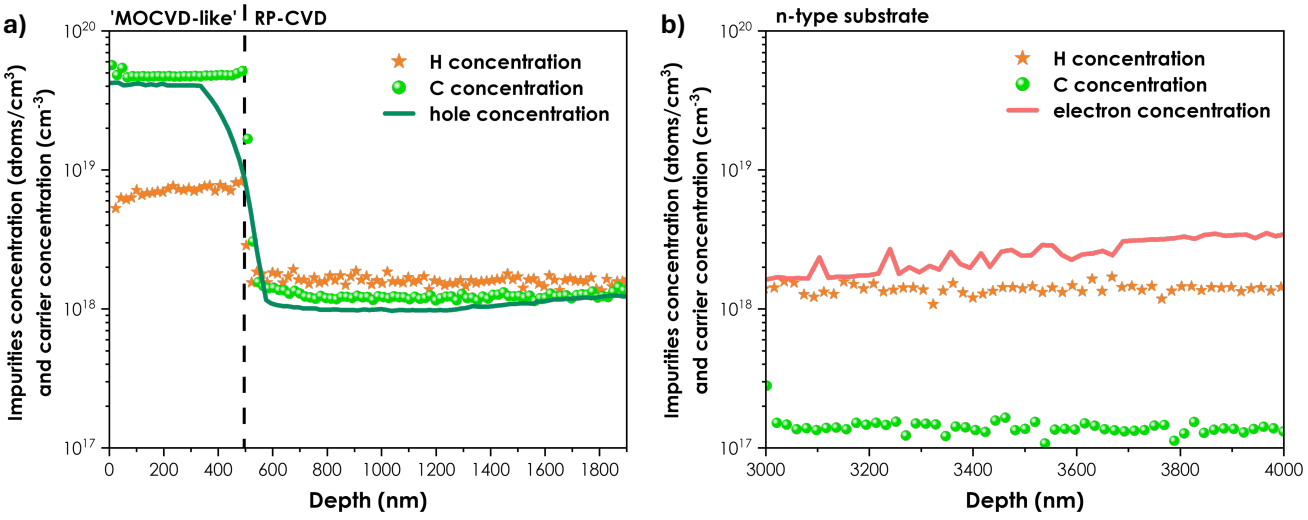

Figure 5.4. *Carrier concentration profiles as deduced from ECV measurements and impurities concentration profiles as deduced from SIMS measurements on a) the stack sample presented in* ***Figure 5.2*** *and b) the n-type substrate.*

2. Plasma benefits for RP-CVD GaAs growth

Let us continue to compare these layers grown with or without plasma using photoluminescence (PL) measurements. **Figure 5.5** shows the results for three samples, a 'MOCVD-like' layer, a RP-CVD layer and a n-type GaAs substrate, as a reference. A shift in the PL peak positions is observed, with the n-doped wafer exhibiting the highest energy peak position at 1.446 eV. This is expected, as the two layers with and without plasma treatment are p-type doped, resulting in their PL peak position shifting to lower energies (1.433 eV and 1.411 eV, respectively). The layer without plasma treatment shows a greater shift to lower energy, consistent with the higher doping level indicated in **Figure 5.4 (**4–5.10^{19} cm^{-3} versus 1–2.10^{18} cm^{-3} for RP-CVD). Additionally, examining the full width at half maximum (FWHM) of the peaks reveals that the sharpest peak belongs to the plasma-assisted deposition layer with a FWHM of 63 meV, compared to 92 meV for the non-plasma grown ('MOCVD-like') sample and 87 meV for the reference wafer. This suggests that the layer grown without plasma is more defective, likely due to higher incorporation of hydrogen and carbon revealed previously using SIMS (**Figure 5.4**).

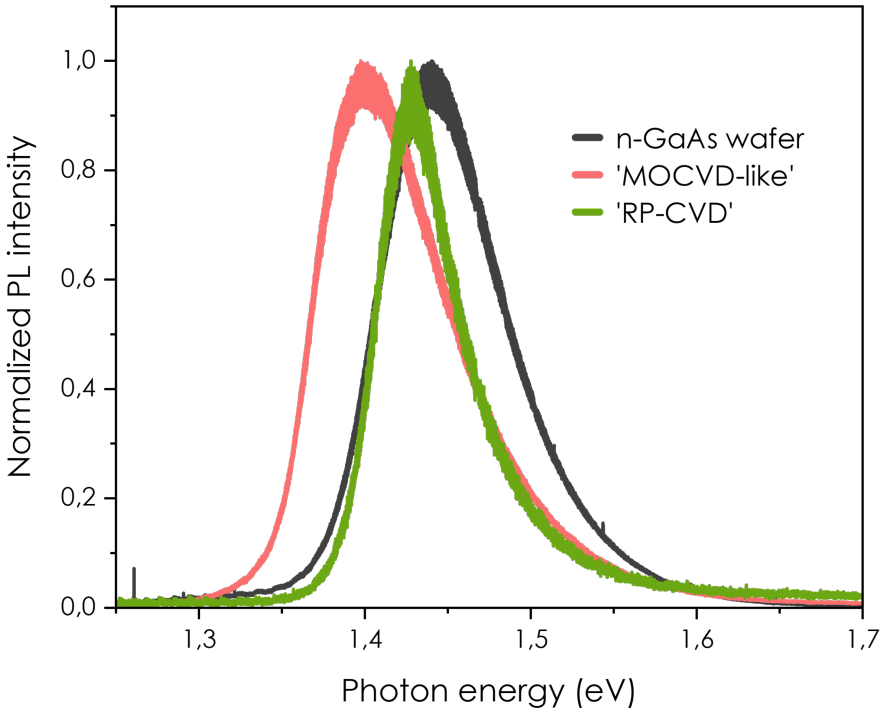

Figure 5.5. *Normalized photoluminescence spectra of homoepitaxial RP-CVD GaAs with (RP-CVD) and without ('MOCVD-like') plasma and n-GaAs wafer.*

In terms of structure, we can look at the Raman spectra of both films. **Figure 5.6** shows the spectrum of GaAs grown via RP-CVD, which features a strong and sharp LO phonon band at 292.05 cm^{-1}, indicating good structural properties as we expected given the excellent properties for this plasma-grown layer presented in **Chapter 4**. In contrast, the spectrum of GaAs grown without plasma shows a weak TO band at 264.92 cm^{-1}. While the LO mode is Raman-active, the TO mode is not for a (100) surface in backscatter geometry[214]. This failure in the selection rule can be attributed to misorientation effects in the growing film, caused by a significant increase in carbon concentration[215]. The presence of the TO mode is likely due to structural disorder or

surface roughness. Consequently, the TO mode is visible in the non-plasma-grown GaAs, unlike in the plasma-grown sample, due to the higher carbon concentration in the layer, as confirmed by SIMS-ECV cross-analysis in **Figure 5.4**. Furthermore, the LO mode is particularly sensitive to the depletion region in GaAs samples[215]. In doped semiconductor materials, the depletion region is influenced by the dopant concentration. As the dopant concentration increases, the depletion region becomes smaller, causing the LO mode to become less visible or even absent[215]. This is because the high concentration of free carriers interacts with the longitudinal vibrations, reducing their intensity. This explains why the LO mode is no longer observed in the non-plasma-grown sample, i.e. the most heavily doped sample.

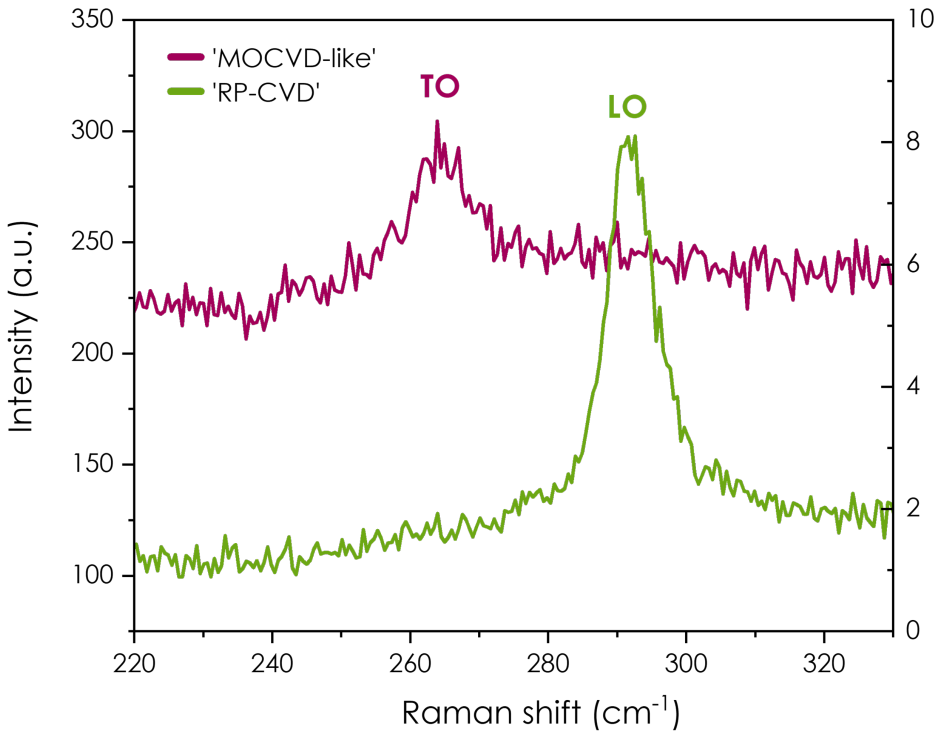

Figure 5.6. *Raman spectra of GaAs samples grown with (RP-CVD) and without plasma ('MOCVD-like') conditions.*

To conclude, under the same growth conditions, i.e. a temperature of 500°C and a pressure of 0.5 mbar, the use of the plasma in the RP-CVD reactor produces high-quality GaAs layers, characterized by the absence of hydrogen (concentration around 1 x 10^{18} cm^{-3}, i.e. level of H content of the chamber), a lower carbon content, and superior electronic and structural properties. The use of plasma is appealing because it allows us to modulate the doping level. This could potentially enable us to grow the p-type absorber layer with plasma for controlled doping and the heavily doped back surface field (BSF) layer without plasma (**Figure 5.1**), all within the same reactor.

B. Fine tuning of the doping level with TMGa

Having demonstrated in **Chapter 4** that we can obtain GaAs with excellent crystalline quality and understood the origins of doping in our layers, we can now transition to optimizing the

absorber layer for our first solar cell. A crucial point will be to understand and optimize the doping level of the layers to approach 1 × 10^{17} cm^{-3}.

To begin, let us take an overview of some data obtained from our optimization series by looking at **Figure 5.7**. In **Figure 5.7. a)**, we observe that we can achieve doping levels ranging from 1 × 10^{18} cm^{-3} to 7 × 10^{19} cm^{-3} using TMGa. Achieving this broad range is interesting because it shows that RP-CVD can be used for solar cells which consist of a stack of gradually doped layers designed to efficiently extract charges (**Figure 5.1**). Moreover, most points on this curve follow the theoretical and experimental trends presented in M. Sotoodeh's paper[216], which compiles several studies (**Figure 5.7. b)**). Therefore, we can say that our RP-CVD layers are within the state of the art. We will further detail this in the subsequent sections by exploring the specific growth conditions that correspond to the best performance data points (giving a high mobility depending on the level of doping) and investigating the reasons behind the suboptimal ones.

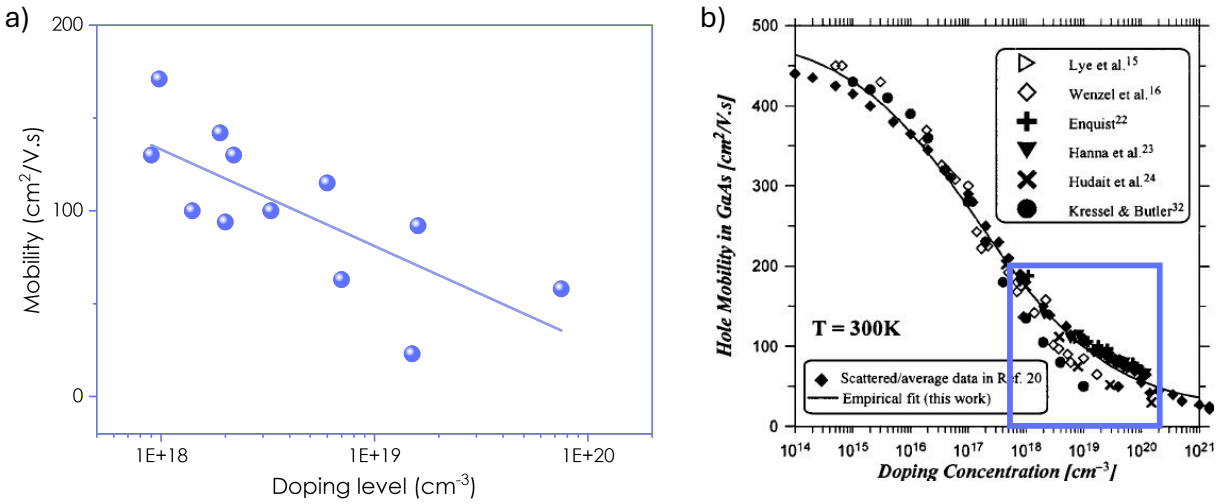

Figure 5.7. a) Mobility vs. doping level plot from our optimization samples with a linear fit and b) mobility vs. doping concentration plot from empirical fit obtained in M. Sotoodeh work[216] with experimental data points taken from some references[217–222].

For use as an absorber layer in a III-V solar cell, our GaAs layer grown by RP-CVD should have a doping level of around 1 x 10^{17} cm^{-3} as explained in section **A.II**. Let us discuss some of the trends observed in tuning the growth parameters, focusing on understanding which parameters have a strong impact on hole concentration.

I. Arsine introduction: in the plasma versus out-of-plasma

We have two options for the introduction of arsine during growth (see **Figure 2.8** of **Chapter 2**): either into the plasma zone via the gas line going to ICP zone ('ICP' line) or directly into the growth zone (via the 'hydride' line). **Figure 5.8** displays in **a)** the growth rate and in **b)** the doping concentration and mobility achieved in both configurations. When arsine (300 sccm of AsH_3 diluted to 3% in H_2) is introduced directly into the growth chamber through the 'Hydride' line, i.e. bypassing the plasma, the growth is carried out using only a hydrogen plasma (with a flow of 100 sccm and under an RF power of 150 W). With arsine introduced through the 'hydride' line, the

growth rate is comparable to that achieved with arsine introduced in the 'ICP' line, which is expected since the deposition temperature of 500°C is sufficient to thermally crack AsH_3 and TMGa. The electronic properties are however significantly degraded when AsH_3 is introduced via the 'hydride' line, resulting in a higher doping concentration of 1.6×10^{19} cm^{-3} and a mobility that decreases to 92 $cm^2/V.s$ (which is still quite good according to **Figure 5.7. b)**). This degradation occurs because there is less hydrogen in the plasma when arsine is injected via the 'hydride' compared to arsine in 'ICP', and thus less atomic hydrogen is available on the substrate level to etch away carbon. This should lead to an increased carbon content and the measured higher doping level.

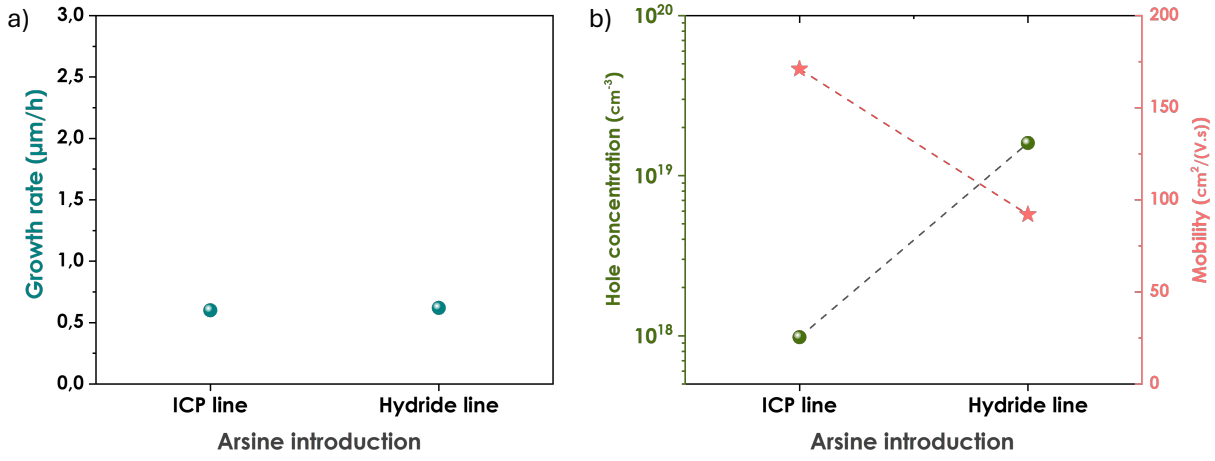

Figure 5.8. *a) Growth rate and b) hole concentration and mobility for arsine introduced either via ICP or hydride lines at 500°C, 150 W, V/III = 18 and 0.5 mbar. The dotted lines are provided as a guide to the eye.*

II. Effect of deposition temperature

Figure 5.9 illustrates the results for layers grown at substrate temperatures of 450°C, 500°C and 550°C. A deposition was attempted at 450°C, but the layer thickness was undetectable, likely due to an extremely thin or nonexistent film. However, at 500°C, we obtained a deposition with a growth rate of 0.6 µm/h. This difference between depositions at 450°C and 500°C is explained by the limitation imposed by the thermal dissociation of TMGa, which decomposes completely above 475°C[192]. The doping concentration is measured at around 1×10^{18} cm^{-3} with a mobility of 171 $cm^2/V.s$, which is in excellent agreement with the typical values theoretically and experimentally reported for this doping level in high-quality GaAs in **Figure 5.7. b)**. At a higher deposition temperature of 550°C, we observe a significantly increased deposition rate of 3 µm/h due to more complete decomposition of TMGa and likely more carbon incorporated as supported by the higher carrier concentration of 2.2×10^{18} cm^{-3} in **Figure 5.9. b)**. Nevertheless, we maintain a good mobility of 130 $cm^2/V.s$, also in line with **Figure 5.7. b)**. This suggests that the growth is limited by TMGa, and that increasing the V/III ratio and plasma power while maintaining a temperature at 550°C could potentially remove carbon and thereby achieve lower doping at high growth rates. We tested this approach (see sample 11 (550°C, 200 W and V/III = 30) in the **Appendix D**), but the results were not conclusive as the doping level remained

unchanged. Since our goal is to achieve a low doping of around 1 x 10^{17} cm^{-3} for the absorber layer in the solar cell and the highest possible electronic mobility, we will select 500°C as the optimal temperature condition, even though it does not yield the highest growth rate.

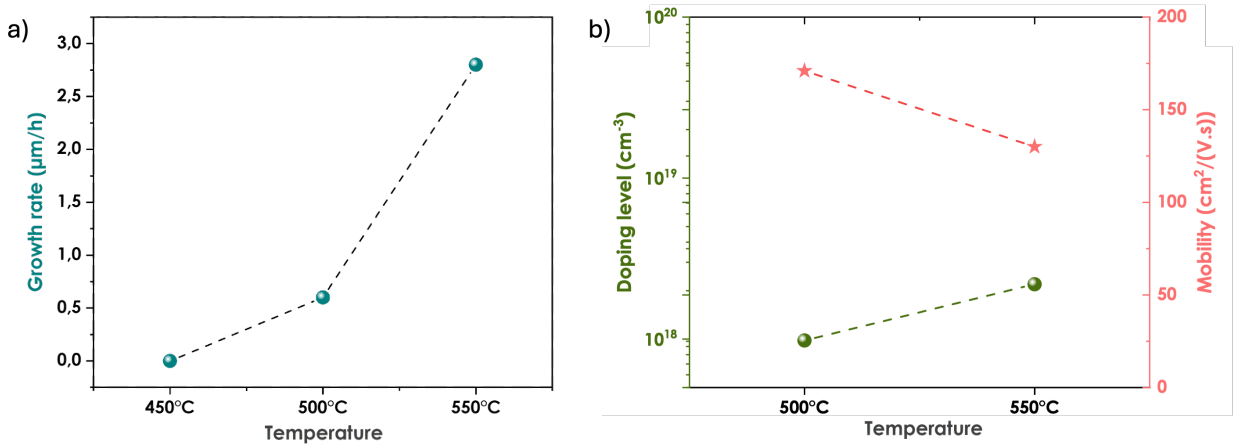

Figure 5.9. *a) Growth rate and b) hole concentration and mobility for different deposition temperatures with AsH_3 in 'ICP' line, at 150 W, V/III = 18 and 0.5 mbar. The dotted lines are provided as a guide to the eye.*

III. Effect of plasma power

Maintaining 500°C as the substrate temperature, we will now examine the effect of plasma power on the film properties. In **Figure 5.10**, we represent the results for films grown at 100 W, 150 W, 200 W and 250 W. We first observe a wide scattering of the growth rate, which is too significant to be attributed solely to thickness inhomogeneities within the same sample. Therefore, we will propose hypotheses to explain the possible causes. At 100 W, the growth rate is 1.1 µm/h, which is actually the same growth rate as a deposition under the same conditions but without plasma (**Figure 5.2**). Thus, this confirms that, at such RF power value, the plasma does not significantly contribute to the growth process, as already shown in **Figure 5.8**. When we increase the plasma power to 150 W, we observe a decrease in the growth rate from 1.1 µm/h to 0.6 µm/h. Examining the electronic properties, we notice that this additional plasma power allows to significantly reduce the doping level from 6 × 10^{18} cm^{-3} to 1 × 10^{18} cm^{-3}. Between 100 and 150 W, it appears that the plasma etching effect on carbon becomes stronger, with this reduction in contamination leading to a corresponding decrease in doping concentration. This is also accompanied by an increase in mobility from 115 to 171 cm^2/V.s, which is consistent with tabulated values[189]. Increasing the plasma power to 200 W results in a growth rate of 1.4 µm/h, suggesting that the plasma is facilitating the growth kinetics. However, it is challenging to explain why and how this enhancement occurs. When the power is increased further to 250 W, the growth rate returns to the level observed at 100 W. This may be because, at this higher power, the plasma begins to etch the entire layer rather than solely removing carbon contamination. This increase in plasma power from 150 W up to 200 and 250 W is accompanied by a rise in the doping concentration of the layer, to about 3 × 10^{18} cm^{-3} for both values of the RF power. This can be reasonably explained for the layer grown at 250 W, as the overall etching of the GaAs layer can result in less effective carbon removal than at 150 W. However, it is somewhat counterintuitive

for the growth at 200 W, as the film is thicker than at 150 W but exhibits higher doping. This may perhaps be explained by the faster growth rate leading to a more defective layer. Further studies are necessary to conclude on the effect of the RF power. Since our goal remains to achieve low doping and the highest possible mobility, we will select 150 W as the actual optimal plasma power condition.

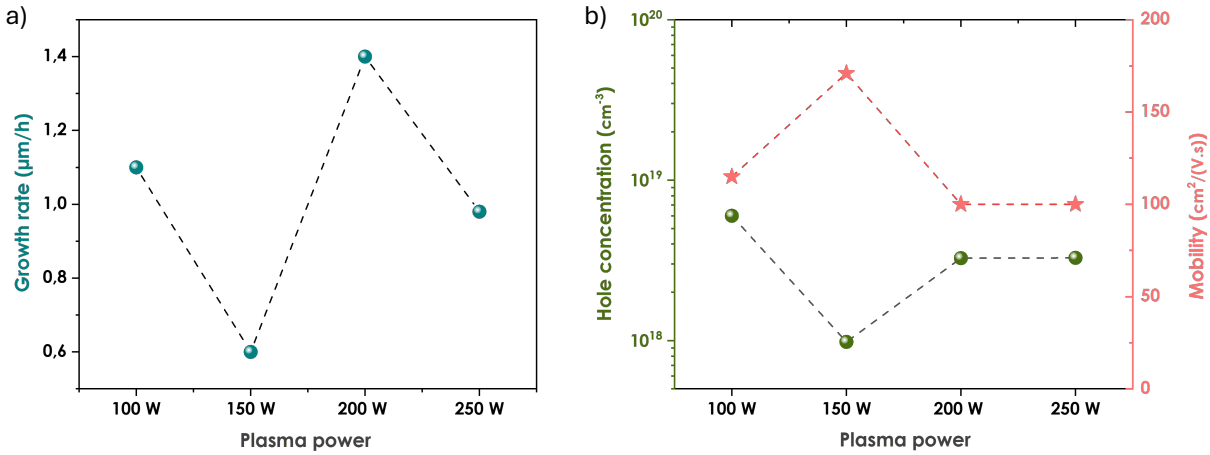

Figure 5.10. *a) Growth rate and b) hole concentration and mobility for different plasma power values with AsH_3 in 'ICP' line, at 500°C, 150 W, V/III = 18 and 0.5 mbar. The dotted lines are provided as a guide to the eye.*

IV. Effect of chamber pressure

Keeping 500°C and 150 W fixed, we now examine the effect of deposition pressure. **Figure 5.11** displays the results for growths conducted at 0.2 mbar, 0.5 mbar, and 0.8 mbar. As shown in **Figure 5.11. a)**, the growth rate of the GaAs film increases with pressure. In contrast, in conventional MOCVD growth of GaAs, the growth rate typically increases as the pressure decreases[187]. This discrepancy may arise because the layers were here deposited in a Ga-rich environment, given the V/III ratio is relatively low compared to classical MOCVD (18 vs. 50-100). Additionally, in RP-CVD, we operate at a lower pressure regime compared to MOCVD, so we are not constrained by the same factors. In MOCVD, limitations are often due to diffusion, whereas in RP-CVD, the constraints are more related to dissociation. As a result, the growth rate is influenced by the cracking efficiency of arsine, which improves with higher deposition pressures because the increased gas density and collision rate can facilitate the dissociation of arsine molecules into arsenic and hydrogen. Optimal electronic properties are observed at 0.5 mbar, the intermediate pressure, which provides the lowest doping level and highest mobility. The higher growth rate at 0.8 mbar may lead to increased contamination. This is because increasing the pressure raises the gas density, so adding more TMGa introduces more carbon contamination. In summary, drawing a definitive conclusion is very challenging for this pressure series as it would require a detailed study of gas kinetics.

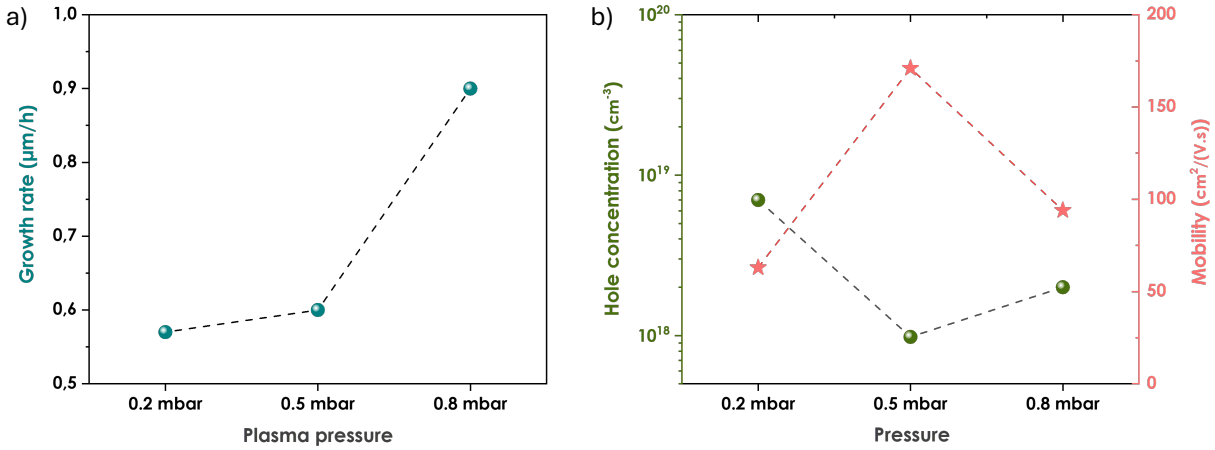

Figure 5.11. *a) Growth rate and b) hole concentration and mobility for different chamber pressures with AsH_3 in 'ICP' line, at 500°C, 150 W and V/III = 18. The dotted lines are provided as a guide to the eye.*

From the previous results we can conclude that the conditions leading to the lower doping level are a deposition temperature of **500°C**, AsH_3 introduced via the **ICP line**, **150 W** of plasma power and a pressure of **0.5 mbar**. Giving a doping level of **1×10^{18} cm^{-3}** and a mobility of **171 cm^2/V.s**.

These results further demonstrate our ability to modulate doping using a wide range of growth conditions. However, despite this improvement, the doping level remains too high relative to our target level of 1×10^{17} cm^{-3}.

C. A drastic approach for doping reduction: TEGa

As shown above, despite testing a variety of process conditions, we have been unable to achieve doping levels well below 10^{18} cm^{-3}. We will now demonstrate an effective way to drastically reduce the doping level in our layers. This involves addressing the primary source of doping, the organometallic gallium precursor. The solution we propose is to replace TMGa by triethylgallium (TEGa). This substitution is expected to reduce doping levels because TEGa is theoretically less prone to decomposing into carbon fragments in MOCVD compared to TMGa, leading to a lower doping concentration in the resulting layers. Let us delve deeper and examine whether this holds true for our specific process, RP-CVD.

I. TMGa versus TEGa precursor decomposition

Incomplete desorption of hydrocarbon products from gallium alkyl decomposition leads to carbon incorporation, which can limit the purity of the GaAs epitaxial layer[223]. However, if well-controlled, this process can also yield highly p-doped layers suitable for forming electrical contacts as we obtained previously using TMGa. The incorporation of carbon depends on the rate of the metal alkyl decomposition reaction[224]. Donnelly and McCaulley investigated the thermal decomposition products of TEGa and TMGa adsorbed on Ga-stabilized GaAs (100) via mass spectrometric studies[225]. They report that the higher carbon levels in GaAs films grown with TMGa

($Ga(CH_3)_3$ compared to TEGa ($Ga(C_2H_5)_3$) can be qualitatively explained by the slower desorption rate of CH_3 from TMGa decomposition, in contrast to the faster desorption of C_2H_4 and C_2H_5 from TEGa decomposition. This is confirmed by the work of Aquino and Jones who used high resolution electron energy loss spectroscopy (HREELS) for the same purpose[226]. Results from HREELS spectra of TEGa adsorption at room temperature show that the dominant surface species consist of intact ethyl (C_2H_5) groups and the diethylgallium surface species remains stable up to 250°C. Heating to 400°C results in the complete decomposition of the molecule via a fast β-elimination mechanism. For TMGa adsorption, HREELS spectra indicate that the stable surface species at room temperature consists of intact methyl (CH_3) groups. Decomposition of these dimethylgallium species occurs with increasing temperature and involves the loss of CH_3 groups from the surface. Unlike TEGa, the TMGa decomposition at elevated temperatures also produces surface methylene (CH_2) species, suggesting an additional decomposition pathway involving dehydrogenation from adsorbed CH_3 groups. This complicates desorption and therefore favors the higher carbon incorporation when TMGa is used compared to TEGa.
Another interesting aspect of using TEGa instead of TMGa is that it allows the kinetically limited growth regime to occur at lower temperatures. Indeed, complete dissociation of TEGa takes place at around 400°C[226], whereas TMGa requires temperatures above 475°C[192]. Lowering the temperature of a process is advantageous because it can reduce thermal stress on the substrate, thus improve material quality by reducing defect formation, and decrease energy consumption, in line with our objective of reducing costs.

II. Evaluation of the doping reduction

To determine whether a doping reduction can be achieved through the use of TEGa in our reactor, we conducted Hall effect measurements on a sample deposited under nearly identical conditions as for TMGa (500°C, 150 W, 0.5 mbar) but replacing TMGa by TEGa, which involved adjusting the canister pressure and temperature accordingly. The results for the sample grown with TMGa and for the one grown with TEGa are shown in **Table 5.1**. For the sample grown with TEGa, we measure an electron concentration of around 1.95×10^{15} cm^{-3} which is indicative of n-type residual doping in the material. These results demonstrate that while the TEGa process achieves a significant reduction in doping levels, a residual doping remains present, similar to other high-quality semiconductor materials. For example, for indium phosphide (InP) not intentionally doped layer grown at III-V Lab, a residual n-type doping of around 10^{14} - 10^{15} cm^{-3} is measured (information provided by Jean Decobert and Nicolas Vaissière from III-V Lab).
However, a mobility of 401 $cm^2/V.s$ is measured, which is much lower than the values typically reported in the literature for this n-type doping level, typically around 7000 $cm^2/V.s$[216]. It should be noted that Hall effect measurements on the TEGa samples were very challenging due to the low doping levels; we were unable to measure on the commonly used n- or p-doped substrates. As a result, we deposited the GaAs on a semi insulating (SI) GaAs substrate to obtain some measurable data. Unfortunately, due to the different emissivity of the SI substrate, the deposition temperature was not reliable as it was measured on a c-Si wafer placed side-by-side with the SI GaAs substrate (we lacked sufficient SI substrates to properly calibrate the pyrometer). Most likely, the actual deposition temperature was lower than the nominal 500°C measured by the

pyrometer on the c-Si substrate. Consequently, the layer appears rough and is probably of lower structural quality than that of the samples presented just below.

Sample	Doping type	Doping level	Mobility
GaAs with **TMGa**	p	9.8×10^{17} cm^{-3}	171 cm^2/V.s
GaAs with **TEGa**	n residual	1.95×10^{15} cm^{-3}	401 cm^2/V.s

Table 5.1. *Hall effect results for GaAs grown using TMGa or TEGa. Both sample deposited at a nominal temperature of 500°C.*

III. Still a wafer-grade film quality

Achieving a reduction in doping levels represents a significant advancement in our optimization of GaAs layers for solar cell integration. However, it is equally crucial to ensure that the crystalline quality of the epitaxial layers remains sufficient with TEGa, as we have demonstrated in **Chapter 4** with the films produced using TMGa. We first investigate the crystallinity of the GaAs film produce with TEGa using XRD, specifically focusing on the rocking curve depicted in **Figure 5.12**. The full width at half maximum (FWHM) of the 004 peak for our GaAs sample grown with TEGa is measured to be of 0.008°. If we compare this to a GaAs wafer, we can see that the diffraction of the homoepitaxial layer is almost as good as that of a reference substrate, which as a FWHM value of 0.0075. It is important to note that these measurements are not directly comparable to those presented in **Chapter 4** for GaAs grown with TMGa (**Figure 4.2**), as the latter were conducted using a tube-based diffractometer with a higher resolution monochromator compared to the rotating anode diffractometer used for the TEGa-grown sample measurement. However, given that the FWHM for GaAs grown with TMGa was also equivalent to that of a wafer, we can infer that the quality of GaAs produced with TEGa is as high as that the one produced with TMGa.

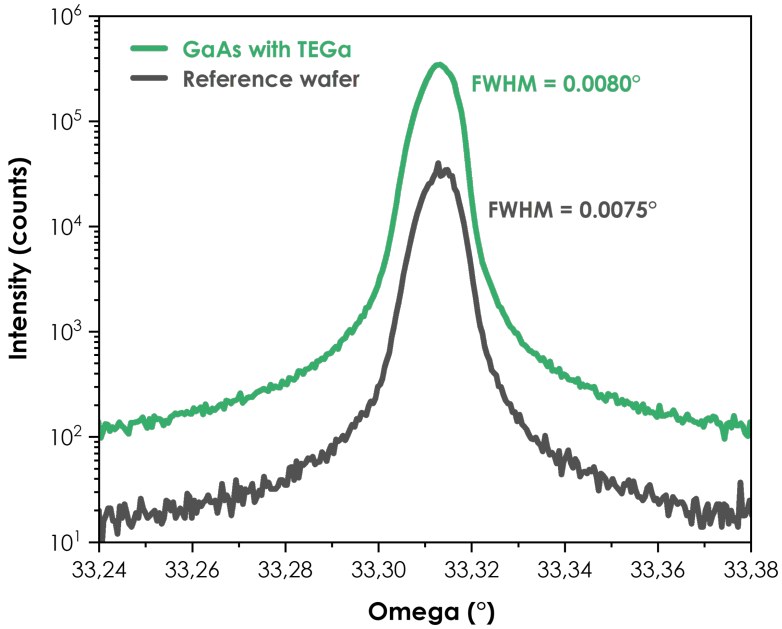

Figure 5.12. *Rocking curve of 004 peak at ϕ = 0° of GaAs grown using TEGa.*

Then, we studied the morphological characteristics of the epitaxial layers with a cross-sectional SEM image of the GaAs grown with TEGa shown in **Figure 5.13**. The layer appears to be continuous without columnar features and with a sharp interface with the substrate, as for GaAs grown using TMGa (**Figure 4.4**). The growth rate is here of 1.64 µm/h, which is quite reasonable. Regarding the surface of the cross-section sample, we can confirm that the film obtained with TEGa is also very smooth.

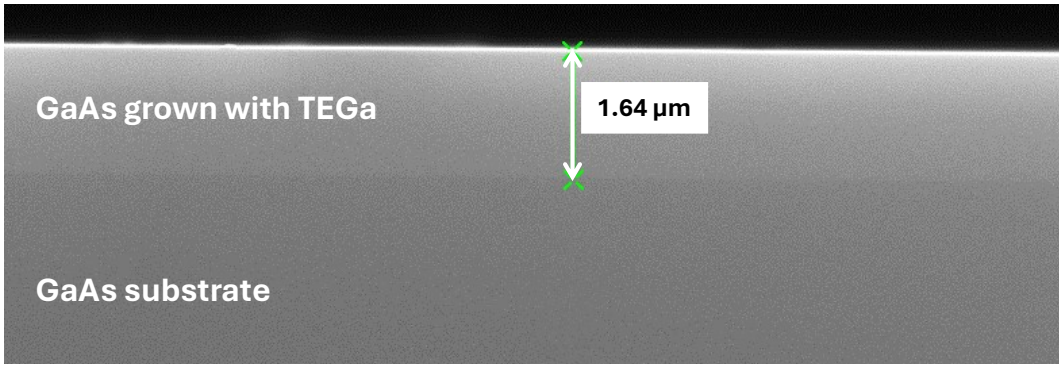

Figure 5.13. *SEM cross-section image of GaAs grown with TEGa at 500°C, 150 W and 0.5 mbar.*

These results underscore the ability of TEGa in achieving high crystallinity GaAs films, making it a viable alternative to TMGa for producing high-quality semiconductor materials with low doping level. Ideally, a mixture of the two gallium precursors, TEGa and TMGa, would be used to achieve intermediate p-type doping levels[227] of around 1 x 10^{17} cm^{-3}. However, our current reactor setup does not allow for the simultaneous connection of two organometallic bubblers, preventing us from leveraging the combined effects of TEGa and TMGa on doping. Introducing this capability would be a valuable enhancement for future work, enabling precise calibration and control of doping across a wide range of levels. Additionally, we aim to incorporate more conventional dopant lines, such as silane, to achieve n-type doping. This would allow us to form both sides of a p-n junction for complete devices fabrication in the same reactor without breaking vacuum.

D. First RP-CVD grown GaAs absorber integration into a solar cell

I. TMGa-based solar cells

The first integration test for the solar cell was initiated while we were awaiting the arrival of the new TEGa canister. Therefore, we chose to begin with a test that incorporated a GaAs layer grown with TMGa, even if it results in a high p-type doping of around 1 × 10^{18} cm^{-3}, as explained in the previous section. We selected the conditions that allowed us to achieve the lowest possible doping obtained with TMGa, i.e. 1 × 10^{18} cm^{-3}. We already know that the hole mobility in that layer

is of 171 cm^2/V.s, which is already a good start. Now, we need to design the solar cell stack before proceeding to device fabrication and characterization.

1. Design of the solar cell device

a. Additional electronic analyses

To design an efficient solar cell, it is essential to ensure several critical parameters that could influence the choice of the cell architecture. Firstly, ensuring the homogeneity of the electronic properties of our epitaxial layer is crucial as variations in these properties can lead to uneven current distribution, localized recombination centers, and decreased carrier collection efficiency, all of which can significantly reduce the overall efficiency of the solar cell. To verify the homogeneity of our epitaxial films, we used hyperspectral PL imaging. **Figure 5.14. a)** shows the mapping of the photoluminescence peak position over a piece of homoepitaxial GaAs sample. The results indicate minimal variations over this area, which measures approximately 3.5 cm in length. This confirms that we can fabricate solar cells on smaller areas with very little difference in PL peak position, and therefore minimal differences in doping levels. Indeed, given that a typical laboratory III-V solar cell measures a few mm^2, this homogeneity is highly satisfactory. Moreover, this level of homogeneity ensures that the cells will exhibit consistent performance across their entire surface, contributing to the overall efficiency and reliability of the device.
Secondly, we examined the minority carrier lifetime as it is a critical parameter that indicates how long charge carriers can exist before recombining. A longer carrier lifetime means that the carriers can travel further, increasing the chances of being collected at the electrodes and contributing to the photocurrent. To measure this carrier lifetime, we use time-resolved photoluminescence (TRPL) which is a technique that involves exciting the sample with a short pulse of light and then measuring the intensity of the emitted photoluminescence as a function of time. The decay of the photoluminescence signal provides information about the recombination processes occurring in the material and by analysing this decay, we can determine the carrier lifetime. The results of this analysis, conducted at different excitation wavelengths, are presented in **Figure 5.14. b)**. We observe that at shorter excitation wavelengths, which probe closer to the surface of the sample, the decay is faster, likely due to surface recombination since the sample is not passivated. The other decays, measured deeper in the bulk (i.e. at higher wavelengths), overlap quite well and from their single exponential behaviour, we can extract a minority carrier lifetime value, which is of the order of 0.84 ns. This is a good value for a non-passivated GaAs layer[228,229] and confirms the high quality of the layer, suggesting that we can expect to have a functional device despite the high doping.

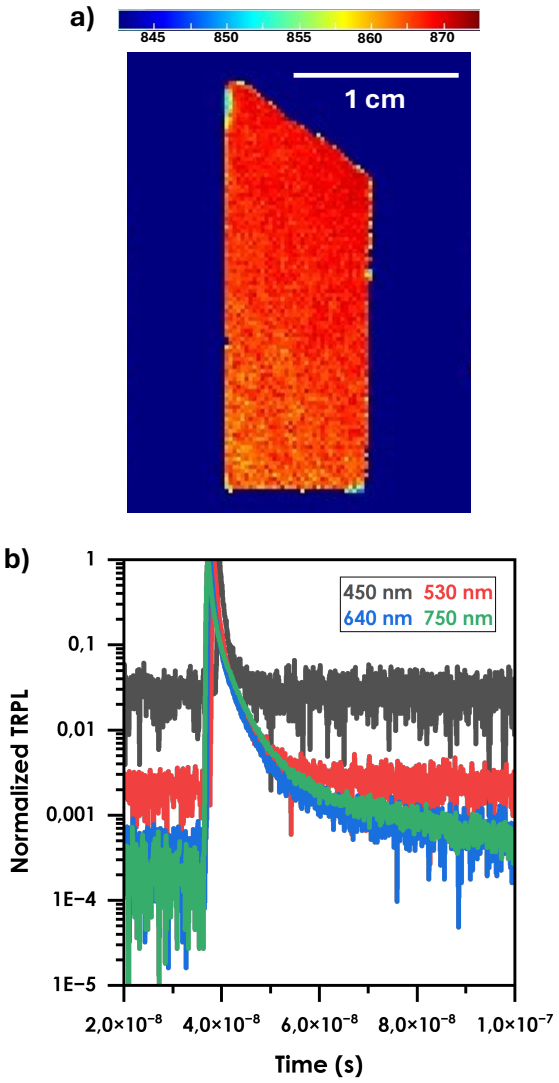

Figure 5.14. *a) Hyperspectral mapping of the PL peak position, b) TRPL decays at different wavelengths of homoepitaxial GaAs grown by RP-CVD at 500°C, 150 W and 0.5 mbar.*

b. Solar cell stack configuration

In **Figure 5.15**, we present the stack of the first solar cell made with a RP-CVD grown GaAs absorber layer. The other layers are produced by MOVPE at the Instituto de Energía Solar (IES) in Madrid. Please refer to **Appendix C** for a detailed information on the process flow as well as on the doping level of the different layers. The RP-CVD absorber layer, with a thickness of 1.1 µm, is grown on the p-type bottom part consisting of a 450 nm thick AlGaAs back surface field (BSF) layer which is a more heavily doped layer and acts as a barrier to minority carrier flow to the rear surface, thus reducing recombination. Then, there is a thin GaAs layer (approximately 60 nm) only used for epitaxial regrowth in the RP-CVD, which is not represented in the figure. The n-type top part of the solar cell includes a 200 nm GaAs emitter layer, which serves to create a p-n junction with the absorber layer, enabling the separation of charge carriers generated by light absorption. Then, a 30 nm GaInP window layer, which is a wide bandgap thin layer used to reduce front surface recombination. Finally, we have a GaAs contact, which facilitates the formation of ohmic contacts for efficient charge carrier collection and transport toward the metallic electrodes,

which provide the necessary electrical connections to external circuits. Note that we did not grow an anti-reflection coating on top of the structure.

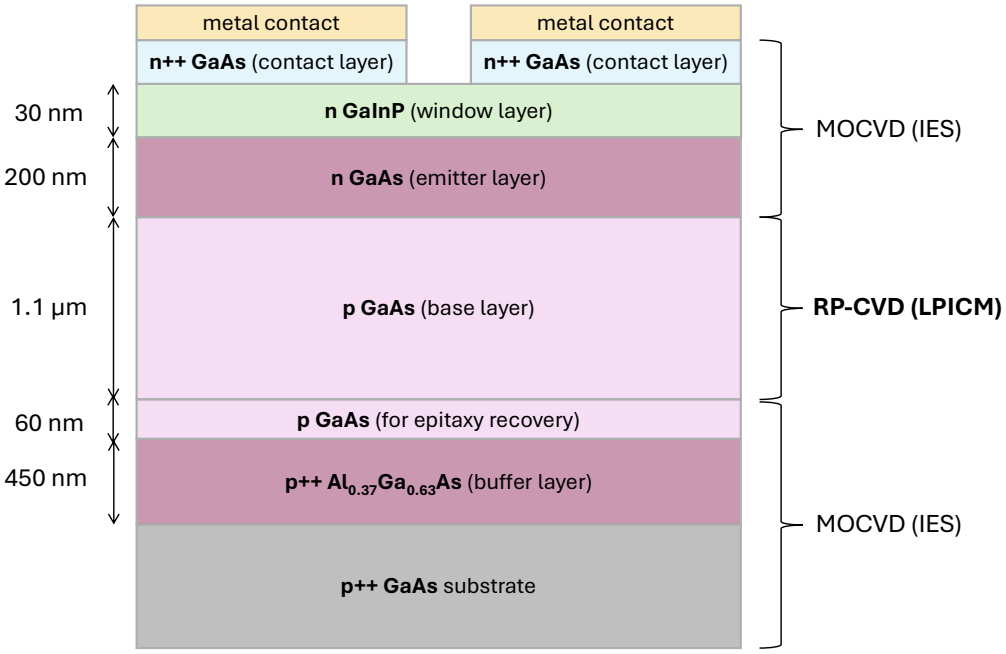

Figure 5.15. Configuration design of the first solar cell fabricated with RP-CVD GaAs grown with TMGa as absorber.

Figure 5.16 shows one of the obtained solar cells observed through an optical microscope. The area of the devices is 3x3 mm^2, defined within the busbar surrounding the device. The homogeneity of the layers discussed above is therefore more than sufficient on this small surface. There is approximately a 100 µm distance between the outside of the bus and the edge of the mesa (see **Appendix C**). In the image, we notice a few minor defects on the active layer, which may have resulted from the transport back-and-forth between Paris and Madrid and the epitaxial regrowth processes. The defects observed on the metallic contacts are likely due to scratches from handling the cells with tweezers or variations in the quality of the lithography and the metal evaporation process.

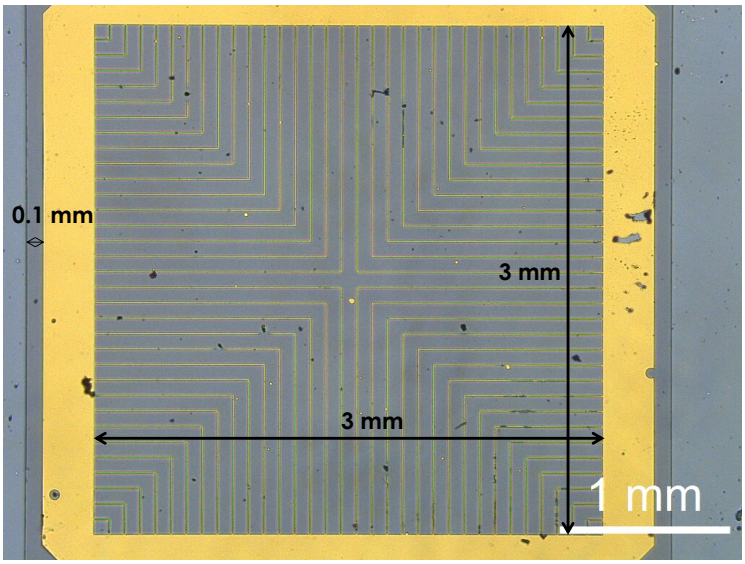

Figure 5.16. Optical microscope image of one of the obtained solar cell.

2. Evaluation of the PV performance

a. I-V characteristics

Figure 5.17 presents the I-V characteristics under illumination and in the dark for the 14 fabricated solar cells. The cells are functional, which is an encouraging result for a first trial; however, the open-circuit voltage (V_{oc}) is quite low for a GaAs cell, for which the typical Voc is usually around 1 V (see **Appendix C**). It should be noted that the measurements were taken under a lamp that did not reach the standard 1 sun (1000 W/m^2) typically used for solar simulations (like the one performed in **Appendix C**). The dark I-V curves suggest the presence of different recombination mechanisms in the base, which could potentially be due to carbon diffusion at the interface or other issues beyond doping concern.

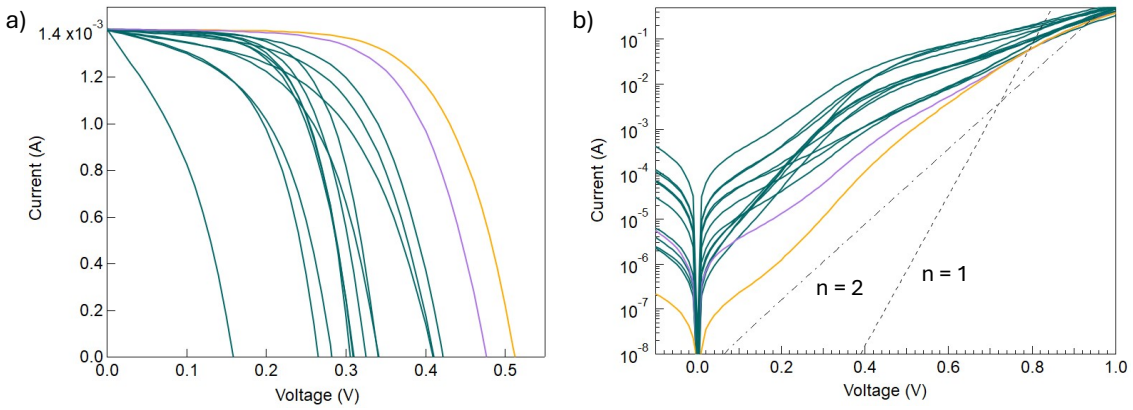

Figure 5.17. *a) Light and b) dark I-V curves of the 1st solar cell made of RP-CVD GaAs absorber.*

Among the tested cells, two stand out in terms of performance, they are presented by the yellow and violet curves in **Figure 5.17**. We remeasured the best-performing solar cell (yellow curve) at IPVF using a well-calibrated setup under standard illumination conditions (1000 W/m^2). The resulting curve is shown in **Figure 5.18**.

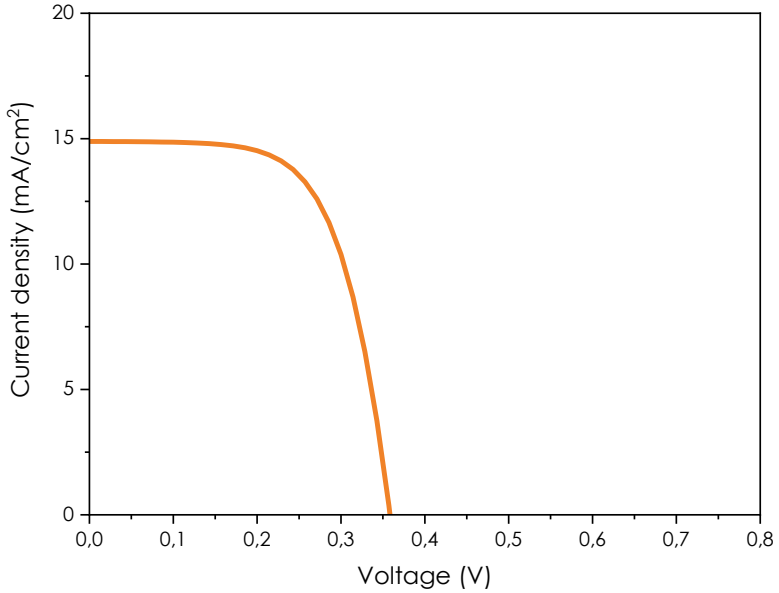

Figure 5.18. *Light I-V curve for the best solar cell grown with TMGa.*

The detailed performance parameters of this cell are provided in **Table 5.2**. While the efficiency was not groundbreaking (around 3%), this outcome was anticipated as high doping levels can result in an decreased open-circuit voltage (Voc) and reduced fill factor (FF), which is precisely what we observed here. However, it was already a significant milestone to see a first functional cell developed using this entirely new growth process.

Jsc	14.9 mA/cm²
Voc	0.35 V
FF	65 %
Eff	3.4 %

Table 5.2. *Performance of the best solar cell grown with TMGa.*

b. External quantum efficiency

Let's try to understand the origin of these relatively low performances, particularly to verify that it indeed stems from the absorber layer and not from another component of the cell, which could otherwise obscure the potentially higher performance of our RF CVD absorber layer. To investigate this, we analyse the quantum efficiency spectra, shown in **Figure 5.19. a)**. Quantum efficiency is the ratio of the number of carriers collected by the solar cell to the number of photons of a given energy incident on the solar cell. We measure both the internal quantum efficiency (IQE) and the external quantum efficiency (EQE). The IQE provides a measure unaffected by losses while the EQE accounts for all photons incident on the cell, including those lost to reflection and transmission, thus typically yielding lower values compared to the IQE. IQE values combined with lower EQE values, as is the case in our cells, suggest that while the absorber material is effective at generating charge carriers, there are significant optical losses that reduce the overall efficiency of the cell.

When we compare our EQE curve to the one of a high-efficiency solar cell fabricated by MBE at IPVF shown in **Appendix C**, we observe our overall EQE is around 60%, compared to 70%. This difference is partly due to reflections, which is expected as we do not have anti-reflective coating and, additionally, the fact that the carrier diffusion length may not be optimal. We also have a lower slope at low photon energies which supports that the blue response is slightly reduced probably due to front surface recombination. Moreover, we can also observe a degradation in the QE at the tail end of the spectrum at higher wavelengths (above 700 nm). This degradation could correspond to rear surface recombination, reduced absorption in this part of the spectrum, or low diffusion lengths. Finally, the QE drops to zero after 900 nm because photons with energy below the band gap cannot generate electron-hole pairs. Additionally, we examined the reflectance (RFL) spectrum, which represents the fraction of light that is reflected by the surface of the solar cell. Notably, there is higher reflectance (~ 40%) at the higher energy side of the spectrum (300 – 400 nm) followed by an average reflectance of 30% for the rest of the spectrum. This is attributed to the front surface of the cell and is expected, given that we did not apply an anti-reflection coating to our cells. The absence of this coating yields an increased reflection of photons, which could otherwise contribute to improving the overall efficiency of the solar cell.

To further analyze the data, we applied fits to the IQE, EQE, and RFL curves. When considering a collection rate of 0.7 for the RP-CVD GaAs absorber layer (**Figure 5.19. b)**), we obtained a good fit of the QE curves. Although a collection rate of 0.7 is relatively low, it is expected given the high doping level of the absorber. From this analysis, we conclude that the low performance originates from the material itself rather than to the interface. The recombination velocity at the interface was set to zero in the simulation.

a)

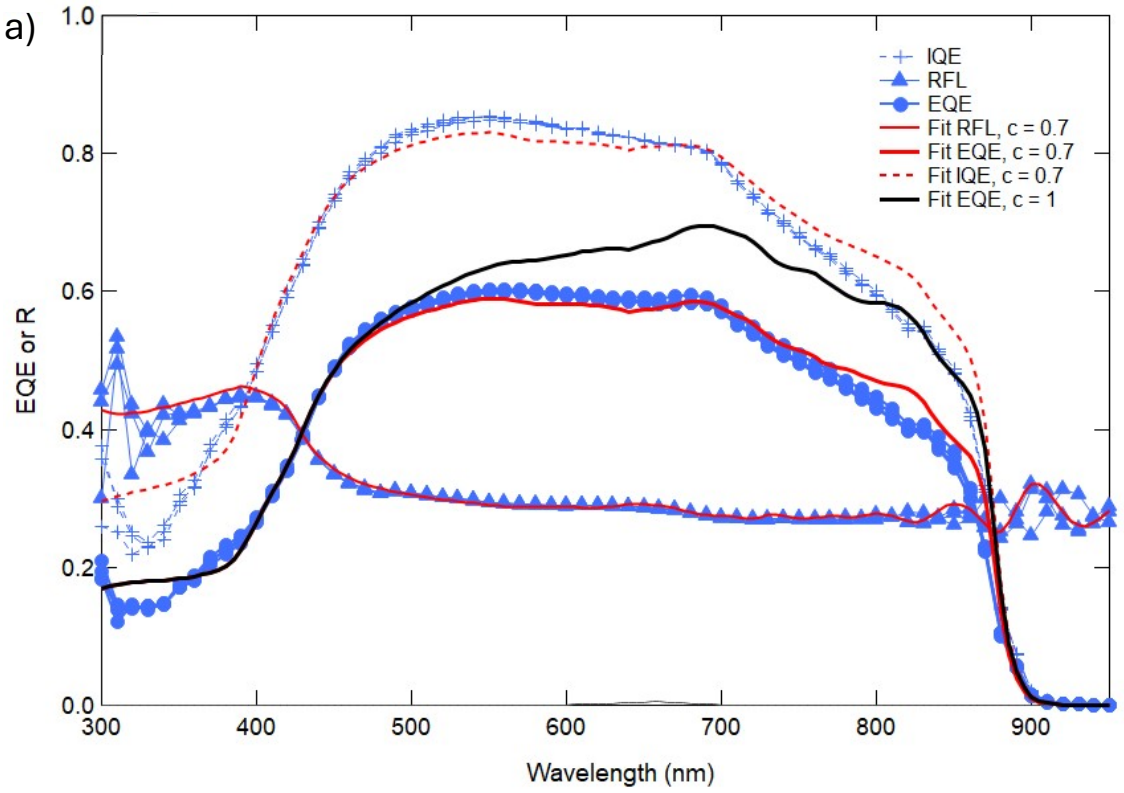

b)

Material	Thickness	Collection rate
GaInP	34 nm	0.25
n-GaAs	200 nm	1
p-GaAs	1100 nm	**0.7**
AlGaAs	450 nm	0
GaAs	--	0

Figure 5.19. *a) IQE, EQE and RFL spectrum of the obtained solar cells and b) fitting parameters for the different layers.*

These results indicate that while the cells are functional, further optimization is necessary to achieve higher solar performance. Decreasing the doping level of the absorber layer will be crucial for improving the efficiency of the solar cells. Unfortunately, due to maintenance of the MBE and MOVPE systems at IPVF and III-V Lab, respectively, it was difficult to produce additional solar cells.

II. TEGa-based solar cells

At the very end of the thesis journey, we had the opportunity to integrate our lightly doped GaAs layers grown using TEGa into a solar cell in collaboration with IES in Madrid, as carried out with the TMGa precursor.

1. Design of the solar cell device

We aimed to replicate the same stack as the one used for the solar cell based on TMGa. However, due to experimental challenges related to the substrate temperature, we obtained a thinner GaAs base layer, 700 nm instead of 1 µm. The final stack is presented in **Figure 5.20**.

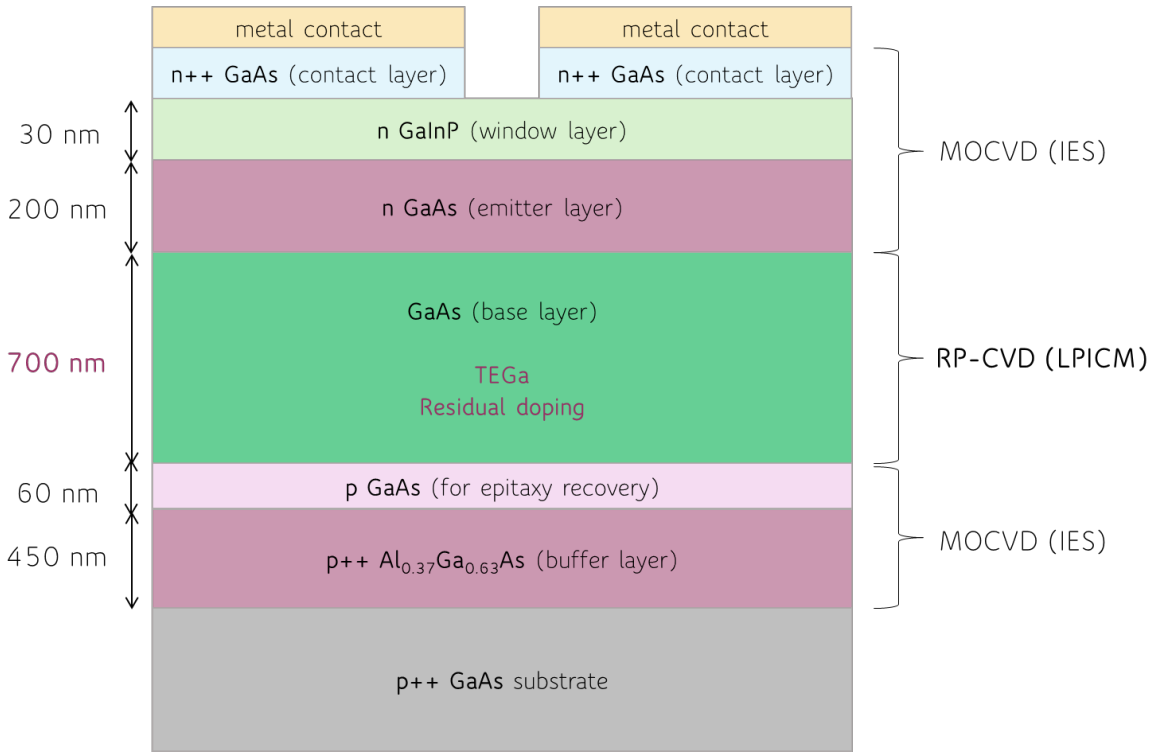

Figure 5.20. *Configuration design of the first solar cell fabricated with RP-CVD GaAs grown with TEGa as absorber.*

2. Evaluation of the PV performance

a. I-V characteristics

The I-V curve and the corresponding performance parameters of the best-performing solar cell are shown in **Figure 5.21** and **Table 5.3**. Remarkably, the efficiency has tripled with TEGa, compared to the solar cell grown using TMGa. This improvement is primarily due to significant increases in both the open-circuit voltage (Voc) and the fill factor (FF), indicating that the optimized base doping level effectively reduces losses. Moreover, despite a thinner base for this solar cell, we obtained a slightly higher Jsc than for the cells grown using TMGa,

demonstrating a better collection efficiency with TEGa. Additionally, the different cells obtained with TEGa exhibited much greater uniformity in performance, highlighting significantly improved reproducibility compared to the TMGa-based cells.

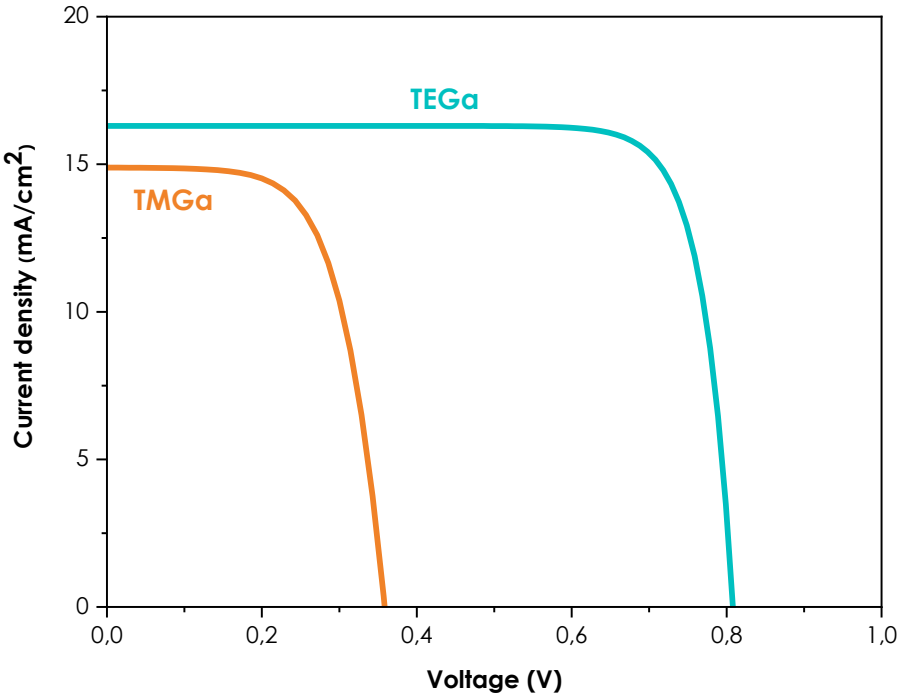

Figure 5.21. *Light I-V curve for the best solar cell grown with TEGa without ARC (compared with TMGa one).*

Jsc	16.3 mA/cm²
Voc	0.79 V
FF	83 %
Eff	10.8 %

Table 5.3. *Performance of the best solar cell grown with TEGa (without ARC).*

b. Anti-reflection coating (ARC) addition

To enhance further efficiency, particularly to improve the short-circuit current density (Jsc), we incorporated an anti-reflection coating (ARC) to mitigate reflection losses, as suggested by its name. An ARC consists of one or a combination of thin layers of dielectric materials, with a specially chosen thickness and refractive index so that interference effects in the coating cause the wave reflected from the anti-reflection coating top surface to be out of phase with the wave reflected from the semiconductor surfaces. These out-of-phase reflected waves destructively interfere with one another, resulting in zero net reflected energy. To achieve optimal performance, we simulated reflectivity by varying the materials and their thicknesses to reach specific optical indices. Based on the simulation results shown in **Figure 5.22**, the selected layer combination was a titanium dioxide (TiO_2) layer of 55 nm deposited by sputtering and a magnesium fluoride

(MgF_2) layer of 105 nm deposited by evaporation. **Figure 5.23** shows a photograph of the cells after the application of this anti-reflection coating.

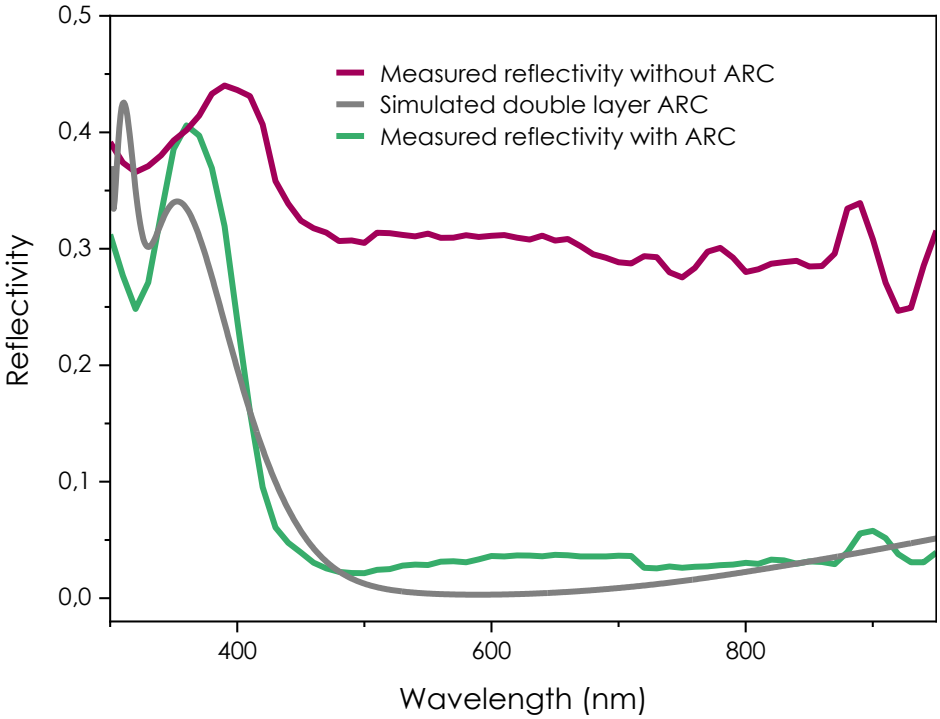

Figure 5.22. *Reflectivity spectra for the ARC stack layer design.*

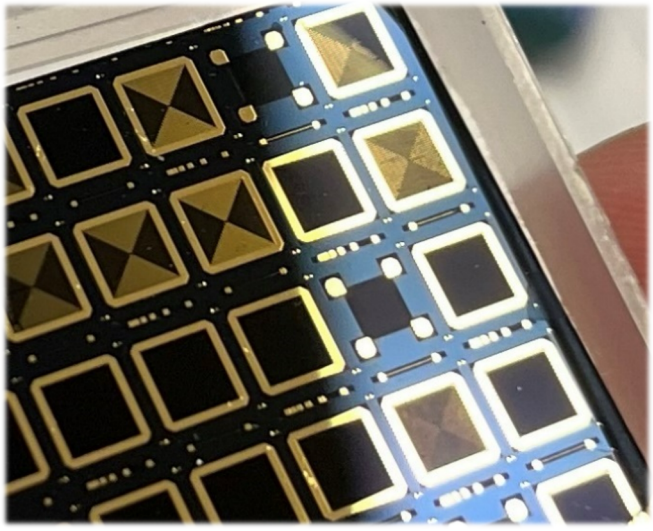

Figure 5.23. *Photograph of the cells grown with TEGa after ARC deposition.*

The results obtained after applying this ARC are highly positive, as they boosted the cell efficiency from 10.8% to 15.5%. This improvement is primarily due to a significant increase in the short-circuit current density, clearly visible in the I-V curve in **Figure 5.24**, which is directly linked to the reduction of reflection losses. The detailed performance parameters are provided in **Table 5.4**.

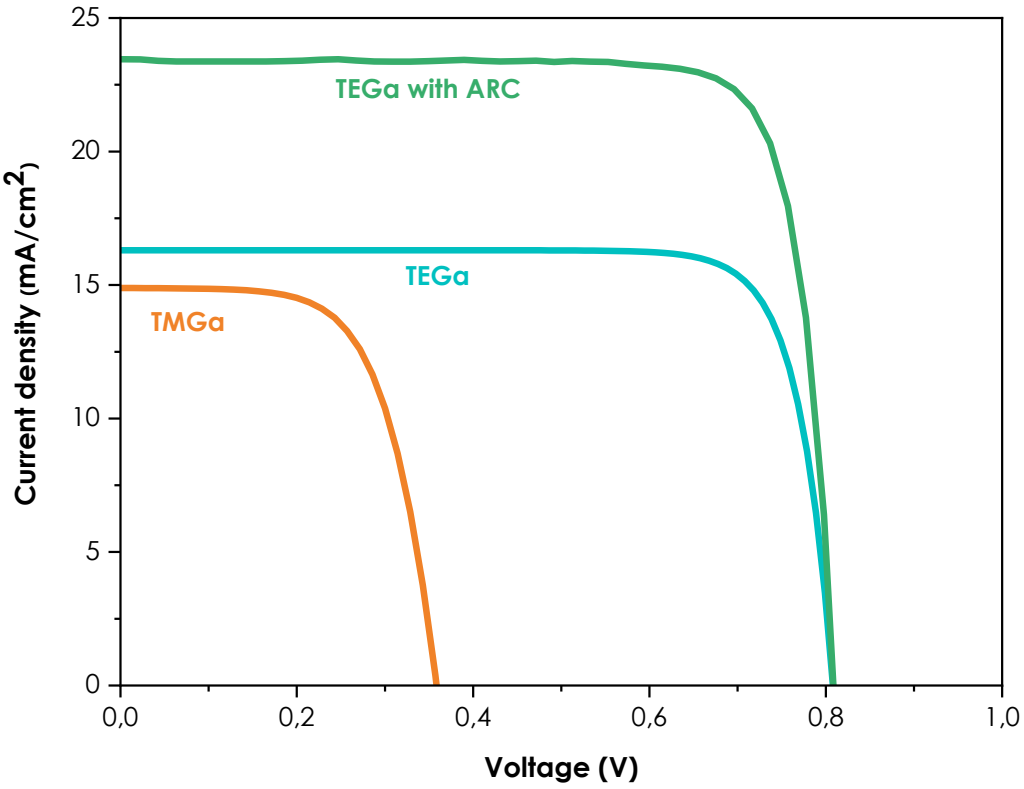

Figure 5.24. *Light I-V curve for the best solar cell grown with TEGa with ARC (compared with TEGa without ARC and TMGa).*

Jsc	23.5 mA/cm²
Voc	0.81 V
FF	82 %
Eff	15.5 %

Table 5.4. *Performance of the best solar cell grown with TEGa with ARC.*

This work marks the beginning of RP-CVD-based solar cells, further optimization will be required to achieve an ideal base thickness and improve interface quality. Nevertheless, we successfully fabricated our first GaAs-based solar cells grown using the RP-CVD process. The initial trial employed GaAs grown with TMGa, serving both as the gallium precursor and dopant source. While this approach produced a functional cell, its performance was limited by an excessively high doping level in the base. In contrast, the second trial demonstrated a significant breakthrough: by using TEGa to grow low-doped GaAs, we achieved a substantial improvement in device performance, with higher open-circuit voltage and fill factor. Moreover, by adding and anti-reflection coating, the best cell reached an efficiency of 15.5%. These results definitively establish RP-CVD as a promising and viable method for the fabrication of low-cost III-V solar cells.

Chapter 5. Summary

This chapter investigated the impact of various process parameters on the p-type doping of our GaAs films. We aimed to optimize the doping to reach the target value suitable for use as an absorber in a solar cell, making our first device fabricated by RP-CVD. The solar performances of this device have been presented.

The preliminary study on the origin of doping through cross-characterization using ECV and SIMS allowed us to conclude that the p-type doping originates entirely from the carbon incorporated via the byproducts of TMGa decomposition and that all the incorporated carbon atoms act as an active dopant. By comparing RP-CVD to MOCVD, we demonstrated that the use of plasma significantly reduces the doping level due to the etching effect of atomic hydrogen generated in the plasma source. It also allows to reduce hydrogen incorporation. This allows us to control doping level in a range of 10^{18} – 10^{20} cm^{-3} with TMGa. Despite this improvement, the doping level remains too high compared to the desired 10^{17} cm^{-3} level for an absorber layer in a III-V solar cell.

The optimization study of doping using TMGa highlighted the importance of deposition conditions such as temperature, plasma power, and deposition pressure. We observed that lower deposition temperatures, combined with optimized plasma power and pressure, can reduce the doping level to 1×10^{18} cm^{-3} with a mobility of 171 $cm^2/V.s$ as expected for this doping level. However, these optimizations are still not sufficient to achieve doping levels low enough for high-efficiency solar cell applications.

Replacing TMGa with TEGa has proven to be an effective method for drastically reducing the doping levels in our layers. ECV measurements, confirmed by Hall effect, have shown that the use of TEGa allows for a reduction in doping to residual n-type levels below 1×10^{16} cm^{-3}. This approach has achieved a film quality comparable to that of GaAs made with TMGa, characterized by a wafer-grade film quality with a FWHM of the 004 peak rocking curve matching that of the GaAs substrate (~ 0.008°).

Thanks to our collaboration with IES Madrid, we fabricated the first solar cell incorporating an absorber layer of GaAs grown by RP-CVD. Solar performance tests demonstrated that despite the high doping level of the layer grown with TMGa the device is operational but with a low efficiency of 3%. By using TEGa, we demonstrated that a properly doped GaAs layer grown by RP-CVD allows to increase drastically the efficiency. Following the application of an anti-reflection coating (ARC), this approach yielded a good final efficiency of **15.5%**.

General conclusion

This thesis has focused on the study of the growth of III-V semiconductors using a remote plasma chemical vapor deposition process, RP-CVD, with the aim of reducing manufacturing costs for high-efficiency III-V solar cells. This reactor, operating at an intermediate pressure between conventional MBE and MOCVD techniques, has introduced new possibilities, especially through the utilization of a plasma that enables: i) in-situ substrate cleaning, ii) the synthesis of a SiN interface, allowing the direct growth of GaN on c-Si, and iii) the enhanced production of atomic hydrogen, which helps in reducing C and O impurities incorporation in the films. To demonstrate the potential of this approach for producing layers of high structural, morphological, and electronic quality, we focused our efforts on optimising the growth of gallium nitride (GaN) and gallium arsenide (GaAs) films.

In the introduction chapter, **Chapter 1**, we highlighted the highly attractive properties of these two compound semiconductors and the challenges of integrating them onto silicon, emphasizing the significance of their development for fabricating high-performance III-V/c-Si tandem cells, which are of high interest for the energy transition.

In **Chapter 2**, we presented the custom-built RP-CVD reactor, carefully designed to avoid the detrimental effects of ion bombardment, while showcasing its advantages in terms of low-pressure, low-temperature operation and surface treatment capabilities. The plasma ability to efficiently dissociate group V precursors, N_2 as well as hydrogen, was also emphasized, through the identification of the E-H transition of the ICP discharge via optical emission spectroscopy.

Chapter 3 explored the feasibility of GaN growth using RP-CVD as a proof of concept to validate the effective operation of our reactor. We demonstrated that crystalline GaN can indeed be produced with this process by examining growth on various substrates, particularly sapphire and silicon for which the same FWHM values of 0.3° was obtained for the 0002 X-ray diffraction peak. On sapphire, epitaxy is maintained for the first 5 nanometers before breaking down, while on c-Si, the GaN film is polycrystalline but highly c-axis oriented, nearly stoichiometric throughout its depth, and free of oxygen. We showed that efficient H_2 dissociation reduces carbon contamination in the layer from 11.5% to 8% when RF power is increased from 150 to 300 W, without altering the Ga/N ratio. We revealed the challenges inherent to GaN heteroepitaxial growth due to differences in lattice parameters and thermal expansion coefficients, as well as strategies to improve interfaces through plasma treatments such as i) surface nitridation of c-Si to prevent mixing of Si and Ga (a phenomenon reported as *meltback etching* in literature) and ii) formation of an AlN layer on sapphire upon a N_2 plasma treatment. Notably, we demonstrated the significant impact of an ultrathin (1.7 nm) SiN barrier in enhancing the GaN/c-Si interface by preventing gallium and silicon intermixing, resulting in a clean and sharp interface. The use of this SiN barrier layer led to a reduction in surface roughness (from 7 nm to 1.7 nm) and a decrease in the FWHM of the 0002 peak, from 0.19° to 0.10° for GaN thin films ~ 0.5 µm thick.

In **Chapter 4**, we discussed the results obtained for GaAs thin film growth. The first part highlighted the capability of RP-CVD to produce wafer-grade quality homoepitaxial GaAs layers

exhibiting the following features: FWHM of the 004 peak rocking curve of 0.004°, low surface roughness of 0.2 nm, high mobility of 172 $cm^2.V^{-1}.s^{-1}$ for a p-type doping of 1 x 10^{18} cm^{-3}, all at a growth rate of 3 µm/h. The composition remained uniform in depth with a consistent 1:1 Ga to As ratio and no detectable oxygen or carbon contamination. This success laid the foundation for more complex investigations on a more cost-effective substrate, namely silicon. To overcome the thermal and crystallographic mismatches, the use of virtual substrates composed of c-Si with an ultrathin Ge layer emerged as a promising solution for heteroepitaxial growth of GaAs on Si. Although a significant dislocation density remains, decreasing from 2–3 × 10^9 cm^{-2} near the Ge interface to 3 × 10^8 cm^{-2} towards the top surface of the GaAs layer, the resulting film has still a monocrystalline structure (FWHM of the 004 peak rocking curve = 0.098°) with a sharp PL peak, demonstrating the viability of this approach and its potential with further optimisation.

Chapter 5 delved into the optimization of doping for the effective integration of RP-CVD grown GaAs into III-V solar cells. We first identified the origin of doping, due to carbon incorporation resulting from TMGa decomposition products, and explored the role of plasma in reducing the doping level by etching carbon species and minimize H incorporation in the layer. Next, thanks to parametric studies, we demonstrate the important role of plasma conditions, growth temperature and pressure on dopant concentration and charge carrier mobility. This allowed us to define a particular set of parameters required to control doping level within a range of 10^{18} to 10^{20} cm^{-3} with mobilities in line with the state-of-the-art literature. Additionally, we showed that replacing TMGa with TEGa is an effective strategy to drastically reduce doping levels to residual n-type values below 1 × 10^{16} cm^{-3} while maintaining wafer-grade film quality. Ultimately, we successfully fabricated our first functional solar cells featuring a GaAs base layer grown by RP-CVD in collaboration with IES in Madrid. Using TMGa resulted in an initial efficiency of approximately 3%, limited by high base doping. By switching to TEGa, we achieved a more than tripled efficiency of 10.8%, which was further enhanced to 15.5% with the application of an anti-reflection coating (ARC).

The findings of this thesis pave the way for a growth technique that aligns with low-cost production of III-V thin films, facilitated by reduced gas consumption from the low-pressure operation of RP-CVD (~ 0.5 mbar). The adoption of this method by the industry could lead to more affordable production of III-V/Si tandem solar cells, thereby enabling this technology to gain a larger share in the photovoltaic market.

Perspectives

This project is still in its early stages, being the first PhD research conducted using this RP-CVD reactor. There remains much to be explored, and the development potential for the reactor is enormous, especially since we have the option to add multiple additional gas lines and organometallic canisters. Here, I will outline some short-term research directions that we have identified based on the findings of this thesis.

For GaN growth, future research should focus on demonstrating the benefits of the AlN interface layer grown on sapphire through the simple N_2 plasma treatment. Additionally, increasing the hydrogen content in the plasma could be explored to better remove the carbon, which is present in significant amounts (8%), thereby improving the quality of GaN films based on insights gained from GaAs growth. We also aim to develop devices using the GaN layers produced, particularly for photovoltaic applications, where GaN could serve as an electron transport layer in solar cell[230].

Regarding GaAs, future work should focus on the growth on virtual substrates by improving the PECVD-grown Ge layer, particularly by optimizing its growth conditions to drastically reduce dislocation density (as investigated in Yves Bois' thesis). Continued optimization of the solar cells is crucial to demonstrate that by achieving the optimal base thickness and improving interface quality, even higher efficiencies can be reached. Additionally, we could explore growing other layers of the solar cell directly in the RP-CVD reactor, starting with the BSF layer, given that we are already capable of producing p++ GaAs.

Finally, the addition of extra gas lines will undoubtedly unlock new possibilities, both in terms of expanding the range of compounds we can grow and enabling the introduction of different dopants (e.g. silane for n-type doping), allowing us to achieve all the doping profiles needed for our solar PV applications.

Appendix A.
Characterization techniques

In this appendix we provide some details on the various characterization techniques used in this the thesis.

1) Spectroscopic ellipsometry (SE)

Spectroscopic ellipsometry (SE) was employed to determine the thicknesses and optical properties of the deposited layers. The measurements were performed using a Horiba Jobin Yvon UVISEL 2 and, subsequently, the data were processed using the DeltaPsi2© software at IPVF or LPICM.

2) X-ray diffraction (XRD)

To analyse the microstructure of the films, we used X-ray diffraction (XRD). For Bragg-Brentano diffraction we used a XRD Empyrean system from Panalytical [CuKα radiation λ = 1.5406 Å] at IPVF.
We also worked at the C2N PANAM platform to further analyse the crystal structure of the films. In particular, we used a Panalytical X'pert Pro diffractometer for out-of-plane ω–2θ scans and a Rigaku SmartLab diffractometer equipped with a rotating anode for in-plane measurements and pole figure.

3) Scanning electron microscopy (SEM)

To gain information on its morphological features, we used a Scanning Electron Microscope (SEM) – Merlin Compact from Zeiss with an electron high tension (EHT) of 15 kV at IPVF.

4) Atomic force microscopy (AFM)

To analyse the topography of the films we used an Atomic Force Microscope (AFM) PicoScan 3000 (resolution XY: 1nm, Z < 1nm) from Agilent at IPVF. It is particularly used to determine the top-surface roughness of films.

5) Transmission electron microscopy (TEM)

Prior to measurements, the surface of the investigated samples was protected by carbon and platinum layers and thin lamellae were prepared using a focused ion beam technique (dual-beam ThermoFisher SCIOS microscope) at C2N using the funding of the French national network RENATECH. The TEM investigation was performed using a FEI ThermoFisher Scientific Titan-Themis G3 electron microscope at LPICM, operating at an acceleration voltage of 300 kV. This microscope is equipped with a CMOS (Ceta 16M) and a direct detection camera (Falcon-2) for both TEM and high-resolution TEM (HRTEM) imaging modes. Additional analyses of the structure were achieved by selected-area electron diffraction (SAED) using a small aperture of 10 µm and a camera length of 37 cm. Moreover, the TEM has bright-field (BF) and high-angle annular dark-field (HAADF) detectors for scanning-TEM (STEM) imaging mode. Chemical analyses were conducted using a silicon drift detector (SDD) from Oxford instruments (XMAX 80T) for energy dispersive X-rays (EDX) spectroscopy.

6) Ion beam analyses (NRA and RBS)

As far as the chemical composition is concerned, ion beam analyses (IBA) using a 4MV Van De Graff accelerator (HVEE, KN4000) at ICube in Strasbourg were performed. Rutherford Backscattering Spectrometry (RBS) was used to determine the gallium content. RBS experiments were carried out with a 2 MeV alpha particle beam (He+) with a scattering angle of 160°. To determine the concentration of the low-Z elements (nitrogen, carbon and oxygen impurities), Nuclear Reaction Analysis (NRA) were performed using a 900 keV deuteron beam (H2+) with a scattering angle of 150°. Under these conditions, light elements (C, N and O) were detected simultaneously in a single measurement.

7) X-ray photoelectron spectroscopy (XPS)

Chemical in-depth composition profiles were obtained by X-ray photoelectron spectroscopy (XPS) at Institut Lavoisier (ILV) in Versailles. We used a Thermo Scientific K-Alpha+ spectrometer equipped with a monochromated Al-Kα x-ray source for excitation at 1486.6 eV and using an X-ray spot size of 400 µm. Calibration of the spectrometer was done using Cu and Au samples following the ASTM-E-902-94 protocol. In complement to surface analyses, in-depth profiling was carried out using a monoatomic ion gun (Ar+) with an energy of 1000 eV, a 10 mA current intensity, and an ion gun orientation of 30° from the sample surface. The Thermo Scientific™ Avantage software was used for the XPS data treatment. Quantification was achieved with a Shirley background subtraction and relative sensitivity factors (RSF) from the constructor library.

8) Secondary ion mass spectrometry (SIMS)

In-depth compositional analysis were performed using the SIMS IMS7f from CAMECA at the GEMaC laboratory of Institut Lavoisier (ILV) in Versailles to determine the impurities concentrations. This was conducted with a cesium (Cs^+) primary ion beam (E_p = 10 keV / I_p = 20 nA / scanned area = (150 × 150) µm) and detection of negative secondary ions. The analyzed area had a diameter of 33 µm, centered on the sputtering crater, with a low mass resolution of M/DM = 400. Data quantification was achieved for the depth by measuring the sputtering crater post-analysis with a contact profilometer (Dektak 8 – Bruker) and for the concentrations using Relative Sensitivity Factor (RSF) calibration constants derived from GaAs samples implanted with known doses of 1H and 12C. A reduction in the scanned area after 3000 seconds of analysis demonstrated that the "atmospheric" signals for 1H, 12C, and 16O remained constant during this period, confirming that these signals originate solely from the SIMS residual vacuum contribution and represent the detection limit for these elements.

9) Raman spectroscopy

The Raman spectra were acquired using a Jobin Yvon Horiba LabRAM HR Raman system with a 532 nm green laser excitation, a Synapse camera, a CCD detector and grating 1800 gr/mm. The laser was focused on the sample surface using different Olympus microscope objectives.

10) Photoluminescence (PL)

To characterize the electronic properties, we used first a Jobin Yvon Horiba LabRAM HR Raman system to perform photoluminescence (PL) measurements at room temperature using a 532 nm green laser excitation, a Synapse camera, a CCD detector and grating 1800 gr/mm. The laser was focused on the sample surface to a spot diameter of around 2µm with an Olympus 10x microscope objective. Photoluminescence mappings were conducted using a Hyperspectral system from Photon etc., with LEDs set to 525 nm at a power density of 24.5 mW/cm^2 and with an acquisition time of 10 seconds.

11) Cathodoluminescence (CL)

Cathodoluminescence (CL) measurements were carried out using the Attolight Allalin 4027 Chronos quantitative cathodoluminescence microscope, located at the C2N-CNRS laboratory (Palaiseau, France). This setup allows hyperspectral mapping with nanoscale spatial resolution and the ability to perform time-resolved CL measurements. A comprehensive description of the setup can be found in the PhD theses of Hung-Ling Chen and Thomas Bidaud[231,232]. For our

acquisitions, we used an acceleration voltage of 6 kV, a gun lens current of 1.2 A, and a 100 µm aperture. By fitting our average CL spectra with the generalized Planck's law, we are able to assess material doping. Indeed, the spectral shift and broadening induced by shallow dopant states and band filling serve as indicators of doping[233]. We fit the entire spectral line shape using generalized Planck's law along with refined absorption models to extract information on bandgap narrowing and the band tail effects.

12) Hall effect

Hall effect measurements at room temperature were performed to determine doping levels and mobilities with the AMP55T system from Ecopia, under a magnetic excitation field intensity of B = 0.56 T, and a current of 1 mA. To perform the measurement, indium contacts were deposited at the four corners of a 1 cm x 1 cm square sample.

13) Electrochemical capacitance voltage (ECV)

Electrochemical Capacitance Voltage (ECV) technique was used to obtain dopant profiles using the Wafer Profiler CVP21 from WEP Control.

14) Time-resolved photoluminescence (TRPL)

Time-resolved photoluminescence (TRPL) measurements were carried out using a 532 nm pulsed laser, with simulations performed at varying power densities.

15) Solar simulations (I-V and EQE)

Solar simulations were performed at IES (Madrid, Spain) using Newport instruments: the solar simulator ORIEL SOL2A for I-V curves with a Xe lamp and the IQE-AC-XEN-EXT1 for quantum efficiency measurements.

Appendix B.
Supplementary TEM images

Figure **B.1** shows the HAADF-STEM cross-section image of the GaN-on-Si sample grown (a) without and (b) with the SiN barrier layer. We observe small grains in the depth of the GaN film when no SiN barrier is used while we have columnar growth when using SiN.

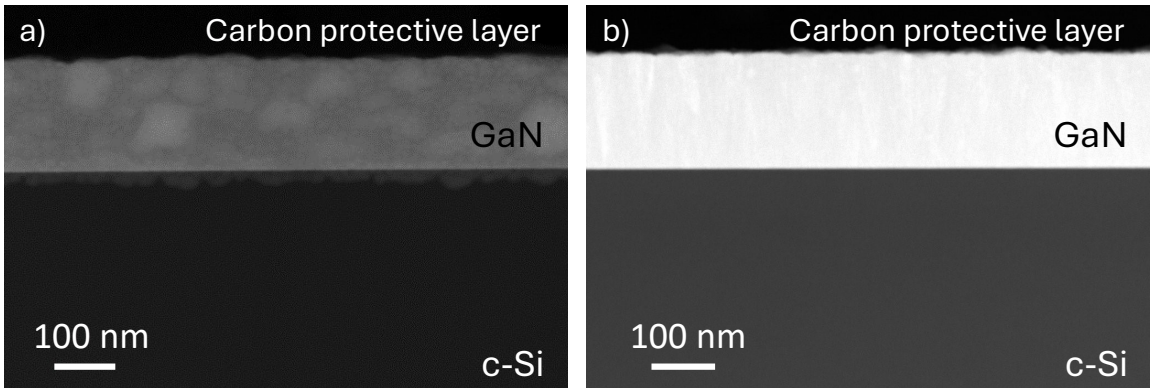

Figure B.1. *Cross-sectional HAADF-STEM image of GaN-on-Si (a) without and (b) with SiN barrier layer.*

Appendix C.
MBE-grown solar cell

To establish a baseline for GaAs solar cells, we used the IPVF facilities to produce devices via MBE. This activity was carried out during the first year of the thesis, while waiting for the RP-CVD reactor to be operational. The idea was also to use the MBE reactor to produce solar cells with the absorber layer produced by RP-CVD. Unfortunately, a direct comparison between MBE cells and MBE plus RP-CVD cells could not be carried out, as the MBE reactor also experienced an extended maintenance period. Consequently, our first solar cell was produced using the MOVPE reactor at IES-UPM in Madrid (Spain) for the layers surrounding the absorber (**Chapter 4**, part **C**). Nevertheless, we detail here the cell fabrication process we use at IPVF, which is close from the one of IES-UPM laboratory and present the results from the best-performing batch to illustrate the complete solar cell fabrication workflow, and give an idea of the performance of a cell manufactured entirely with a conventional MBE process.

A. MBE solar cell fabrication

The growth of the epitaxial layer stack is conducted using a C21 MBE system from Riber (**Figure C.1**). The chamber is degassed by heating at 400°C and a 2-inch p-type GaAs (100) wafer doped with Zn ($\rho \approx 0.008$ Ohm.cm) is introduced into the MBE chamber.

Figure C.1. *Photo of the MBE system C21 of Riber.*

The substrate holder is rotated (~ 10 rpm), and when the temperature reaches 650°C the deoxidation process can start, monitored by tracking the in-situ Reflection High-Energy Electron Diffraction (RHEED) pattern. The temperature is then lowered to 550°C. The deposition of the different layers of the cell architecture is subsequently performed, with each layer temperature, dopants, and doping levels specific to the respective compounds from **Figure C.2**. The solar architecture of this MBE-grown cell is very similar to the one grown in **Chapter 5**.

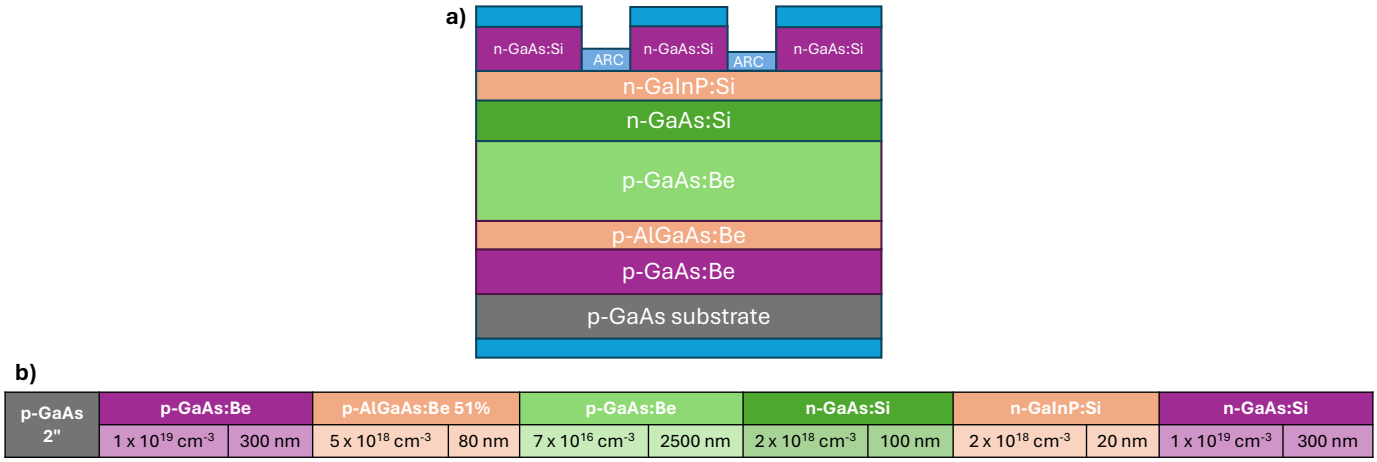

p-GaAs 2"	p-GaAs:Be		p-AlGaAs:Be 51%		p-GaAs:Be		n-GaAs:Si		n-GaInP:Si		n-GaAs:Si	
	1×10^{19} cm^{-3}	300 nm	5×10^{18} cm^{-3}	80 nm	7×10^{16} cm^{-3}	2500 nm	2×10^{18} cm^{-3}	100 nm	2×10^{18} cm^{-3}	20 nm	1×10^{19} cm^{-3}	300 nm

Figure C.2. *a) MBE-grown solar cell architecture and b) detailed composition of the solar cell layers stack.*

The various steps involved in fabricating the metallic contacts on the resulting epitaxial stack are outlined in **Figure C.3** and the process details for each of the post-MBE steps are compiled in the **Table C.1**.

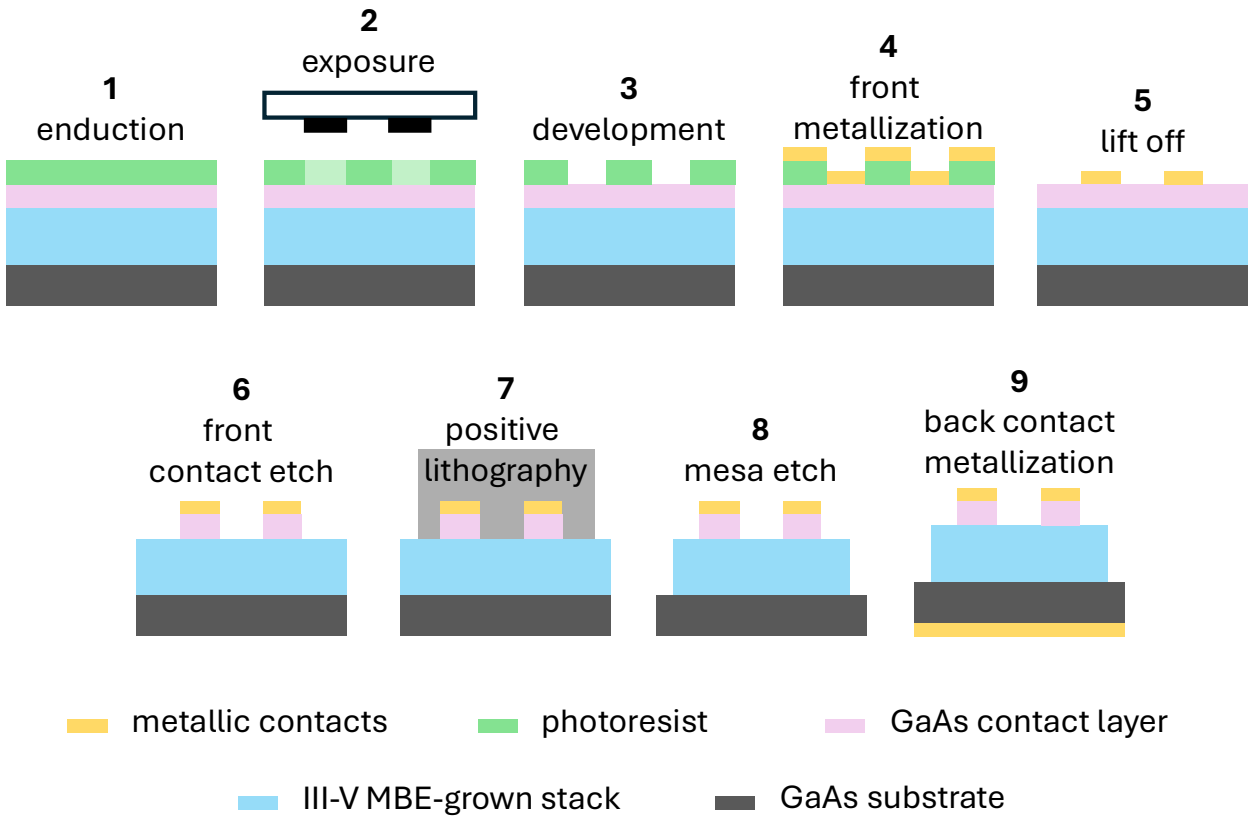

Figure C.3. *Process flow of solar cell fabrication from Amadeo Michaud thesis*[234].

At the end of this process, the solar cell performance was tested for the first time (**Figure C.4. a)**). Following this, an anti-reflection coating (ARC) was deposited to further enhance the performance (**Figure C.4. b)**). An ARC consists of one or a combination of thin layers of dielectric materials, with a specially chosen thickness so that interference effects in the coating cause the wave reflected from the anti-reflection coating top surface to be out of phase with the wave reflected from the semiconductor surfaces. These out-of-phase reflected waves destructively interfere with one another, resulting in zero net reflected energy. Our ARC consists of a stack of a TiO_2 film of 46 nm deposited by sputtering and a MgF_2 film of 98 nm deposited by evaporation.

	Process contact deposition on GaAs solar cells - Lise Watrin (IPVF)		
Désoxidation	Wash in running DI water		
	50% HCl for 1 min		
	Di water for 1 min		
Lithography	Photoresist	Photo resist AZ5214 / Az nLof 2070	
		Program 2 for 1.4µm	4000rpm/2000/30s
		Prebake 128°C for 1min	
	Optical exposure	Mask VCSEL III: Negative pattern	
		4s exposure under UV3 filter	Hard contact
		Post bake 128°C for 1min	
		Flood exposure 28s	
	Develop	MIF XXXX 1min10s	
Désoxidation	Wash in running DI water		
	50% HCl for 1 min		
	Di water for 1 min		
E-beam evaporation	Cover one side for p-contact	small corner	Max 2 days after litho
	Ni/Au/Ge/Au	5/10/60/200nm	
Metal lift-off	Acetone for 2-3min	Siringe-blow on the sample gently	Max 1 day after evap
	N2 dry		
Lithography	Photoresist	Spin coat AZ5214	
		Program 2 for 1.4µm	4000rpm/2000/30s
		Prebake for 1 min	
	Optical exposure	Mask VCSEL III:Positive	
		12s hard contact	
	Develop	MIF XXXX for 1min10s	
		Hard bake 1min @ 128°C	
Désoxidation	Wash in running DI water		
	50% HCl for 1 min		
	Di water for 1 min		
Mesa etching	Check dektak	1.3µm	
	(C6H8O7/H2O:1/1)/H2O2:5/1)	etch GaAs 216nm/min	A adapter en fonction du stack
	H3PO4/HCl 1:1	etch GaInP and AlInP 500nm/min	
	Check dektak	Until reaching back GaAs contact	
Desoxidation	Wash in running DI water		
	30% HCl for 1 min		
	Di water for 1 min		
E-beam evaporation	protect front side	photo resist	
	back side metalisation		
	Ti/Au	20/200nm	
Clean Photo resist	Acetone for 1 min		
Etching GaAs	HCl 50% for 1 min		
	DI water for 1 min		
	(C6H8O7/H2O:1/1)/H2O2:5/1)	etching rate 216nm/min	for 300nm 1min45s + Di water for 1min30
	Check dektak		

Table C.1. *Table of detailed parameters for each step of the process.*

B. MBE solar cell performance

Here, we examine the performance of the solar cells fabricated according to the stack shown in **Figure C.2**. The averaged I-V measurements across the 16 grown cells are presented in **Figure C.4**, with a) showing the performance before the application of the ARC and b) displaying the performance after the ARC deposition.

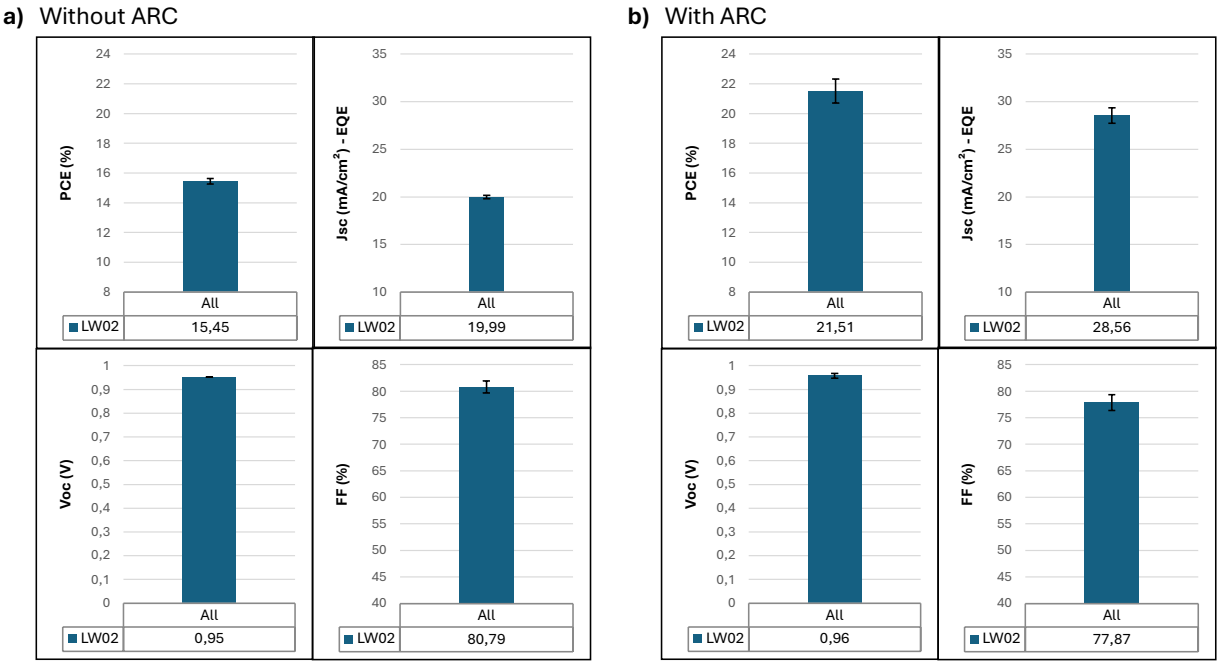

Figure C.4. *MBE-grown solar cell a) before ARC and b) after ARC, with error bars.*

Without the ARC, our cells achieve an average efficiency of nearly 16%, with a V_{oc} around 0.95 V and a J_{sc} of 19.99 mA/cm^2 resulting in a high fill factor of 80.79%. This is interesting to compare with the cells produced by RP-CVD in **Chapter 5**, where a Jsc of 16.3 mA/cm^2 was achieved with an absorber of only about 0.7 µm, which is not too bad. However, the Voc is much lower (~ 0.79 V) (**Table 5.3**). Now, focusing on our MBE cell, after applying the ARC, we observe a significant improvement in Jsc, increasing from an average of 19.99 mA/cm^2 to 28.56 mA/cm^2. As expected, the ARC minimizes reflections, which enhances the light absorption by the cell and subsequently boosts the current density. This additional process step, when applied to our RP-CVD grown solar cells in **Chapter 5**, resulted in a Jsc of 23.5 mA/cm^2 and an efficiency of 15.5% (**Table 5.4**).

Appendix D.
Optimization of homoepitaxial GaAs electronic properties

Figure **D.1** shows in a) the process conditions and in b) the electronic properties of the different samples. We are interested here in the level of doping as a function of mobility (measured by the Hall effect).

a)

	Temp °C	Power W	V/III	Pres mb
04-b	**500**	150	18	0.5
04-c	**550**	150	18	0.5
05-a	500	150	18 (**hyd**)	0.5
08-a	500	**0**	18	0.5
09-a	500	**200**	18	0.5
09-b	500	**250**	18	0.5
11	**550**	**200**	**30**	0.5
12	**500**	**300**	**60**	0.5
13	500	**100**	18	0.5
14-a	500	**150**	18	**0.2**
14-b	500	150	18	**0.8**
15	500	**100**	**30**	**0.5**

b)

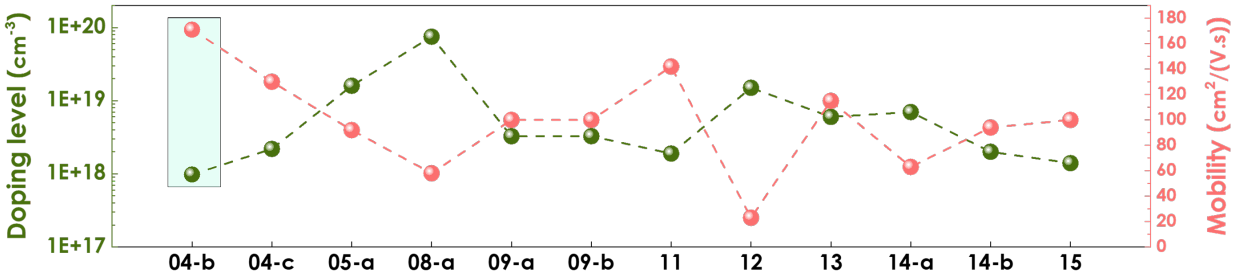

Figure D.1. *a) Table of process conditions and b) doping levels and mobilities for each sample of the optimization study.*

Appendix E.
Résumé long en français

Croissance de semi-conducteurs III-V élaborés par dépôt chimique en phase vapeur assisté par plasma déporté :
Vers une réduction des coûts d'industrialisation des cellules solaires

Introduction : objectif et approche

Les cellules solaires composées de semi-conducteurs III-V ont atteint le rendement le plus élevé parmi toutes les technologies actuellement disponibles, affichant une efficacité dépassant les 47% sous concentration[1]. Cependant, leur coût de production est environ cent fois supérieur à celui du silicium[2], la technologie qui domine le marché (95% en 2023) mais qui plafonne aujourd'hui à un rendement photovoltaïque d'environ 23%. Réduire le coût des III-V représenterait une avancée majeure vers l'accroissement de la part du solaire dans le mix énergétique. En effet, combiner les III-V avec le silicium, en configuration « tandem » bas coût, permettrait de convertir un maximum d'énergie du spectre solaire. Le prix élevé de cette technologie s'explique notamment par le coût afférent au processus de fabrication des cellules solaires III-V, à celui du substrat et au procédé d'épitaxie des matériaux III-V. Les travaux de cette thèse s'attaquent spécifiquement à ce défi. Conventionnellement, les techniques sous vide utilisées pour produire des couches minces III-V dans l'industrie sont l'épitaxie en phase vapeur aux organométalliques (MOCVD) et l'épitaxie par jets moléculaires (MBE)[3]. Elles présentent l'inconvénient d'être à la fois coûteuses et complexes car elles impliquent respectivement une pression élevée (~500 mbar) ou un vide très poussé (ultravide). Dans ma thèse, j'ai exploré une plage de pression intermédiaire, rendue accessible grâce à l'utilisation d'un réacteur de dépôt chimique en phase vapeur assisté par un plasma déporté (RP-CVD). Cette approche conduit à un procédé moins gourmand en précurseurs que la MOCVD, tout en restant moins complexe à mettre en place que la MBE. Nous avons développé et optimisé ce réacteur, entièrement construit dans le laboratoire LPICM de l'École polytechnique, pour la croissance de matériaux III-V destinés au photovoltaïque.

Innovation et pertinence scientifique de la méthode

La croissance assistée par plasma, comme dans le cas du dépôt chimique en phase vapeur assisté par plasma (PECVD) couramment utilisé pour la production industrielle de matériaux à base de silicium, offre une méthode plus rentable dans laquelle un plasma est utilisé pour dissocier les précurseurs gazeux à une pression intermédiaire (0,1-1 mbar)[4]. Dans les années 80, des études ont été menées pour montrer la faisabilité de procédés assistés par plasma dans le dépôt de III-V, mais n'ont pas été approfondies, ni poursuivies[5]. Cependant, ce domaine est

actuellement sujet à un regain d'intérêt en raison de la croissance soutenue du marché des semi-conducteurs III-V. La particularité de notre réacteur de RP-CVD est d'avoir un plasma déporté de la zone de croissance, ce qui permet de prévenir les impacts négatifs du bombardement ionique habituellement engendré lorsque la PECVD est utilisée. L'avantage du plasma par rapport aux techniques citées en introduction réside dans l'application d'un champ électrique qui apporte l'énergie aux électrons pour dissocier efficacement les précurseurs, générant ainsi un milieu hautement réactif composé d'ions, d'espèces excitées, de radicaux, tout en maintenant une température globale (du gaz) proche de la température ambiante. Par conséquent, il devient envisageable de réaliser des dépôts à des températures nettement plus basses, offrant ainsi un avantage significatif pour prévenir les défauts liés au stress thermique et à d'autres réactions indésirables. Le réacteur RP-CVD développé durant ma thèse est constitué de plusieurs éléments clés permettant la croissance de matériaux III-V. Le plasma est généré par une antenne à bobine plate alimentée par un générateur radiofréquence connecté à une boîte d'accord. Une fenêtre en alumine permet de transmettre le champ électromagnétique. Les précurseurs du groupe V (arsine dans du dihydrogène pour la croissance du GaAs, azote pour le GaN), sont introduits dans la zone plasma, i.e. au-dessus de la douche, pour être dissociés en radicaux et traversent ensuite la douche vers la zone de croissance. Le précurseur du groupe III, le triméthylgallium (TMGa) (sous forme liquide dans un barboteur) et son gaz vecteur (dihydrogène), sont directement injectés dans la tête de douche vers la chambre de croissance et donc à l'écart du plasma afin d'éviter une trop forte dissociation des radicaux méthyles qui entraînerait une détérioration de la couche par contamination au carbone. Les réactions entre les espèces des groupes III et V se déroulent alors dans la zone de croissance, au niveau du substrat chauffé. Le porte-substrat est composé d'une base en acier inoxydable surmontée d'une cloche en quartz protégeant le système de chauffage inductif, elle est équipée d'une entretoise en quartz sur laquelle un suscepteur en graphite peut recevoir des substrats d'un diamètre allant jusqu'à 4 pouces. Un couplage inductif est utilisé pour assurer un chauffage local sur le substrat.

Résultats marquants

J'ai consacré la moitié de mon aventure de thèse au développement et à l'optimisation du réacteur de RP-CVD, autant d'un point de vue mécanique que logiciel. Une fois le réacteur opérationnel, nous avons pu examiner les caractéristiques de notre source de plasma à l'aide d'OES (optical emission spectroscopy), en nous concentrant notamment sur l'influence de la puissance RF sur le procédé. Cette analyse nous a permis de positionner la puissance ICP afin optimiser la contribution du plasma au processus de croissance.

Nous avons ainsi pu passer à l'optimisation du réacteur pour la croissance de couches minces de GaN puis de GaAs, matériau d'intérêt pour les panneaux photovoltaïques III-V à hauts rendements. Pour cela, une optimisation fine des conditions de dépôt via un certain nombre de paramètres (flux des gaz, puissance du plasma, pression de la chambre et température du substrat) a été réalisée pour chaque matériau. Ainsi, concernant le GaN, nous avons obtenu une croissance épitaxiée sur saphir et une croissance fortement orientée sur silicium à une basse température de 500°C (contre plus de 1000°C dans les procédés conventionnels) et une basse pression de 0,3 mbar, donc en consommant peu de gaz précurseurs coûteux. Nous avons proposé une solution innovante pour la croissance directe de GaN sur silicium et relevé les défis

associés à l'utilisation de techniques standards pour analyser la composition de matériaux produits par des procédés non conventionnels. Nous avons ensuite démontré la capacité du réacteur à fabriquer des couches homoépitaxiées de GaAs à basse pression (0,5 mbar). Les couches obtenues sont d'excellente qualité structurale et cristalline, comparable à du GaAs commercial. En effet, nous avons obtenu des couches monocristallines présentant une rugosité très faible (0,2 nm) à un taux de croissance élevé d'environ 3 µm/h, des caractéristiques comparables aux procédés de l'industrie, mais à moindre coût. De plus, des études paramétriques ont clairement démontré que l'ajout d'un plasma permet de réduire de façon significative (près d'un facteur 100) la contamination en carbone et ainsi le taux de dopage des couches, tout en maintenant une faible température de dépôt. Une demande de brevet a été déposée pour une solution mise au point au cours de ma thèse, facilitant l'intégration de nos couches de GaAs épitaxiées par RP-CVD directement sur des substrats de silicium à faible coût. À la suite de cette démonstration des performances élevées du réacteur dans la production de matériaux de haute qualité, les couches obtenues ont été intégrées pour fabriquer nos premières cellules solaires par RP-CVD. Malgré le temps limité restant dans le cadre de cette thèse, des cellules fonctionnelles avec un rendement de 15,5 % ont pu être réalisées. Ce résultat, proche des performances typiques des cellules solaires fabriquées en laboratoire par MBE, confirme la capacité de notre réacteur de RP-CVD à produire des cellules solaires III-V performantes.

En conclusion, les résultats de cette thèse ouvrent la voie à une technique de croissance adaptée à la production à faible coût de cellules solaires III-V, grâce à une consommation réduite de gaz permise par le fonctionnement à basse pression de la RP-CVD (~ 0,5 mbar). L'adoption de cette méthode par l'industrie pourrait rendre la fabrication des panneaux solaires III-V et de la nouvelle technologie tandem III-V/Si (notamment via le brevet) plus économique, permettant ainsi à ces technologies hautement performantes de conquérir une part plus importante du marché photovoltaïque. En rendant les technologies photovoltaïques plus efficaces et accessibles aux particuliers comme aux collectivités, ce type d'innovation a le potentiel d'accroître la compétitivité du photovoltaïque et son rôle dans l'accélération nécessaire de la transition énergétique.

Références

[1]Geisz, J. F.; France, R. M.; Schulte, K. L.; Steiner, M. A.; Norman, A. G.; Guthrey, H. L.; Young, M. R.; Song, T.; Moriarty, T., Six-junction III-V solar cells with 47.1% conversion efficiency under 143 suns concentration, Nature Energy, 5 (4), 326-335, 2020

[2]Smith, B.; Woodhouse, M.; Horowitz, K.; Silverman, T.; Zuboy, J.; Margolis, R., Photovoltaic (PV) Module Technologies: 2020 Benchmark Costs and Technology Evolution Framework Results, Golden, CO: National Renewable Energy Laboratory, Technical report NREL/TP-7A40-78173, 2021

[3]Murali, R.; Jayachandran, M.; Rangarajan, Review of techniques on growth of GaAs and relatedcompounds, B. Electrochem, (3), 261-265, 1987

[4]Randhawa, H., Review of Plasma-Assisted Deposition Processes, Thin Solid Films, 196 (2), 329–349, 1991

[5]Pande, K. P.; Seabaugh, A. C., Low Temperature Plasma-Enhanced Epitaxy of GaAs, J. Electrochem. Soc., 131 (6),1357, 1984

General bibliography

(1) Sze, S. M.; Ng, K. K. *Physics of Semiconductor Devices, 3rd Edition | Wiley*. Wiley.com. https://www.wiley.com/en-us/Physics+of+Semiconductor+Devices%2C+3rd+Edition-p-9780470068328 (accessed 2024-03-13).

(2) Colinge, J.-P.; Colinge, C. A. *Physics of Semiconductor Devices*; Springer Science & Business Media, 2002.

(3) Semiconductor Optoelectronic Devices. In *Choice Reviews Online*; 1994; Vol. 31, pp 31-4379-31–4379. https://doi.org/10.5860/CHOICE.31-4379.

(4) Pakhanov, N. A.; Andreev, V. M.; Shvarts, M. Z.; Pchelyakov, O. P. State-of-the-Art Architectures and Technologies of High-Efficiency Solar Cells Based on III–V Heterostructures for Space and Terrestrial Applications. *Optoelectron.Instrument.Proc.* **2018**, *54* (2), 187–202. https://doi.org/10.3103/S8756699018020115.

(5) Convertino, C.; Zota, C. B.; Schmid, H.; Ionescu, A. M.; Moselund, K. E. III–V Heterostructure Tunnel Field-Effect Transistor. *J. Phys.: Condens. Matter* **2018**, *30* (26), 264005. https://doi.org/10.1088/1361-648X/aac5b4.

(6) Haggren, T.; Tan, H. H.; Jagadish, C. III–V Thin Films for Flexible, Cost-Effective, and Emerging Applications in Optoelectronics and Photonics. *Acc. Mater. Res.* **2023**, *4* (12), 1046–1056. https://doi.org/10.1021/accountsmr.3c00138.

(7) Maddox, S. Scott-Maddox/Openbandparams, 2023. https://github.com/scott-maddox/openbandparams (accessed 2024-03-22).

(8) Liang, D.; Bowers, J. E. Recent Progress in Heterogeneous III-V-on-Silicon Photonic Integration. *gxjzz* **2021**, *2* (1), 59–83. https://doi.org/10.37188/lam.2021.005.

(9) Liu, A. Y.; Bowers, J. Photonic Integration With Epitaxial III–V on Silicon. *IEEE Journal of Selected Topics in Quantum Electronics* **2018**, *24* (6), 1–12. https://doi.org/10.1109/JSTQE.2018.2854542.

(10) Cariou, R.; Benick, J.; Feldmann, F.; Höhn, O.; Hauser, H.; Beutel, P.; Razek, N.; Wimplinger, M.; Bläsi, B.; Lackner, D.; Hermle, M.; Siefer, G.; Glunz, S. W.; Bett, A. W.; Dimroth, F. III–V-on-Silicon Solar Cells Reaching 33% Photoconversion Efficiency in Two-Terminal Configuration. *Nat Energy* **2018**, *3* (4), 326–333. https://doi.org/10.1038/s41560-018-0125-0.

(11) Nakamura, S.; Mukai, T. M. T.; Senoh, M. S. M. High-Power GaN P-N Junction Blue-Light-Emitting Diodes. *Jpn. J. Appl. Phys.* **1991**, *30* (12A), L1998. https://doi.org/10.1143/JJAP.30.L1998.

(12) Wang, R.; Ruden, P. P.; Kolnik, J.; Oguzman, I.; Brennan, K. F. Dielectric Properties of Wurtzite and Zincblende Structure Gallium Nitride. *Journal of Physics and Chemistry of Solids* **1997**, *58* (6), 913–918. https://doi.org/10.1016/S0022-3697(96)00219-3.

(13) *International Tables for Crystallography, Volume A: Space-group Symmetry, 6th Edition | Wiley*. Wiley.com. https://www.wiley.com/en-cn/International+Tables+for+Crystallography%2C+Volume+A%3A+Space+group+Symmetry%2C+6th+Edition-p-9780470974230 (accessed 2024-06-03).

(14) Morkoç, H. Handbook of Nitride Semiconductors and Devices. *Handbook of Nitride Semiconductors and Devices* **2009**, *1*, 1–1255. https://doi.org/10.1002/9783527628438.

(15) Ambacher, O. Growth and Applications of Group III-Nitrides. *J. Phys. D: Appl. Phys.* **1998**, *31* (20), 2653. https://doi.org/10.1088/0022-3727/31/20/001.

(16) Mishra, U. K.; Shen, L.; Kazior, T. E.; Wu, Y.-F. GaN-Based RF Power Devices and Amplifiers. *Proceedings of the IEEE* **2008**, *96* (2), 287–305. https://doi.org/10.1109/JPROC.2007.911060.

(17) Hussain, S. Structural and Optical Characterization of Green-Yellow Light Emitting Devices with High Indium Concentrated (In,Ga)N Quantum Wells. **2014**.

(18) Monroy, E.; Muñoz, E.; Sánchez, F. J.; Calle, F.; Calleja, E.; Beaumont, B.; Gibart, P.; Muñoz, J. A.; Cussó, F. High-Performance GaN p-n Junction Photodetectors for Solar Ultraviolet Applications. *Semicond. Sci. Technol.* **1998**, *13* (9), 1042. https://doi.org/10.1088/0268-1242/13/9/013.

(19) Würtele, M. A.; Kolbe, T.; Lipsz, M.; Külberg, A.; Weyers, M.; Kneissl, M.; Jekel, M. Application of GaN-Based Ultraviolet-C Light Emitting Diodes – UV LEDs – for Water Disinfection. *Water Research* **2011**, *45* (3), 1481–1489. https://doi.org/10.1016/j.watres.2010.11.015.

(20) Strite, S.; Morkoç, H. GaN, AlN, and InN: A Review. *Journal of Vacuum Science & Technology B: Microelectronics and Nanometer Structures Processing, Measurement, and Phenomena* **1992**, *10* (4), 1237–1266. https://doi.org/10.1116/1.585897.

(21) Polyakov, A. Y.; Pearton, S. J.; Frenzer, P.; Ren, F.; Liu, L.; Kim, J. Radiation Effects in GaN Materials and Devices. *J. Mater. Chem. C* **2013**, *1* (5), 877–887. https://doi.org/10.1039/C2TC00039C.

(22) Levinshtein, M. E.; Rumyantsev, S. L.; Shur, M. S. *Properties of Advanced Semiconductor Materials: GaN, AIN, InN, BN, SiC, SiGe*; John Wiley & Sons, 2001.

(23) Ehrentraut, D.; Meissner, E.; Bockowski, M. *Technology of Gallium Nitride Crystal Growth*; 2010; Vol. 133. https://doi.org/10.1007/978-3-642-04830-2.

(24) Shur, M. *Physics of Semiconductor Devices*; Prentice Hall, 1990.

(25) Neufeld, C. J.; Toledo, N. G.; Cruz, S. C.; Iza, M.; DenBaars, S. P.; Mishra, U. K. High Quantum Efficiency InGaN/GaN Solar Cells with 2.95 EV Band Gap. *Applied Physics Letters* **2008**, *93* (14), 143502. https://doi.org/10.1063/1.2988894.

(26) Valdueza-Felip, S.; Mukhtarova, A.; Grenet, L.; Bougerol, C.; Durand, C.; Eymery, J.; Monroy, E. Improved Conversion Efficiency of As-Grown InGaN/GaN Quantum-Well Solar Cells for Hybrid Integration. *Appl. Phys. Express* **2014**, *7* (3), 032301. https://doi.org/10.7567/APEX.7.032301.

(27) Mead, C. A. Schottky Barrier Gate Field Effect Transistor. *Proceedings of the IEEE* **1966**, *54* (2), 307–308. https://doi.org/10.1109/PROC.1966.4661.

(28) Laskey, R. *Comprehensive roadmap to drive the integrated photonics industry forward unveiled*. PhotonDelta. https://www.photondelta.com/news/ipsr-i-2024-press-release/ (accessed 2024-04-17).

(29) Brozel, M. Gallium Arsenide. In *Springer Handbook of Electronic and Photonic Materials*; Kasap, S., Capper, P., Eds.; Springer US: Boston, MA, 2007; pp 499–536. https://doi.org/10.1007/978-0-387-29185-7_23.

(30) Kayali, S. I. GaAs Material Properties; 1997.

(31) Becquerel. Recherches Sur Les Effets de La Radiation Chimique de La Lumiere Solaire Au Moyen Des Courants Electriques. *Comptes Rendus de L´Academie des Sciences* **1839**, *9*, 145–149.

(32) Lincot, D. Énergie solaire photovoltaïque et transition énergétique : Leçon inaugurale prononcée au Collège de France le jeudi 20 janvier 2022. In *Énergie solaire photovoltaïque et transition énergétique : Leçon inaugurale prononcée au Collège de France le jeudi 20 janvier 2022*; Leçons inaugurales; Collège de France: Paris, 2022. https://doi.org/10.4000/books.cdf.14107.

(33) *John Perlin - 6000 Years of Solar Architecture and Technology*. https://john-perlin.com/let-it-shine.html (accessed 2024-03-28).

(34) Riordan, M.; Hoddeson, L. The Origins of the Pn Junction. *IEEE Spectrum* **1997**, *34* (6), 46–51. https://doi.org/10.1109/6.591664.

(35) *World Energy Outlook 2023 – Analysis*. IEA. https://www.iea.org/reports/world-energy-outlook-2023 (accessed 2024-04-02).

(36) Renewable Energy Market Update - June 2023. **2023**.

(37) *Net Zero by 2050 – Analysis*. IEA. https://www.iea.org/reports/net-zero-by-2050 (accessed 2024-03-29).

(38) *Best Research-Cell Efficiency Chart*. https://www.nrel.gov/pv/cell-efficiency.html (accessed 2024-03-28).
(39) *Renewable Power Generation Costs in 2022*. https://www.irena.org/Publications/2023/Aug/Renewable-Power-Generation-Costs-in-2022 (accessed 2024-04-02).
(40) Wang, X.; Tian, X.; Chen, X.; Ren, L.; Geng, C. A Review of End-of-Life Crystalline Silicon Solar Photovoltaic Panel Recycling Technology. *Solar Energy Materials and Solar Cells* **2022**, *248*, 111976. https://doi.org/10.1016/j.solmat.2022.111976.
(41) Sopian, K.; Cheow, S. L.; Zaidi, S. H. An Overview of Crystalline Silicon Solar Cell Technology: Past, Present, and Future. *AIP Conference Proceedings* **2017**, *1877* (1), 020004. https://doi.org/10.1063/1.4999854.
(42) Dai, H.; Yang, L.; He, S. < 50-Mm Thin Crystalline Silicon Heterojunction Solar Cells with Dopant-Free Carrier-Selective Contacts. *Nano Energy* **2019**, *64*, 103930. https://doi.org/10.1016/j.nanoen.2019.103930.
(43) Ehrler, B.; Alarcón-Lladó, E.; Tabernig, S. W.; Veeken, T.; Garnett, E. C.; Polman, A. Photovoltaics Reaching for the Shockley–Queisser Limit. *ACS Energy Lett.* **2020**, *5* (9), 3029–3033. https://doi.org/10.1021/acsenergylett.0c01790.
(44) Chopra, K. L.; Paulson, P. D.; Dutta, V. Thin-Film Solar Cells: An Overview. *Progress in Photovoltaics: Research and Applications* **2004**, *12* (2–3), 69–92. https://doi.org/10.1002/pip.541.
(45) Ma, F.; Zhao, Y.; Qu, Z.; You, J. Developments of Highly Efficient Perovskite Solar Cells. *Acc. Mater. Res.* **2023**, *4* (8), 716–725. https://doi.org/10.1021/accountsmr.3c00068.
(46) Diouf, B.; Muley, A.; Pode, R. Issues, Challenges, and Future Perspectives of Perovskites for Energy Conversion Applications. *Energies* **2023**, *16* (18), 6498. https://doi.org/10.3390/en16186498.
(47) Horowitz, K. A.; Remo, T. W.; Smith, B.; Ptak, A. J. *A Techno-Economic Analysis and Cost Reduction Roadmap for III-V Solar Cells*; 2018. https://doi.org/10.2172/1484349.
(48) Bosi, M.; Pelosi, C. The Potential of III-V Semiconductors as Terrestrial Photovoltaic Devices. *Progress in Photovoltaics: Research and Applications* **2007**, *15* (1), 51–68. https://doi.org/10.1002/pip.715.
(49) Shockley, W.; Queisser, H. J. Detailed Balance Limit of Efficiency of P-n Junction Solar Cells. *Journal of Applied Physics* **1961**, *32*, 510–519. https://doi.org/10.1063/1.1736034.
(50) Polman, A.; Knight, M.; Garnett, E. C.; Ehrler, B.; Sinke, W. C. Photovoltaic Materials: Present Efficiencies and Future Challenges. *Science* **2016**, *352* (6283), aad4424. https://doi.org/10.1126/science.aad4424.
(51) Eperon, G. E.; Hörantner, M. T.; Snaith, H. J. Metal Halide Perovskite Tandem and Multiple-Junction Photovoltaics. *Nat Rev Chem* **2017**, *1* (12), 1–18. https://doi.org/10.1038/s41570-017-0095.
(52) VanSant, K. T.; Tamboli, A. C.; Warren, E. L. III-V-on-Si Tandem Solar Cells. *Joule* **2021**, *5* (3), 514–518. https://doi.org/10.1016/j.joule.2021.01.010.
(53) Schygulla, P.; Müller, R.; Höhn, O.; Schachtner, M.; Chojniak, D.; Cordaro, A.; Tabernig, S.; Bläsi, B.; Polman, A.; Siefer, G.; Lackner, D.; Dimroth, F. Wafer-bonded Two-terminal III-V//Si Triple-junction Solar Cell with Power Conversion Efficiency of 36.1% at AM1.5g. *Progress in Photovoltaics* **2024**, pip.3769. https://doi.org/10.1002/pip.3769.
(54) Park, J.-S.; Tang, M.; Chen, S.; Liu, H. Heteroepitaxial Growth of III-V Semiconductors on Silicon. *Crystals* **2020**, *10* (12), 1163. https://doi.org/10.3390/cryst10121163.
(55) Yamaguchi, M.; Ohmachi, Y.; Kadota, Y.; Imaizumi, M.; Matsuda, S. High Performance and Radiation-Resistance of GaAs-on-Si Solar Cells with Novel Structures. In *Conference Record of the Twenty-Ninth IEEE Photovoltaic Specialists Conference, 2002.*; IEEE: New Orleans, LA, USA, 2002; pp 860–863. https://doi.org/10.1109/PVSC.2002.1190715.
(56) Andre, C. L.; Boeckl, J. J.; Wilt, D. M.; Pitera, A. J.; Lee, M. L.; Fitzgerald, E. A.; Keyes, B. M.; Ringel, S. A. Impact of Dislocations on Minority Carrier Electron and Hole Lifetimes in GaAs

Grown on Metamorphic SiGe Substrates. *Applied Physics Letters* **2004**, *84* (18), 3447–3449. https://doi.org/10.1063/1.1736318.

(57) Lu, L.; Gao, Z. Y.; Shen, B.; Xu, F. J.; Huang, S.; Miao, Z. L.; Hao, Y.; Yang, Z. J.; Zhang, G. Y.; Zhang, X. P.; Xu, J.; Yu, D. P. Microstructure and Origin of Dislocation Etch Pits in GaN Epilayers Grown by Metal Organic Chemical Vapor Deposition. *J. Appl. Phys.*

(58) Yao, Y.; Ishikawa, Y.; Sudo, M.; Sugawara, Y.; Yokoe, D. Characterization of Threading Dislocations in GaN (0001) Substrates by Photoluminescence Imaging, Cathodoluminescence Mapping and Etch Pits. *Journal of Crystal Growth* **2017**, *468*, 484–488. https://doi.org/10.1016/j.jcrysgro.2017.01.017.

(59) Ayers, J. E. The Measurement of Threading Dislocation Densities in Semiconductor Crystals by X-Ray Diffraction. *Journal of Crystal Growth* **1994**, *135* (1–2), 71–77. https://doi.org/10.1016/0022-0248(94)90727-7.

(60) Sakai, A.; Sunakawa, H.; Usui, A. Defect Structure in Selectively Grown GaN Films with Low Threading Dislocation Density. *Applied Physics Letters* **1997**, *71* (16), 2259–2261. https://doi.org/10.1063/1.120044.

(61) Maloufi, N. Imagerie par contraste de canalisation des électrons (ECCI) et défauts cristallins. *Étude et propriétés des métaux* **2021**. https://doi.org/10.51257/a-v1-m4145.

(62) Ye, T.; Suo, Z.; Evans, A. G. Thin Film Cracking and the Roles of Substrate and Interface. *International Journal of Solids and Structures* **1992**, *29* (21), 2639–2648. https://doi.org/10.1016/0020-7683(92)90227-K.

(63) Hayafuji, N.; Kizuki, H.; Miyashita, M.; Kadoiwa, K.; Nishimura, T.; Ogasawara, N.; Kumabe, H.; Tada, T. M. Crack Propagation and Mechanical Fracture in GaAs-on-Si. *Jpn. J. Appl. Phys.* **1991**, *30* (3R), 459. https://doi.org/10.1143/JJAP.30.459.

(64) Yang, V. K.; Groenert, M.; Leitz, C. W.; Pitera, A. J.; Currie, M. T.; Fitzgerald, E. A. Crack Formation in GaAs Heteroepitaxial Films on Si and SiGe Virtual Substrates. *Journal of Applied Physics* **2003**, *93* (7), 3859–3865. https://doi.org/10.1063/1.1558963.

(65) Pal, S.; Jacob, C. Silicon—a New Substrate for GaN Growth. *Bull Mater Sci* **2004**, *27* (6), 501–504. https://doi.org/10.1007/BF02707276.

(66) Du, Y.; Xu, B.; Wang, G.; Miao, Y.; Li, B.; Kong, Z.; Dong, Y.; Wang, W.; Radamson, H. H. Review of Highly Mismatched III-V Heteroepitaxy Growth on (001) Silicon. *Nanomaterials* **2022**, *12* (5), 741. https://doi.org/10.3390/nano12050741.

(67) Zhang, Z.; Yang, J.; Zhao, D.; Wang, B.; Zhang, Y.; Liang, F.; Chen, P.; Liu, Z.; Ben, Y. The Melt-Back Etching Effect of the Residual Ga in the Reactor for GaN Grown on (111) Si. *AIP Advances* **2022**, *12* (9), 095106. https://doi.org/10.1063/5.0105524.

(68) Yamane, K.; Kobayashi, T.; Furukawa, Y.; Okada, H.; Yonezu, H.; Wakahara, A. Growth of Pit-Free GaP on Si by Suppression of a Surface Reaction at an Initial Growth Stage. *Journal of Crystal Growth* **2009**, *311* (3), 794–797. https://doi.org/10.1016/j.jcrysgro.2008.09.097.

(69) Takemoto, K.; Murakami, H.; Iwamoto, T.; Matsuo, Y.; Kangawa, Y.; Kumagai, Y.; Koukitu, A. Growth of GaN Directly on Si(111) Substrate by Controlling Atomic Configuration of Si Surface by Metalorganic Vapor Phase Epitaxy. *Jpn. J. Appl. Phys.* **2006**, *45* (No. 18), L478–L481. https://doi.org/10.1143/JJAP.45.L478.

(70) Nasser, N. m; Ye Zhi, Z.; Li, J.; Xu Ya, B. GAN HETEROEPTAXIAL GROWTH TECHNIQUES. *Journal of Microwaves, Optoelectronics and Electromagnetic Applications (JMOe)* **2001**, *2* (3), 22–31.

(71) Song, N.; Deng, S. Thin Film Deposition Technologies and Application in Photovoltaics; 2022. https://doi.org/10.5772/intechopen.108026.

(72) Cho, A. Y. Morphology of Epitaxial Growth of GaAs by a Molecular Beam Method: The Observation of Surface Structures. *Journal of Applied Physics* **1970**, *41* (7), 2780–2786. https://doi.org/10.1063/1.1659315.

(73) Ptak, A. J. 4 - Principles of Molecular Beam Epitaxy. In *Handbook of Crystal Growth (Second Edition)*; Kuech, T. F., Ed.; Handbook of Crystal Growth; North-Holland: Boston, 2015; pp 161–192. https://doi.org/10.1016/B978-0-444-63304-0.00004-4.

(74) Simon, J.; Roberts, D. M.; Boyer, J.; Schulte, K. L.; Braun, A.; Perna, A. N.; Ptak, A. J. Recent HVPE Grown Solar Cells at NREL: Preprint. *Renewable Energy* **2022**.

(75) Morkoc, H.; Peng, C. K.; Henderson, T.; Kopp, W.; Fischer, R.; Erickson, L. P.; Longerbone, M. D.; Youngman, R. C. High-Quality GaAs MESFET's Grown on Silicon Substrates by Molecular-Beam Epitaxy. *IEEE Electron Device Letters* **1985**, *6* (7), 381–383. https://doi.org/10.1109/EDL.1985.26162.

(76) Zamir, S.; Meyler, B.; Zolotoyabko, E.; Salzman, J. The Effect of AlN Buffer Layer on GaN Grown on (111)-Oriented Si Substrates by MOCVD. *Journal of Crystal Growth* **2000**, *218* (2), 181–190. https://doi.org/10.1016/S0022-0248(00)00570-4.

(77) Semond, F. EASYGaN Templates: The Shortcut to GaN-on-Si Technology. *impact* **2017**, *2017* (5), 41–43. https://doi.org/10.21820/23987073.2017.5.41.

(78) Freedsman, J. J.; Watanabe, A.; Yamaoka, Y.; Kubo, T.; Egawa, T. Influence of AlN Nucleation Layer on Vertical Breakdown Characteristics for GaN-on-Si. *physica status solidi (a)* **2016**, *213* (2), 424–428. https://doi.org/10.1002/pssa.201532601.

(79) Volz, K.; Beyer, A.; Witte, W.; Ohlmann, J.; Németh, I.; Kunert, B.; Stolz, W. GaP-Nucleation on Exact Si (0 0 1) Substrates for III/V Device Integration. *Journal of Crystal Growth* **2011**, *315* (1), 37–47. https://doi.org/10.1016/j.jcrysgro.2010.10.036.

(80) Bolkhovityanov, Y. B.; Pchelyakov, O. P. GaAs Epitaxy on Si Substrates: Modern Status of Research and Engineering. *Phys.-Usp.* **2008**, *51* (5), 437. https://doi.org/10.1070/PU2008v051n05ABEH006529.

(81) Zytkiewicz, Z. R. Epitaxial Lateral Overgrowth - a Tool for Dislocation Blockade in Multilayer System. *Acta Physica Polonica Series A* **1998**, *94* (2), 219–227.

(82) Renard, C.; Molière, T.; Cherkashin, N.; Alvarez, J.; Vincent, L.; Jaffré, A.; Hallais, G.; Connolly, J. P.; Mencaraglia, D.; Bouchier, D. High Current Density GaAs/Si Rectifying Heterojunction by Defect Free Epitaxial Lateral Overgrowth on Tunnel Oxide from Nano-Seed. *Sci Rep* **2016**, *6* (1), 25328. https://doi.org/10.1038/srep25328.

(83) *Epitaxial Lateral Overgrowth of GaN - Beaumont - 2001 - physica status solidi (b) - Wiley Online Library*. https://onlinelibrary.wiley.com/doi/abs/10.1002/1521-3951%28200109%29227%3A1%3C1%3A%3AAID-PSSB1%3E3.0.CO%3B2-Q (accessed 2024-04-15).

(84) Macías, C.; Tamsaout, D.; Cavanna, A.; Madouri, A.; Bechu, S.; Travers, L.; Harmand, J.-C.; Collin, S.; Cattoni, A.; Delamarre, A. *Graphene Assisted III-V Layer Epitaxy for Transferable Solar Cells*; 2023. https://doi.org/10.1117/12.2651667.

(85) Kim, Y.; Cruz, S. S.; Lee, K.; Alawode, B. O.; Choi, C.; Song, Y.; Johnson, J. M.; Heidelberger, C.; Kong, W.; Choi, S.; Qiao, K.; Almansouri, I.; Fitzgerald, E. A.; Kong, J.; Kolpak, A. M.; Hwang, J.; Kim, J. Remote Epitaxy through Graphene Enables Two-Dimensional Material-Based Layer Transfer. *Nature* **2017**, *544* (7650), 340–343. https://doi.org/10.1038/nature22053.

(86) Manzo, S.; Strohbeen, P. J.; Lim, Z. H.; Saraswat, V.; Du, D.; Xu, S.; Pokharel, N.; Mawst, L. J.; Arnold, M. S.; Kawasaki, J. K. Pinhole-Seeded Lateral Epitaxy and Exfoliation of GaSb Films on Graphene-Terminated Surfaces. *Nat Commun* **2022**, *13* (1), 4014. https://doi.org/10.1038/s41467-022-31610-y.

(87) Macías, C.; Tamsaout, D.; Cavanna, A.; Madouri, A.; Bechu, S.; Travers, L.; Harmand, J.-C.; Collin, S.; Cattoni, A.; Delamarre, A. Graphene Assisted III-V Layer Epitaxy for Transferable Solar Cells. In *Physics, Simulation, and Photonic Engineering of Photovoltaic Devices XII*; SPIE, 2023; Vol. 12416, pp 27–33. https://doi.org/10.1117/12.2651667.

(88) Vauche, L.; Veinberg-Vidal, E.; Weick, C.; Morales, C.; Larrey, V.; Lecouvey, C.; Martin, M.; Fonseca, J.; Jany, C.; Desrues, T.; Brughera, C.; Voarino, P.; Salvetat, T.; Fournel, F.; Baudrit, M.; Dupre, C. *Wafer Bonding Approaches for III-V on Si Multi-Junction Solar Cells*; 2017.

(89) Randhawa, H. Review of Plasma-Assisted Deposition Processes. *Thin Solid Films* **1991**, *196* (2), 329–349. https://doi.org/10.1016/0040-6090(91)90377-A.

(90) Roca i Cabarrocas, P. Plasma Enhanced Chemical Vapor Deposition of Amorphous, Polymorphous and Microcrystalline Silicon Films. *Journal of Non-Crystalline Solids* **2000**, *266–269*, 31–37. https://doi.org/10.1016/S0022-3093(99)00714-0.

(91) Ouaras, K.; Filonovich, S.; Bruneau, B.; Wang, J.; Ghosh, M.; Johnson, E. Maskless Interdigitated A-Si:H PECVD Process on Full M0 c-Si Wafer: Homogeneity and Passivation Assessment. *Solar Energy Materials and Solar Cells* **2022**, *246*, 111927. https://doi.org/10.1016/j.solmat.2022.111927.

(92) Kabongo, G. L.; Mothudi, B. M.; Dhlamini, M. S. Advanced Development of Sustainable PECVD Semitransparent Photovoltaics: A Review. *Front. Mater.* **2021**, *8*, 762030. https://doi.org/10.3389/fmats.2021.762030.

(93) Samukawa, S.; Hori, M.; Rauf, S.; Tachibana, K.; Bruggeman, P.; Kroesen, G.; Whitehead, J. C.; Murphy, A. B.; Gutsol, A. F.; Starikovskaia, S.; Kortshagen, U.; Boeuf, J.-P.; Sommerer, T. J.; Kushner, M. J.; Czarnetzki, U.; Mason, N. The 2012 Plasma Roadmap. *J. Phys. D: Appl. Phys.* **2012**, *45* (25), 253001. https://doi.org/10.1088/0022-3727/45/25/253001.

(94) Segui, Y.; Carrere, F.; Bui, A. Plasma Deposition of GaAs. *Thin Solid Films* **1982**, *92* (4), 303–308. https://doi.org/10.1016/0040-6090(82)90152-3.

(95) Pande, K. P.; Seabaugh, A. C. Low Temperature Plasma-Enhanced Epitaxy of GaAs. *J. Electrochem. Soc.* **1984**, *131* (6), 1357. https://doi.org/10.1149/1.2115821.

(96) Heinecke, H.; Brauers, A.; Lüth, H.; Balk, P. Plasma Stimulated MOCVD of GaAs. *Journal of Crystal Growth* **1986**, *77* (1–3), 241–249. https://doi.org/10.1016/0022-0248(86)90308-8.

(97) Huelsman, A. D.; Reif, R.; Fonstad, C. G. Plasma-enhanced Metalorganic Chemical Vapor Deposition of GaAs. *Appl. Phys. Lett.* **1987**, *50* (4), 206–208. https://doi.org/10.1063/1.97662.

(98) Leiber, J.; Brauers, A.; Heinecke, H.; Lüth, H.; Balk, P. Growth of GaAs and InP on Si Using Plasma Stimulated MOCVD. *Journal of Crystal Growth* **1989**, *96* (3), 483–489. https://doi.org/10.1016/0022-0248(89)90042-0.

(99) Liang, Q.; Wang, R.-Z.; Yang, M.-Q.; Ding, Y.; Wang, C.-H. A Green, Low-Cost Method to Prepare GaN Films by Plasma Enhanced Chemical Vapor Deposition. *Thin Solid Films* **2020**, *710*. https://doi.org/10.1016/j.tsf.2020.138266.

(100) Emanuel Thomet, J.; Kamlesh Singh, A.; Nelly Rouèche, M.; Toggwyler, N.; Haug, F.-J.; Christmann, G.; Nicolay, S.; Ballif, C.; Wyrsch, N.; Hessler-Wyser, A.; Boccard, M. Bandgap Engineering of Indium Gallium Nitride Layers Grown by Plasma-Enhanced Chemical Vapor Deposition. *Journal of Vacuum Science & Technology A* **2022**, *40* (6), 063102. https://doi.org/10.1116/6.0002039.

(101) Gudovskikh, A. S.; Morozov, I. A.; Uvarov, A. V.; Kudryashov, D. A.; Nikitina, E. V.; Bukatin, A. S.; Nevedomskiy, V. N.; Kleider, J.-P. Low Temperature Plasma Enhanced Deposition of GaP Films on Si Substrate. *Journal of Vacuum Science & Technology A: Vacuum, Surfaces, and Films* **2018**, *36* (2), 021302. https://doi.org/10.1116/1.4999409.

(102) Srinivasan, L.; Jadaud, C.; Silva, F.; Vanel, J.-C.; Maurice, J.-L.; Johnson, E.; Roca I Cabarrocas, P.; Ouaras, K. Reactive Plasma Sputtering Deposition of Polycrystalline GaN Thin Films on Silicon Substrates at Room Temperature. *Journal of Vacuum Science & Technology A* **2023**, *41* (5), 053407. https://doi.org/10.1116/6.0002718.

(103) Li, X.; Li, P.; Wu, Z.; Luo, D.; Yu, H.-Y.; Lu, Z.-H. Review and Perspective of Materials for Flexible Solar Cells. *Materials Reports: Energy* **2021**, *1* (1), 100001. https://doi.org/10.1016/j.matre.2020.09.001.

(104) Hariu, T.; Takenaka, K.; Shibuya, S.; Komatsu, Y.; Shibata, Y. Plasma-Assisted Deposition and Epitaxy of GaAs Films. *Thin Solid Films* **1981**, *80* (1), 235–239. https://doi.org/10.1016/0040-6090(81)90227-3.

(105) Liu, S.; Zhao, G.; He, Y.; Wei, H.; Li, Y.; Qiu, P.; Song, Y.; An, Y.; Wang, X.; Wang, X.; Cheng, J.; Peng, M.; Zheng, X. Interfacial Tailoring for the Suppression of Impurities in GaN by In Situ Plasma Pretreatment via Atomic Layer Deposition. *ACS Applied Materials & Interfaces* **2019**. https://doi.org/10.1021/acsami.9b08816.

(106) Gupta, V.; Madaan, N.; Jensen, D. S.; Kunzler, S. C.; Linford, M. R. Hydrogen Plasma Treatment of Silicon Dioxide for Improved Silane Deposition. *Langmuir* **2013**, *29* (11), 3604–3609. https://doi.org/10.1021/la304491x.

(107) Thomas, R. E.; Mantini, M. J.; Rudder, R. A.; Malta, D. P.; Hattangady, S. V.; Markunas, R. J. Carbon and Oxygen Removal from Silicon (100) Surfaces by Remote Plasma Cleaning Techniques. *Journal of Vacuum Science & Technology A* **1992**, *10* (4), 817–822. https://doi.org/10.1116/1.577678.

(108) Kondo, N.; Nanishi, Y. Low-Temperature Surface Cleaning of GaAs by Electron Cyclotron Resonance (ECR) Plasma. *Jpn. J. Appl. Phys.* **1989**, *28* (1A), L7. https://doi.org/10.1143/JJAP.28.L7.

(109) Angermann, H.; Henrion, W.; Röseler, A.; Rebien, M. Wet-Chemical Passivation of Si(111)- and Si(100)-Substrates. *Materials Science and Engineering: B* **2000**, *73* (1), 178–183. https://doi.org/10.1016/S0921-5107(99)00457-2.

(110) Ghosh, M.; Bulkin, P.; Silva, F.; Johnson, E. V.; Florea, I.; Funes-Hernando, D.; Tanguy, A.; Renard, C.; Vaissiere, N.; Decobert, J.; García, I.; Rey-Stolle, I.; Roca i Cabarrocas, P. Ultrathin Ge Epilayers on Si Produced by Low-Temperature PECVD Acting as Virtual Substrates for III-V / c-Si Tandem Solar Cells. *Solar Energy Materials and Solar Cells* **2022**, *236*, 111535. https://doi.org/10.1016/j.solmat.2021.111535.

(111) Roca i Cabarrocas, P.; Kim, K. H.; Cariou, R.; Labrune, M.; Johnson, E. V.; Moreno, M.; Rios, A. T.; Abolmasov, S.; Kasouit, S. Low Temperature Plasma Synthesis of Nanocrystals and Their Application to the Growth of Crystalline Silicon and Germanium Thin Films. *MRS Proc.* **2012**, *1426*, 319–329. https://doi.org/10.1557/opl.2012.1094.

(112) Le, H.-L. T.; Jardali, F.; Vach, H. Deposition of Hydrogenated Silicon Clusters for Efficient Epitaxial Growth. *Phys. Chem. Chem. Phys.* **2018**, *20* (23), 15626–15634. https://doi.org/10.1039/C8CP00764K.

(113) Vach, H.; Brulin, Q. Controlled Growth of Silicon Nanocrystals in a Plasma Reactor. *Phys. Rev. Lett.* **2005**, *95* (16), 165502. https://doi.org/10.1103/PhysRevLett.95.165502.

(114) Perrin, J.; Cabarrocas, P. R. i; Allain, B.; Friedt, J.-M. A-Si:H Deposition from SiH4 and Si2H6 Rf-Discharges: Pressure and Temperature Dependence of Film Growth in Relation to α-γ Discharge Transition. *Jpn. J. Appl. Phys.* **1988**, *27* (11R), 2041. https://doi.org/10.1143/JJAP.27.2041.

(115) Roca i Cabarrocas, P.; Cariou, R.; Labrune, M. Low Temperature Plasma Deposition of Silicon Thin Films: From Amorphous to Crystalline. *Journal of Non-Crystalline Solids* **2012**, *358* (17), 2000–2003. https://doi.org/10.1016/j.jnoncrysol.2011.12.113.

(116) Cariou, R.; Chen, W.; Maurice, J.-L.; Yu, J.; Patriarche, G.; Mauguin, O.; Largeau, L.; Decobert, J.; Roca i Cabarrocas, P. Low Temperature Plasma Enhanced CVD Epitaxial Growth of Silicon on GaAs: A New Paradigm for III-V/Si Integration. *Sci Rep* **2016**, *6* (1), 25674. https://doi.org/10.1038/srep25674.

(117) Cariou, R.; Ruggeri, R.; Tan, X.; Mannino, G.; Nassar, J.; Roca i Cabarrocas, P. Structural Properties of Relaxed Thin Film Germanium Layers Grown by Low Temperature RF-PECVD Epitaxy on Si and Ge (100) Substrates. *AIP Advances* **2014**, *4* (7), 077103. https://doi.org/10.1063/1.4886774.

(118) Chen, W.; Hamon, G.; Léal, R.; Maurice, J.-L.; Largeau, L.; Roca i Cabarrocas, P. Growth of Tetragonal Si via Plasma-Enhanced Epitaxy. *Crystal Growth & Design* **2017**, *17* (8), 4265–4269. https://doi.org/10.1021/acs.cgd.7b00601.

(119) Piel, A. *Plasma Physics: An Introduction to Laboratory, Space, and Fusion Plasmas*; Springer Berlin Heidelberg: Berlin, Heidelberg, 2010. https://doi.org/10.1007/978-3-642-10491-6.

(120) Tabares, F. L.; Junkar, I. Cold Plasma Systems and Their Application in Surface Treatments for Medicine. *Molecules* **2021**, *26* (7), 1903. https://doi.org/10.3390/molecules26071903.

(121) Chabert, P.; Braithwaite, N. *Physics of Radio-Frequency Plasmas*; Cambridge University Press: Cambridge, 2011. https://doi.org/10.1017/CBO9780511974342.

(122) Chen, F. F. *Introduction to Plasma Physics*; New York, Plenum Press, 1974.
(123) Kim, T. H.; Kim, K. N.; Mishra, A. K.; Seo, J. S.; Jeong, H. B.; Bae, J. O.; Yeom, G. Y. Plasma Characteristics of Inductively Coupled Plasma Using Dual-Frequency Antennas. *Jpn. J. Appl. Phys.* **2013**, *52* (5S2), 05EA02. https://doi.org/10.7567/JJAP.52.05EA02.
(124) Franz, G. *Low Pressure Plasmas and Microstructuring Technology*; 2009. https://doi.org/10.1007/978-3-540-85849-2.
(125) Stringfellow, G. b. Fundamental Aspects of MOVPE. In *Metalorganic Vapor Phase Epitaxy (MOVPE)*; John Wiley & Sons, Ltd, 2019; pp 19–69. https://doi.org/10.1002/9781119313021.ch2.
(126) Lieberman, M. A.; Lichtenberg, A. J. *Principles of Plasma Discharges and Materials Processing*, 1st ed.; Wiley, 2005. https://doi.org/10.1002/0471724254.
(127) i Cabarrocas, P. R. In-Situ Kelvin Probe Study of the SnO2/p (a-Si: H) Interface. Effects of Hydrogen and Argon Plasma Treatment. *MRS Online Proceedings Library (OPL)* **1989**, *149*, 681.
(128) i Morral, A. F.; i Cabarrocas, P. R. Etching and Hydrogen Diffusion Mechanisms during a Hydrogen Plasma Treatment of Silicon Thin Films. *Journal of Non-Crystalline Solids* **2002**, *299*, 196–200.
(129) Martın, I.; Vetter, M.; Orpella, A.; Voz, C.; Puigdollers, J.; Alcubilla, R.; Kharchenko, A. V.; Roca i Cabarrocas, P. Improvement of Crystalline Silicon Surface Passivation by Hydrogen Plasma Treatment. *Applied physics letters* **2004**, *84* (9), 1474–1476.
(130) Thanu, D. P. R.; Srinadhu, E. S.; Zhao, M.; Dole, N. V.; Keswani, M. Chapter 8 - Fundamentals and Applications of Plasma Cleaning. In *Developments in Surface Contamination and Cleaning: Applications of Cleaning Techniques*; Kohli, R., Mittal, K. L., Eds.; Elsevier, 2019; pp 289–353. https://doi.org/10.1016/B978-0-12-815577-6.00008-6.
(131) Choi, S. W.; Bachmann, K. J.; Lucovsky, G. Deposition of GaN by Remote Plasma-Enhanced Chemical-Vapor Deposition (Remote PECVD). *MRS Online Proceedings Library* **1990**, *204* (1), 195–200. https://doi.org/10.1557/PROC-204-195.
(132) Choi, S. W.; Bachmann, K. J.; Lucovsky, G. Growth Kinetics and Characterizations of Gallium Nitride Thin Films by Remote PECVD. *J. Mater. Res.* **1993**, *8* (4), 847–854. https://doi.org/10.1557/JMR.1993.0847.
(133) Losurdo, M.; Capezzuto, P.; Bruno, G. GaN Growth by Remote Plasma MOCVD: Chemistry and Kinetics by Real Time Ellipsometry. *MRS Internet Journal of Nitride Semiconductor Research* **1999**, *4* (1), 173–178. https://doi.org/10.1557/S1092578300002416.
(134) Martin, C.; Butcher, K. S. A.; Wintrebert-Fouquet, M.; Fernandes, A.; Dabbs, T.; Chen, P. P.-T.; Carmen, R. Modeling and Experimental Analysis of RPCVD Based Nitride Film Growth; Morkoç, H., Litton, C. W., Chyi, J.-I., Nanishi, Y., Yoon, E., Eds.; San Jose, CA, 2008; p 689407. https://doi.org/10.1117/12.762537.
(135) Barik, S.; Liu, D.; Brown, J. D.; Wintrebert-Fouquet, M.; Fernandes, A. J.; Chen, P. P.-T.; Gao, Q.; Chan, V.; Mann, I. Remote Plasma Chemical Vapour Deposition of Group III-Nitride Tunnel Junctions for LED Applications. In *Light-Emitting Devices, Materials, and Applications*; SPIE, 2019; Vol. 10940, pp 181–188. https://doi.org/10.1117/12.2513261.
(136) Knights, J. C.; Lujan, R. A. Plasma Deposition of GaP and GaN. *Journal of Applied Physics* **1978**, *49* (3), 1291–1293. https://doi.org/10.1063/1.325024.
(137) Pande, K. P.; Aina, O. Plasma-assisted Low Temperature Epitaxy. *Journal of Vacuum Science & Technology A: Vacuum, Surfaces, and Films* **1986**, *4* (3), 673–676. https://doi.org/10.1116/1.573830.
(138) Huelsman, A. D.; Zien, L.; Reif, R. Plasma-controlled Deposition of GaAs and GaAsP by Metalorganic Chemical Vapor Deposition. *Appl. Phys. Lett.* **1988**, *52* (9), 726–727. https://doi.org/10.1063/1.99360.
(139) Pihlstrom, B. G.; Sheng, T. Y.; Thompson, L. R.; Collins, G. J. Organometallic Vapor-phase Homoepitaxy of Gallium Arsenide Assisted by a Downstream Hydrogen Afterglow Plasma in

the Growth Region. *Appl. Phys. Lett.* **1992**, *60* (25), 3144–3146. https://doi.org/10.1063/1.106750.

(140) Sato, M. Plasma-Assisted MOCVD Growth of GaAs/ GaN / GaAs Thin-Layer Structures by N-As Replacement Using N-Radicals. **1995**, *34* (2).

(141) Lu, Y.; Kondo, H.; Ishikawa, K.; Oda, O.; Takeda, K.; Sekine, M.; Amano, H.; Hori, M. Epitaxial Growth of GaN by Radical-Enhanced Metalorganic Chemical Vapor Deposition (REMOCVD) in the Downflow of a Very High Frequency (VHF) N2/H2 Excited Plasma – Effect of TMG Flow Rate and VHF Power. *Journal of Crystal Growth* **2014**, *391*, 97–103. https://doi.org/10.1016/j.jcrysgro.2014.01.014.

(142) Zhang, Z.; Luo, Y.; Yu, J.; Li, X.; Wang, J.; Yu, W.; Wang, L.; Hao, Z.; Sun, C.; Han, Y.; Xiong, B.; Li, H. An Inductively Coupled Plasma Metal Organic Chemical Vapor Deposition Based on Showerhead Structure for Low Temperature Growth. *Mater. Res. Express* **2021**, *8* (9), 095903. https://doi.org/10.1088/2053-1591/ac22c5.

(143) Yu, J.; Zhang, Z.; Luo, Y.; Wang, J.; Wang, L.; Li, X.; Hao, Z.; Sun, C.; Han, Y.; Xiong, B.; Li, H. Thin Film Transistors and Metal–Semiconductor–Metal Photodetectors Based on GaN Thin Films Grown by Inductively Coupled Plasma Metal-Organic Chemical Vapor Deposition. *J. Phys. D: Appl. Phys.* **2022**, *55* (35), 354002. https://doi.org/10.1088/1361-6463/ac7263.

(144) Fan, Z.; Maurice, J.-L.; Chen, W.; Guilet, S.; Cambril, E.; Lafosse, X.; Couraud, L.; Merghem, K.; Yu, L.; Bouchoule, S.; Roca I Cabarrocas, P. On the Mechanism of In Nanoparticle Formation by Exposing ITO Thin Films to Hydrogen Plasmas. *Langmuir* **2017**, *33* (43), 12114–12119. https://doi.org/10.1021/acs.langmuir.7b01743.

(145) Turner, M. M.; Lieberman, M. A. Hysteresis and the E-to-H Transition in Radiofrequency Inductive Discharges. *Plasma Sources Sci. Technol.* **1999**, *8* (2), 313. https://doi.org/10.1088/0963-0252/8/2/312.

(146) Cottrell, T. L. (Tom L. The Strengths of Chemical Bonds. *(No Title)*.

(147) Melton, W. A.; Pankove, J. I. GaN Growth on Sapphire. *Journal of Crystal Growth* **1997**, *178* (1), 168–173. https://doi.org/10.1016/S0022-0248(97)00082-1.

(148) Kosicki, B. B.; Kahng, D. Preparation and Structural Properties of GaN Thin Films. *Journal of Vacuum Science and Technology* **1969**, *6* (4), 593–596. https://doi.org/10.1116/1.1315693.

(149) Ryou, J.-H. 3 - Gallium Nitride (GaN) on Sapphire Substrates for Visible LEDs. In *Nitride Semiconductor Light-Emitting Diodes (LEDs)*; Huang, J., Kuo, H.-C., Shen, S.-C., Eds.; Woodhead Publishing, 2014; pp 66–98. https://doi.org/10.1533/9780857099303.1.66.

(150) Amano, H. Nobel Lecture: Growth of GaN on Sapphire via Low-Temperature Deposited Buffer Layer and Realization of p-Type GaN by Mg Doping Followed by Low-Energy Electron Beam Irradiation. *Rev. Mod. Phys.* **2015**, *87* (4), 1133–1138. https://doi.org/10.1103/RevModPhys.87.1133.

(151) Dadgar, A. Sixteen Years GaN on Si: Sixteen Years GaN on Si. *Phys. Status Solidi B* **2015**, *252* (5), 1063–1068. https://doi.org/10.1002/pssb.201451656.

(152) Guha, S.; Bojarczuk, N. A. Ultraviolet and Violet GaN Light Emitting Diodes on Silicon. *Applied Physics Letters* **1998**, *72* (4), 415–417. https://doi.org/10.1063/1.120775.

(153) Guha, S.; Bojarczuk, N. A. Multicolored Light Emitters on Silicon Substrates. *Applied Physics Letters* **1998**, *73* (11), 1487–1489. https://doi.org/10.1063/1.122181.

(154) Czerwiec, T.; Greer, F.; Graves, D. B. Nitrogen Dissociation in a Low Pressure Cylindrical ICP Discharge Studied by Actinometry and Mass Spectrometry. *J. Phys. D: Appl. Phys.* **2005**, *38* (24), 4278–4289. https://doi.org/10.1088/0022-3727/38/24/003.

(155) Watrin, L.; Silva, F.; Jadaud, C.; Bulkin, P.; Vanel, J.-C.; Muller, D.; Johnson, E. V.; Ouaras, K.; Cabarrocas, P. R. I. Direct Growth of Highly Oriented GaN Thin Films on Silicon by Remote Plasma CVD. *Journal of Physics D: Applied Physics* **2024**, *57* (31), 315106. https://doi.org/10.1088/1361-6463/ad436c.

(156) Motamedi, P.; Dalili, N.; Cadien, K. A Route to Low Temperature Growth of Single Crystal GaN on Sapphire. *J. Mater. Chem. C* **2015**, *3* (28), 7428–7436. https://doi.org/10.1039/C5TC01556A.

(157) Daudin, B.; Feuillet, G.; Mula, G.; Mariette, H.; Rouviére, J. L.; Pelekanos, N.; Fishman, G.; Adelmann, C.; Simon, J. Epitaxial Growth of GaN, AlN and InN: 2D/3D Transition and Surfactant Effects. *phys. stat. sol. (a)* **1999**, *176* (1), 621–627. https://doi.org/10.1002/(SICI)1521-396X(199911)176:1<621::AID-PSSA621>3.0.CO;2-Y.

(158) Liu, A.-C.; Tu, P.-T.; Langpoklakpam, C.; Huang, Y.-W.; Chang, Y.-T.; Tzou, A.-J.; Hsu, L.-H.; Lin, C.-H.; Kuo, H.-C.; Chang, E. The Evolution of Manufacturing Technology for GaN Electronic Devices. *Micromachines* **2021**, *12*, 737. https://doi.org/10.3390/mi12070737.

(159) Kappers, M. J.; Moram, M. A.; Sridhara Rao, D. V.; McAleese, C.; Humphreys, C. J. Low Dislocation Density GaN Growth on High-Temperature AlN Buffer Layers on (0 0 0 1) Sapphire. *Journal of Crystal Growth* **2010**, *312* (3), 363–367. https://doi.org/10.1016/j.jcrysgro.2009.11.014.

(160) Huang, W.-C.; Chu, C.-M.; Wong, Y.-Y.; Chen, K.-W.; Lin, Y.-K.; Wu, C.-H.; Lee, W.-I.; Chang, E.-Y. Investigations of GaN Growth on the Sapphire Substrate by MOCVD Method with Different AlN Buffer Deposition Temperatures. *Materials Science in Semiconductor Processing* **2016**, *45*, 1–8. https://doi.org/10.1016/j.mssp.2016.01.008.

(161) Hongbo Yu; Kemal Ozturk, M.; Ozcelik, S.; Ozbay, E. A Study of Semi-Insulating GaN Grown on AlN Buffer/Sapphire Substrate by Metalorganic Chemical Vapor Deposition. *Journal of Crystal Growth* **2006**, *293* (2), 273–277. https://doi.org/10.1016/j.jcrysgro.2006.05.056.

(162) Losurdo, M.; Capezzuto, P.; Bruno, G. Plasma Cleaning and Nitridation of Sapphire (α-Al2O3) Surfaces: New Evidence from in Situ Real Time Ellipsometry. *Journal of Applied Physics* **2000**, *88* (4), 2138–2145. https://doi.org/10.1063/1.1305926.

(163) Chen, Y.-C.; Chang, L. Epitaxial AlN on C-Plane Sapphire by Plasma Nitriding. *Jpn. J. Appl. Phys.* **2019**, *58* (SC), SC1012. https://doi.org/10.7567/1347-4065/ab07a0.

(164) Nakashima, K.; Ishii, M.; Tajima, I.; Yamamoto, M. Existence of Threshold Density in Silicon Surface Cleaning Using Hydrogen Electron Cyclotron Resonance Plasma. *Applied Physics Letters* **1991**, *58* (23), 2663–2665. https://doi.org/10.1063/1.104800.

(165) Zaumseil, P. High-Resolution Characterization of the Forbidden Si 200 and Si 222 Reflections. *J Appl Crystallogr* **2015**, *48* (2), 528–532. https://doi.org/10.1107/S1600576715004732.

(166) Dadgar, A.; Schulze, F.; Wienecke, M.; Gadanecz, A.; Bläsing, J.; Veit, P.; Hempel, T.; Diez, A.; Christen, J.; Krost, A. Epitaxy of GaN on Silicon—Impact of Symmetry and Surface Reconstruction. *New J. Phys.* **2007**, *9* (10), 389–389. https://doi.org/10.1088/1367-2630/9/10/389.

(167) Schneider, C. A.; Rasband, W. S.; Eliceiri, K. W. NIH Image to ImageJ: 25 Years of Image Analysis. *Nat Methods* **2012**, *9* (7), 671–675. https://doi.org/10.1038/nmeth.2089.

(168) Tautz, M.; Díaz Díaz, D. Wet-Chemical Etching of GaN: Underlying Mechanism of a Key Step in Blue and White LED Production. *ChemistrySelect* **2018**, *3* (5), 1480–1494. https://doi.org/10.1002/slct.201702267.

(169) Pampili, P.; Zubialevich, V. Z.; Parbrook, P. J. Geometrically Controlled Microscale Patterning and Epitaxial Lateral Overgrowth of Nitrogen-Polar GaN. *Crystal Growth & Design* **2024**, *24* (15), 6095–6100. https://doi.org/10.1021/acs.cgd.4c00235.

(170) Hellman, E. S. The Polarity of GaN: A Critical Review. *MRS Internet j. nitride semicond. res.* **1998**, *3*, e11. https://doi.org/10.1557/S1092578300000831.

(171) Sone, C.; Hong Kim, M.; Jin Kim, H.; Yoon, E. Effects of Hydrogen on Carbon Incorporation in GaN Grown by Remote Plasma-Enhanced Metal-Organic Chemical Vapor Deposition. *Journal of Crystal Growth* **1998**, *189–190*, 321–324. https://doi.org/10.1016/S0022-0248(98)00278-4.

(172) Masi, M.; Sirnka, H.; Jensen, K. F.; Kuech, T. F. Simulation of Carbon Doping of GaAs during MOVPE.

(173) Webb, J. B.; Tang, H.; Rolfe, S.; Bardwell, J. A. Semi-Insulating C-Doped GaN and High-Mobility AlGaN/GaN Heterostructures Grown by Ammonia Molecular Beam Epitaxy. *Applied Physics Letters* **1999**, *75* (7), 953–955. https://doi.org/10.1063/1.124252.

(174) Tang, H.; Webb, J. B.; Bardwell, J. A.; Raymond, S.; Salzman, J.; Uzan-Saguy, C. Properties of Carbon-Doped GaN. *Applied Physics Letters* **2001**, *78* (6), 757–759. https://doi.org/10.1063/1.1345816.

(175) Khoury, M.; Tottereau, O.; Feuillet, G.; Vennéguès, P.; Zúñiga-Pérez, J. Evolution and Prevention of Meltback Etching: Case Study of Semipolar GaN Growth on Patterned Silicon Substrates. *Journal of Applied Physics* **2017**, *122* (10), 105108. https://doi.org/10.1063/1.5001914.

(176) Seon, M.; Prokofyeva, T.; Holtz, M.; Nikishin, S. A.; Faleev, N. N.; Temkin, H. Selective Growth of High Quality GaN on Si(111) Substrates. *Applied Physics Letters* **2000**, *76* (14), 1842–1844. https://doi.org/10.1063/1.126186.

(177) Amano, H.; Sawaki, N.; Akasaki, I.; Toyoda, Y. Metalorganic Vapor Phase Epitaxial Growth of a High Quality GaN Film Using an AlN Buffer Layer. *Applied Physics Letters* **1986**, *48* (5), 353–355. https://doi.org/10.1063/1.96549.

(178) Yang, Y.; Xiang, P.; Liu, M.; Chen, W.; He, Z.; Han, X.; Ni, Y.; Yang, F.; Yao, Y.; Wu, Z.; Liu, Y.; Zhang, B. Effect of Compositionally Graded AlGaN Buffer Layer Grown by Different Functions of Trimethylaluminum Flow Rates on the Properties of GaN on Si (111) Substrates. *Journal of Crystal Growth* **2013**, *376*, 23–27. https://doi.org/10.1016/j.jcrysgro.2013.04.043.

(179) Hiroyama, Y. H. Y.; Tamura, M. T. M. Effect of Very Thin SiC Layer on Heteroepitaxial Growth of Cubic GaN on Si (001). *Jpn. J. Appl. Phys.* **1998**, *37* (6A), L630. https://doi.org/10.1143/JJAP.37.L630.

(180) Palik, E. D. *Handbook of Optical Constants of Solids: Volume 1*; Elsevier, 2012.

(181) Dadgar, A.; Poschenrieder, M.; Bläsing, J.; Contreras, O.; Bertram, F.; Riemann, T.; Reiher, A.; Kunze, M.; Daumiller, I.; Krtschil, A.; Diez, A.; Kaluza, A.; Modlich, A.; Kamp, M.; Christen, J.; Ponce, F. A.; Kohn, E.; Krost, A. MOVPE Growth of GaN on Si(111) Substrates. *Journal of Crystal Growth* **2003**, *248*, 556–562. https://doi.org/10.1016/S0022-0248(02)01894-8.

(182) Jacquot, C.; Takadoum, J. A Study of Adhesion Forces by Atomic Force Microscopy. *Journal of Adhesion Science and Technology* **2001**. https://doi.org/10.1163/156856101750430422.

(183) Frank, F. C. The Influence of Dislocations on Crystal Growth. *Discuss. Faraday Soc.* **1949**, *5* (0), 48–54. https://doi.org/10.1039/DF9490500048.

(184) Li, J.; Aierken, A.; Liu, Y.; Zhuang, Y.; Yang, X.; Mo, J. H.; Fan, R. K.; Chen, Q. Y.; Zhang, S. Y.; Huang, Y. M.; Zhang, Q. A Brief Review of High Efficiency III-V Solar Cells for Space Application. *Front. Phys.* **2021**, *8*. https://doi.org/10.3389/fphy.2020.631925.

(185) Perovic, D. D.; Castell, M. R.; Howie, A.; Lavoie, C.; Tiedje, T.; Cole, J. S. W. Field-Emission SEM Imaging of Compositional and Doping Layer Semiconductor Superlattices. *Ultramicroscopy* **1995**, *58* (1), 104–113. https://doi.org/10.1016/0304-3991(94)00183-N.

(186) Elliott, S. L.; Broom, R. F.; Humphreys, C. J. Dopant Profiling with the Scanning Electron Microscope—A Study of Si. *Journal of Applied Physics* **2002**, *91* (11), 9116–9122. https://doi.org/10.1063/1.1476968.

(187) Stringfellow, G. B. *Organometallic Vapor-Phase Epitaxy: Theory and Practice*; Elsevier, 1999.

(188) Ben Saddik, K.; Braña, A. F.; López, N.; García, B. J.; Fernández-Garrido, S. Growth of Silicon- and Carbon-Doped GaAs by Chemical Beam Epitaxy Using H2-Diluted DTBSi and CBr4 Precursors. *Journal of Crystal Growth* **2021**, *571*, 126242. https://doi.org/10.1016/j.jcrysgro.2021.126242.

(189) Wolf, H. F. Semiconductors. *(No Title)*.

(190) Fang, S. F.; Adomi, K.; Iyer, S.; Morkoç, H.; Zabel, H.; Choi, C.; Otsuka, N. Gallium Arsenide and Other Compound Semiconductors on Silicon. *Journal of Applied Physics* **1990**, *68* (7), R31–R58. https://doi.org/10.1063/1.346284.

(191) Kroemer, H.; Liu, T.-Y.; Petroff, P. M. GaAs on Si and Related Systems: Problems and Prospects. *Journal of Crystal Growth* **1989**, *95* (1–4), 96–102. https://doi.org/10.1016/0022-0248(89)90359-X.

(192) DenBaars, S. P.; Maa, B. Y.; Dapkus, P. D.; Danner, A. D.; Lee, H. C. Homogeneous and Heterogeneous Thermal Decomposition Rates of Trimethylgallium and Arsine and Their Relevance to the Growth of GaAs by MOCVD. *Journal of Crystal Growth* **1986**, *77* (1), 188–193. https://doi.org/10.1016/0022-0248(86)90300-3.

(193) Bobb, L. C.; Holloway, H.; Maxwell, K. H.; Zimmerman, E. Oriented Growth of Semiconductors. III. Growth of Gallium Arsenide on Germanium. *Journal of Applied Physics* **1966**, *37* (13), 4687–4693. https://doi.org/10.1063/1.1708118.

(194) Müller, E. K. Structure of Oriented, Vapor-Deposited GaAs Films, Studied by Electron Diffraction. *Journal of Applied Physics* **1964**, *35* (3), 580–585. https://doi.org/10.1063/1.1713420.

(195) Dushaq, G.; Rasras, M. Mechanical Nano-Patterning: Toward Highly-Aligned Ge Self-Assembly on Low Lattice Mismatched GaAs Substrate. *Sci Rep* **2019**, *9* (1), 14221. https://doi.org/10.1038/s41598-019-50633-y.

(196) Labrune, M.; Bril, X.; Patriarche, G.; Largeau, L.; Mauguin, O.; Cabarrocas, P. R. i. Epitaxial Growth of Silicon and Germanium on (100)-Oriented Crystalline Substrates by RF PECVD at 175 °C. *EPJ Photovolt.* **2012**, *3*, 30303. https://doi.org/10.1051/epjpv/2012010.

(197) Sridhar, N.; Rickman, J. M.; Srolovitz, D. J. Twinning in Thin Films—II. Equilibrium Microstructures. *Acta Materialia* **1996**, *44* (10), 4097–4113. https://doi.org/10.1016/S1359-6454(96)00059-6.

(198) Shimamura, K.; Yuan, Z.; Shimojo, F.; Nakano, A. Effects of Twins on the Electronic Properties of GaAs. *Applied Physics Letters* **2013**, *103* (2), 022105. https://doi.org/10.1063/1.4811746.

(199) Novikova, S. I. Chapter 2 Thermal Expansion. In *Semiconductors and Semimetals*; Willardson, R. K., Beer, A. C., Eds.; Physics of III-V Compounds; Elsevier, 1966; Vol. 2, pp 33–48. https://doi.org/10.1016/S0080-8784(08)60160-X.

(200) Carles, R.; Landa, G.; Renucci, J. B. Bond Relaxation Phenomenon and Impurity Modes Frequencies in III–V Compounds. *Solid State Communications* **1985**, *53* (2), 179–182. https://doi.org/10.1016/0038-1098(85)90121-8.

(201) Blakemore, J. S. Semiconducting and Other Major Properties of Gallium Arsenide. *Journal of Applied Physics* **1982**, *53* (10), R123–R181. https://doi.org/10.1063/1.331665.

(202) Glas, F.; Patriarche, G.; Largeau, L.; Lemaître, A. Determination of the Local Concentrations of Mn Interstitials and Antisite Defects in G a M n A s. *Physical review letters* **2004**, *93*, 086107. https://doi.org/10.1103/PhysRevLett.93.086107.

(203) Ye, H.; Yu, J. Germanium Epitaxy on Silicon. *Sci. Technol. Adv. Mater.* **2014**, *15* (2), 024601. https://doi.org/10.1088/1468-6996/15/2/024601.

(204) *Full article: Germanium epitaxy on silicon*. https://www.tandfonline.com/doi/full/10.1088/1468-6996/15/2/024601 (accessed 2024-07-17).

(205) Liu, J. L.; Tong, S.; Luo, Y. H.; Wan, J.; Wang, K. L. High-Quality Ge Films on Si Substrates Using Sb Surfactant-Mediated Graded SiGe Buffers. *Applied Physics Letters* **2001**, *79* (21), 3431–3433. https://doi.org/10.1063/1.1421092.

(206) Brunner, F.; Bergunde, T.; Richter, E.; Kurpas, P.; Achouche, M.; Maaßdorf, A.; Würfl, J.; Weyers, M. Carbon Doping for the GaAs Base Layer of Heterojunction Bipolar Transistors in a Production Scale MOVPE Reactor. *Journal of Crystal Growth* **2000**, *221* (1–4), 53–58. https://doi.org/10.1016/S0022-0248(00)00648-5.

(207) Kohda, H.; Wada, K. The Carbon Doping Mechanism in GaAs Using Trimethylgallium and Trimethylarsenic. *Journal of Crystal Growth* **1996**, *167* (3), 557–565. https://doi.org/10.1016/0022-0248(96)00264-3.

(208) Konagai, M.; Yamada, T.; Akatsuka, T.; Nozaki, S.; Miyake, R.; Saito, K.; Fukamachi, T.; Tokumitsu, E.; Takahashi, K. Metallic P-Type GaAs and InGaAs Grown by MOMBE. *Journal of Crystal Growth* **1990**, *105* (1), 359–365. https://doi.org/10.1016/0022-0248(90)90386-Y.

(209) Richter, E.; Kurpas, P.; Sato, M.; Trapp, M.; Zeimer, U.; Hähle, S.; Weyers, M. Hydrogen in Carbon-Doped GaAs Base Layer of GaInP/GaAs Heterojunction Bipolar Transistors. *Materials Science and Engineering: B* **1997**, *44* (1), 337–340. https://doi.org/10.1016/S0921-5107(96)01736-9.

(210) Kang, D.; Arab, S.; Cronin, S. B.; Li, X.; Rogers, J. A.; Yoon, J. Carbon-Doped GaAs Single Junction Solar Microcells Grown in Multilayer Epitaxial Assemblies. *Applied Physics Letters* **2013**, *102* (25), 253902. https://doi.org/10.1063/1.4812399.

(211) Augustine, G.; Rohatgi, A.; Jokerst, N. M. Base Doping Optimization for Radiation-Hard Si, GaAs, and InP Solar Cells. *IEEE Transactions on Electron Devices* **1992**, *39* (10), 2395–2400. https://doi.org/10.1109/16.158814.

(212) Singh, B.; Roshi; Gupta, V. Impact of Different Parameters on the Performance of GaAs Solar Cell Using PC1D Simulation. *Materials Today: Proceedings* **2022**, *62*, 6407–6411. https://doi.org/10.1016/j.matpr.2022.03.675.

(213) Ren, Z.; Thway, M.; Liu, Z.; Wang, Y.; Ke, C.; Yaung, K. N.; Wang, B.; Tan, C. S.; Lin, F.; Aberle, A. G.; Buonassisi, T.; Peters, I. M. Ultra-Thin GaAs Double-Junction Solar Cell With Carbon-Doped Emitter. *IEEE Journal of Photovoltaics* **2018**, *8* (6), 1627–1634. https://doi.org/10.1109/JPHOTOV.2018.2870721.

(214) Matsuda, Y.; Fujita, K.; Hinotani, S. Raman Studies on GaAs Epitaxial Films on Si. *Applied Surface Science* **1991**, *48–49*, 231–236. https://doi.org/10.1016/0169-4332(91)90336-I.

(215) Abstreiter, G.; Bauser, E.; Fischer, A.; Ploog, K. Raman Spectroscopy—A Versatile Tool for Characterization of Thin Films and Heterostructures of GaAs and AlxGa1−xAs. *Appl. Phys.* **1978**, *16* (4), 345–352. https://doi.org/10.1007/BF00885858.

(216) Sotoodeh, M.; Khalid, A. H.; Rezazadeh, A. A. Empirical Low-Field Mobility Model for III–V Compounds Applicable in Device Simulation Codes. *Journal of Applied Physics* **2000**, *87* (6), 2890–2900. https://doi.org/10.1063/1.372274.

(217) Lye, B.-C.; Houston, P. A.; Yow, H.-K.; Button, C. C. GaInP/AlGaAs/GaInP Double Heterojunction Bipolar Transistors with Zero Conduction Band Spike at the Collector. *IEEE Transactions on Electron Devices* **1998**, *45* (12), 2417–2421. https://doi.org/10.1109/16.735717.

(218) Wenzel, M.; Irmer, G.; Monecke, J.; Siegel, W. Determination of the Effective Hall Factor in P-Type Semiconductors. *Semicond. Sci. Technol.* **1998**, *13* (5), 505. https://doi.org/10.1088/0268-1242/13/5/011.

(219) Enquist, P. M. P-type Doping Limit of Carbon in Organometallic Vapor Phase Epitaxial Growth of GaAs Using Carbon Tetrachloride. *Applied Physics Letters* **1990**, *57* (22), 2348–2350. https://doi.org/10.1063/1.103889.

(220) Hanna, M. C.; Lu, Z. H.; Majerfeld, A. Very High Carbon Incorporation in Metalorganic Vapor Phase Epitaxy of Heavily Doped P-type GaAs. *Applied Physics Letters* **1991**, *58* (2), 164–166. https://doi.org/10.1063/1.104960.

(221) Hudait, M. K.; Modak, P.; Hardikar, S.; Krupanidhi, S. B. Zn Incorporation and Band Gap Shrinkage in P-Type GaAs. *Journal of Applied Physics* **1997**, *82* (10), 4931–4937. https://doi.org/10.1063/1.366359.

(222) Kressel, H. *Semiconductor Lasers and Herterojunction LEDs*; Elsevier, 2012.

(223) Pütz, N.; Heinecke, H.; Heyen, M.; Balk, P.; Weyers, M.; Lüth, H. A Comparative Study of Ga(CH3)3 and Ga(C2H5)3 in the Mombe of GaAs. *Journal of Crystal Growth* **1986**, *74* (2), 292–300. https://doi.org/10.1016/0022-0248(86)90118-1.

(224) Fraas, L. M.; McLeod, P. S.; Partain, L. D.; Weiss, R. E.; Cape, J. A. GaP and GaAs Films Grown by Vacuum Chemical Epitaxy Using TEGa and TMGa Sources. *Journal of Crystal Growth* **1986**, *77* (1), 386–391. https://doi.org/10.1016/0022-0248(86)90328-3.

(225) Donnelly, V. M.; McCaulley, J. A. Products of Thermal Decomposition of Triethylgallium and Trimethylgallium Adsorbed on Ga-Stabilized GaAs(100). *Surface Science* **1990**, *238* (1), 34–52. https://doi.org/10.1016/0039-6028(90)90063-E.

(226) Aquino, A. A.; Jones, T. S. A Comparative Study of the Adsorption and Thermal Decomposition of Triethylgallium and Trimethylgallium at GaAs(100) Surfaces Studied by Electron Energy Loss Spectroscopy. *Applied Surface Science* **1996**, *104–105*, 304–311. https://doi.org/10.1016/S0169-4332(96)00162-6.

(227) Hardtdegen, H.; Raafat, T.; Hollfelder, M.; Ungermanns, Ch. A New Method for Controlled Carbon Doping in LP-MOVPE of GaAs Using TMAs and Mixtures of TMGaTEGa<math><mtext>TMGa</Mtext><mtext>TEGa</Mtext></Math>. *Journal of Crystal Growth* **1995**, *156* (4), 333–336. https://doi.org/10.1016/0022-0248(95)00299-5.

(228) Lovejoy, M. L.; Melloch, M. R.; Lundstrom, M. S.; Keyes, B. M.; Ahrenkiel, R. K.; de Lyon, T. J.; Woodall, J. M. Comparative Study of Minority Electron Properties in P+-GaAs Doped with Beryllium and Carbon. *Applied Physics Letters* **1992**, *61* (7), 822–824. https://doi.org/10.1063/1.107756.

(229) de Lyon, T. J.; Woodall, J. M.; Kash, J. A.; McInturff, D. T.; Bates, R. J. S.; Kirchner, P. D.; Cardone, F. Minority Carrier Lifetime and Photoluminescent Response of Heavily Carbon-doped GaAs Grown with Gas Source Molecular-beam Epitaxy Using Halomethane Doping Sources. *Journal of Vacuum Science & Technology B: Microelectronics and Nanometer Structures Processing, Measurement, and Phenomena* **1992**, *10* (2), 846–849. https://doi.org/10.1116/1.586132.

(230) Wei, H.; Wu, J.; Qiu, P.; Liu, S.; He, Y.; Peng, M.; Li, D.; Meng, Q.; Zaera, F.; Zheng, X. Plasma-Enhanced Atomic-Layer-Deposited Gallium Nitride as an Electron Transport Layer for Planar Perovskite Solar Cells. *J. Mater. Chem. A* **2019**, *7* (44), 25347–25354. https://doi.org/10.1039/C9TA08929B.

(231) Chen, H.-L. Ultrathin and Nanowire-Based GaAs Solar Cells. phdthesis, Université Paris Saclay (COmUE), 2018. https://theses.hal.science/tel-02100507 (accessed 2024-08-14).

(232) Bidaud, T. Characterization of Nanomaterials by Cathodoluminescence for Photovoltaic Applications. phdthesis, Université Paris-Saclay, 2021. https://theses.hal.science/tel-03283375 (accessed 2024-08-14).

(233) Chen, H.-L.; Scaccabarozzi, A.; De Lépinau, R.; Oehler, F.; Lemaître, A.; Harmand, J.-C.; Cattoni, A.; Collin, S. Quantitative Assessment of Carrier Density by Cathodoluminescence. I. $\mathrm{Ga}\mathrm{As}$ Thin Films and Modeling. *Phys. Rev. Appl.* **2021**, *15* (2), 024006. https://doi.org/10.1103/PhysRevApplied.15.024006.

(234) Michaud, A. III-V / Silicon Tandem Solar Cell Grown with Molecular Beam Epitaxy. phdthesis, Sorbonne Université, 2019. https://theses.hal.science/tel-02985382 (accessed 2024-08-15).

List of figures

Figure 1.1. a) III and V elements highlighted in the periodic table and b) some examples of III-V applications. 14
Figure 1.2. III-V semiconductors bandgap versus lattice parameter at 300 K[7]. 15
Figure 1.3. GaN hexagonal wurtzite structure. 16
Figure 1.4. Schematic illustration of polarity along c-axis in wurtzite crystal. Adapted from [17]. 16
Figure 1.5. GaAs zinc-blende structure. 18
Figure 1.6. Drawing of the electrochemical cell designed by Edmond Becquerel and his table of results on the influence of wavelength on photocurrent[31]. 19
Figure 1.7. a) Working principle of a solar cell and b) band diagram representation of the p-n junction. 19
Figure 1.8. Solar PV capacity additions in the Stated Policies Scenario and manufacturing capacities, 2015-2030[35]. 20
Figure 1.9. Evolution of the efficiency of solar cells using different technologies over time, adapted from[38]. 21
Figure 1.10. Representation of Shockley-Queisser detailed-balance limit (black line) achieved by record cells, grey lines showing 75% and 50% of the limit (grey lines). Figure taken from the work of A. Polman [50]. 22
Figure 1.11. Theoretical maximum power conversion efficiency (PCE) as a function of front (top) and rear sub-cell bandgap for 2T (left) and 4T (right) architectures, assuming no absorption losses. The dashed line traces the peak efficiency for the whole range of front-cell bandgaps, and the white circles indicate the maximum power conversion efficiencies. Figure taken from the work of G.E. Eperon[51]. 23
Figure 1.12. Diagram of the architecture of two-terminal (2T) and four-terminal (4T) tandem solar cells. Figure taken from the work of G.E. Eperon[51]. 24
Figure 1.13. Schematic diagram of a MOCVD reactor and table of MOCVD typical process conditions[71]. 27
Figure 1.14. Schematic diagram of a MBE reactor and table of MBE typical process conditions[73]. 28
Figure 1.15. Example of buffer layer stack taken from Bolkhovityanov et al.[80] 29
Figure 1.16. Example of ELO of GaAs taken from Renard et al.[82] 29
Figure 1.17. Representation of existing III-V fabrication processes compared to RP-CVD in terms of pressure. 32
Figure 2.1. Classification of plasmas based on electron densities, energies and temperatures. Adapted from the review of Francisco L. Tabares and Ita Junkar[120]. 37
Figure 2.2. Schematic of reactors with a) capacitively coupled plasma and b) inductively coupled plasma. 38
Figure 2.3. Photo and schematic representation of the RP-CVD reactor. 42
Figure 2.4. a) Helicoidal and b) flat coils for ICP antennas. 43
Figure 2.5. Scheme of the ICP source integration in the plasma reactor. 43
Figure 2.6. Ellipsometry mapping showing GaN thickness variations. 44
Figure 2.7. SEM top view images of different areas of the ITO sample after H_2 plasma exposure. 44
Figure 2.8. Simplified gas panel schematic. 45
Figure 2.9. Substrate holder system diagram with the susceptor in transparency. 46
Figure 2.10. Substrate heating system diagram. 46
Figure 2.11. a), b) Simulations of the substrate heating system using Ansys® and c) a photo of the heated susceptor. 47

Figure 2.12. Photos of results of thermal sticker tests on the substrate at 0.5 mbar and for a setpoint temperature of a) 190°C and b) 240°C. 48
Figure 2.13. Diagram of the E-H transition taken from Piel book[119]. 49
Figure 2.14. Optical emission spectra of (a) H_2/N_2 (1:40) plasma at 3 W, 10 W and 50 W under a total pressure of 0.3 mbar, (b) N_2 C-B (1-0) line tracking as a function of plasma power to identify the E-H transition. 49
Figure 2.15. (a) A pure H_2 plasma at different plasma powers and (b) H_α line tracking as a function of plasma power. 50
Figure 3.1. a) θ-2θ scans of GaN-on-sapphire by RP-CVD at 500°C, 150 W and 0.5 mbar. The inset in b) shows a zoom on the (0002) GaN peak. 56
Figure 3.2. a) SEM surface image and b) SEM cross-section image of GaN-on-sapphire sample. 56
Figure 3.3. a) Cross-sectional STEM-HAADF with the upper part of the film (dotted line area) containing small grains and b) HRTEM image of GaN-on-sapphire sample. 57
Figure 3.4. Schematic diagram of the GaN growth process from the nucleation stage to the merging stage of the crystal islands on (a) sapphire substrate and (b) AlN/sapphire template[142]. 58
Figure 3.5. Ellipsometry measurement of GaN-on-sapphire by RP-CVD with N_2 plasma pretreatment with the corresponding optical model (layer stack) used to fit the data (the symbols represent the measured data points, while the lines correspond to the fit). 59
Figure 3.6. Optimization of growth conditions with parameter-by-parameter effect on growth rate. 61
Figure 3.7. XRD spectrum of a GaN thin film grown by remote-plasma CVD. Operating conditions of sample S9 (see **Table 3.2**). 61
Figure 3.8. Ellipsometry measurement of GaN-on-Si by RP-CVD with the corresponding optical model (layer stack) used to fit the data. Operating conditions of sample S9 (see **Table 3.2**). 63
Figure 3.9. Cross-section a) and top-view b) SEM images of a 550 nm thick GaN film on c-Si, b') statistical distribution of the grain size and c) AFM image of the GaN thin film. Operating conditions of sample S9 (see **Table 3.2**). 64
Figure 3.10. SEM surface image (a) before and (b) after KOH etching on GaN thin film by RP-CVD. 65
Figure 3.11. Plot of combined RBS-NRA in-depth profile of GaN on Si by RP-CVD. Operating conditions of sample S9 (see **Table 3.2**). 66
Figure 3.12. Carbon concentration and III/V ratio over the thickness of the GaN layer as a function of RF plasma power from combined NRA and RBS analyses. Operating conditions of sample 9 except for the RF power (see **Table 3.2**). 67
Figure 3.13. a) The growth process of GaN via RP-CVD including the in-situ surface cleaning step (2) and the silicon surface nitridation step (3). b) Ellipsometry measurement of the SiN layer formed on silicon substrate with the corresponding optical model used to fit the data. 69
Figure 3.14. a)[181], b)[175] Examples of SEM images highlighting macroscopic effects of 'meltback etching' at the GaN/Si interface from the literature and c) SEM image of our sample. 70
Figure 3.15. a_1) SEM top-view at early stages of GaN direct growth with AFM inset showing the height of the Ga puddles, b_1) similar image obtained on the sample having a SiN barrier layer. a_2), b_2) SEM cross-section of thick GaN films grown on c-Si without and with SiN barrier layer respectively. 71
Figure 3.16. TEM analysis of GaN-on-Si a) without nitridation and b) with nitridation. a_1), b_1) BF-STEM images, a_2), b_2) HR-TEM images and a_3), a_4) and b_3) local fast Fourier transforms images. 72
Figure 3.17. STEM-EDX a_1), b_1) mapping and a_2), b_2) line-scan of gallium and silicon elements for GaN-on-Si growth (a) without and (b) with SiN. 73
Figure 3.18. GaN-on-Si a) without and b) with SiN. a_1), a_2) AFM images of GaN surface. a_2), b_2) intensity scans of HRTEM FFT pattern parallel and perpendicular to the interface and c) superposed XRD spectra. 74

Figure 3.19. Proposed growth scenarios for GaN-on-Si by RP-CVD for A) without nitridation and B) with nitridation. 75
Figure 4.1. XRD 2theta-omega scan with HRXRD rocking curve of 004 peak at ϕ = 0° in inset of homoepitaxial GaAs grown by RP-CVD. 81
Figure 4.2. 111 in-plane pole figure of homoepitaxial GaAs grown by RP-CVD. 81
Figure 4.3. a) BF-STEM image of homoepitaxial GaAs grown by RP-CVD and b) the SAED pattern corresponding to the star symbol zone in inset. 82
Figure 4.4. a) SEM cross section image and b) AFM surface image of homoepitaxial GaAs grown by RP-CVD on a n-type GaAs substrate (doping level of 1.10^{18} cm^{-3}). 83
Figure 4.5. a) In-depth profile of As, Ga, C and O from the surface to the bulk of the GaAs layer grown by RP-CVD and b-f) corresponding high energy resolution spectra of As 3d, Ga 3d, C 1s, O 1s photopics and O-KLL transition. Note that after the first etching, the peaks shapes and intensity remain the same, what is an indication that de composition and chemistry are remarkably constant inside the layer. The stoichiometry was calculated by averaging the 10 analysis points within 100-1000 s etch time. 84
Figure 4.6. a) Photoluminescence spectra and b) ECV profile of homoepitaxial GaAs grown by RP-CVD and GaAs n-type wafer. 85
Figure 4.7. Cathodoluminescence mapping of a) the energy peak position and b) the intensity around the CL peak at 1.42 eV (with width of 0.1 eV) of homoepitaxial GaAs grown by RP-CVD. 85
Figure 4.8. Photos of GaAs samples on c-Si produced at different substrate temperatures, after 30 minutes of growth with in blue a representation of the thickness profile according to the region, either diffuse or non-diffuse. 86
Figure 4.9. XRD spectra of GaAs on c-Si at different temperatures for acquisitions taken from a) the bright center and b) the rough edge of the samples. 87
Figure 4.10. SEM surface images of GaAs-on-Si grown at 550°C for different positions on the wafer as shown on the left. 88
Figure 4.11. SEM cross section images GaAs samples on c-Si produced at different substrate heating temperatures, after 30 minutes of growth. 88
Figure 4.12. a) BF-STEM image, b) higher magnification TEM image and c) HRTEM image of GaAs-on-Si grown at 550°C. 89
Figure 4.13. Schematic illustration of the experimental process flow for the production of virtual (epi Ge/c-Si) substrates and their application for the growth of GaAs layers by RP-CVD[110]. 90
Figure 4.14. Ellipsometry measurement of GaAs grown on virtual substrate with the corresponding optical model (layer stack) used to fit the data. 90
Figure 4.15. a) 111 in-plane pole figure of GaAs and Si and b) the corresponding scheme showing the crystal twinning of the GaAs grown layer. 91
Figure 4.16. a), b) HRTEM images of a crystal twinning in GaAs on virtual substrate and c) its local fast Fourier transforms image. 92
Figure 4.17. HR-XRD measurement of reflection from the (004) planes of the GaAs thin film grown on a virtual substrate. 92
Figure 4.18. In-plane grazing incidence XRD measurement of reflections from the {220} planes of the GaAs thin film grown on a virtual substrate. 93
Figure 4.19. HRXRD rocking curve of 004 peak at ϕ = 0° of homoepitaxial GaAs grown by RP-CVD on Ge-virtual substrate. 94
Figure 4.20. a) Low magnification TEM image and b) higher magnification BF-TEM image with the arrow showing the ultrathin Ge layer between the GaAs RP-CVD grown layer and the virtual substrate. 95
Figure 4.21. TEM cross-section image with the TDD values on different areas. 95
Figure 4.22. STEM-EDX mapping of GaAs grown on a virtual substrate made of ultrathin Ge on c-Si substrate. 96
Figure 4.23. Normalized photoluminescence spectra of GaAs on virtual substrate and GaAs wafer. 97

Figure 4.24. Cathodoluminescence mapping of a) the energy peak position and b) the intensity around the CL peak at 1.42 eV (with width of 0.1 eV) of GaAs grown on a virtual substrate. 97
Figure 5.1. Targeted solar cell stack. 103
Figure 5.2. a) Sample stack with analysis acquisition direction and b) table of RP-CVD growth conditions used. 104
Figure 5.3. SEM cross section image of the stack described in **Figure 5.2**. 104
Figure 5.4. Carrier concentration profiles as deduced from ECV measurements and impurities concentration profiles as deduced from SIMS measurements on a) the stack sample presented in **Figure 5.2** and b) the n-type substrate. 105
Figure 5.5. Normalized photoluminescence spectra of homoepitaxial RP-CVD GaAs with (RP-CVD) and without ('MOCVD-like') plasma and n-GaAs wafer. 106
Figure 5.6. Raman spectra of GaAs samples grown with (RP-CVD) and without plasma ('MOCVD-like') conditions. 107
Figure 5.7. a) Mobility vs. doping level plot from our optimization samples with a linear fit and b) mobility vs. doping concentration plot from empirical fit obtained in M. Sotoodeh work[216] with experimental data points taken from some references[217–222]. 108
Figure 5.8. a) Growth rate and b) hole concentration and mobility for arsine introduced either via ICP or hydride lines at 500°C, 150 W, V/III = 18 and 0.5 mbar. The dotted lines are provided as a guide to the eye. 109
Figure 5.9. a) Growth rate and b) hole concentration and mobility for different deposition temperatures with AsH_3 in 'ICP' line, at 150 W, V/III = 18 and 0.5 mbar. The dotted lines are provided as a guide to the eye. 110
Figure 5.10. a) Growth rate and b) hole concentration and mobility for different plasma power values with AsH_3 in 'ICP' line, at 500°C, 150 W, V/III = 18 and 0.5 mbar. The dotted lines are provided as a guide to the eye. 111
Figure 5.11. a) Growth rate and b) hole concentration and mobility for different chamber pressures with AsH_3 in 'ICP' line, at 500°C, 150 W and V/III = 18. The dotted lines are provided as a guide to the eye. 112
Figure 5.12. Rocking curve of 004 peak at $\phi = 0°$ of GaAs grown using TEGa. 114
Figure 5.13. SEM cross-section image of GaAs grown with TEGa at 500°C, 150 W and 0.5 mbar. 115
Figure 5.14. a) Hyperspectral mapping of the PL peak position, b) TRPL decays at different wavelengths of homoepitaxial GaAs grown by RP-CVD at 500°C, 150 W and 0.5 mbar. 117
Figure 5.15. Configuration design of the first solar cell fabricated with RP-CVD GaAs grown with TMGa as absorber. 118
Figure 5.16. Optical microscope image of one of the obtained solar cell. 118
Figure 5.17. a) Light and b) dark I-V curves of the 1st solar cell made of RP-CVD GaAs absorber. 119
Figure 5.18. Light I-V curve for the best solar cell grown with TMGa. 119
Figure 5.19. a) IQE, EQE and RFL spectrum of the obtained solar cells and b) fitting parameters for the different layers. 121
Figure 5.20. Configuration design of the first solar cell fabricated with RP-CVD GaAs grown with TEGa as absorber. 122
Figure 5.21. Light I-V curve for the best solar cell grown with TEGa without ARC (compared with TMGa one). 123
Figure 5.22. Reflectivity spectra for the ARC stack layer design. 124
Figure 5.23. Photograph of the cells grown with TEGa after ARC deposition. 124
Figure 5.24. Light I-V curve for the best solar cell grown with TEGa with ARC (compared with TEGa without ARC and TMGa). 125
Figure D.1. a) Table of process conditions and b) doping levels and mobilities for each sample of the optimization study. 139

List of tables

Table 1.1. Some GaN material properties at room temperature[22–24]. 17
Table 1.2. Some GaAs material properties at room temperature[24,30]. 18
Table 2.1. Different frequency ranges for plasma sources[121]. 37
Table 2.2. Bibliographical survey on plasma CVD growth of III-V materials. 41
Table 3.1. Comparison of buffer layer growth techniques, temperatures and GaN crystalline quality obtained. 54
Table 3.2. Growth conditions for 11 samples of GaN thin films produced by RP-CVD. S9 conditions have been chosen for the detailed characterization of the film in this section. 60
Table 3.3. Crystallite size calculation from Scherrer formula. Operating conditions of sample S9 (see **Table 3.2**). 62
Table 5.1. Hall effect results for GaAs grown using TMGa or TEGa. Both sample deposited at a nominal temperature of 500°C. 114
Table 5.2. Performance of the best solar cell grown with TMGa. 120
Table 5.3. Performance of the best solar cell grown with TEGa (without ARC). 123
Table 5.4. Performance of the best solar cell grown with TEGa with ARC. 125

Scientific contributions

Patent – *Growth of low-cost GaAs on Si using virtual substrate and RP-CVD*.
With Pere Roca i Cabarrocas and Karim Ouaras.

a. Publications

- *Direct growth of highly oriented GaN thin films on Si by remote plasma CVD*.
  Lise Watrin, François Silva, Cyril Jadaud, Pavel Bulkin, Jean-Charles Vanel, Dominique Muller, Erik V. Johnson, Karim Ouaras, and Pere Roca i Cabarrocas
  Journal of Physics D: Applied Physics
  May 2024
  https://iopscience.iop.org/article/10.1088/1361-6463/ad436c

- *Homoepitaxial growth of high-quality GaAs using remote plasma CVD*.
  Lise Watrin, François Silva, Cyril Jadaud, Pavel Bulkin, Jean-Charles Vanel, Erik V. Johnson, Karim Ouaras, and Pere Roca i Cabarrocas
  Materials Science in Semiconductor Processing
  August 2024
  https://doi.org/10.1016/j.mssp.2024.109069

- *Self-formation of SiGe oxide, Ge, and void multilayers via thermal oxidation of hydrogenated epitaxial SiGe films*.
  Junyang An, Ruiling Gong, Xinyu Li, Ileana Florea, Lise Watrin, Pere Roca i Cabarrocas, Wanghua Chen
  Vacuum
  April 2023
  https://doi.org/10.1016/j.vacuum.2023.112072

- *Ultrathin SiN barrier enables improved GaN growth on Si by remote-plasma CVD*.
  Lise Watrin, Kassiogé Dembélé, François Silva, Cyril Jadaud, Pavel Bulkin, Jean-Charles Vanel, Jean-Luc Maurice, Erik V. Johnson, Karim Ouaras, and Pere Roca i Cabarrocas
  Submitted to Applied Surface Science
  August 2024

- *Low-cost doped GaAs layers by RP-CVD for affordable solar cells*.
  Lise Watrin, François Silva, Cyril Jadaud, Pavel Bulkin, Jean-Charles Vanel, Erik V. Johnson, Karim Ouaras, and Pere Roca i Cabarrocas
  Under preparation

- *Challenges in accurate quantification of GaN chemical composition: a comparative study of characterization tools*.
  Lise Watrin, François Silva, Cyril Jadaud, Pavel Bulkin, Jean-Charles Vanel, Muriel Bouttemy, Mirella Al Katrib, Dominique Muller, François Jomard, Erik V. Johnson, Karim Ouaras, and Pere Roca i Cabarrocas
  Under preparation

b. Conferences

- **Oral presentation** – *Low temperature plasma deposition processes for GaN thin films*.
  Lise Watrin, Lakshman Srinivasan, François Silva, Cyril Jadaud, Pavel Bulkin, Jean-Charles Vanel, Erik V. Johnson, Karim Ouaras, and Pere Roca i Cabarrocas
  International Conference on Amorphous and Nanocrystalline Semiconductors (ICANS30), *August 5-8, 2024, Manchester (UK)*

- **Poster** – *Remote-plasma CVD as a new process for III-V thin films growth*.
  Lise Watrin, François Silva, Cyril Jadaud, Pavel Bulkin, Jean-Charles Vanel, Erik V. Johnson, Karim Ouaras, and Pere Roca i Cabarrocas
  42nd European Photovoltaic Solar Energy Conference *(EUPVSEC), Septembre 23-27, 2024, Vienna (Austria)*

- **Invited talk** – *Study of III-V thin films growth directly on silicon by remote-plasma CVD: Towards a reduction in solar cell industrialisation costs*.
  Lise Watrin, François Silva, Cyril Jadaud, Pavel Bulkin, Jean-Charles Vanel, Erik V. Johnson, Karim Ouaras, and Pere Roca i Cabarrocas
  20th International Conference on Crystal Growth and Epitaxy *(ICCGE20), July 30 - August 4, 2023, Naples (Italy)*

- **Oral presentation** – *Study of III-V thin films growth directly on silicon by remote-plasma CVD: Towards a reduction in solar cell industrialisation costs*.
  Lise Watrin, François Silva, Cyril Jadaud, Pavel Bulkin, Jean-Charles Vanel, Erik Johnson, Karim Ouaras, Pere Roca i Cabarrocas
  Plasma Thin Film International Union Meeting *(PLATHINIUM), September 11-15, 2023, Antibes (France)*

- **Oral presentation** – *Routes for low cost III-V solar cells*.
  Lise Watrin, François Silva, Cyril Jadaud, Pavel Bulkin, Jean-Charles Vanel, Erik V. Johnson, Karim Ouaras, and Pere Roca i Cabarrocas
  3rd Momentom International Congress *(MOMENTOM2023), March 8-10, 2023, Gif-sur-Yvette (France)*

- **Poster** – *Study of III-V semiconductors growth by PECVD: Towards a reduction in solar cell industrialization costs*.
  Lise Watrin, François Silva, Cyril Jadaud, Pavel Bulkin, Jean-Charles Vanel, Erik V. Johnson, Karim Ouaras, and Pere Roca i Cabarrocas
  7th European Conference on Crystal Growth *(ECCG7), July 25-27, 2022, Paris (France)*

- **Poster** – *Low-temperature growth of GaN directly on silicon by remote plasma CVD: Towards a reduction in III-V solar cell costs*.
  Lise Watrin, François Silva, Cyril Jadaud, Pavel Bulkin, Jean-Charles Vanel, Mirella Al Katrib, Muriel Bouttemy, Erik V. Johnson, Karim Ouaras, and Pere Roca i Cabarrocas
  Journées Nationales du Photovoltaïque *(JNPV), November 29 – December 2, 2022, Dourdan (France)*

- **Oral presentation** - *EBSD analysis of III-V layers on Ge:Si virtual substrates for multijunction solar cells*
  Elisa García-Tabarés, Víctor Orejuela, Lise Watrin, Beatriz Galiana, Pere Roca i Cabarrocas, Ignacio Rey-Stolle, Iván García
  19th International Conference on Thin Films *(ICTF2023), September 26-29, 2023, Burgos (Spain)*

ECOLE DOCTORALE

Titre : Épitaxie de III-V par RP-CVD : de la croissance de couches minces aux dispositifs de cellules solaires

Mots clés : semi-conducteurs III-V, épitaxie, PECVD, couche mince, plasma, cellule solaire

Résumé : Les cellules solaires composées de semi-conducteurs III-V ont atteint le rendement le plus élevé parmi toutes les technologies actuellement disponibles, affichant une efficacité dépassant les 47% sous concentration. Cependant, leur coût de production est environ cent fois supérieur à celui des cellules solaires en silicium, la technologie qui domine le marché (95% en 2023). Réduire le coût des semi-conducteurs III-V représenterait une avancée majeure vers l'accroissement de la part du solaire dans le mix énergétique. En particulier, combiner les III-V avec le silicium, en configuration « tandem », permettrait de convertir un maximum d'énergie du spectre solaire. Le prix élevé de cette technologie s'explique notamment par le coût afférent au processus de fabrication des cellules solaires III-V, à celui du substrat et au procédé d'épitaxie de III-V. Les travaux de cette thèse s'attaquent spécifiquement à ce troisième défi. À cette fin, nous avons développé une nouvelle approche utilisant un réacteur de dépôt chimique en phase vapeur par plasma déporté (RP-CVD). L'ajout d'un plasma dans le réacteur s'avère très avantageux car il permet (i) une croissance à basse pression (~1 mbar) qui contribue à une réduction de la consommation de gaz, (ii) une dissociation efficace des précurseurs conduisant à une réduction de la température de croissance, et (iii) des traitements de surface in situ, réduisant le nombre et la complexité des étapes du procédé. Nous avons développé et optimisé ce réacteur, entièrement construit dans le laboratoire (LPICM, Ecole polytechnique), pour la croissance de matériaux III-V, à savoir le nitrure de gallium (GaN) puis l'arséniure de gallium (GaAs). Pour le GaN, nous avons réalisé une croissance épitaxiée sur saphir et une croissance fortement orientée selon (0002) sur du c-Si à une basse température de 500°C. Nous avons proposé une solution innovante pour la croissance directe de GaN sur c-Si et relevé les défis associés à l'utilisation de techniques standard pour analyser la composition de matériaux produits par des procédés non conventionnels. Pour le GaAs, nous avons obtenu une croissance homoépitaxiale de haute qualité à 500°C et 3 µm/h, optimisé le dopage et développé des cellules solaires de démonstration atteignant une efficacité de 15,5 %. Ces travaux abordent également la question du coût des substrats grâce à la réalisation d'une croissance hétéroépitaxiale sur des substrats virtuels, le tout à basse pression, proposant un ensemble de solutions viables pour produire des cellules solaires à haut rendement et à faible coût.

Title: III-V epitaxy by RP-CVD: from thin film growth to solar cell devices

Key words: III-V semiconductors, epitaxy, PECVD, thin film, plasma, solar cell

Abstract: Solar cells based on III-V materials have reached the highest efficiency of any technology available today, i.e. up to 47% under concentration. However, their production cost is approximately a hundred times higher than that of c-Si solar cell, the technology that dominates the market (95% in 2023). Reducing the cost of III-V semiconductors would represent a major advancement towards increasing the share of solar energy in the energy mix. Specifically, combining III-V with silicon in tandem configuration would maximize energy conversion from the solar spectrum. The high price of this technology is mainly due to the III-V solar cell processing, the substrate and the III-V epitaxy process. This PhD thesis specifically addresses this third challenge. To this end, we have developed a new approach by using a Remote Plasma Chemical Vapor Deposition (RP-CVD) reactor. The addition of a plasma in the reactor proves advantageous, as it allows (i) low pressure growth (~1 mbar) which contribute to a reduction of gases consumption, (ii) efficient dissociation of precursors leading to a reduction in growth temperature and (iii) in-situ surface treatments, reducing the number and complexity of processing steps. We have developed and optimized this innovative reactor, entirely built in the laboratory (LPICM, Ecole Polytechnique), for the growth of III-V materials, namely gallium nitride (GaN) and then gallium arsenide (GaAs). For GaN, we have achieved epitaxial growth on sapphire and highly (0002) oriented growth on c-Si at a low temperature of 500°C. We have proposed an innovative solution for the direct growth of GaN on c-Si and addressed the challenges associated with using standard techniques to analyze the composition of materials produced through non-conventional processes. For GaAs, we have obtained high-quality homoepitaxial growth at 500°C and 3 µm/h, optimized doping, and developed proof-of-concept solar cells with an efficiency of 15,5%. This work also tackles the issue of substrate cost by achieving heteroepitaxial growth on virtual substrates, all at low pressure, proposing a set of viable solutions for producing high-efficiency, low-cost solar cells.

Institut Polytechnique de Paris
91120 Palaiseau, France